Galaxy clustering in standard and non-standard cosmologies

CESAR HERNANDEZ-AGUAYO

Galaxy clustering in standard and non-standard cosmologies

César Hernández Aguayo

A Thesis presented for the degree of
Doctor of Philosophy

Institute for Computational Cosmology
Department of Physics
University of Durham
United Kingdom

July 2020

To Sebastián and our new sunshine, Emiliano

Galaxy clustering in standard and non-standard cosmologies

César Hernández Aguayo

Submitted for the degree of Doctor of Philosophy
July 2020

Abstract

We study the formation, evolution and clustering of galaxies in standard and modified gravity universes and prepare synthetic catalogues for future galaxy surveys, such as DESI. To do this, we have run and analysed N-body and hydrodynamical simulations of different gravity models. In the first part, we focus our attention on two of the most representative and popular families of modified gravity models: the Hu & Sawicki $f(R)$ gravity and the normal-branch Dvali-Gabadadze-Porrati (nDGP) braneworld model. We use mock galaxy catalogues constructed from a halo occupation distribution (HOD) prescription with the HOD parameters in the modified gravity models tuned to match with the number density and the real-space clustering of BOSS-CMASS galaxies to analyse the marked correlation function in three variants of the $f(R)$ gravity model and to measure galaxy clustering in redshift space in both $f(R)$ and nDGP models. In addition, we introduce the first set of full-hydrodynamical simulations of galaxy formation in the nDGP model using a new modified version of the Arepo code and the IllustrisTNG galaxy formation model. In the second half, we explore if there is an optimal way to select a galaxy sample in order to measure the baryon acoustic oscillation (BAO) scale, which is used as a standard ruler to constrain the cosmic expansion. Also, we present a covariance and clustering analysis of DESI-like luminous red galaxies (LRGs). For the latter, the mock catalogues are built with a novel technique using the semi-analytical model of galaxy formation Galform and a large number of halo catalogues generated using the Parallel-PM N-body glam code.

Declaration

The work described in this thesis was undertaken between 2016 and 2020 while the author was a research student under the supervision of Prof. Carlton M. Baugh, Prof. Baojiu Li and Dr. Christian Arnold at the Institute for Computational Cosmology in the Department of Physics at the University of Durham. No part of this thesis has been submitted for any other degree at the University of Durham or any other university.

The contents of this work have appeared in the following papers:

- **C. Hernández-Aguayo**, C. M. Baugh and B. Li, "Marked clustering statistics in $f(R)$ gravity cosmologies", Mon. Not. Roy. Astron. Soc. **479** (2018) no.4, 4824-4835 doi:10.1093/mnras/sty1822 [arXiv:1801.08880 [astro-ph.CO]] (**Chapter 2**).

- **C. Hernández-Aguayo**, J. Hou, B. Li, C. M. Baugh and A. G. Sánchez, "Large-scale redshift space distortions in modified gravity theories", Mon. Not. Roy. Astron. Soc. **485** (2019) no.2, 2194-2213 doi:10.1093/mnras/stz516 [arXiv:1811.09197 [astro-ph.CO]] (**Chapter 3**).

- **C. Hernández-Aguayo**, C. Arnold, B. Li and C. M. Baugh, "Galaxy formation in the brane world I: overview and first results", 2020, submitted to Mon. Not. Roy. Astron. Soc. [arXiv:2006.15467 [astro-ph.CO]] (**Chapter 4**).

- **C. Hernández-Aguayo**, M. Cautun, A. Smith, C. M. Baugh and B. Li, "Measuring the BAO peak position with different galaxy selections", Mon. Not. Roy. Astron. Soc. **494** (2020) no.3, 3120-3130 doi:10.1093/mnras/staa973 [arXiv:1912.01099 [astro-ph.CO]] (**Chapter 5**).

- **C. Hernández-Aguayo**, F. Prada, C. M. Baugh and A. Klypin, "Building a digital twin of a luminous red galaxy spectroscopic survey: galaxy properties and clustering covariance", 2020, submitted to Mon. Not. Roy. Astron. Soc. [arXiv:2006.00612 [astro-ph.CO]] (**Chapter 6**).

The analysis presented in Section 3.4.2 of Chapter 3 and in Appendix A was performed by Jiamin Hou, but is included here for completeness.

Acknowledgements

First of all, I am very grateful to my supervisors, Carlton Baugh, Baojiu Li and Christian Arnold for your enthusiasm, guidance and support and for allowing me to get involve in such amazing and exciting projects during my PhD. I hope to continue working with you in future projects. I am so glad for being part of the modified gravity group at the ICC.

I am also grateful to all my collaborators: Jiamin Hou, Ariel Sánchez, Marius Cautun, Alex Smith, Paco Prada and Anatoly Klypin. Many thanks for contributing to the work presented in this thesis. A special thanks goes to the COSMA support team.

I am thankful to all my friends inside Astronomy: Jiamin, Omar, Cristian, Carol, Christoph, Lizelke and Sutieng. Many thanks to all for sharing with me so lovely experiences during these four years. Particular thanks to Anna, for being such amazing office mate. To Maura, for becoming a part of my small family in Durham.

I would like to thank to the Consejo Nacional de Ciencia y Tecnología (CONACyT) for providing me the scholarship to pursue this degree.

A mis padres, J. Carmen y María de los Ángeles. Gracias por su apoyo incondicional. Simplemente sin su ayuda, hoy no estaría cumpliendo mi sueño de venir a estudiar al extranjero.

Por último, estoy eternamente agradecido con Alma por darme los mejores regalos de la vida: Sebastián y nuestro nuevo pequeño, Emiliano. Alma, muchas gracias por estar siempre apoyándome y dándome ánimos, sabes que eres el pilar más importante de nuestra pequeña familia.

Contents

List of Figures

List of Tables

Chapter 1

Introduction

1.1 Standard cosmological model

The standard cosmological model is based on the cosmological principle which states that the Universe is homogeneous and isotropic over sufficiently large scales ($\gtrsim 100$ Mpc[1]). It also establishes that the matter content of the Universe is currently dominated by two exotic components: dark energy in the form of a cosmological constant (Λ) and cold dark matter (CDM). Both components contribute to the $\sim 95\%$ of the energy density of the Universe at the present time ($\sim 69\%$ from dark energy and $\sim 26\%$ from dark matter), the remaining $\sim 5\%$ is in the form of known baryonic matter, such as stars and gas (Planck Collaboration, 2018). However, the identities of the dark energy and dark matter remain unknown. Therefore, one of the key aims of modern cosmology is to reveal the identities of these two dark components by exploring the Universe with galaxy surveys. Additionally, the standard cosmological paradigm assumes that the gravitational interactions in the Universe are described by the theory of General Relativity (GR) on all scales.

The cosmological principle implies that the metric of the background homogeneous and isotropic Universe is given by the Friedmann-Lemaître-Robertson-Walker

[1]One parsec (1pc) is defined as the distance at which one astronomical unit (the distance from the Earth to the Sun) subtends an angle of one arcsecond (1/3600 of a degree). In the SI metric system: $1\text{pc} = 3.0857 \times 10^{16}\text{m}$ and $1\text{Mpc} = 10^{6}\text{pc}$.

(FLRW) space-time,

$$\mathrm{d}s^2 = g_{\mu\nu}\mathrm{d}x^\mu \mathrm{d}x^\nu = -\mathrm{d}t^2 + a^2(t)\left[\frac{\mathrm{d}r^2}{1-Kr^2} + r^2(\mathrm{d}\theta^2 + \sin^2\theta \mathrm{d}\phi^2)\right], \tag{1.1.1}$$

where $g_{\mu\nu}$ is the metric tensor, t is the cosmic time, $a(t)$ is the scale factor, K characterises the geometry or curvature of the universe and r, θ, ϕ are spherical comoving coordinates. To derive the above expression, we have used the convention that the speed of light has a value of $c = 1$, Greek indices μ, ν, run over $0, 1, 2, 3$ and the metric convention $(-, +, +, +)$. Throughout this thesis, we will continue using this convention unless otherwise stated. From the FLRW metric we can see that K may take units of length^{-2} if r has units of length and $a(t)$ is unitless. Also, K can take values of $K < 0, K = 0, K > 0$ to represent an open, flat or closed universe.

The dynamics of the ΛCDM model is given by the Friedmann equations (Friedmann, 1924) which are derived from Einsten's field equations (Einstein, 1916),

$$R_{\mu\nu} - \frac{1}{2}g_{\mu\nu}R + \Lambda g_{\mu\nu} = 8\pi G T_{\mu\nu}\,, \tag{1.1.2}$$

where $R_{\mu\nu}$ is the Ricci curvature tensor, R is the Ricci curvature scalar and $T_{\mu\nu}$ is the energy-momentum tensor of matter components. We assume that $T_{\mu\nu}$ takes the form of the perfect fluid,

$$T_{\mu\nu} = (\rho + p)u_\mu u_\nu + p g_{\mu\nu}\,, \tag{1.1.3}$$

where u_μ is the 4-velocity of the fluid, ρ and p are the mean energy density and pressure of the fluid as a function of time, respectively.

Finally, using Eqs. (1.1.1) and (1.1.3) into Eqs. 1.1.2 we obtain the Friedmann equations,

$$H^2 = \frac{8\pi G}{3}\rho + \frac{\Lambda}{3} - \frac{K}{a^2}\,, \tag{1.1.4}$$

$$\frac{\ddot{a}}{a} = -\frac{4\pi G}{3}(\rho + 3p) + \frac{\Lambda}{3}\,. \tag{1.1.5}$$

Where $H(t) \equiv \dot{a}/a$ is the Hubble factor which describes the expansion rate of the Univere, G is the gravitational constant. The overdot in above expressions denotes a derivative with respect to the cosmic time, t.

Equation 1.1.4 can be written as,

$$\Omega_{\rm m} + \Omega_\Lambda + \Omega_K = 1\,, \tag{1.1.6}$$

where

$$\Omega_{\rm m} \equiv \frac{8\pi G\rho}{3H^2}\,, \quad \Omega_\Lambda \equiv \frac{\Lambda}{3H^2}\,, \quad \Omega_K \equiv -\frac{K}{(aH)^2}\,, \tag{1.1.7}$$

are the so-called density parameters for matter components, $\Omega_{\rm m}$, cosmological constant, Ω_Λ, and curvature, Ω_K, respectively. Current cosmological measurements set the present-day value of $\Omega_K^{(0)} = 0.001 \pm 0.002$ (Planck Collaboration, 2018). Therefore, we can conclude that we inhabit a flat universe.

We can also obtain the continuity equation of the fluid from $\nabla_\mu T^{\mu\nu} = 0$ (where ∇_μ is the covariant derivative),

$$\dot\rho + 3H(\rho + p) = 0\,. \tag{1.1.8}$$

and the relation between energy density and pressure is given by the equation of state,

$$w(t) = p(t)/\rho(t)\,. \tag{1.1.9}$$

If we assume $w = $ const., and $K = 0$, the solutions of Eqs. (1.1.4), (1.1.5) and (1.1.8) are,

$$\rho(t) = \rho_0 a(t)^{-3(1+w)}\,, \quad a(t) = a_0 t^{2/[3(1+w)]}\,, \quad H(t) = \frac{2}{3(1+w)t}\,, \tag{1.1.10}$$

where ρ_0 and a_0 are constants. For relativistic species (electrons and photons), non-relativistic matter (dark matter and baryons) and the cosmological constant, the equation of state, Eq. (1.1.9), takes values of $w = 1/3, 0, -1$, respectively. For example, the evolution of a radiation-dominated universe is given by $\rho \propto a^{-4}$ and $a \propto t^{1/2}$. The evolution of the matter-dominated universe is given by $\rho \propto a^{-3}$ and $a \propto t^{2/3}$. For the cosmological constant-dominated universe, the energy density is constant and $a \propto e^{Ht}$, where $H = $ const.

As we mentioned above, the cosmological principle states homogeneity and isotropy in the Universe. However, we do observe inhomogeneities and irregularities in the local region of the Universe such as stars and galaxies. These inhomogeneities can be related to small perturbations evolving on the background (homogeneous) Universe

that have grown in time due to gravitational instabilities overcoming the expansion of the Universe, until collapse to form a dark matter halo. It has been proposed that galaxies form inside those dark matter haloes (White & Rees, 1978).

To explore the formation and growth of structures in the Universe we can consider the evolution of the initial density field using linear perturbation theory. Hence, it is useful to express the matter density in terms of the background density ($\bar{\rho}(t)$) and the density contrast or overdensity ($\delta(t, \boldsymbol{x})$),

$$\rho(t, \boldsymbol{x}) = \bar{\rho}(t)[1 + \delta(t, \boldsymbol{x})]\,. \tag{1.1.11}$$

Then, the relevant equations of motion for the overdensity (δ) using the Newtonian approximation are the continuity equation, Euler's equation and the Poisson equation:

$$\frac{\partial \delta}{\partial t} + \frac{1}{a}\boldsymbol{\nabla} \cdot [(1+\delta)\boldsymbol{v}] = 0\,, \tag{1.1.12}$$

$$\frac{\partial \boldsymbol{v}}{\partial t} + \frac{\dot{a}}{a}\boldsymbol{v} + \frac{1}{a}(\boldsymbol{v}\cdot\boldsymbol{\nabla})\boldsymbol{v} = -\frac{\boldsymbol{\nabla}\Phi}{a} - \frac{\boldsymbol{\nabla} p}{a\bar{\rho}(1+\delta)}\,, \tag{1.1.13}$$

$$\boldsymbol{\nabla}\Phi = 4\pi G\bar{\rho}a\delta\,, \tag{1.1.14}$$

where $\boldsymbol{\nabla}$ is the differential operator over the comoving coordinates, Φ is the gravitational potential and $\boldsymbol{v}$ is the peculiar velocity of the fluid.

For non-relativistic matter, e.g., dark matter, $p = 0$. Then, we can combine Eqs. (1.1.12)−(1.1.14) into a single equation written as,

$$\frac{\partial^2 \delta}{\partial t^2} + 2\frac{\dot{a}}{a}\frac{\partial \delta}{\partial t} - 4\pi G\bar{\rho}\delta = 0\,, \tag{1.1.15}$$

and therefore the solution for the growing mode is given by,

$$\delta(t) \propto D(t)\,, \tag{1.1.16}$$

where $D(t)$ is the linear growth factor, which determines the normalisation of the linear matter power spectrum relative to the initial density perturbation power spectrum. For a matter-dominated universe, the linear growth factor is $D(t) \propto t^{2/3} \propto a(t)$. When the overdensity reaches a value of $\delta \sim 1$, the linear perturbation (analytical) treatment is no longer valid, therefore the non-linear evolution of structures is treated with numerical simulations.

1.2 Modified gravity theory

Theoretically, the ΛCDM model is somewhat unappealing due to the presence of the cosmological constant, the agent behind the accelerating cosmic expansion. The magnitude of the cosmological constant is hard to motivate from a particle physics perspective. There is also a "Why now?" problem: a strong coincidence seems to be required for us to be at the right point in cosmic history to experience comparable energy densities in matter and the cosmological constant, with the latter dominating the current expansion. As a result, alternatives to the cosmological constant have been studied extensively in recent years: one possibility is adding more matter species to the energy-momentum tensor (the so-called dark energy models; see e.g., Copeland et al. 2006); on the other hand there are models that change the left-hand side of Einstein's equations (these models are called modified gravity (MG) models, for reviews see Joyce et al. 2015; Koyama 2016). Here, we focus our attention in MG models.

Moreover, modifications to Einstein's general relativity can lead to interesting effects on all scales. In order to satisfy Solar System constraints these modifications should be hidden in the local environment, hence screening mechanisms have been proposed to recover GR predictions in high-density regions (see Sec. 1.2.3).

As we will show in this thesis, future galaxy surveys such as the Dark Energy Spectroscopic Instrument (DESI, DESI Collaboration et al., 2016) and the space mission Euclid (Laureijs et al., 2011) will be offering the possibility to test the nature of gravity on cosmological scales; allowing us to put tight constraints on the parameter space of such MG models or potentially to rule out deviations from the standard cosmological paradigm.

Here, we give a brief introduction to two of the most representative and popular families of modified gravity models: the Hu & Sawicki $f(R)$ gravity (Hu & Sawicki, 2007) and the normal-branch Dvali-Gabadadze-Porrati (nDGP) braneworld model (Dvali et al., 2000) (see Sec. 1.2.1). Then we present the equations in these models that govern non-linear structure formation (Sec. 1.2.2) and finally briefly explain the screening mechanisms necessary to suppress the effects of modified gravity and recover GR in regions such as the Solar System (Sec. 1.2.3).

1.2.1 Models

$f(R)$ gravity

The modified Einstein equations in $f(R)$ gravity can be obtained by varying the modified Einstein-Hilbert action

$$S = \frac{1}{16\pi G}\int \mathrm{d}^4x\sqrt{-g}(R + f(R)) + S_{\mathrm{m}}(g_{\mu\nu}, \psi_i)\,, \tag{1.2.17}$$

with respect to the metric, $g_{\mu\nu}$,

$$G_{\mu\nu} + f_R R_{\mu\nu} - g_{\mu\nu}\left(\frac{1}{2}f(R) - \Box f_R\right) - \nabla_\mu\nabla_\nu f_R = 8\pi G T^{\mathrm{m}}_{\mu\nu}\,, \tag{1.2.18}$$

where $G_{\mu\nu}$ is Einstein tensor, $\Box = \nabla^\mu\nabla_\mu$ the d'Alambertian, G is the gravitational constant, g is the determinant of the metric, S_{m} is the action of the matter fields ψ_i.

Eq. (1.2.18) contains a new dynamical degree of freedom, known as the *scalaron* field and defined by

$$f_R \equiv \frac{\mathrm{d}f(R)}{\mathrm{d}R}\,. \tag{1.2.19}$$

The amplitude of this scalaron field determines the deviations from GR, with larger $|f_R|$ meaning stronger deviations.

The evolution of the scalaron field is obtained by taking the trace of the modified Einstein equations, Eq. (1.2.18),

$$\Box f_R = \frac{1}{3}(R - f_R R + 2f(R) + 8\pi G\rho_{\mathrm{m}})\,, \tag{1.2.20}$$

where ρ_{m} is the non-relativistic matter density of the Universe.

Various functional forms of $f(R)$ have been proposed in the literature to study modifications to general relativity (for reviews see e.g. De Felice & Tsujikawa 2010; Sotiriou & Faraoni 2010). Here we consider the Hu & Sawicki (2007) model

$$f(R) = -m^2\frac{c_1}{c_2}\frac{(R/m^2)^n}{(R/m^2)^n + 1}\,, \tag{1.2.21}$$

$$f_R = -\frac{c_1}{c_2^2}\frac{n(R/m^2)^{n-1}}{[(R/m^2)^n + 1]^2}\,, \tag{1.2.22}$$

where m is a new mass scale defined as $m^2 \equiv H_0^2\Omega_{\mathrm{m}}$, H_0 is the current value of the Hubble expansion rate, Ω_{m} is the current density parameter of non-relativistic

matter, n, c_1 and c_2 are free dimensionless parameters of the model. To obtain Eqs. (1.2.21) and (1.2.22) we have used the metric signature convention $(-,+,+,+)$ as mentioned above. This specific $f(R)$ model can approximately mimic the background expansion of the ΛCDM model if we fix $c_1/c_2 = 6(\Omega_\Lambda/\Omega_\mathrm{m})$, where $\Omega_\Lambda \equiv 1-\Omega_\mathrm{m}$. Recall that we are assuming a flat universe, i.e., $K = 0$.

Eq. (1.2.22) can be approximated as

$$f_R \approx -n\frac{c_1}{c_2^2}\left(\frac{m^2}{R}\right)^{n+1}, \tag{1.2.23}$$

in the limit $|\bar{R}| \approx 40m^2 \gg m^2$, a condition that is satisfied throughout the cosmic history with reasonable parameter values $\Omega_\mathrm{m} \approx 0.3$ and $\Omega_\Lambda \approx 0.7$, with

$$\bar{R} \approx 3m^2\left[a^{-3} + \frac{2}{3}\frac{c_1}{c_2}\right], \tag{1.2.24}$$

where a is the scale factor, normalised to $a = 1$ at the present time.

From the functional form of the scalaron field, Eq. (1.2.22), we can see that this model has two free parameters, n and c_1/c_2^2. In the literature it is common to use f_{R0}, which has the physical meaning of being the value of f_R today, instead of c_1/c_2^2, where

$$\frac{c_1}{c_2^2} = -\frac{1}{n}\left[3\left(1+4\frac{\Omega_\Lambda}{\Omega_\mathrm{m}}\right)\right]^{n+1} f_{R0}\,. \tag{1.2.25}$$

Therefore, a particular choice of n and f_{R0} fully specifies the Hu-Sawicki $f(R)$ model. In this thesis we focus on the cases of $n = 1$ and $f_{R0} = -10^{-6}, -10^{-5}, -10^{-4}$, referred as F6, F5 and F4, respectively.

Dvali-Gabadadze-Porrati model

In the Dvali, Gabadadze & Porrati (DGP) braneworld model, the Universe is a four-dimensional brane that is embedded in a five-dimensional spacetime (the bulk). The gravitational action of the model is given by

$$\begin{aligned} S \;=\; & \int_\mathrm{brane} \mathrm{d}^4x\sqrt{-g}\left(\frac{R}{16\pi G}\right) + \int_\mathrm{bulk} \mathrm{d}^5x\sqrt{-g^{(5)}}\left(\frac{R^{(5)}}{16\pi G^{(5)}}\right) \\ & + S_\mathrm{m}(g_{\mu\nu},\psi_i), \end{aligned} \tag{1.2.26}$$

where g, R, G and $S_\mathrm{m}(g_{\mu\nu},\psi_i)$ have the same meaning as before on the 4D brane, while $g^{(5)}$, $R^{(5)}$ and $G^{(5)}$ are respectively their equivalents in the 5D bulk. A new

parameter can be defined as the ratio of $G^{(5)}$ and G and is known as the crossover scale, r_c,

$$r_c \equiv \frac{1}{2}\frac{G^{(5)}}{G}. \tag{1.2.27}$$

Here we focus on the normal branch DGP (nDGP) model (Sahni & Shtanov, 2003; Lombriser et al., 2009; Schmidt, 2009b), where the variation of the action, Eq. (1.2.26), yields the modified Friedmann equation

$$\frac{H(a)}{H_0} = \sqrt{\Omega_{\rm m}a^{-3} + \Omega_{\rm DE}(a) + \Omega_{\rm rc}} - \sqrt{\Omega_{\rm rc}}\,, \tag{1.2.28}$$

in a homogeneous and isotropic Universe with $\Omega_{\rm rc} = 1/(4H_0^2r_c^2)$. In this model, deviations from GR can be quantified by the parameter H_0r_c. As we can see from Eq. (1.2.28) if $H_0r_c \to \infty$ then the expansion of the Universe is closer to ΛCDM. Therefore, we consider two nDGP models with $H_0r_c = 5$ and $H_0r_c = 1$ where hereinafter referred as to N5 and N1 which represent a weak and medium deviation from GR, respectively.

1.2.2 Structure formation in modified gravity models

Since we are interested in the growth of structure in different gravity models, we work with the perturbed Friedmann-Robertson-Walker (FRW) metric in the Newtonian gauge

$$\mathrm{d}s^2 = -(1+2\Phi)\mathrm{d}t^2 + a^2(t)(1-2\Psi)\gamma_{ij}\mathrm{d}\vec{x}^2\,, \tag{1.2.29}$$

where Φ and Ψ are the gravitational potentials, and $\vec{x}$ represents comoving coordinates.

In the case of $f(R)$ gravity, non-linear structure formation is determined by the following equations in the quasi-static and weak-field approximations which are known to be good approximations for the regime we are interested in (Bose et al., 2015)

$$\nabla^2\Phi = \frac{16\pi G}{3}a^2\delta\rho_{\rm m} - \frac{a^2}{6}\delta R\,. \tag{1.2.30}$$

for Φ and

$$\nabla^2 f_R = \frac{a^2}{3}\left(\delta R - 8\pi G\delta\rho_{\rm m}\right)\,, \tag{1.2.31}$$

for f_R. ∇^2 is the three-dimensional Laplacian operator, $\delta\rho_{\rm m}$ and δR are the perturbations of non-relativistic matter density and the scalar curvature, respectively. The modified Poisson equation in $f(R)$ gravity, Eq. (1.2.30), can be written as,

$$\nabla^2\Phi = 4\pi G a^2 \delta\rho_{\rm m} - \frac{1}{2}\nabla^2 f_R \,. \tag{1.2.32}$$

On the other hand, structure formation in the nDGP model is governed by the following equations in the quasi-static and weak-field limits (Koyama & Silva, 2007),

$$\nabla^2\Phi = 4\pi G a^2 \delta\rho_{\rm m} + \frac{1}{2}\nabla^2\varphi \,, \tag{1.2.33}$$

$$\nabla^2\varphi + \frac{r_{\rm c}^2}{3\beta_{\rm nDGP}\, a^2}\left[(\nabla^2\varphi)^2 - (\nabla_i\nabla_j\varphi)^2\right] = \frac{8\pi\, G\, a^2}{3\beta_{\rm nDGP}}\delta\rho_{\rm m} \,, \tag{1.2.34}$$

where φ is the scalar degree of freedom in the nDGP model and

$$\beta_{\rm nDGP} = 1 + 2H\, r_{\rm c}\left(1 + \frac{\dot{H}}{3H^2}\right) = 1 + \frac{\Omega_{\rm m} a^{-3} + 2\Omega_\Lambda}{2\sqrt{\Omega_{\rm rc}(\Omega_{\rm m} a^{-3} + \Omega_\Lambda)}}. \tag{1.2.35}$$

In the last expression we have assumed a ΛCDM background.

If we linearise Eq. (1.2.34), the two nonlinear terms in the squared brackets vanish and the modified Poisson equation in the nDGP model, Eq. (1.2.33), can be re-expressed as

$$\nabla^2\Phi = 4\pi G a^2 \left(1 + \frac{1}{3\beta_{\rm nDGP}}\right)\delta\rho_{\rm m}, \tag{1.2.36}$$

which represents a time-dependent and scale-independent rescaling of Newton's constant. Since $\beta_{\rm nDGP}$ is always positive, the formation of structure is enhanced in this model with respect to ΛCDM.

The linear growth for the matter fluctuations in these gravity models can be obtained by solving the equation of the linear growth factor, D,

$$D'' + \left(2 - \frac{3}{2}\Omega_{\rm m}(a)\right) D' - \frac{3}{2}\frac{G_{\rm eff}}{G}\Omega_{\rm m}(a) D = 0 \,, \tag{1.2.37}$$

where $'$ denotes a derivative with respect $\ln a$ and $G_{\rm eff}$ takes values of

$$\frac{G_{\rm eff}}{G} = \begin{cases} 1 & \text{GR}\,, \\ 1 + k^2/[3(k^2 + a^2 m_{f_R}^2)] & f(R)\,, \\ 1 + 1/[3\beta_{\rm nDGP}(a)] & \text{nDGP}\,, \end{cases} \tag{1.2.38}$$

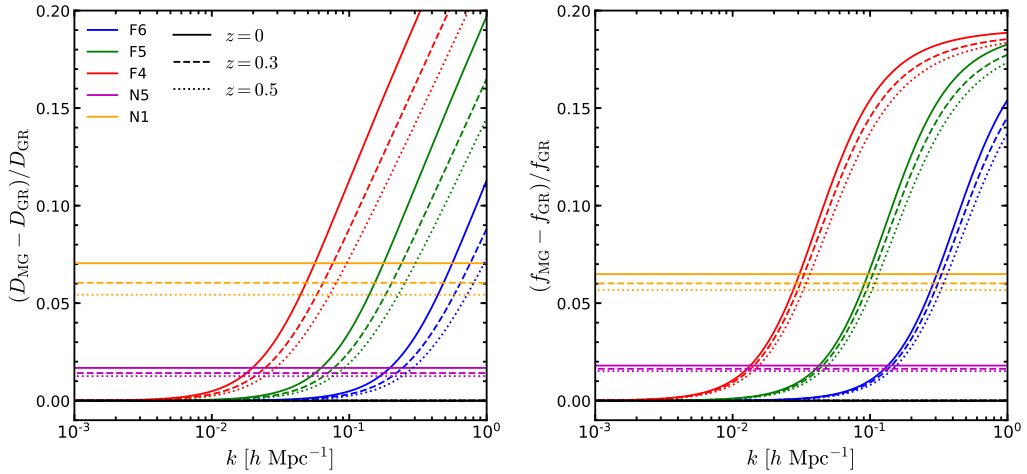

Figure 1.1: Relative difference of the linear growth factor (D Eq. (1.2.37), *left panel*) and the linear growth rate (f Eq. (1.2.39), *right panel*) between different gravity models (F6, F5, F4, N5 and N1) and GR at different redshifts as a function of the wavenumber, k. The colour scheme and line styles are specified in the legend and show different models and redshifts.

here k is the wavenumber, m_{f_R} is the mass of the scalaron field defined by $m^2_{f_R} \simeq [3f_{RR}]^{-1}$. Note that $G^{f(R)}_{\rm eff}$ is a function of time and scale, which means that the linear growth of structure for $f(R)$ gravity is scale dependent. This arises because the scalaron (f_R) is a massive field, while for GR and nDGP is scale independent.

In galaxy surveys we can extract information about the growth of structure through the linear growth rate, f, which is defined as

$$f \equiv \frac{{\rm d}\ln D}{{\rm d}\ln a}\,. \tag{1.2.39}$$

Fig. 1.1 shows the relative difference of the linear growth factor, D, and the linear growth rate, f, at the three redshifts of interest, $z = 0, 0.3, 0.5$, between different modified gravity models and GR (ΛCDM) as a function of scale, k. The relative differences for the nDGP models remain constant because $D_{\rm nDGP}$ and $f_{\rm nDGP}$ are scale-independent. In the case of $f(R)$ gravity, the difference with respect to GR becomes larger at smaller scales ($k > 0.1\,h\,{\rm Mpc}^{-1}$) and lower redshifts, while at $k < 0.01\,h\,{\rm Mpc}^{-1}$ the growth of structure is almost indistinguishable from that in GR.

1.2.3 Screening mechanisms

Chameleon mechanism

In $f(R)$ gravity, the chameleon mechanism (Khoury & Weltman, 2004) is introduced to suppress the enhancement of gravity under certain environmental conditions. Since the scalaron field is massive, with a mass given by

$$m_{f_R}^2 \equiv \frac{\mathrm{d}}{\mathrm{d}f_R}\left(\frac{\mathrm{d}V_{\rm eff}}{\mathrm{d}f_R}\right) \simeq \frac{1}{3f_{RR}}\,, \tag{1.2.40}$$

where the effective potential $V_{\rm eff}$ is defined such that $\mathrm{d}V_{\rm eff}/\mathrm{d}f_R = \Box f_R$; the second equality comes from applying this definition to Eq. (1.2.20). Hence, for $f_{RR} > 0$, the effective potential $V_{\rm eff}$ has a minimum at $f_{R,\rm min}$ satisfying $\partial V_{\rm eff}(f_{R,\rm min})/\partial f_R = 0$. In high-density regions, where $\rho_{\rm m}$ is large, it can be shown, using the expressions of $f(R), f_R$ given above, that m_{f_R} becomes heavy in such that the fifth force decays exponentially as $r^{-2}\exp(-m_{f_R}r)$, leading to recovery of GR. In low-density regions, the fifth force can propagate a further distance, modifying the force law between matter particles. This environmental dependence of the fifth force behaviour earns the screening mechanism the name 'chameleon'.

Vainshtein mechanism

The nDGP model is a representative class of modified gravity models that feature the Vainshtein screening mechanism (Vainshtein, 1972). To illustrate how the Vainshtein mechanism works, let us for simplicity consider solutions in spherical symmetry, where Eq. (1.2.34) can be written in the following form

$$\frac{2r_{\rm c}^2}{3\beta_{\rm nDGP}c^2a^2}\frac{1}{r^2}\frac{\mathrm{d}}{\mathrm{d}r}\left[r\left(\frac{\mathrm{d}\varphi}{\mathrm{d}r}\right)^2\right] + \frac{1}{r^2}\frac{\mathrm{d}}{\mathrm{d}r}\left[r^2\frac{\mathrm{d}\varphi}{\mathrm{d}r}\right] = \frac{8\pi G}{3\beta_{\rm nDGP}}\delta\rho_{\rm m}a^2\,. \tag{1.2.41}$$

Defining the mass enclosed in radius r as

$$M(r) \equiv 4\pi\int_0^r \delta\rho_{\rm m}(r')r'^2\mathrm{d}r', \tag{1.2.42}$$

we can rewrite Eq. (1.2.41) as

$$\frac{2r_{\rm c}^2}{3\beta_{\rm nDGP}c^2}\frac{1}{r}\left(\frac{\mathrm{d}\varphi}{\mathrm{d}r}\right)^2 + \frac{\mathrm{d}\varphi}{\mathrm{d}r} = \frac{2}{3\beta_{\rm nDGP}}\frac{GM(r)}{r^2} \equiv \frac{2}{3\beta_{\rm nDGP}}g_{\rm N}(r), \tag{1.2.43}$$

in which for simplicity we have set $a = 1$, and $g_{\rm N}$ is the Newtonian acceleration caused by the mass $M(r)$ at distance r from the centre, Eq. (1.2.42).

If we assume that $\delta\rho_{\rm m}$ is a constant within radius R and zero outside, then Eq. (1.2.43) has the physical solution

$$\frac{{\rm d}\varphi}{{\rm d}r} = \frac{4}{3\beta_{\rm nDGP}}\frac{r^3}{r_{\rm V}^3}\left[\sqrt{1+\frac{r_{\rm V}^3}{r^3}}-1\right] g_{\rm N}(r), \tag{1.2.44}$$

for $r \geq R$ and

$$\frac{{\rm d}\varphi}{{\rm d}r} = \frac{4}{3\beta_{\rm nDGP}}\frac{R^3}{r_V^3}\left[\sqrt{1+\frac{r_V^3}{R^3}}-1\right] g_{\rm N}(r) \tag{1.2.45}$$

for $r \leq R$. In these expressions $r_{\rm V}$ is the Vainshtein radius which can be written as

$$r_{\rm V} \equiv \left(\frac{8r_{\rm c}^2 r_{\rm S}}{9\beta_{\rm nDGP}^2}\right)^{1/3} = \left(\frac{4GM(R)}{9\beta_{\rm nDGP}^2 H_0^2 \Omega_{\rm rc}}\right)^{1/3}, \tag{1.2.46}$$

where $r_{\rm S} \equiv 2GM(R)/c^2$ is the Schwarzschild radius and $M(R) \equiv 4\pi \int_0^R \delta\rho_{\rm m}(r')r'^2{\rm d}r'$.

According to Eq. (1.2.33), the fifth force is given by $\frac{1}{2}{\rm d}\varphi/{\rm d}r$. Thus when $r \gg r_{\rm V}$ we have

$$\frac{1}{2}\frac{{\rm d}\varphi}{{\rm d}r} \to \frac{1}{3\beta_{\rm nDGP}} g_N(r), \tag{1.2.47}$$

meaning on scales larger than the Vainshtein radius gravity is enhanced (because $\beta_{\rm nDGP} > 0$ for the normal branch of the DGP model). On the other hand, for $r, R \ll r_{\rm V}$ we have

$$\frac{1}{2}\frac{{\rm d}\varphi}{{\rm d}r} \to \frac{2}{3\beta_{\rm nDGP}}\frac{R^{3/2}}{r_{\rm V}^{3/2}} g_{\rm N}(r) \ll g_{\rm N}(r), \tag{1.2.48}$$

indicating that the fifth force is suppressed (or screened) well within the Vainshtein radius.

1.3 Cosmological simulations

Cosmological simulations are the standard tool to explore and understand the formation and evolution of non-linear structures in the Universe.

Dark matter-only (DMO) simulations are the more widely used cosmological simulations (see Springel et al., 2005; Angulo et al., 2012; Klypin et al., 2016). Such simulations do not include baryons, therefore it is computationally possible to

generate a large number of DMO simulations to study halo and galaxy clustering (see e.g., Garrison et al., 2018; Klypin & Prada, 2018; Hernández-Aguayo et al., 2020a). To populate these simulations with realistic galaxy populations we opt to use empirical models such as the halo occupation distribution (HOD) (Berlind & Weinberg, 2002; Kravtsov et al., 2004; Zheng et al., 2005) or the (sub)halo abundance matching techniques (SHAM) (Vale & Ostriker, 2004; Conroy et al., 2006; Reddick et al., 2013; Klypin et al., 2013).

Hydrodynamical simulations attempt to simulate the evolution and distribution of both dark matter and baryonic structures together. These simulations aim to explore galaxy formation by incorporating astrophysical processes such as gas cooling, stellar and active galactic nuclei (AGN) feedback, star formation, magnetic fields and even cosmic rays in a cosmological context (see, e.g., Vogelsberger et al., 2014; Schaye et al., 2015; Feng et al., 2016; McCarthy et al., 2017; Pillepich et al., 2018a, 2019; Lee et al., 2020). Such simulations are possible thanks to the advances in numerical codes and techniques (see e.g, Springel, 2010; Schaller et al., 2018). More recently, Arnold et al. (2019) and Hernández-Aguayo et al. (2020b) have started to explore the interplay between baryonic physics and modified gravity in full-hydrodynamical simulations. Unfortunately, not all the astrophysical processes in galaxy formation simulations can be simulated with such high precision, for this reason it is necessary to include "subgrid physics" models (Crain et al., 2015) to alleviate the finite resolution. Also, subgrid models need to be tuned using observations to reproduce the observed galaxy population.

In addition, semi-analytical models of galaxy formation (SAM) offer the possibility to explore galaxy formation without the need to run computationally expensive full-hydrodynamical simulations (Somerville & Primack, 1999; Cole et al., 2000; Baugh, 2006; Benson, 2010). Basically, SAMs populate DMO simulations with galaxies by solving a set of coupled differential equations which describe the cooling of gas in haloes, the formation of stars and black holes, feedback due to supernovae and heating by AGN, metal enrichment, etc. Disadvantages of SAMs include the need for relatively high-resolution DMO simulations with the storage of a large number of particle snapshots to construct merger trees. Also SAMs make

simplifying assumptions (e.g. spherical symmetry) to model the flow of gas in and out of galaxies and do not provide detailed information about the distribution of gas.

1.4 Galaxy surveys

Several large international survey projects are underway which aim to determine what is behind the accelerating expansion of the Universe, such as the Dark Energy Survey (DES; Dark Energy Survey Collaboration, 2016), the Dark Energy Spectrographic Instrument survey (DESI; DESI Collaboration et al., 2016), the European Space Agency's Euclid mission (Laureijs et al., 2011), the 4-metre Multi-Object Spectroscopic Telescope (4MOST; de Jong et al., 2016), the Subaru Prime Focus Spectrograph (PFS; Tamura et al., 2016) and the Vera C. Rubin Observatory (formerly known as the Large Synoptic Survey Telescope; LSST Science Collaboration, 2009). These surveys aim to measure the position of millions of galaxies to map the large-scale structure of the Universe, a key component to unveil the nature of the dark matter and dark energy, and to test the theory of gravity at an unprecedented level of precision. To fully exploit these data it is essential to provide accurate theoretical predictions for as wide a range of cosmological models as possible.

Different targeting strategies are driven partly by observational and instrumental considerations, such as the visibility of a particular emission line over a given redshift interval or the number of fibres available in the field of view. For example, over several phases, the Sloan Digital Sky Survey (SDSS) measured redshifts for an $r-$band selected main galaxy sample (Strauss et al., 2002) at low redshift ($z < 0.2$), and colour and magnitude selected samples of luminous red galaxies (LRGs) and emission line galaxies (ELGs) at intermediate redshifts and quasars at high redshifts (Dawson et al., 2013, 2016) to make measurements of the BAO scale from the correlation function and power spectrum (Eisenstein et al., 2005; Sánchez et al., 2012; Ross et al., 2015; Ata et al., 2018). LRGs are the main targets of the SDSS-III Baryon Oscillation Spectroscopic Survey (BOSS; Dawson et al., 2013), in the redshift range $0.2 < z < 0.75$. This survey has provided the most precise mea-

surements to date of cosmological distances using BAO and the growth rate using RSDs at redshifts $z = 0.38$, 0.51, and 0.61 (see Alam et al., 2017, and references therein). Recently, the SDSS-IV extended-BOSS survey (eBOSS; Dawson et al., 2016; Prakash et al., 2016) has presented the first clustering measurements of LRGs at $z \sim 0.7$ (Zhai et al., 2017; Bautista et al., 2018; Icaza-Lizaola et al., 2020).

As another example, the DESI survey aims to target luminous red galaxies in the redshift range from $z = 0.4$ to $z = 1$ (the DESI LRG target selection at $z < 0.6$ will be complementary to that performed in the SDSS-IV/eBOSS (Prakash et al., 2016)), [OII] emission-line galaxies in the range $0.6 < z < 1.6$, quasi-stellar objects (QSOs; tracers) up to $z = 2.1$, and QSOs (Ly-α) at higher redshifts ($2.1 < z < 3.5$). In addition to a bright galaxy sample at low redshifts $z < 0.4$, DESI will provide a total of ~ 35 million biased tracers of the large-scale structure of the Universe over $14\,000\,\mathrm{deg}^2$ (see Kitanidis et al., 2020, for details), which is an order of magnitude more than previous spectroscopic surveys, allowing even tighter constraints to be placed on cosmological models.

1.5 Outline of the thesis

In this thesis, we aim to provide the cosmological tools needed to explore the impact of modifications of gravity on the formation, evolution and clustering of galaxies using large N-body cosmological simulations and small but high-resolution hydrodynamical simulations. The thesis is split into two parts as described below.

The first part of the thesis is organised as follows. In Chapter 2, we present a new cosmological probe to test $f(R)$ gravity models using marked correlation functions, where the marks are defined as a function of environment. In Chapter 3, we explore the large-scale redshift space distortions (RSD) in both $f(R)$ and nDGP models. We put constraints on the linear distortion parameter, which is related to the linear growth rate, using a linear and a non-linear RSD model. Using a new modified version of the Arepo code and the IllustrisTNG galaxy formation model, In Chapter 4, we present the first full-hydrodynamical simulations of galaxy formation in the nDGP model.

In the second part, we study the large-scale clustering of galaxies in the ΛCDM model. In Chapter 5, we assess whether or not there is an optimal way to select galaxies to extract the baryon acoustic oscillations (BAO) scale. In Chapter 6, we present a novel technique to build galaxy mock catalogues for the luminous red galaxy sample of the DESI survey. The results of Chapters 5 and 6 will hopefully help in the preparation and analysis of future galaxy surveys.

Finally, in Chapter 7, we present our general conclusions and give a brief description of future projects that will complement the results presented in this thesis.

Chapter 2

Marked clustering statistics in $f(R)$ gravity cosmologies

2.1 Introduction

The Λ cold dark matter (ΛCDM) model is currently the most widely accepted description of the Universe (e.g. see Ade et al. 2014). In this model small ripples in the density of the Universe at early times, seeded during a period of rapid expansion called inflation, were boosted by gravity to form the cosmic web of voids, galaxies and clusters of galaxies that we see today. The ΛCDM model works remarkably well on large scales, with the highlight being the prediction of the temperature fluctuations in the cosmic microwave background (CMB) radiation (e.g. Planck Collaboration XIII 2016). However, the model arguably runs into difficulties on small scales (scales smaller than a few Mpc), which could be related to the nature of the dark matter particle or could be solved by appealing to the physics of galaxy formation (for reviews see Weinberg et al. 2014; Del Popolo & Le Delliou 2017; Bullock & Boylan-Kolchin 2017). For example, the inner structure of dark matter haloes has a cusp profile, whereas observations suggested a core one (Flores & Primack, 1994; Moore, 1994). A possible solution is that baryonic feedback alters the inner structure of dark-matter haloes producing core-like density profiles in hydrodynamical simulations (Read et al., 2016; Fitts et al., 2017). Also, numerical simulations predict many more subhaloes than observed galaxies (Klypin et al., 1999; Moore

et al., 1999), however it has been shown that such subhaloes are not able to form luminous structures (see e.g., Sawala et al., 2016).

Here, given the challenges faced by ΛCDM as set out in Chapter 1, we focus our attention on a particular class of modified gravity models – Hu & Sawicki (2007) chameleon $f(R)$ gravity as described in Sec. 1.2.1. This model is obtained by adding a general function of the Ricci scalar, $f(R)$, to the Einstein-Hilbert action. This modification gives rise to a new scalar degree of freedom in gravity (Carroll et al., 2004). In order to recover GR, the new scalar field becomes massive in high-density regions (i.e., the Solar System) and its interactions are suppressed by the so-called chameleon screening mechanism (Khoury & Weltman, 2004).

The standard tool to model the growth of large scale structure into the non-linear regime is N-body simulation. In order to robustly test gravity on cosmological scales, reliable N-body simulations of modified gravity models are essential. The non-linear nature of the scalar field equation requires the implementation of novel numerical techniques, which is what makes N-body simulations of modified gravity challenging (Winther et al., 2015; Barreira et al., 2015; Bose et al., 2017b). Once such simulations are ready, we can use measurements of clustering statistics from surveys to test and constrain cosmological models (see e.g., Reid et al. 2010).

Several recent works have studied clustering in $f(R)$ gravity. For example, Li et al. (2013b) predicted the matter and velocity divergence power spectra and their time evolution measured from several large-volume N-body simulations with varying box sizes and resolution. Jennings et al. (2012) predicted the clustering of dark matter in redshift space, finding significant deviations from the clustering signal in standard gravity, with an enhanced boost in power on large scales and stronger damping on small scales in the $f(R)$ models compared to GR at redshifts $z < 1$. More recently, Arnalte-Mur et al. (2017) compared the time evolution of the two-point correlation function of dark matter haloes in real and redshift space in modified gravity and GR.

An approach related to the two-point correlation function has been proposed to test modified gravity models, called the marked correlation function (Sheth, Connolly & Skibba, 2005). Marked statistics offer the possibility of testing how galaxy

properties correlate with environment. Previous applications of the marked correlation function range from the analysis of the environmental dependence of bars and bulges in disc galaxies (see e.g., Skibba et al. 2012) to breaking degeneracies in halo occupation distribution modelling (White & Padmanabhan, 2009).

White (2016) proposed that marked statistics might provide a means to distinguish between modified gravity models and GR, due to the environmental dependence of the strength of gravity (for earlier work on environmental dependence in modified gravity, see, e.g., Zhao et al., 2011; Winther et al., 2012; Lombriser et al., 2015; Shi et al., 2017). The environment can be defined as regions in the Universe (or simulations) that can be quantified by observations such as density fields or the gravitational potential. For example, one can quantify how many galaxies are within a spherical (cubic) region of a given size in the Universe (simulations). We will discuss our definitions of environment in Sec. 2.3.2. Marks can be designed which down-weight high-density regions, for which modifications to gravity are screened, and up-weight low-density, unscreened regions to maximise the differences in the clustering signal. Valogiannis & Bean (2018) tested this idea by using the dark matter particle distribution from N-body simulations of symmetron and $f(R)$ modified gravity models. In the case of $f(R)$ gravity with $|f_{R0}| = 10^{-4}$, they found a maximum difference of 37% with respect to GR. Armijo et al. (2018) studied the galaxy marked correlation function by up-weighting low and high-density regions using marks in function of the galaxy density field and the host halo mass of galaxies, they found significant differences between the $f(R)$ and GR models. Here, we focus our attention on the clustering of dark matter haloes and HOD galaxies for $f(R)$ gravity models to make a more direct connection with observations.

This Chapter is organised as follows. Section 2.2 explains the numerical set-up of the simulations and the generation of halo and galaxy catalogues. The main results are presented in Section 2.3. Finally, in Section 2.4 we present a brief discussion of our results.

2.2 Simulations and halo/galaxy catalogues

Here we present a description of the simulations used, the construction of halo catalogues, and the HOD prescription used to populate dark matter haloes with galaxies.

2.2.1 Numerical simulations

As we are interested in the effects of $f(R)$ gravity on large scales, we choose three Hu-Sawicki models with $n = 1$ and $|f_{R0}| = 10^{-6}, 10^{-5}, 10^{-4}$ (which we hereafter refer to as F6, F5 and F4, respectively) and the ΛCDM model which assumes GR. Despite the observational tensions from optical and X-ray galaxy clusters observations and weak lensing peak statistics faced by $f(R)$ models with $|f_{R0}| > 10^{-5}$ (see e.g., Lombriser 2014; Cataneo et al. 2015; Liu et al. 2016) and the constraint imposed if the Milky Way is screened ($|f_{R0}| < 10^{-6}$; Burrage & Sakstein, 2018; Koyama, 2018) it is interesting to consider a wide range of $f(R)$ models to study their impact on the halo/galaxy clustering.

We use the ELEPHANT (Extended LEnsing PHysics using ANalaytic ray Tracing) simulations executed using the code ECOSMOG (Li et al., 2012), which is based on the adaptive mesh refinement (AMR) N-body code RAMSES (Teyssier, 2002). Table 2.1 lists the properties of the simulations used in our analysis. The cosmological parameters were adopted from the best-fitting values to the WMAP 9 year CMB measurements (Hinshaw et al., 2013). All simulations use $N_{\rm p} = 1024^3$ particles with a mass of $m_{\rm p} = 7.798 \times 10^{10} h^{-1} M_{\odot}$ to follow the evolution of the dark matter distribution in a volume of $V_{\rm box} = (1024\ h^{-1}{\rm Mpc})^3$. The initial conditions were generated at $z_{\rm ini} = 49$ using the MPGRAFIC code (Prunet et al., 2008). All simulations were run using the same initial conditions up to the present time, $z_{\rm fi} = 0$, generating $37 + 1$ snapshots. Here, we analyse the outputs at $z = 0.5$.

2.2.2 Halo catalogues and mass function

Dark matter haloes are the building blocks of large-scale structure and the hosts of galaxies. Therefore, the study of their statistical properties, such as their abundance

Table 2.1: Numerical parameters of the simulations used.

Labels	GR, F6, F5, F4
Present value of the scalaron field	$\|f_{R0}\| = 0, 10^{-6}, 10^{-5}, 10^{-4}$
Box size	$L_{\rm box} = 1024\ h^{-1}$Mpc
Number of DM particles	$N_{\rm p} = 1024^3$
Mass of DM particle	$m_{\rm p} = 7.798 \times 10^{10} h^{-1} M_\odot$
Initial redshift	$z_{\rm ini} = 49$
Final redshift	$z_{\rm fi} = 0$
Realisations	5
Cosmological parameters:	
Total matter density	$\Omega_{\rm m} = 0.281$
$1 - \Omega_{\rm m}$	$\Omega_\Lambda = 0.719$
Baryonic matter density	$\Omega_{\rm b} = 0.046$
Cold dark matter density	$\Omega_{\rm cdm} = 0.235$
Dimensionless Hubble parameter	$h = 0.697$
Primordial power spectral index	$n_s = 0.971$
rms linear density fluctuation	$\sigma_8 = 0.840$

and clustering, is of great importance in understanding the nature of gravity. The halo catalogues were produced using the ROCKSTAR halo finder code (Behroozi et al., 2013a). ROCKSTAR calculates halo masses using the spherical overdensity (SO) approach (Cole & Lacey, 1996), including all particles and substructures in the halo. We keep only the 'parent' halo, omitting other substructures from our analysis.

We define the mass of a halo as M_{200c}, the mass within a sphere of radius r_{200c}, which is the radius within which the mean overdensity is 200 times the critical density of the universe ρ_c,

$$M_{200c} = \frac{4\pi}{3} 200 \rho_c r_{200c}^3 \,. \tag{2.2.1}$$

The dark matter halo mass function (HMF) quantifies the number density of dark matter haloes as a function of their mass. The HMF is sensitive to the cosmological parameters, $\Omega_{\rm m}$, Ω_Λ, and σ_8, and to modifications to gravity. The ΛCDM model predicts an HMF in which the number of haloes increases with decreasing halo mass. $f(R)$ models predict more haloes than the ΛCDM model at almost all masses due to the enhancement of gravity. Theoretically, the halo mass function is given by (Press & Schechter, 1974)

$$\frac{{\rm d}n}{{\rm d}M_{200c}} = f(\sigma) \frac{\bar{\rho}_{\rm m}}{M_{200c}^2} \left| \frac{{\rm d} \ln \sigma^{-1}}{{\rm d} \ln M_{200c}} \right| , \tag{2.2.2}$$

where σ is the linear theory variance in the matter perturbation, $\bar{\rho}_{\rm m}$ is the mean density of the Universe and $f(\sigma)$ is an analytical fitting formula. The cumulative number density of haloes above the mass M_{200c} is:

$$n(> M_{200c}) = \int_{M_{200c}}^{\infty} \frac{{\rm d}n}{{\rm d} \log_{10} M_{200c}} {\rm d} \log_{10} M_{200c} \,. \tag{2.2.3}$$

We compare the fitting formula of Tinker et al. (2010) (hereafter Tinker10) to the simulation results. Tinker10 calibrated their fitting formula using a SO algorithm to identify dark matter haloes in numerical simulations which is consistent with the approach used in ROCKSTAR. The analytical predictions were computed by using the online tool HMFCALC[1] (Murray et al., 2013).

Fig. 2.1 shows the cumulative halo mass function (cHMF) measured from the simulations and the relative difference between the $f(R)$ models and GR at $z = 0.5$.

[1] http://hmf.icrar.org/

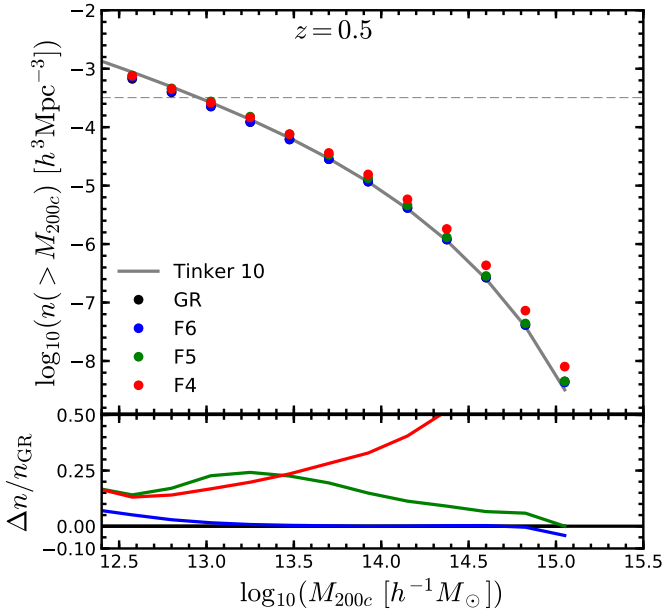

Figure 2.1: The cumulative halo mass function in the models at $z = 0.5$. Different colours represent different models, as labelled. The values for each model correspond to the average over the 5 realisations. The horizontal dashed line shows the number density we use to define our halo sample ($n_{\mathrm{h}} = 3.2 \times 10^{-4}\ h^3\,\mathrm{Mpc}^{-3}$). The grey curve shows the Tinker10 cHMF for GR at $z = 0.5$. The lower panel shows the relative difference with respect to the ΛCDM (GR) model.

As expected, the largest deviation from GR is displayed by the F4 model (red line; Schmidt et al. 2009; Lombriser et al. 2013; Cataneo et al. 2016). The lower panel of Fig. 2.1 shows that the cumulative halo mass function in the F4 model reaches a difference with respect to GR of >50 percent for haloes of mass $M_{200c} > 10^{14.3}h^{-1}\mathrm{M}_{\odot}$. The maximum difference found between F5 (green line) and GR reaches 25 percent for haloes with mass $M_{200c} \approx 10^{13.2}h^{-1}M_{\odot}$. On the other hand, for the F6 model (blue line) we see that for very massive haloes, the halo mass function is the same as that in GR. This is because the chameleon mechanism works efficiently for such haloes to suppress the effects of the enhancement to gravity. These differences are purely the result of the modified gravitational force in $f(R)$ models. The stronger deviation of F4 from GR is due to the inefficient screening mechanism in this model which allows the production of more massive haloes. For F5 the screening mechanism is less efficient in haloes whit masses $10^{13} < M_{200c}/[h^{-1}M_{\odot}] < 10^{14}$ compared to the screening in the F6 model which efficiently moderates the formation of haloes with mass $M_{200c} > 10^{13}h^{-1}M_{\odot}$.

To make a direct comparison between the halo and galaxy clustering we select a halo population from the simulations by fixing the halo number density (in this case we take the number density of the BOSS-CMASS-DR9 sample at $z = 0.5$, $n_{\rm h} = n_{\rm g} = 3.2\times10^{-4}\ h^3\mathrm{Mpc}^{-3}$; Anderson et al. 2012) and selecting haloes above the mass threshold corresponding to that number density. The horizontal dashed line in Fig. 2.1 corresponds to the halo number density used to define our halo sample. The minimum mass that defines the halo sample for each model is: $7.643 \times 10^{12}h^{-1}M_{\odot}$ (GR), $7.798 \times 10^{12}h^{-1}\mathrm{M}_{\odot}$ (F6), $9.124 \times 10^{12}h^{-1}\mathrm{M}_{\odot}$ (F5) and $8.734 \times 10^{12}h^{-1}\mathrm{M}_{\odot}$ (F4). The fact that F5 has a higher minimum mass is because this model produces more haloes with mass $M_{200c} \sim 10^{13}h^{-1}\mathrm{M}_{\odot}$ (as we can see from the lower panel of Fig. 2.1) than F6 and F4. For F4, many of the medium-mass haloes have merged to form more massive haloes, hence this model predicts fewer smaller haloes than F5.

2.2.3 HOD prescription and galaxy catalogues

To compare the simulations with observations one has to populate dark matter haloes with galaxies. This can be done using one of a number of empirical tech-

niques depending on the physical application we are interested in, such as subhalo abundance matching (Vale & Ostriker, 2004; Conroy et al., 2006; Reddick et al., 2013; Klypin et al., 2013), the conditional luminosity function (Yang et al., 2003; Cooray & Milosavljevic, 2005) or the halo occupation distribution (Berlind & Weinberg, 2002; Kravtsov et al., 2004; Zheng et al., 2005). These empirical descriptions of the galaxy-halo connection have the flexibility to give accurate reproductions of observational estimates of galaxy clustering. A second, more expensive but physically motivated method is hydrodynamical simulation (Schaye et al., 2015; Vogelsberger et al., 2014). A third possibility, which retains the physical basis of hydrodynamical simulation at a fraction of the computational cost is semi-analytical modelling of galaxy formation (Somerville & Primack, 1999; Cole et al., 2000; Baugh, 2006; Benson, 2010) in which an N-body dark matter-only simulation is populated with galaxies after solving a set of coupled differential equations. To date, little work has been done to study galaxy formation and clustering in modified gravity models (see Fontanot et al. 2013 for an example), so here we will resort to the empirical approach of HOD modelling.

We populate haloes using a functional form for the halo occupation distribution (HOD; Peacock & Smith 2000; Berlind & Weinberg 2002) with five parameters, as used by Zheng et al. (2007).

In this form, the mean number of galaxies in a halo of mass M_h (in our case $M_\mathrm{h} = M_{200c}$) is the sum of the mean number of central galaxies plus the mean number of satellite galaxies,

$$\langle N(M_\mathrm{h})\rangle = \langle N_\mathrm{c}(M_\mathrm{h})\rangle + \langle N_\mathrm{s}(M_\mathrm{h})\rangle \,, \tag{2.2.4}$$

$$\langle N_\mathrm{c}(M_\mathrm{h})\rangle = \frac{1}{2}\left[1 + \mathrm{erf}\left(\frac{\log_{10} M_\mathrm{h} - \log_{10} M_\mathrm{min}}{\sigma_{\log M}}\right)\right] , \tag{2.2.5}$$

$$\langle N_\mathrm{s}(M_\mathrm{h})\rangle = \langle N_\mathrm{c}(M_\mathrm{h})\rangle \left(\frac{M_\mathrm{h} - M_0}{M_1}\right)^\alpha , \tag{2.2.6}$$

and $\langle N_\mathrm{s}(M_\mathrm{h})\rangle = 0$ if $M_\mathrm{h} < M_0$. $\langle N_\mathrm{c/s}(M_\mathrm{h})\rangle$ is the average number of central or satellite galaxies, respectively, in a halo of mass M_h. The model depends on five parameters: M_min, M_0, M_1, $\sigma_{\log M}$ and α. From Eqs. (2.2.5) and (2.2.6) we can see that M_min and M_0 represent the halo mass threshold to host one central or one satellite galaxy, respectively. Also, we assume that central galaxies are placed

at the centre of their host haloes and satellite galaxies are orbiting inside haloes with $M_{\rm h} \geq M_0$. The satellite galaxies are radially distributed, between $r = [0, r_{200c}]$, following the Navarro-Frenk-White (NFW) profiles of their host halo (Navarro et al., 1996, 1997).

We generate five galaxy catalogues (one for each independent realisation of the density field) for every gravity model following the prescription described above. The galaxy catalogues match the galaxy number density of the BOSS-CMASS-DR9 sample at $z = 0.5$ ($n_{\rm g} = 3.2 \times 10^{-4}\ h^3\,{\rm Mpc}^{-3}$; Anderson et al. 2012) and the galaxy two-point correlation function across all gravity models (more details are presented below). The BOSS-CMASS sample is dominated by LRGs which are massive galaxies typically residing in haloes with $M_h \sim 10^{13} h^{-1} M_\odot$ (Anderson et al., 2012). Hence, given the mass resolution of the ELEPHANT simulations, these runs are suitable to study the impact of $f(R)$ gravity on galaxy clustering.

The values of the HOD parameters used to populate the GR simulations are those inferred from the abundance and clustering measured for the BOSS-CMASS-DR9 galaxy sample (Manera et al., 2012):

$$\begin{aligned} \log_{10}(M_{\rm min}/[h^{-1}M_\odot]) &= 13.09\,, \\ \log_{10}(M_1/[h^{-1}M_\odot]) &= 14.00\,, \\ \log_{10}(M_0/[h^{-1}M_\odot]) &= 13.077\,, \\ \sigma_{\log M} &= 0.596\,, \\ \alpha &= 1.0127. \end{aligned} \tag{2.2.7}$$

To find the $f(R)$ HOD parameters, we use the simplex algorithm of Nelder & Mead (1965) to search through the 5D parameter space. We start the algorithm with an initial guess at the values of the HOD parameters, then the code walks through the 5-dimensional HOD parameter space looking for the values that minimise the root-mean-square difference ($\Delta_{\rm rms}$) of the real-space two-point correlation function between $f(R)$ and GR models given by,

$$\Delta_{\rm rms} = \sqrt{\sum_{i=1}^{N} \left(\xi_{f(R),i}/\xi_{{\rm GR},i} - 1\right)^2}\,. \tag{2.2.8}$$

Where we measured the correlation function using $N = 40$ logarithmically spaced radial bins between $1 - 80\ h^{-1}$Mpc. The relative difference of the galaxy number density ($\Delta n = n_{f(R)}/n_{\rm GR} - 1$) is added to $\Delta_{\rm rms}$ to ensure that all models have similar number of tracers. We stop the search when $\Delta_{\rm rms} < 0.02$ (this means that the overall agreement is better than 2%). For the F4 model, the minimum value of $\Delta_{\rm rms}$ we could obtain in practice was $\Delta_{\rm rms} \sim 0.03$.

Here, we are interested in the marked correlation function (mCF), which was proposed to highlight the environmental dependence in modified gravity models (White, 2016). Hence, the most natural choice is to make the unmarked two-point correlation functions (2PCFs) of the different models as close to each other as possible; otherwise when there is a difference in their mCFs we can not be sure how much of this is due to the different 2PCFs.

The $f(R)$ HOD parameters were tuned for each model and realisation to match the clustering displayed in the counterpart simulation from the GR suite. The best-fitting values of the HOD parameters for the different realisations are listed in Table 2.2. The variation in the best-fitting parameter values is larger as the modification to gravity increases. We note that, despite the differences between the values of the best-fitting parameters between different models and realisations, the resulting correlation functions and galaxy number densities agree with the GR results to within our target accuracy.

Note that the HOD parameters are degenerate to some extent, so that a comparison of the values of any single parameter across realisations or models should not be over interpreted. For instance, consider the parameter α that governs the number of satellite galaxies in haloes of a given mass: in the case of the most extreme model, F4, the variation between realisations is $\sim 3\%$. This difference is small compared with the 1σ scatter of HOD parameter fittings, e.g., White et al. (2011).

The left panel of Fig. 2.2 shows the HOD for CMASS galaxies at $z = 0.5$. The gradual transition from zero to one galaxy per halo is determined by the values adopted for $\log M_{\rm min}$ and $\sigma_{\log M}$ for central galaxies (dashed lines). The appearance of satellites in haloes (dotted lines) is dictated by the values of M_1 and M_0, and the rapid increase in the satellite content of haloes with increasing halo mass is governed

Table 2.2: Values of the HOD parameters (columns 2-6) for $f(R)$ models (F6, F5, F4) at $z = 0.5$ and different realisations (Box 1 − Box 5).

	$\log_{10}(M_{\rm min}/[h^{-1}{\rm M}_\odot])$	$\log_{10}(M_1/[h^{-1}{\rm M}_\odot])$	$\log_{10}(M_0/[h^{-1}{\rm M}_\odot])$	$\sigma_{\log M}$	α
F6 (Box 1)	13.092	14.004	13.082	0.538	1.0125
F6 (Box 2)	13.093	14.004	13.081	0.539	1.0128
F6 (Box 3)	13.092	14.006	13.083	0.554	1.0131
F6 (Box 4)	13.093	14.002	13.082	0.545	1.0132
F6 (Box 5)	13.094	14.008	13.078	0.547	1.0129
F5 (Box 1)	13.101	14.050	13.077	0.434	1.0643
F5 (Box 2)	13.100	14.045	13.078	0.449	1.0674
F5 (Box 3)	13.134	14.043	13.085	0.525	1.0982
F5 (Box 4)	13.110	14.041	13.078	0.470	1.0710
F5 (Box 5)	13.108	14.041	13.080	0.462	1.0440
F4 (Box 1)	13.084	14.092	13.076	0.394	1.0921
F4 (Box 2)	13.075	14.113	13.073	0.345	1.0804
F4 (Box 3)	13.063	14.113	13.072	0.333	1.0974
F4 (Box 4)	13.076	14.109	13.070	0.353	1.1110
F4 (Box 5)	13.053	14.105	13.075	0.290	1.1143

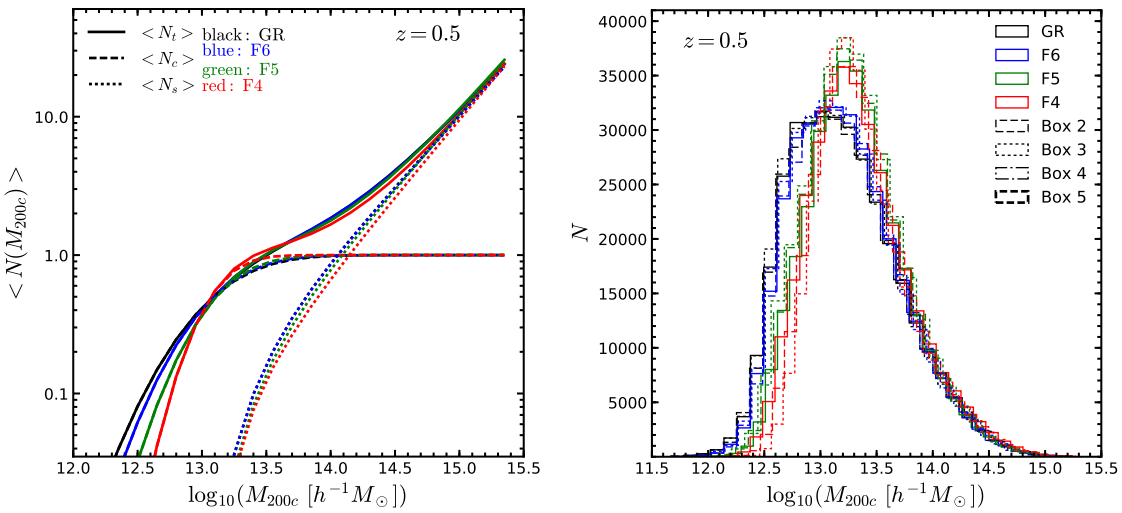

Figure 2.2: Left panel: The mean number of central and satellite galaxies as a function of halo mass, $\langle N_{c/s}(M_{200c})\rangle$. Dashed lines show the HOD for central galaxies and dotted lines show satellite galaxies while solid lines represent the total averaged number of galaxies, calculated from Eqs. (2.2.4) – (2.2.6) with parameters (2.2.7) for GR and the result of Box 1 listed in Table 2.2 for the $f(R)$ models, as labelled. Right panel: the number of galaxies in the simulation as a function of the host halo mass, the same distribution at $z = 0.5$ for different realisations: Box 1 (solid lines), Box 2 (dashed lines), Box 3 (dotted lines), Box 4 (dashed-dotted lines) and Box 5 (thick-dashed lines).

by α. The HOD parameters are adjusted in the $f(R)$ models to approximately reproduce the abundance and clustering of CMASS galaxies realised in GR. We note that the resulting HODs are very similar between $f(R)$ gravity and GR.

The right panel of Fig. 2.2 shows the distribution of the number of galaxies as a function of the host halo mass (M_{200c}). We see that most galaxies are found in haloes with mass $10^{13} < M_{200c}/[h^{-1}\mathrm{M}_{\odot}] < 10^{14}$. We also note that the F5 and F4 models produce more galaxies than GR and F6 in this mass range. This is because the abundance of haloes in this mass range is boosted in F5 and F4, as we can see from the relative differences of the cHMFs presented in the lower panel of Fig. 2.1. Analysing the distribution of galaxies, we find good agreement between the five realisations.

From the distribution of galaxies as a function of host halo mass plotted in Fig. 2.2 we note that $\approx 0.1\%$ galaxies reside in poorly resolved haloes ($M_{200c} < 10^{12}h^{-1}M_{\odot}$). The inclusion of these galaxies in the final catalogues does not affect the clustering results.

2.3 Results

Upcoming galaxy surveys will allow us to measure the clustering of galaxies to an unprecedented level of accuracy with the aim of developing a better understanding of the nature of dark matter, dark energy and the evolution of galaxies through cosmic time. In this section we present the statistical tools which can be used to characterise the halo and galaxy distributions in different gravity models. This is the first time that the halo and galaxy clustering has been studied to this level of detail in $f(R)$ gravity models.

2.3.1 2-point correlation function

To characterise the clustering of dark matter haloes and galaxies, we use the two-point correlation function, $\xi(r)$. This is defined as the excess probability, compared with that expected for a random distribution, of finding two haloes (or galaxies)

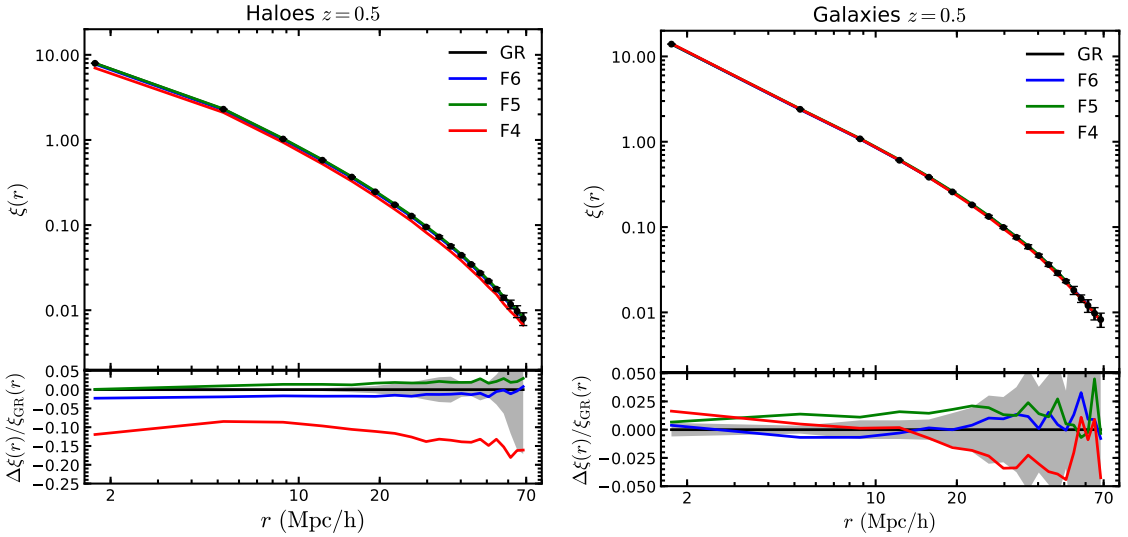

Figure 2.3: Two–point correlation function in real space measured for haloes (left panel) with $n_{\rm h} = 3.2 \times 10^{-4} h^3 {\rm Mpc}^{-3}$ and HOD galaxies (right panel) in the four gravity models at $z = 0.5$. The plotted values correspond to the average of the 5 realisations for each model. Different colour lines correspond to different gravity models as labelled. The lower subpanels show the relative difference between the results from the $f(R)$ and ΛCDM (GR) models. Error bars and shaded regions correspond to 1σ standard deviation over the 5 GR realisations.

contained in volume elements $\mathrm{d}V_1$ and $\mathrm{d}V_2$ at a separation r (Peebles, 1980):

$$\mathrm{d}P_{12}(r) \equiv \bar{n}^2[1 + \xi(r)]\mathrm{d}V_1\mathrm{d}V_2\,, \tag{2.3.9}$$

where $\bar{n}$ is the mean halo (galaxy) number density. The 2-point correlation functions and therefore the marked correlation functions are measured within the range $1 - 80\,h^{-1}$Mpc (for details see Sec. 2.2.3).

First we study the clustering of dark matter haloes, $\xi_{\rm h}$, (left panel of Fig. 2.3), for our halo samples with $n_{\rm h} = 3.2 \times 10^{-4} h^3 {\rm Mpc}^{-3}$. Although this statistic is not directly observable, it is instructive to study the properties of $\xi_{\rm h}$, since this is a first step towards understanding differences in the clustering of galaxies.

The first thing we notice is that the deviation from GR does not show a monotonic dependence on $|f_{R0}|$. More explicitly, F6 and F4 models have weaker clustering than GR, while F5 haloes are more clustered than GR.

These perhaps counterintuitive results can be explained by considering the following two effects of the enhanced gravity.

Firstly, stronger gravity means a faster growth of initial density peaks, and therefore more massive structures at late times. This generally leads to a higher mean halo number density above a fixed halo mass threshold. The enhancement of halo formation is not uniform: when screening is efficient, it is stronger in low-density regions than it is in high-density regions; when the screening is less efficient, then the growth of haloes is boosted in all environments, and those in dense regions can be boosted more because they have more matter around them to accrete.

Secondly, enhanced gravity generally leads to a stronger clustering of the structures that are formed from these initial density peaks. However, stronger gravity also means that we can expect more mergers in dense regions, reducing the number of haloes there. The latter effect can be seen by comparing the cHMFs of F5 and F4 in Fig. 2.1.

As we choose the halo mass cut to ensure that we consider the same number of haloes in each model any differences in $\xi_{\rm h}$ come from the different spatial distributions of haloes in the models. For F6, the deviation from GR is weak and the fifth force is suppressed in high-density regions. As a result small density peaks in low-density regions grow faster than similar density peaks in high-density regions, and more of them make it into the fixed number density halo catalogue than in GR. This makes the haloes less clustered and $\xi_{\rm h}(r)$ smaller.

For F5, the enhancement of gravity is stronger and the screening is weaker, so that haloes in all regions experience faster growth; those in high-density environments have a larger supply of raw materials for accretion and growth, so that they are more likely ending up in the final halo catalogue, leading to a stronger clustering and $\xi_{\rm h}$. For F4, the even stronger enhancement of gravity causes more mergers of haloes in dense regions to form even larger haloes, and to maintain the same $\bar{n}_{\rm h}$ more haloes in low-density regions have to be included into the halo catalogue, leading to less clustering and smaller $\xi_{\rm h}$.

In the case of the galaxy correlation function (right panel of Fig. 2.3), as we said before, the HOD catalogues for the $f(R)$ models were created by tuning the

parameters (2.2.7; see Table 2.2) to approximately match the two-point correlation function in GR (to within $1-3\%$).

2.3.2 Marked correlation function

In this subsection we consider the marked correlations, in which one weights galaxies[2] by some property or 'mark' when estimating clustering statistics. Marked correlations are particularly well-suited to quantifying how the properties of galaxies correlate with environment (Sheth et al., 2005; Skibba et al., 2006; White & Padmanabhan, 2009; Skibba et al., 2009, 2012). Here, we test the idea proposed by White (2016) that marked correlation functions may show a clearer signature of modified gravity in the large-scale clustering of galaxies, by up-weighting low density regions, where screening is weak and deviations from GR are strong.

The marked correlation function is defined as (Sheth et al., 2005):

$$M(r) \equiv \frac{1}{n(r)\bar{m}^2} \sum_{ij} m_i m_j = \frac{1+W(r)}{1+\xi(r)}\,, \tag{2.3.10}$$

where the sum is over all pairs with a given separation, r, $n(r)$ is the number of such pairs and $\bar{m}$ is the mean mark for the entire sample. In the second equality $\xi(r)$ is the two-point correlation function in which all galaxies (or haloes) are weighted equally. $W(r)$ is derived from a similar sum over galaxy (halo) pairs separated by r, as used to estimate $\xi(r)$, but now each member of the pair is weighted by the ratio of its mark to the mean mark of the full sample. The marked correlation function $M(r)$ can be estimated approximately using the simple pair count ratio WW/DD (where DD is the count of data–data pairs and WW represents the corresponding weighted counts). Hence, no random catalogue is needed for its computation.

The choice of the mark is flexible and depends on the application. Since we are interested in isolating the effects of the chameleon screening mechanism on structure formation, we study the clustering of HOD galaxies using two different definitions of environment: a) the number density field and b) the Newtonian gravitational potential (Shi et al., 2017).

[2]For simplicity, we talk about galaxies here, but the same calculation can (and will) be applied to haloes.

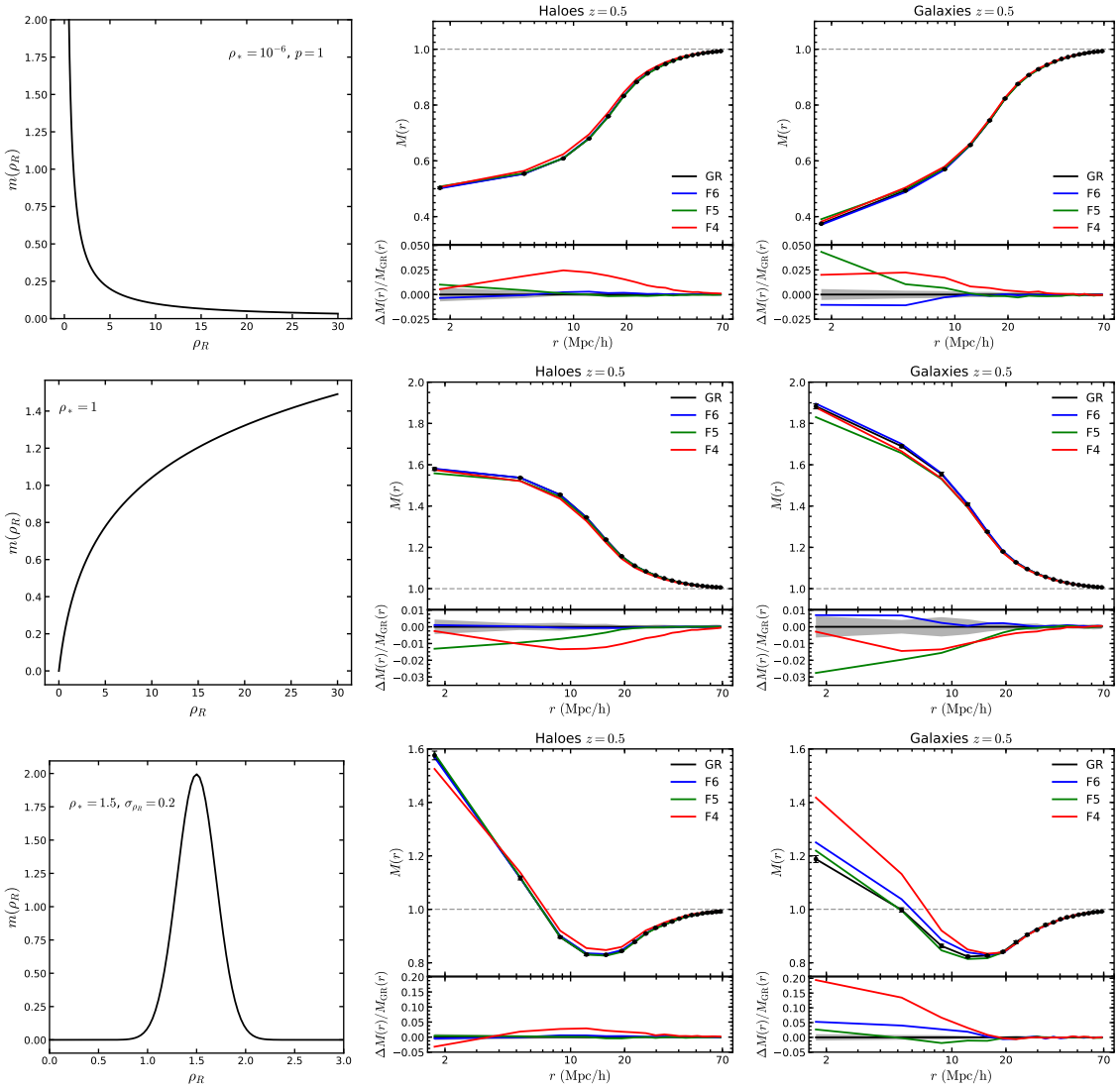

Figure 2.4: Marked correlation functions of haloes and CMASS galaxies at $z = 0.5$; mark in function of number density field. Left: functional form of the mark in function of density field, middle: halo marked correlation functions and right: galaxy marked correlation functions. Plots from upper to bottom: White mark (2.3.11), log–mark (2.3.12) and Gaussian-ρ_R mark (2.3.13). All lower subpanels show the relative difference between $f(R)$ models and GR. The plotted values correspond to the average over the 5 realisations. Errors correspond to 1σ standard deviation over the 5 GR realisations.

Density

For this environment definition we use three marks with an adjustable dependence on density:

$$m = \left(\frac{\rho_* + 1}{\rho_* + \rho_R}\right)^p , \tag{2.3.11}$$

$$m = \log_{10}(\rho_R + \rho_*) , \tag{2.3.12}$$

$$m = \frac{1}{\sqrt{2\pi}\sigma_{\rho_R}} \exp\left(-\frac{(\rho_R - \rho_*)^2}{2\sigma^2_{\rho_R}}\right) , \tag{2.3.13}$$

where ρ_R is the galaxy number density in units of the mean galaxy number density, $\bar{\rho}$, and p, ρ_* and σ_{ρ_R} are adjustable parameters.

A crucial step in the estimation of the marked correlation function is the definition of the density. We measure the galaxy number density using counts-in-cells (see, for example, Baugh et al. 1995). We divide the simulation box into cells (or cubical boxes) of the same size, and then count the number of galaxies inside each cell. Hence, we can compute the overdensity, δ, as:

$$1 + \delta = \frac{N}{\bar{N}} \equiv \rho_R , \tag{2.3.14}$$

where N is the number of galaxies in each cell and $\bar{N}$ is the mean number of galaxies in cells of a given size over the simulation volume. To compute the density we have used 60^3 cells of size $\sim 17h^{-1}$ Mpc. Given the mean galaxy number density of CMASS galaxies, $n_{\rm g} = 3.2 \times 10^{-4}\ h^3{\rm Mpc}^{-3}$, we have a mean number of galaxies in the cells of $\bar{N} = 1.59$. We checked that reducing the number of cells to $30^3 - 40^3$ does not affect our results significantly, while further reducing the number of cells makes the signal weaker; in the limit of 1^3 cell, $W(r)$ becomes identical to $\xi(r)$, as expected.

The first mark, Eq. (2.3.11), was proposed by White (2016) (hereafter the White–mark), with the motivation being that by up-weighting low density regions (i.e. by choosing $p > 0$), one might be able to find a signature of modified gravity, since previous studies have shown that the properties of voids are different in modified gravity theories than in GR (Clampitt et al., 2013; Cai et al., 2015; Zivick et al., 2015; Cautun et al., 2018). The log mark, Eq. (2.3.12), allows us to up-weight regions with $\rho_R > 1$, i.e., intermediate and high-density regions. Finally, using the

Gaussian-ρ_R mark, Eq. (2.3.13), we are able to control the regions we want to up-weight. Previously, Llinares & McCullagh (2017) found that by using a Gaussian transformation of the density field is it possible to up-weight intermediate density regions and find bigger differences between the clustering of objects in modified gravity and GR models. Keeping this in mind, we use the Gaussian-ρ_R mark to up-weight only intermediate density regions.

It is evident that by using Eq. (2.3.11) one can control the up-weighting by varying the power p and the parameter ρ_*. For simplicity we chose $p = 1$ and $\rho_* = 10^{-6}$. With the log-mark, a natural choice of the parameter which controls the enhancement is $\rho_* = 1$, given $m = 0$ for voids ($\rho_R = 0$). The parameters we chose for the Gaussian-ρ_R mark are: $\rho_* = 1.5$ and $\sigma_{\rho_R} = 0.2$, which ensures that we up-weight intermediate-density regions of interest. The functional form of the marks, Eqs. (2.3.11) – (2.3.13), is shown in the left-hand panels of Fig. 2.4. We have tried using different values of p, ρ_R and ρ_* but found that our results do not show significant differences on varying these parameters. We refer to low-, intermediate- and high-density regions as those for which the cells contain $N = 1$, $2 - 3$ and > 4 objects or, equivalently, to cells with $\rho_R = 0.62$, $1.25 - 1.88$ and > 2.51, respectively (see Eq. (2.3.14)).

Fig. 2.4 shows the marked correlation functions (mCFs) at $z = 0.5$ measured from the halo (middle panels) and the HOD (left panels) catalogues in the $f(R)$ and GR models. In all cases the marked correlation function goes to unity on large scales as expected (see right-hand expression of Eq. (2.3.10)). The first row of plots in Fig. 2.4 shows the mCF using the mark defined by Eq. (2.3.11), the White-mark, with $p = 1$ and $\rho_* = 10^{-6}$, the second row shows the log-mark, Eq. (2.3.12) with $\rho_* = 1$, and the third row shows the Gaussian-ρ_R mark with $\rho_* = 1.5$ and $\sigma_{\rho_R} = 0.2$. We observe different behaviours: for the White-mark, Eq. (2.3.11), the marked correlation function is $M(r) \leq 1$ at small separations, for the log mark, Eq. (2.3.12), we have $M(r) \geq 1$, while for the Gaussian-ρ_R we notice a transition from $M(r) \leq 1$ to $M(r) > 1$ at intermediate scales.

Analysing the behaviour of the halo marked correlation functions (see middle panel of Fig. 2.4) we find the following features:

- The clustering of F6 is almost indistinguishable from that of GR for all three marks, because of the efficient screening.

- For F5, the stronger growth (see Sec. 2.3.1) means more clustering of haloes on small scales, which is why $W(r)$ and therefore the marked correlation function is more affected at smaller r.

- In the case of F4, the higher production rate of massive haloes, driven by the more frequent mergers of lower mass haloes (see Sec. 2.3.1), leads to the incorporation of haloes into the fixed number density sample which correspond to low density peaks and which are more likely to come from low-density regions. Hence, the probability of finding a pair of tracers (haloes or galaxies) increases at intermediate separation r due to presence of these low mass haloes.

The right columns of Fig. 2.4 show that galaxies qualitatively mimic the marked clustering of haloes (at least for the White and log marks). Hence, the behaviour of the galaxy marked correlation functions can be understood following the same explanation as presented above for haloes. It is interesting to notice that even with the added complexity of populating haloes with HOD galaxies, the qualitative behaviour of the marked correlation functions preserves, suggesting that a true physical feature is being observed here.

For the Gaussian$-\rho_R$ mark, Eq. (2.3.13), which enhances intermediate-density regions (cells with 2 or 3 haloes/galaxies), we found that the F4 galaxy marked correlation function reaches a maximum of 20% for the lowest separation bin, while F6 predicts a difference of 5% and F5 keeps closer to GR with a difference of $\sim 3\%$.

Gravitational potential

Our second definition of environment is based on the Newtonian gravitational potential produced by dark matter haloes. The dark matter haloes in our simulations are reasonably well described by a NFW density profile (Navarro et al., 1996, 1997):

$$\rho_{\rm NFW} = \frac{\rho_{\rm s}}{(r/r_{\rm s})(1+r/r_{\rm s})^2}\,, \tag{2.3.15}$$

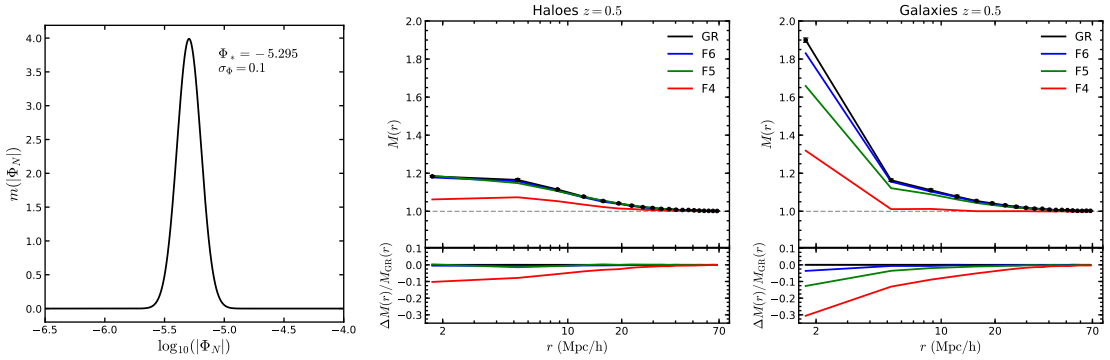

Figure 2.5: Marked correlation functions of haloes and CMASS galaxies at $z = 0.5$; mark in function of the Newtonian gravitational potential. Left-hand side panel shows the functional form of the Gaussian-Φ_N mark (2.3.17); the values of the parameters Φ_* and σ_Φ are shown in the legend. Middle and right-hand side plots show the marked correlation function using the mark given by Eq. (2.3.17) for haloes and galaxies, respectively. All lower subpanels for middle and right-hand side plots show the relative difference between $f(R)$ models and GR. The plotted values correspond to the average over the 5 realisations. Errors correspond to 1σ standard deviation over the 5 GR realisations.

where $r_{\rm s}$ is the scale radius where the profile has a slope of -2 and $\rho_{\rm s}$ is the characteristic density. The Newtonian gravitational potential is obtained by solving the Poisson equation, $\nabla^2\Phi_{\rm N} = 4\pi G\rho_{\rm NFW}$, for the NFW density profile Eq. (2.3.15) (Cole & Lacey, 1996; Navarro, Frenk & White, 1997; Lokas & Mamon, 2001):

$$\Phi_{\rm N} = -\frac{GM_{200c}}{r_{200c}}\frac{\ln(1+c)}{\ln(1+c)-c/(1+c)}\,, \tag{2.3.16}$$

where G is Newton's gravitational constant, M_{200c} was defined in Eq. (2.2.1) and c is the concentration parameter defined as $c \equiv r_{200c}/r_{\rm s}$. Previous studies have used the Newtonian gravitational potential in modified gravity to characterise local variations in the strength of gravity (see e.g., Cabre et al. 2012; Stark et al. 2016; Shi et al. 2017).

For this environment definition we define a Gaussian mark which allows us to up-weight galaxies in some regions of interest,

$$m = \frac{1}{\sqrt{2\pi}\sigma_\Phi}\exp\left[-\frac{(\log_{10}(|\Phi_{\rm N}|)-\Phi_*)^2}{2\sigma_\Phi^2}\right]\,, \tag{2.3.17}$$

where Φ_* and σ_Φ are free parameters of the mark which control the amplitude and width of the regions highlighted. As we can see from the distribution of galaxies as a function of host halo mass (right panel of Fig. 2.2), most galaxies live in haloes with masses between $10^{13} < M_{200c}/[h^{-1}M_\odot] < 10^{14}$ (which correspond to the mass range of groups of galaxies). Hence, we use the Gaussian-$\Phi_{\rm N}$ mark to up-weight galaxies contained in these haloes. In principle we should be able to find a bigger difference in the clustering between the GR and $f(R)$ models using this mark, as suggested by the cumulative halo mass function (lower panel of Fig. 2.1).

The value of the centre of the Gaussian is $\Phi_* = -5.295$. This value was found by computing the Newtonian gravitational potential for each galaxy in Box 1 for GR, then we pick the maximum value found for haloes with $M_{200c} = 10^{14}h^{-1}M_\odot$ ($\Phi_{\rm max}$) and the minimum value for haloes with $M_{200c} = 10^{13}h^{-1}M_\odot$ ($\Phi_{\rm min}$), finally we take $\Phi_* = (\Phi_{\rm max} + \Phi_{\rm min})/2$. We tried different values of the width, finding that $\sigma_\Phi = 0.1$ best ensures that we only up-weight galaxies in the haloes of interest. The functional form of the Gaussian-$\Phi_{\rm N}$ mark, Eq. (2.3.17), is shown in the left-hand panel of Fig. 2.5.

The halo and galaxy marked correlation function is presented in the middle and right panels of Fig. 2.5, respectively. The results can be summarised as follows:

- In the case of the halo/galaxy marked correlation function (middle and right panels of Fig. 2.5, respectively), the two-point correlation function (used as the denominator of Eq. (2.3.10)) is lower than the weighted correlation function, leading to $M(r) \geq 1$ for all gravity models, due to the stronger clustering of the up-weighted haloes in the mass range $M_{200c}/[h^{-1}M_{\odot}] = [10^{13}, 10^{14}]$.

- F6 predicts almost an identical halo/galaxy marked clustering to that in GR, which is consistent to our understanding that the screening mechanism in this model works efficiently in haloes of the mass range up-weighted.

- For F4 haloes, the mCF is higher than the 2PCF for the reason given in the first bullet point above. However, in this model a larger fraction of haloes in the mass range $M_{200c}/[h^{-1}M_{\odot}] \in [10^{13}, 10^{14}]$ are formed from low initial density peaks (due to stronger gravity) which are not very strongly clustered, such that the up-weighting of them – while making $M(r) \geq 1$ – does not lead to a $M(r)$ as large as in GR. This leads to $\Delta M(r)/M_{\rm GR}(r) < 0$ for F4. For F5 haloes, the fifth force is strong enough to enhance their clustering, but not too strong to produce excessive merging, and so the up-weighting using the Gaussian mark increases the mCF as significantly as in GR.

- For galaxies, a key difference from haloes is that a halo can host several galaxies while some haloes do not host galaxies at all. In F4 and F5, more relatively low initial density peaks have been promoted to the halo mass range $M_{200c}/[h^{-1}M_{\odot}] \in [10^{13}, 10^{14}]$ due to the enhanced gravity, and at the same time some high density peaks have grown out of this mass range. This means that if we up-weight galaxies whose host haloes are in this mass range, we end up with more central and fewer satellite galaxies, and more of them are hosted by haloes from lower initial density peaks. By the same reasoning as above, while we still have $M(r) > 1$ for these models, it is smaller than in GR and F6. In particular, we have noticed that $\Delta M(r)/M_{\rm GR}(r)$ reaches $5 \sim 10\%$ for

F5 and 20 $\sim$ 30% for F4 in $r = 2 \sim 5h^{-1}$Mpc. These results are very stable, and change very little across the different simulation realisations.

Also we note that the differences between the $f(R)$ and GR models are boosted when we use additional information to the density field. This can be seen by comparing the right panels of Fig. 2.4 with the right panel of Fig. 2.5. The differences get larger in such cases because the galaxy density field and galaxy distribution have been tuned to match between the different models (see Sec. 2.2.3). In all cases we observe that signals above 20 h^{-1} Mpc become identical between models. This is because the marked correlation function is the ratio of two correlation functions (see right hand expression of Eq. (2.3.10)) and we have $\xi(r) \sim W(r)$ for $r > 20\ h^{-1}$ Mpc.

From the observational point of view, we can measure the Newtonian gravitational potential from the X-ray temperature of galaxy clusters (see e.g., Allen et al. 2004, 2008; Li et al. 2016), the gas mass fractions of clusters and the escape velocity profile, $v_{\rm esc}(r)$ (Stark et al., 2016). Hence, if we reconstruct the gravitational potential from the observations mentioned above and use a mark that is a function of the potential, similar to Eq. (2.3.17), then we can test this approach and potentially find a measurable signature of modified gravity. One caveat is that the gravitational potential constructed in this way is the dynamical potential, while in this study we have used lensing potential of haloes (see, e.g., He & Li, 2016).

2.4 Summary

In this Chapter, we studied the clustering of haloes and galaxies in four different cosmologies: a ΛCDM model which is based on general relativity and three Hu & Sawicki $f(R)$ chameleon models with fixed $n = 1$ and $|f_{R0}| = 10^{-6}, 10^{-5}, 10^{-4}$ (denoted F6, F5 and F4). We analyse the output of dark matter-only N-body simulations related to these models at $z = 0.5$.

First, we studied the cumulative halo mass function, finding that the F4 model predicts more haloes than GR at all masses probed by our simulations, with the maximum difference reaching an excess of more than 50 percent for haloes with mass $M_{200c} > 10^{14.3}h^{-1}{\rm M}_{\odot}$. These differences occur due to the enhancement of gravity in

$f(R)$ gravity, which results in the production of more massive haloes in F4 than GR through faster accretion and more frequent merging of small haloes. The differences found in F5 reach 25% for haloes with masses $10^{13}h^{-1}M_{\odot} < M_{200c} < 10^{14}h^{-1}M_{\odot}$ where the screening mechanism at this mass scale is inefficient for this model. F6 shows the smallest difference from GR because in this model the chameleon screening is strong in haloes with mass $M_{200c} > 10^{13}h^{-1}\mathrm{M}_{\odot}$, thereby suppressing the effects of the fifth force.

We populated dark matter haloes with galaxies using a halo occupation distribution, using a five-parameter model which treats separately central and satellite galaxies, with the values of the parameters as used in Manera et al. (2012) to reproduce the clustering of CMASS galaxies with a density number, $n_{\mathrm{g}} = 3.2 \times 10^{-4}h^{3}\mathrm{Mpc}^{-3}$ (Anderson et al., 2012) for our GR simulations. We tuned the parameters to match the galaxy number density and two-point correlation function of GR to within $1-3\%$ for the $f(R)$ models. The galaxy two-point correlation functions for the $f(R)$ and GR models are presented in the right plot of Fig. 2.3.

Then we studied the two-point clustering of dark matter haloes. We chose samples of haloes with fixed halo number density, $n_{\mathrm{h}} = n_{\mathrm{g}}$, resulting to different mass cutoffs in our halo catalogues for all gravity models: $7.643 \times 10^{12}h^{-1}M_{\odot}$ (GR), $7.798 \times 10^{12}h^{-1}M_{\odot}$ (F6), $9.124 \times 10^{12}h^{-1}M_{\odot}$ (F5) and $8.734 \times 10^{12}h^{-1}M_{\odot}$ (F4). We find significant differences in the clustering of dark matter haloes for $f(R)$ models with respect to the GR predictions. The maximum difference between F4 and GR is $\sim 20\%$, while for F5 and F6 it is less than 5%. Also we note that haloes in F5 are more clustered than those haloes in the ΛCDM model, whereas for F6 and F4 haloes are less clustered than their GR counterparts. These results are the combination of two effects, on one hand the enhancement of gravity which means a stronger growth of density peaks and therefore more massive structures at late times which gives a stronger clustering of the structures that are formed from these density peaks. On the other hand, enhanced gravity leads to enhanced merger rates of low-mass haloes formed from lower initial density peaks. The former effect tends to increase halo clustering while the latter effect tends to do the opposite.

We found that the halo and galaxy marked correlation functions for F6 is indis-

tinguishable from GR using all marks, except for the galaxy Gaussian (ρ_R and $\Phi_{\rm N}$) marked correlation functions which predict differences at most $\sim 5\%$ from GR. For the F5 (F4) model, we notice that galaxies mimic the marked clustering at least for the White and log density-marks finding differences of 5% (2.5%) and 2.5% (2.5%), respectively. On the other hand, we observe that with the Gaussian marks (density field and gravitational potential) the difference in the galaxy marked correlation function is boosted, especially for F4, producing a difference of 20% (using density field) and 30% (using gravitational potential) with respect GR.

The galaxy marked correlation functions showed smaller differences between the $f(R)$ and GR models for the density marks, Eqs. (2.3.11)–(2.3.13), than in the case when using the gravitational potential mark, Eq. (2.3.17), this is because the galaxy density field has been tuned to match between the different models. One caveat for our results is that there will be systematics when estimating the mark for observational samples.

Another important feature we observed from marked correlation functions is that the signal above $20\,h^{-1}$ Mpc does not distinguish between models (see corresponding plots of Figs. 2.4 and 2.5). Instead, the measurable differences are on small scales. To improve our predictions on sub-Mpc scales we need to perform higher resolution simulations, but we leave this for future work.

Valogiannis & Bean (2018) recently found that using the dark matter distribution and the White-mark, Eq. (2.3.11) with $\rho_* = 4$ and $p = 10$, the difference between F4 and GR marked correlation functions can reach a maximum of 37% at $r = 1.81h^{-1}$ Mpc. These results can not readily be compared with ours, since we consider dark matter haloes and galaxies rather than the dark matter itself. Furthermore, we employ a different definition of density (counts-in-cells versus the cloud-in-cell smoothing used by Valogiannis & Bean). Although their simulations are similar resolution to the ones we use, the volume of our boxes is ~ 60 times larger, which allows more robust clustering measurements.

Chapter 3

Large-scale redshift space distortions in modified gravity theories

3.1 Introduction

One complication when using observational data provided by galaxy surveys is that the distance to the galaxies is inferred from their redshifts by assuming a cosmological model, to give positions in "redshift space". The peculiar velocities of galaxies along the line of sight (LOS), gravitationally induced motions in addition to the Hubble flow, cause a displacement to the position of the galaxy in redshift space compared to its true position, which is known as the redshift space distortion (RSD) of galaxy clustering. This phenomenon is demonstrated in simulations with "emulated" galaxies (see e.g. Tinker et al. 2006; Tinker 2007; Kwan et al. 2012; Marulli et al. 2017). The RSD effect can be combined with other observables such as the baryon acoustic oscillation (BAO) pattern to put constraints on the growth rate of the large-scale structures as well as the cosmological parameters. A wide range of tracers, including luminous red galaxies (Cabre & Gaztanaga, 2009a; Sánchez et al., 2009), cosmic voids (Hamaus et al., 2015, 2017; Cai et al., 2016) and quasi-stellar-objects (QSOs) (Hou et al., 2018; Gil-Marín et al., 2018; Zarrouk et al., 2018) have been successfully used to extract cosmological information by assuming a standard

cosmological model (ΛCDM) based on General Relativity (GR).

Alternative theories of gravity can have a similar cosmic expansion history to that in ΛCDM but with different evolution of the growth rate, usually parametrised as $f(z) \simeq \Omega_{\rm m}^{\gamma}(z)$, which depends on the mass density parameter $\Omega_{\rm m}(z)$ and a fitting index γ (Linder & Cahn, 2007). A deviation of the index from $\gamma = 0.55$ would indicate a different theory than GR with distinctive gravitational evolution, and therefore has a direct impact on the anisotropic clustering caused by the RSD effect. Due to the degeneracy between the growth rate and the matter fluctuation amplitude, instead of probing $f(z)$ directly, we use the linear distortion parameter, $\beta(z) = f(z)/b(z)$, where $b(z)$ is the linear tracer bias (Kaiser, 1987; Hamilton, 1992). Two representative families of MG models are the Hu-Sawicki $f(R)$ gravity model (Hu & Sawicki, 2007) and the normal branch of the Dvali−Gabadadze−Porrati model (nDGP; Dvali et al. 2000) which, as we shall see later, make distinct predictions for the linear growth rate $f(z)$ (recall that the linear growth rate in $f(R)$ gravity models is scale dependent, $f(k, z)$).

The impact of modified gravity on RSD has been studied in a number of previous works. For instance, Jennings et al. (2012) and Xu (2015) presented predictions for the RSD in $f(R)$ gravity in Fourier space and Arnalte-Mur et al. (2017) complemented these results in configuration space by measuring the correlation function. These studies are based either on the matter or halo density fields as predicted using N-body simulations of modified gravity, or using analytical fitting formulae for matter clustering which are themselves derived from simulations. This demonstrates the importance of using cosmological simulations to study the RSD effect on mildly and strongly nonlinear scales. Recently, He et al. (2018) used high-resolution simulations of ΛCDM and $f(R)$ gravity to study the small-scale RSD effect. These authors found that the predictions of $f(R)$ gravity are strongly disfavoured by current measurements of galaxy clustering in redshift-space on scales between $1 \sim 10\,h^{-1}$Mpc, while the data is in excellent agreement with ΛCDM. Song et al. (2015) used the BOSS DR11 to measure the redshift space correlation function and put constraints on $f(R)$ gravity.

Recently, Barreira et al. (2016) used the same model for non-linearities, bias,

and RSD to estimate the growth rate in nDGP models, also using mock galaxy catalogues built from N-body simulations. There are several differences in the work presented here compared with that of Barreira et al. (2016). Firstly, we consider a wider variety of models by including also variants of $f(R)$ gravity and different parameter values for nDGP. Secondly, we conduct an explicit comparison of linear Kaiser and nonlinear models, considering different estimators and ranges of scales in the parameter fitting to test for systematic effects. Thirdly, the mock galaxy catalogues used here are constructed in a different way from that used by Barreira et al. (2016), using larger simulations.

Arguably, simulations are the only way to accurately predict RSD effects down to such small scales, but the main disadvantage of this approach is the high cost of running large suites of high-resolution simulations to explore the parameter space, and the uncertainties in the connection between galaxies and simulated dark matter haloes. Regarding the galaxy-dark matter halo connection, hydrodynamical simulations and semi-analytical modelling, two approaches which add elements of the physics of galaxy formation to the modelling of the growth of structure in the dark matter, will inform empirical treatments of the galaxy-halo connection, such as the one used in this Chapter (e.g. Contreras et al. 2013; Chaves-Montero et al. 2016; Desmond et al. 2017). In the mean time, the importance of the theoretical modelling of RSD in modified gravity is being realised and increasing effort is being devoted to improving the description of the RSD effects in $f(R)$ gravity and nDGP models on mildly nonlinear scales, based on higher-order perturbation theory (see, e.g., the pioneering works of Taruya et al., 2014; Bose & Koyama, 2016; Taruya, 2016; Bose et al., 2017a; Bose & Koyama, 2017). In particular, the theoretical modelling developed by Taruya et al. (2014) and Taruya (2016) was implemented by Bose & Koyama (2016) and Bose & Koyama (2017) which has been carefully compared against N-body simulations and found to show good agreement with the results for the power spectrum and correlation function in real and redshift space. These authors have gone to great lengths to include higher-order perturbation terms in the description of the MG effects to ensure that the latter are modelled consistently and accurately. These analytical or semi-numerical approaches are much more efficient

than full N-body or hydrodynamical simulations, though their validity is usually restricted to mildly nonlinear scales, such as $k \leq 0.1 - 0.3\,h\,\mathrm{Mpc}^{-1}$.

Here, we explore the following questions: (1) Do galaxy catalogues from the current and next generations of galaxy surveys offer the realistic possibility to constrain or rule out some of the leading modified gravity models in the literature using RSD? (2) Given reasonable estimates of theoretical and observational uncertainties, is a simpler treatment of the RSD effect (which ideally does not involve new theoretical templates – based on simulations or perturbation theory – to be developed each time the gravity model or its parameter is changed) sufficient to measure β and distinguish between models? The simpler treatments we consider include (i) a linear theory model (Kaiser, 1987; Hamilton, 1992) and (ii) a model that accounts for nonlinear matter evolution following the approach of Crocce, Blas & Scoccimarro (in prep.), who extend renormalised perturbation theory (RPT, Crocce & Scoccimarro, 2006) by using Galilean invariance to find a resummation of the mode-coupling power spectrum, galaxy bias as in Chan et al. (2012), and a detailed description of RSD (Scoccimarro, 2004), which does *not* incorporate any MG effect. The approach we take is to directly confront the RSD predicted by these simplified treatments against RSD measurements from mock galaxy catalogues built on simulations of different gravity models, and check if the input β values can be faithfully recovered. The linear theory prediction is model-independent, and the nonlinear model used is for GR only so that it is also effectively model-independent

The Chapter is organised as follows. Section 3.2 describes the N-body simulations and the construction of mock galaxy catalogues in real and redshift space. In Sect. 3.3 we outline the theoretical aspects of redshift space distortions. Results from the linear and non-linear RSD models are presented in 3.4.1 and 3.4.2 of Section 3.4, respectively, and we discuss the results in Section 3.4.3. Finally, Sect. 3.5 contains the summary of the Chapter.

3.2 N-body simulations and galaxy catalogues

N-body cosmological simulations have played an important role in the analysis of alternative gravity models to GR. Nowadays, these simulations are necessary for the construction of synthetic galaxy catalogues and study the impact of modifications of gravity on the distribution and clustering of galaxies. In this section we present the technical details of the simulations we use and the prescription we follow to generate mock catalogues.

3.2.1 N-body simulations of modified gravity

We use the Extended LEnsing PHysics using ANalaytic ray Tracing (ELEPHANT) dark matter only N-body simulations which have been run using the ECOSMOG (Li et al., 2012) and ECOSMOG-V (Li et al., 2013a) codes for $f(R)$ gravity and nDGP models respectively. ECOSMOG and ECOSMOG-V are modified versions of the publicly available N-body and hydrodynamical simulation code RAMSES (Teyssier, 2002). These codes are efficiently optimised and implemented with methods that speed up the calculations of the non-linear partial differential equations that characterise these models (Barreira et al., 2015; Bose et al., 2017b).

The cosmological parameters are the best-fit values from the WMAP9 collaboration (Hinshaw et al., 2013)

$$\{\Omega_{\rm b}, \Omega_{\rm CDM}, h, n_s, \sigma_8\} = \{0.046, 0.235, 0.697, 0.971, 0.84\}.$$

The simulations follow the evolution of $N_{\rm p} = 1024^3$ particles with mass $m_{\rm p} = 7.798 \times 10^{10}\, h^{-1}{\rm M}_\odot$ in a cubical box of comoving size $L_{\rm box} = 1024\, h^{-1}{\rm Mpc}$ from their initial conditions (generated with the MPGRAFIC code, Prunet et al. 2008) at $z_{\rm ini} = 49$ up to today ($z_{\rm fi} = 0$). In this work we used five independent realisations of the matter field for each gravity model. For each realisation the simulations of all gravity models start from the same initial condition, because at $z_{\rm ini} = 49$ the effects of modified gravity on large-scale structure formation were negligible for all MG models considered here.

Halo catalogues for all gravity models were constructed using the ROCKSTAR halo finder (Behroozi et al., 2013a) at $z = 0$, 0.3 and 0.5. We chose M_{200c} as the

halo mass definition, which is the mass enclosed within a sphere of radius r_{200c} with 200 times the critical density of the Universe.

The ELEPHANT simulations have been used to study the properties of voids for chameleon and Vainshtein mechanism models (Cautun et al., 2018; Paillas et al., 2019) and the halo and galaxy marked correlation functions (Armijo et al., 2018; Hernández-Aguayo et al., 2018) in $f(R)$ gravity.

3.2.2 Mock galaxy catalogues

The next step to measure the impact of modified gravity on redshift space distortions is the generation of mock galaxy catalogues. For this purpose, we built the catalogues by implementing a five-parameter halo occupation distribution (HOD) (Zheng et al., 2005, 2007) model. This HOD model determines the numbers of central ($\langle N_{\rm c}\rangle$) and satellite ($\langle N_{\rm s}\rangle$) galaxies inside dark matter haloes as functions of the halo mass ($M = M_{200c}$) by following a distribution given by,

$$\langle N_{\rm c}(M)\rangle = \frac{1}{2}\left[1 + {\rm erf}\left(\frac{\log_{10} M - \log_{10} M_{\rm min}}{\sigma_{\log M}}\right)\right], \tag{3.2.1}$$

$$\langle N_{\rm s}(M)\rangle = \langle N_{\rm c}(M)\rangle \left(\frac{M - M_0}{M_1}\right)^{\alpha}. \tag{3.2.2}$$

The mean total number of galaxies in each halo is given by $\langle N_{\rm t}\rangle = \langle N_{\rm c}\rangle + \langle N_{\rm s}\rangle$. As we can see from Eq. (3.2.1), $M_{\rm min}$ and $\sigma_{\log M}$ determine the occupancy of central galaxies while the whole set of parameters determine the mean number of satellite galaxies in each halo (see Eq. (3.2.2)).

We follow the same prescription as Manera et al. (2012) and Hernández-Aguayo et al. (2018) to construct mock catalogues in real space **(see Sec. 2.2.3)**. In summary, when a central galaxy is placed inside a halo we assume that this galaxy is located at the centre of mass of its host halo and takes its coordinates and velocity information. Satellite galaxies (which orbit around central galaxies in haloes with $M_{200c} \geq M_0$) are radially distributed following an Navarro-Frenk-White (NFW) profile (Navarro et al., 1996, 1997), with a uniform angular distribution. The position of satellite galaxies is randomly chosen within the halo radius ($0 < r < r_{200c}$), and their velocity is the halo velocity plus a perturbation along the x, y and z coordinates

drawn from a Gaussian distribution with variance equal to the 1D velocity dispersion of the host halo.

One of the key steps of the HOD approach is to set the HOD parameters in Eqs. (3.2.1) and (3.2.2) to reproduce the galaxy clustering in real galaxy surveys. In addition, given that we only observe one Universe, we need to demand that all galaxy catalogues from all gravity models are consistent with observations. For these reasons, in this work the MG HOD parameters have been calibrated to match with the galaxy number density and the real-space two-point correlation function (which is directly related to the projected correlation function) of the same galaxy sample. In practice, in the case of GR, we take the values of the parameters from the BOSS CMASS DR9 sample (Manera et al., 2012): $\log_{10}(M_{\rm min}/[h^{-1}M_\odot]) = 13.09$, $\log_{10}(M_1/[h^{-1}M_\odot]) = 14.00$, $\log_{10}(M_0/[h^{-1}M_\odot]) = 13.077$, $\sigma_{\log M} = 0.596$ and $\alpha = 1.0127$. Note that the CMASS sample has a redshift distribution between $0.4 < z < 0.7$, which is compatible with one of the three redshifts considered in this work ($z = 0.5$); however, we adopt the same HOD parameter values for GR at the other two redshifts ($z = 0.3$ and $z = 0$) as well, as our objective is to study the measurement of growth rate using RSD for galaxy catalogues with similar real-space clustering, rather than to make precise mock galaxy catalogues for the different gravity models (the latter will be left for future studies). To calibrate the HOD parameters for the various MG models, we used the simplex algorithm presented in Sec. 2.2.3.

Finally, we use the distant-observer approximation to shift the positions of galaxies from real to redshift space. We use the three coordinates, $\hat{x}$, $\hat{y}$ and $\hat{z}$, as the line-of-sight (LOS) to generate three redshift-space catalogues for one real-space catalogue where the new coordinates are,

$$\mathbf{s} = \mathbf{r} + \frac{(1+z)v_\parallel}{H(z)}\hat{e}_\parallel \,, \tag{3.2.3}$$

where $\mathbf{r}$ is the coordinate vector in real space, z is the redshift of the snapshot used to generate the catalogues, $H(z)$ is the Hubble parameter as a function of z, $v_\parallel$ is the component of the velocity along the LOS and $\hat{e}_\parallel$ is the unitary vector of the LOS direction. So, in total we have fifteen redshift space catalogues for each gravity model and each redshift.

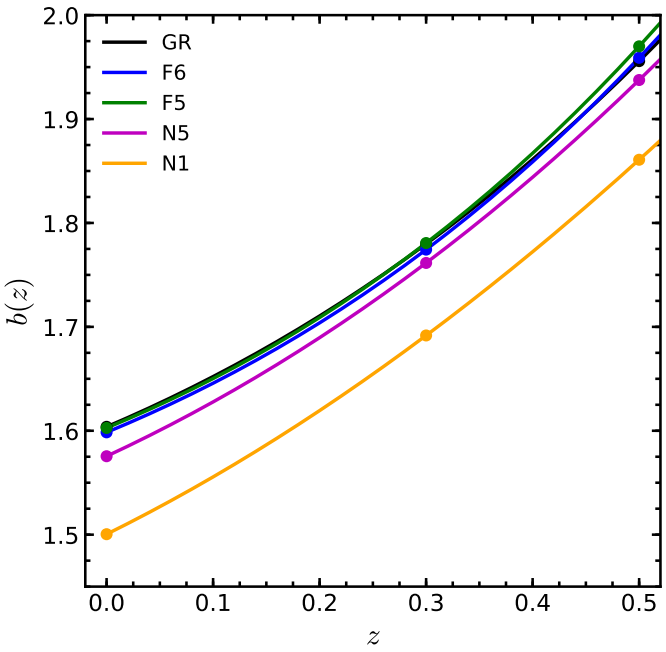

Figure 3.1: Linear galaxy bias measured from our galaxy mock catalogues at $z = 0$, $z = 0.3$ and $z = 0.5$ (see Table 3.1) for the five gravity models: GR (black), F6 (blue), F5 (green), N5 (magenta) and N1 (orange). The solid lines represent an extrapolation between points at $z = 0$, 0.3 and 0.5.

Linear galaxy bias

Galaxies are biased tracers of the dark matter density field, hence the relation between the distribution of galaxies and matter is given by the linear galaxy bias b defined as

$$b \equiv \delta_{\rm g}/\delta \,, \tag{3.2.4}$$

where $\delta_{\rm g}$ is the galaxy density contrast and δ is the density contrast of matter. In terms of the correlation function, the linear galaxy bias can be estimated in different ways,

$$b(r) = \sqrt{\frac{\xi_{\rm gg}(r)}{\xi_{\rm mm}(r)}} = \frac{\xi_{\rm gg}(r)}{\xi_{\rm gm}(r)} = \frac{\xi_{\rm gm}(r)}{\xi_{\rm mm}(r)} \,, \tag{3.2.5}$$

where $\xi_{\rm gg}(r)$ and $\xi_{\rm mm}(r)$ are respectively the galaxy-galaxy and matter-matter auto-correlation functions, and $\xi_{\rm gm}(r)$ is the galaxy-matter cross-correlation function, all in real space. Li & Shirasaki (2018) showed that the galaxy-matter cross-correlation coefficient, $R_{\rm gm}(r) \equiv \xi_{\rm gm}(r)/\sqrt{\xi_{\rm gg}(r)\xi_{\rm mm}(r)}$, approaches unity on scales

Table 3.1: Linear galaxy bias, b, estimated by Eq. (6.5.6) for all gravity models at $z = 0$, 0.3 and 0.5.

	Linear galaxy bias b		
	$z = 0$	$z = 0.3$	$z = 0.5$
GR	1.6038	1.7798	1.9557
F6	1.5985	1.7743	1.9589
F5	1.6027	1.7807	1.9699
N5	1.5756	1.7615	1.9375
N1	1.5004	1.6917	1.8608

$r \geq 2\,h^{-1}$Mpc, hence the linear bias measured in different ways agree well with each other. Therefore, we measure the linear galaxy bias from our mock catalogues as

$$b(r, z) \equiv \frac{\xi_{\rm gg}(r, z)}{\xi_{\rm gm}(r, z)}\,, \tag{3.2.6}$$

which is less expensive to compute than $\xi_{\rm gm}/\xi_{\rm mm}$. At sufficiently large scales we expect $b(r) \approx$ const., hence to measure the linear galaxy bias from our mock catalogues we make a fit of Eq. (3.2.6) to a constant function using data in the range $r_{\rm min} \leq r \leq r_{\rm max}$, with $r_{\rm max} = 150\,h^{-1}$Mpc and $10 < r_{\rm min}/(\,h^{-1}{\rm Mpc}) < 45$, then we take the mean over all best-fitting values. Fig. 3.1 shows the evolution of $b(r, z)$ as a function of z. We observe that, for the same number density, galaxies at higher redshifts are more biased tracers of the underlying dark matter field, which is due to faster growth of clustering of dark matter than of galaxies. Since the clustering amplitude of galaxies in real space is tuned to be the same for different cosmological models, by the construction of HOD, models with higher σ_8 (such as N1) have a lower linear bias as is shown in Fig. 3.1.

The linear bias values measured from the mock galaxy catalogues for the different gravity models at the three different redshifts are listed in Table 3.1.

3.3 Galaxy clustering in redshift space

Peculiar velocities of galaxies induce anisotropies in redshift space and leave distinctive imprints on the clustering pattern at different regimes. On large (linear) scales, galaxies infall into high-density regions such as clusters producing a squashing effect of these regions along the line-of-sight: this is the Kaiser effect (Kaiser, 1987). On smaller (nonlinear) scales, the random motions of galaxies in virialised objects produce the Fingers-of-God (FoG) effect where the density field becomes stretched and structures seem elongated along the line of sight (Jackson, 1972). The amplitude of the RSD is related to the distortion parameter β, defined as

$$\beta(z) \equiv \frac{f(z)}{b(z)}\,, \tag{3.3.7}$$

where f is the linear growth rate (Eq.(1.2.39)) and b is the linear galaxy bias (Eq.(3.2.6)) as a function of redshift.

The fiducial value of β for the five gravity models (GR, F6, F5, N5 and N1) at $z = 0$, 0.3 and 0.5 are presented in Table 3.2. Given the fact the linear growth rate, f, is scale-dependent in $f(R)$ gravity we present the fiducial values at two different wavenumbers ($k = 0.1\,h\,\mathrm{Mpc}^{-1}$ and $k = 0.01\,h\,\mathrm{Mpc}^{-1}$) corresponding to quasilinear and linear scales. The estimation of the linear bias parameter is taken from Table 3.1.

The effects of redshift space distortions can be measured using the redshift-space correlation function of galaxies, $\xi(r_p, r_\pi)$, which is the excess probability of finding a pair of galaxies at separations transverse (r_p) and parallel (r_π) to the LOS. Fig. 3.2 shows the redshift space correlation function $\xi(r_p, r_\pi)$ as a function of separation (r_p, r_π) at $z = 0.5$, for the different gravity models. The black dashed curve corresponds to the two-dimensional correlation function in real-space (since the clustering for different gravity models have been tuned to match each other, for demonstration, we just show the GR result). We can clearly see that along the LOS at $r_p \lesssim 2\,h^{-1}$Mpc the clustering is enhanced by the peculiar velocities of galaxies producing the FoG effect, while at $r_p > 2\,h^{-1}$Mpc the clustering pattern is squashed thanks to the Kaiser effect. We observe that for nDGP models the contours become more flattened compared with GR because of the stronger linear

Table 3.2: True theoretical values of the β parameter at $z = 0$, 0.3 and 0.5 for the five gravity models. Since the growth rate is scale-dependent in $f(R)$ gravity we present the true values at 2 scales, $k = 0.01\,h\,\mathrm{Mpc}^{-1}$ and $k = 0.1\,h\,\mathrm{Mpc}^{-1}$.

	$\beta_{\rm true}$		
	$z = 0$	$z = 0.3$	$z = 0.5$
GR	0.3081	0.3671	0.3749
N5	0.3193	0.3769	0.3842
N1	0.3507	0.4094	0.4164
($k = 0.01\,h\,\mathrm{Mpc}^{-1}$)			
F6	0.3091	0.3682	0.3744
F5	0.3087	0.3672	0.3725
($k = 0.1\,h\,\mathrm{Mpc}^{-1}$)			
F6	0.3124	0.3716	0.3773
F5	0.3292	0.3893	0.3925

growth rate (see Fig. 1.1). In the linear regime the overdensity grows proportional to the linear growth factor $\delta_{\rm m}(z) \propto D(z)$, therefore, the matter power spectra for the modified gravity models have higher amplitude and resulting in a higher matter fluctuation, σ_8, compared to GR. A higher matter fluctuation produces an increase of galaxies that infall into high-density regions and makes the Kaiser effect stronger (Tinker et al., 2006). At the same time, we note that the FoG effect is very similar for the N1 and GR models, which is likely due to the effective Vainshtein screening mechanism on small scales in real space (e.g., Paillas et al., 2019), which makes the velocity dispersion comparable for these models.

In the case of $f(R)$ gravity models the two-dimensional correlation functions are indistinguishable from the one measured from the GR model. This is different from the behaviour of the nDGP models. A likely reason for this difference is the fact that in nDGP the fifth force is unscreened on large scales (i.e., beyond the Vainshtein radius of massive objects) so that the infall on scales of order $10\,h^{-1}$Mpc is enhanced, while for the $f(R)$ models considered here the fifth force is short ranged and cannot affect such scales.

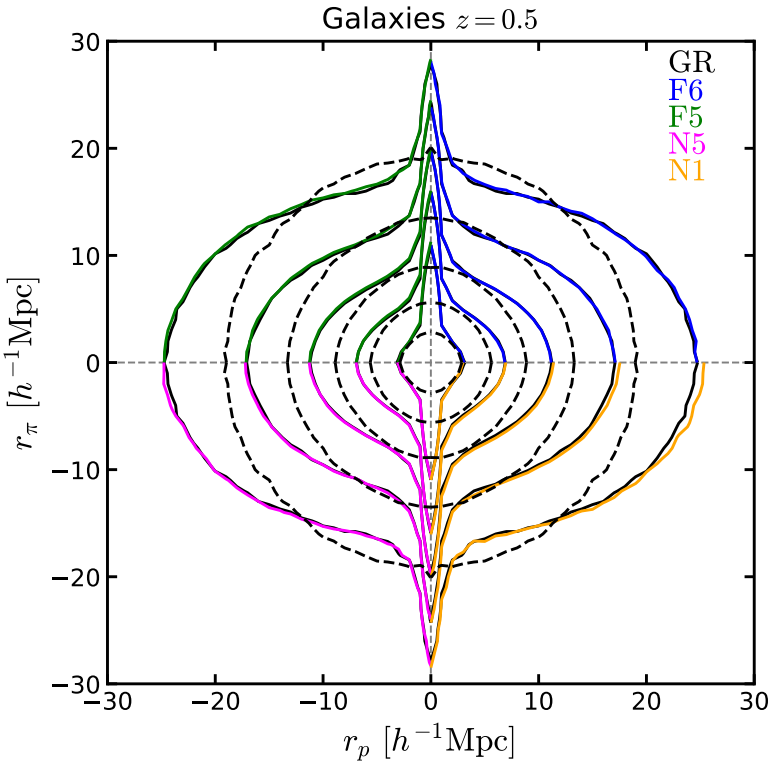

Figure 3.2: The two dimensional galaxy correlation function $\xi(r_p, r_\pi)$ measured from our mock catalogues at $z = 0.5$ as a function of separation across (r_p) and along (r_π) the line-of-sight. Contours show lines of constant $\xi(r_p, r_\pi)$ at $\xi(r_p, r_\pi) = 5$, 2, 1, 0.5, 0.25. The correlation functions correspond to the average of fifteen measurements obtained by projecting five realisations over the three LOS directions. For clarity we have projected $\xi(r_p, r_\pi)$ for GR for positive r_p and r_π over four quadrants and displayed the MG correlation function in different quadrants as follows: (r_p, r_π) for F6, $(-r_p, r_\pi)$ for F5, $(-r_p, -r_\pi)$ for N5 and $(r_p, -r_\pi)$ for N1. The black dashed contours correspond to the real-space measurements of the correlation function at the same values of its counterpart in redshift-space, since all galaxy catalogues produce the same real-space clustering we show the GR case only. Different colour line correspond to different gravity model as specified in the legend.

In order to increase the signal-to-noise ratio, it is helpful to further project the two-dimensional correlation function $\xi(r_p, r_\pi)$ onto a one-dimensional object. Given the symmetry along the line-of-sight, we first express the transverse and parallel separation (r_p, r_π) as separation in redshift space and the cosine of the angle between s and the LOS direction,

$$s = \sqrt{r_\pi^2 + r_p^2}\,, \qquad \mu = \frac{r_\pi}{s}\,. \tag{3.3.8}$$

We decompose $\xi(s, \mu)$ into multipole moments,

$$\xi_l(s) = (2l+1) \int_0^1 \xi(s, \mu) P_l(\mu)\, \mathrm{d}\mu\,, \tag{3.3.9}$$

where $P_l(\mu)$ are the Legendre polynomials. In the linear regime, the $l = 0$, 2 and 4 moments are non-zero with $P_0(\mu) = 1$, $P_2(\mu) = (3\mu^2+1)/2$, $P_4(\mu) = (35\mu^4 - 30\mu^2 + 3)/8$, corresponding to the monopole, quadrupole and hexadecapole moments. We measured $\xi(s, \mu)$ from our galaxy catalogues using linear bins centred at 2.5 to 147.5 h^{-1}Mpc with separation $\Delta s = 5\,h^{-1}$Mpc. For μ, we use 30 linearly spaced bins between 0 and 1.

The left panel of Fig. 3.3 shows the multipole moments $(\xi_l(s))$ of the correlation functions measured from our galaxy catalogues at $z = 0.5$ for the different gravity models. From the monopole, $\xi_0(s)$ (upper curves of left panel in Fig. 3.3), we observe that the position of the baryon acoustic oscillation (BAO) peak is not affected by modified gravity and can be found at a scale of $s_{\rm BAO} \simeq 105\,h^{-1}$Mpc or 150 Mpc. Higher order multipole moments such as the quadrupole $(\xi_2(s))$ and the hexadecapole $(\xi_4(s))$ encode the degree of anisotropy produced by redshift distortions. In the case of the quadrupole, $\xi_2(s)$, N1 shows the strongest deviation with respect to GR especially on scales $s > 20\,h^{-1}$Mpc, followed by N5. This is a direct consequence of a more squashed contour for the nDGP models caused by higher growth rate and stronger matter fluctuation. Our measurements of the hexadecapole are almost indistinguishable when compare the MG models with GR. This is due to the fact that higher order multipoles $(l \geq 4)$ do not have a big impact on the estimation of the correlation function and are noisier than the monopole and quadrupole (Hamilton, 1998).

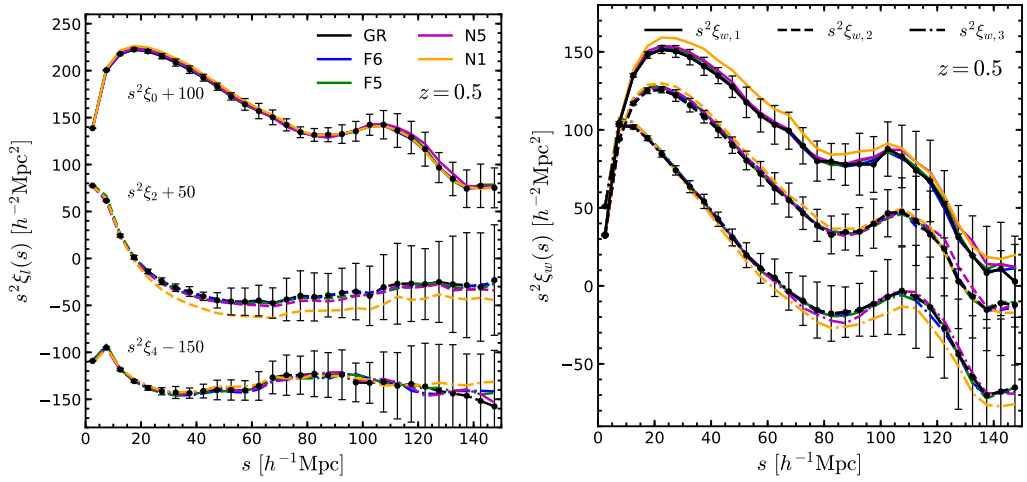

Figure 3.3: *Left panel*: Monopole, quadrupole and hexadecapole moments of the correlation function, Eq. (6.5.8), for our five gravity models at $z = 0.5$. The moments have been shifted by a factor of 100, 50 and -150 for better visualization. *Right panel*: Clustering wedges, Eq. (3.3.10), measured at $z = 0.5$ for all gravity models as labelled, the upper wedge (solid lines) correspond to angles with $0 < \mu < 1/3$, the middle wedge (dashed lines) to $1/3 < \mu < 2/3$ and the lower wedge (dot-dashed lines) to $2/3 < \mu < 1$. The error bars correspond to the standard deviation over fifteen GR measurements.

As an alternative to the multipoles, we also measured the clustering wedges which correspond to angle-averaged measurements of the correlation function (Kazin et al., 2012),

$$\xi_w(s) = \frac{1}{\mu_2 - \mu_1} \int_{\mu_1}^{\mu_2} \xi(s, \mu)\ \mathrm{d}\mu. \tag{3.3.10}$$

In this work we choose the intervals $(i-1)/3 < \mu < i/3$ with $i = 1, 2, 3$, which are commonly used in the literature (for instance, see Sánchez et al. 2017). The relation between multipoles and wedges is given by the transformation,

$$\xi_w(s) = \sum_l \xi_l(s) \bar{P}_l\,, \tag{3.3.11}$$

where $\bar{P}_l$ is the average of the Legendre polynomial over the μ-bin. When the higher order statistics can be truly neglected, an explicit expression can be written down as the transformation between the multipoles and wedges,

$$\xi_\ell(s) = \begin{bmatrix} 1/3 & 1/3 & 1/3 \\ -9/14 & -15/28 & 33/28 \\ 54/35 & -81/35 & 27/35 \end{bmatrix} \xi_w(s)\,. \tag{3.3.12}$$

Where the mean of the three clustering wedges correspond to the monopole of the correlation function,

$$\xi_0(s) = \frac{\xi_{w,1}(s) + \xi_{w,2}(s) + \xi_{w,3}(s)}{3}\,. \tag{3.3.13}$$

The measured clustering wedges ($\xi_w(s)$) at $z = 0.5$ are shown in the right panel of Fig. 3.3. The behaviour of the 2D two-point correlation functions, $\xi(r_p, r_\pi)$, shown in Fig. 3.2, can be quantified and described by the clustering wedges. The first wedge, $\xi_{w,1}$, encodes information about the correlation function closer to the transverse (or perpendicular) direction (r_p). Here, the FoG effect is not significant and the Kaiser effect governs the clustering of galaxies. For this reason (see the description of $\xi(r_p, r_\pi)$ above) N1 has a larger positive amplitude compared to GR, followed by N5 but with a weaker deviation. The second or intermediate wedge, $\xi_{w,2}$, corresponds to $\bar{\mu} = 0.5$ and is the closest to the monopole in shape and amplitude. Finally, the third wedge, $\xi_{w,3}$, which is closer (or parallel) to the LOS (r_π), is the most impacted by the random motions of galaxies due to the FoG effect. The shape of the parallel

wedge is slightly different to the transverse and intermediate wedges, and on smaller scales it has a steeper slope. In this case, we found a negative difference between the MG models with respect to GR (opposite to the difference found in the transverse wedge).

In general, both the multipoles and the wedges of the correlation function for $f(R)$ gravity models show a weaker deviation from GR and this is expected to impact on the estimation of β. In the following sections we discuss how to estimate β from theoretical models based on perturbation theory.

3.4 Theoretical RSD models and parameter estimation

In this section we give the main results of this Chapter, namely the validation of the inference of β based on a number of estimators of RSD, using the redshift-space mock galaxy catalogues mentioned above. For a given set of model parameters (e.g., β), the theoretical predictions of the estimators are obtained using two methods – linear perturbation theory (Kaiser model) and the Galilean-invariant renormalized perturbation theory (gRPT) based on higher-order perturbation theory. We shall discuss these two methods and their results in two separate subsections, and discuss the implications of the results in a third subsection.

3.4.1 Linear model

In linear perturbation theory, the relation between the redshift-space galaxy power spectrum with its counterpart in real space is given by the Kaiser formula (Kaiser, 1987):

$$P_{\rm s}(k,\mu) = (1+\beta\mu^2)^2 P_{\rm r}(k)\,. \tag{3.4.14}$$

As we are interested in the effects of RSD on the correlation function, we need to have a similar relation in configuration space. Under the plane parallel approximation of the distortion operator, the correlation function is expressed as follows (Hamilton,

1992, 1998),

$$\xi(s,\mu) = [1+\beta(\partial/\partial z)^2(\nabla^2)^{-1}]^2\xi(r)\,, \tag{3.4.15}$$

$$= \xi_0(s)P_0(\mu)+\xi_2(s)P_2(\mu)+\xi_4(s)P_4(\mu)\,. \tag{3.4.16}$$

In linear theory, the multipoles of the correlation function can be estimated as follows (Hamilton, 1992),

$$\xi_0(s) = \left(1+\frac{2\beta}{3}+\frac{\beta^2}{5}\right)\xi(r)\,, \tag{3.4.17}$$

$$\xi_2(s) = \left(\frac{4\beta}{3}+\frac{4\beta^2}{7}\right)[\xi(r)-\bar{\xi}(r)]\,, \tag{3.4.18}$$

$$\xi_4(s) = \frac{8\beta^2}{35}\left[\xi(r)+\frac{5}{2}\bar{\xi}(r)-\frac{7}{2}\bar{\bar{\xi}}(r)\right]\,, \tag{3.4.19}$$

where $\xi(r)$ is the galaxy correlation function in real-space and

$$\bar{\xi}(r) = \frac{3}{r^3}\int_0^r \xi(r')r'^2\,\mathrm{d}r'\,, \tag{3.4.20}$$

$$\bar{\bar{\xi}}(r) = \frac{5}{r^5}\int_0^r \xi(r')r'^4\,\mathrm{d}r'\,. \tag{3.4.21}$$

From Eqs. (6.5.21) and (6.5.22) we can define two estimators to obtain the distortion parameter, β (Hawkins et al., 2003),

$$R(s) \equiv \frac{\xi_0(s)}{\xi(r)} = 1+\frac{2\beta}{3}+\frac{\beta^2}{5}\,, \tag{3.4.22}$$

and

$$Q(s) \equiv \frac{\xi_2(s)}{\xi_0(s)-\bar{\xi}_0(s)} = \frac{(4/3)\beta+(4/7)\beta^2}{1+(2/3)\beta+(1/5)\beta^2}\,, \tag{3.4.23}$$

where

$$\bar{\xi}_0(s) = \frac{3}{s^3}\int_0^s \xi_0(s')s'^2\,\mathrm{d}s'\,, \tag{3.4.24}$$

is the volume average of the monopole in redshift space. For the estimation of clustering wedges in the linear theory model we simply substitute Eqs. (3.4.17)-(3.4.19) into Eq. (3.3.11).

Figure 3.4 compares the theoretical and measured values of the two estimators – $R(s)$ on the left and $Q(s)$ on the right. In both panels the dashed horizontal lines represent the theoretical predictions for GR and nDGP models of $R(s)$ and $Q(s)$; for $f(R)$ gravity models the theoretical predictions are shown as horizontal shaded

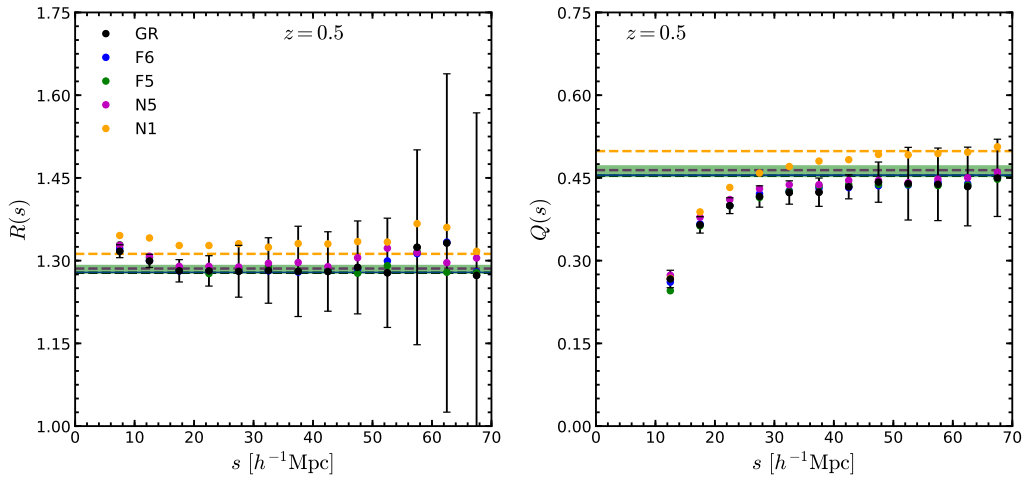

Figure 3.4: *Left panel*: Ratio of the monopole in redshift space to the real space correlation function, $R(s)$ Eq. (3.4.22), as a function of separation at $z = 0.5$. *Right panel*: $Q(s)$ estimator defined by Eq.(3.4.23) as a function of separation at $z = 0.5$. In both panels we plot the estimators up to a scale of $s = 70\,h^{-1}$Mpc for better visualisation and to avoid the transition to negative values of $\xi_0(s)$. Horizontal dashed lines represent the theoretical predictions of the linear model for GR, N5 and N1 models, for the case of $f(R)$ gravity the theoretical predictions are shown as horizontal shaded bands. The error bars correspond to the standard deviation over fifteen GR measurements.

bands for wavenumbers $0.01 < k/(\,h\,\mathrm{Mpc}^{-1}) < 0.1$. The theoretical estimations of $R(s)$ and $Q(s)$ are calculated with the second equality of Eqs. (3.4.22) and (3.4.23), respectively, where the values of β are taken from Table 3.2.

The symbols in the left panel of Fig. 3.4 show the measurements of $R(s)$ (first equality of Eq. (3.4.22)) from our galaxy catalogues at $z = 0.5$ for the different gravity models. Let us recall that the real space correlation functions have been tuned to be within 2-3% for all gravity models (see Section 3.2.2). Hence, the difference in $R(s)$ between models is mainly caused by the difference in the redshift space monopole, $\xi_0(s)$. From the measurements from the simulations, we find that all models reach an asymptotic value at $s \approx 10\,h^{-1}$Mpc as expected (Tinker et al., 2006; Marulli et al., 2017). We also find that for all models the mean values of $R(s)$ are above the theoretical expectation. The reason for which is that the Kaiser model, Eq. (3.4.14), does not contain a FoG term which models the power of galaxies on small separations and hence underestimates the clustering on all scales when Fourier transforming to get the correlation function. Nevertheless, given the size of the error bars, all models show a good agreement with the fiducial values.

The $Q(s)$ estimator at $z = 0.5$ is presented in the right panel of Fig. 3.4. The measurements are obtained by taking the ratio in the first equality of Eq. (3.4.23). In this case the mean values from all models reach an asymptotic value at separations $s = 40\,h^{-1}$Mpc but are still below the fiducial values (opposite to $R(s)$), only matching with the theoretical expectation at $s \sim 70\,h^{-1}$Mpc. On scales below $s = 30\,h^{-1}$Mpc non-linearities produce smaller values of $Q(s)$. Our results are consistent with previous observational and theoretical findings (see e.g. Hawkins et al. 2003; Tinker et al. 2006; Tinker 2007).

Parameter estimation using the linear model

To estimate $\beta(z)$ from $R(s)$, $Q(s)$ and $\xi_w(s)$ using the linear theory model, we use a χ^2-test by minimising the χ^2 defined as

$$\chi^2(\beta) = \sum_i \left(\frac{E(s_i) - E^{\mathrm{th}}(s_i;\beta)}{\sigma_{E_i}} \right)^2 , \tag{3.4.25}$$

where $E(s)$ is the average measured linear estimator (i.e. $R(s)$, $Q(s)$ or $\xi_w(s)$), σ_{E_i} is the measured error of the linear estimator and $E^{\rm th}(s;\beta)$ is the theoretical prediction of each estimator. Since the linear model estimators only depend on one parameter (β), we opt to use the standard deviation over 15 measurements in Eq. (3.4.25) rather than construct a covariance matrix for estimating the error.

To obtain the best-fitting value of β, we searched in a grid of values in the range $\beta \in [0,1]$, with a step size of $\Delta\beta = 0.0001$, for the theoretical estimators and identified the value of β that minimises the χ^2, Eq. (3.4.25), as $\chi^2_{\rm min} = \chi^2(\beta_{\rm fit})$. Since we vary only one parameter, the 1σ error bar on β corresponds to $\Delta\chi^2 \equiv \chi^2 - \chi^2_{\rm min} = 1$. We fit our measurements using two ranges of scales: $s = 20 - 150\,h^{-1}$Mpc ($s_{\rm min} = 20\,h^{-1}$Mpc) and $s = 40 - 150\,h^{-1}$Mpc ($s_{\rm min} = 40\,h^{-1}$Mpc). These particular values of $s_{\rm min}$ are inside the range of values used to constrain the growth rate in different studies of BOSS and eBOSS samples (White et al., 2015; Sánchez et al., 2017; Hou et al., 2018).

In Fig. 3.5 we show the best-fitting β values for all gravity models at $z = 0$, 0.3 and 0.5 for the linear (Kaiser) model, with 1σ error bars, compared to with their theoretical prediction. The left column corresponds to the fits using the range $s = 20 - 150\,h^{-1}$Mpc and the right column shows the fits for the range $s = 40 - 150\,h^{-1}$Mpc. The first row corresponds to the monopole to real space correlation function ratio, $R(s)$, the second row shows the best-fit values from using the $Q(s)$ estimator and the third row presents our results from using three clustering wedges, $\xi_w(s)$.

We find that the best-fitting β values using $R(s)$ are above the theoretical expectations, in particular for the nDGP models, which is not surprising if we look at the left panel of Fig. 3.4 and note that our measurements for these models show an offset compared to the theoretical predictions. However, the size of the 1σ error bar is large enough to give a good agreement between the best-fitting and fiducial values, especially for the range $s_{\rm min} = 40\,h^{-1}$Mpc. From the $Q(s)$ panels of Fig. 3.5, we observe an underestimation of β for all gravity models at all measured redshifts, especially for the range $s = 20 - 150\,h^{-1}$Mpc. As we said above, non-linearities produce smaller values of $Q(s)$ at all redshifts and therefore we estimate a smaller

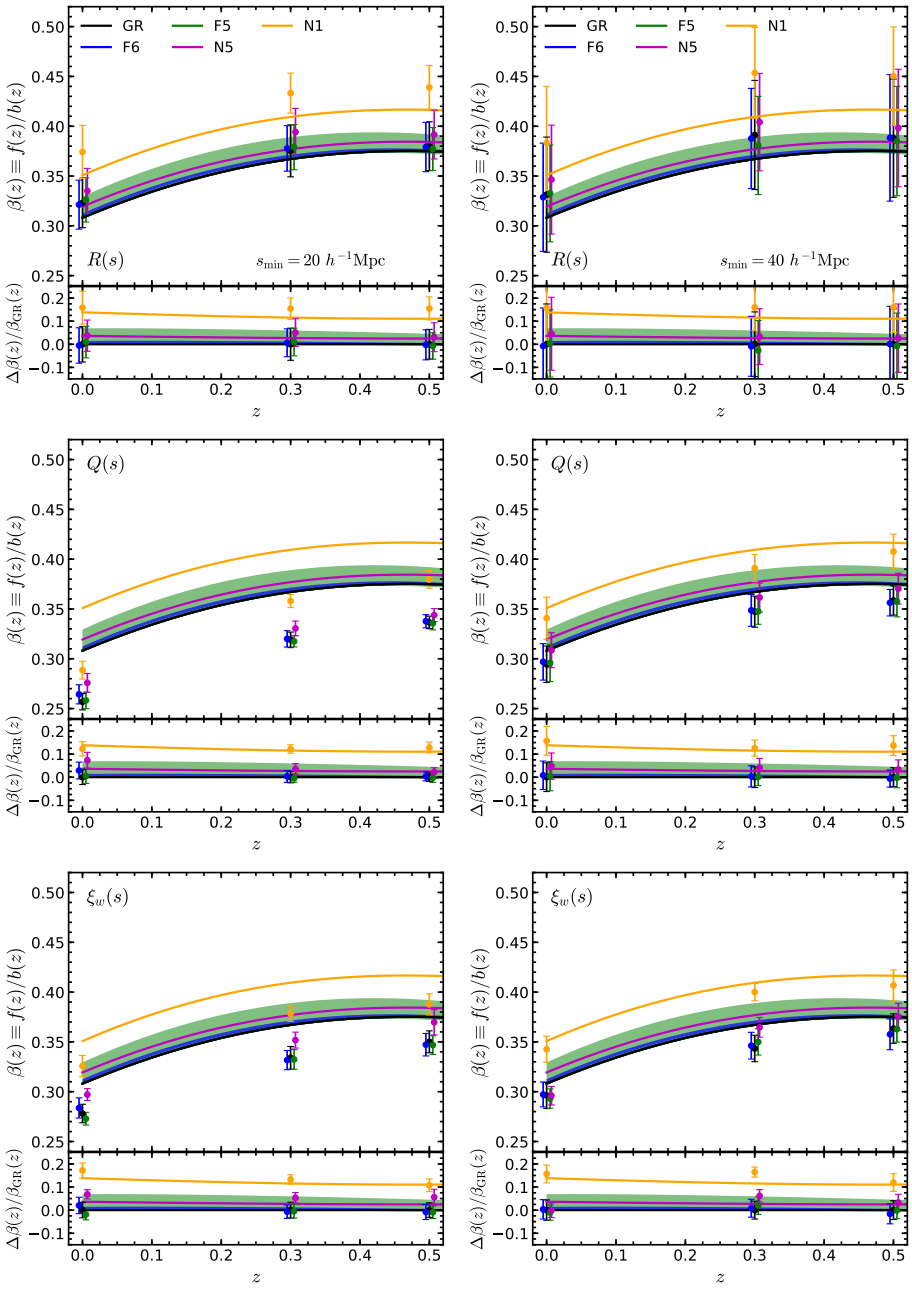

Figure 3.5: Evolution of β as a function of redshift. Solid curves show the theoretical predictions for the gravity models as shown in the legend, for $f(R)$ gravity models the theoretical predictions are shown as a shaded region for wavenumbers $0.01 \leq k/[\,h\,\mathrm{Mpc}^{-1}] \leq 0.1$. Each panel shows the best-fitting β values (filled symbols) using the estimators: $R(s)$ Eq. 3.4.22 (upper panels), $Q(s)$ Eq. (3.4.23) (middle panels) and $\xi_w(s)$ Eq. (3.3.11) (lower panels) with $s_{\rm min} = 20\,h^{-1}$Mpc (left panels) and $s_{\rm min} = 40\,h^{-1}$Mpc (right panels). The lower subpanels show the relative difference between the modified gravity models and GR. Error bars correspond to the 1σ confidence level.

value of β even on scales with $s_{\rm min} = 40\,h^{-1}$Mpc. When we use clustering wedges, $\xi_w(s)$, to estimate β (see the bottom panels of Fig. 3.5), we find a similar trend consistent to that seen for $Q(s)$. This is because there is a relation between clustering wedges and multipole moments (see Eq. 3.3.11). When we measure $Q(s)$, we only use information about the monopole and the quadrupole moments of the correlation function, while the linear prediction of the clustering wedges uses information about the monopole, quadrupole and hexadecapole moments. The comparison between constraints using $\xi_w(s)$ and $Q(s)$ therefore indicates that the hexadecapole moment does not have much impact on the estimation of β. In general, the linear Kaiser model fails to model RSD in configuration space even in the linear regime ($s_{\rm min} = 40\,h^{-1}$Mpc).

The lower subpanels of each plot in Fig. 3.5 show the relative difference between the MG models and GR. We notice that in all cases the difference between $f(R)$ models (F6 and F5) is $\lesssim 1\%$ with respect to GR, making these models statistically indistinguishable from each other. On the other hand, N5 and N1 models hold a difference of $\sim 2.5\%$ and $\sim 12\%$ with respect to GR. Also, while the $R(s)$, $Q(s)$ and $\xi_w(s)$ estimators all lead to biased constraints on β for all models and redshifts, it appears that the bias is the same for the different gravity models such that the relative model differences from GR can be more accurately recovered.

In Appendix A.2 we will show the estimation of β by using an alternative method to estimate the error budget in the χ^2-test.

3.4.2 The nonlinear model

A more rigorous and accurate modelling of the clustering signal of galaxies in redshift space than the linear theory prediction can be achieved by accounting for three important ingredients: the nonlinear evolution of the underlying matter field, the redshift space distortion effects, and the biasing relation between the galaxy and dark matter fields. Within the redshift range we are concerned with in this work, apart from the linear theory prescription described above, one needs in principle to include also the cross coupling between the matter field with the velocity field, the higher order and nonlocal bias to account for the nonlinear and nonlocal formation process

as well as a modelling of the virialized random motion of the objects (galaxies). The anisotropic correlation function can be obtained as the Fourier transform of the power spectrum, where the full expression of $P(k,\mu)$ is given by

$$P(k,\mu) = F_{\rm FoG}(k,\mu) P_{\rm novir}(k,\mu)\,, \tag{3.4.26}$$

where

$$F_{\rm FoG}(k,\mu) = \frac{1}{\sqrt{1+f^2k^2\mu^2a_{\rm vir}^2}} \exp\left(\frac{-f^2k^2\mu^2\sigma_v^2}{1+f^2k^2\mu^2a_{\rm vir}^2}\right), \tag{3.4.27}$$

is a non-Gaussian term that contains small-scale information about the Fingers-of-God effect due to virialised motions of galaxies, $a_{\rm vir}$ is a free parameter that describes the kurtosis of the velocity distribution on small scales and σ_v is the velocity dispersion (Scoccimarro, 2004). The derivation of the non-virial power spectrum $P_{\rm nonvir}$ is based on Scoccimarro et al. (1999); Scoccimarro (2004), followed by three components,

$$P_{\rm novir}(k,\mu) = P^{(1)}_{\rm novir}(k,\mu) + (k\mu f)P^{(2)}_{\rm novir}(k,\mu) + (k\mu f)^2 P^{(3)}_{\rm novir}(k,\mu), \tag{3.4.28}$$

where

$$P^{(1)}_{\rm novir}(k,\mu) = P_{\rm gg}(k) + 2f\mu^2 P_{\rm g\theta}(k) + f^2\mu^4 P_{\theta\theta}(k)\,, \tag{3.4.29}$$

$$P^{(2)}_{\rm novir}(k,\mu) = \int \frac{{\rm d}^3p}{(2\pi)^3}\frac{p_z}{p}[B_\sigma(\mathbf{p},\mathbf{k}-\mathbf{p},-\mathbf{k}) - B_\sigma(\mathbf{p},\mathbf{k},-\mathbf{k}-\mathbf{p})]\,, \tag{3.4.30}$$

$$P^{(3)}_{\rm novir}(k,\mu) = \int \frac{{\rm d}^3p}{(2\pi)^3} F(\mathbf{p})F(\mathbf{k}-\mathbf{p})\,. \tag{3.4.31}$$

Here, $P^{(1)}_{\rm novir}$ is a non-linear version of the Kaiser formula, Eq. (6.5.16), $P_{\rm gg} \equiv \langle\delta_{\rm g}\delta_{\rm g}\rangle$ is the galaxy auto power spectrum, $P_{\rm g\theta} \equiv \langle\delta_{\rm g}\theta\rangle$ is the cross spectrum between the galaxy density ($\delta_{\rm g}$) and velocity divergence ($\theta \equiv \nabla\cdot\mathbf{v}$, and assuming there is no velocity bias) fields, and $P_{\theta\theta} \equiv \langle\theta\theta\rangle$. The calculation of $P_{\rm gg}$, $P_{\rm g\theta}$ and $P_{\theta\theta}$ are up to one loop and the exact expressions for the first two terms can be found in Appendix A of Sánchez et al. (2017). The calculation of the nonlinear matter power spectrum is done using the Galilean-invariant renormalized perturbation theory (gRPT; Crocce & Scoccimarro 2006; Crocce, Blas & Scoccimarro in prep.).

When calculating the ensemble average of the product of the density field in redshift space (c.f. Eq. (15) of Taruya et al. (2010)), there is coupling between the FoG and the Kaiser effect as $P^{(2)}_{\rm novir}$ and $P^{(3)}_{\rm novir}$ and add correction to the Kaiser term. $P^{(2)}_{\rm novir}$ is given by the tree-level PT bispectrum between densities and velocities. $P^{(3)}_{\rm novir}$ is the quartic linear power spectrum at the order $\mathcal{O}\left(P^2\right)$ with the kernel $F(\mathbf{P}) = (b_1 + f\mu_p^2)\frac{p_z}{p^2}\left(P_{\delta\theta}(p) + f\frac{p_z^2}{p^2}P_{\theta\theta}(p)\right)$. Eq. (3.4.26) encodes effects of both the RSD and nonlinear evolution.

The galaxy bias in this model is expanded as follows (Chan et al., 2012),

$$\delta_{\rm g} = b_1\delta + \frac{b_2}{2}\delta^2 + \gamma_2\mathcal{G}_2 + \gamma_3^-\Delta_3\mathcal{G} + ... \tag{3.4.32}$$

with the Galileon operators for the gravitational potential Φ and the velocity potential $\Phi_{\rm v}$ defined as

$$\mathcal{G}_2\left(\Phi_v\right) \equiv \nabla^i\nabla^j\Phi_v\nabla_i\nabla_j\Phi_v - \left(\nabla^2\Phi_v\right)^2, \tag{3.4.33}$$

and

$$\Delta_3\mathcal{G} \equiv \mathcal{G}_2\left(\Phi\right) - \mathcal{G}_2\left(\Phi_v\right). \tag{3.4.34}$$

The non-local bias coefficients γ_2 and γ_3^- are related to the linear bias parameter, b_1, as (Fry, 1996; Catelan et al., 1998; Chan et al., 2012)

$$\gamma_2 = -\frac{2}{7}(b_1 - 1), \tag{3.4.35}$$

and

$$\gamma_3^- = \frac{11}{42}(b_1 - 1). \tag{3.4.36}$$

We have tried both fixing and varying γ_3^- in our fitting. When fixing the parameter using the local Lagrangian relation, Eq. (3.4.36), we found the linear bias is biased low compared to the true value. There are two possible reasons for this behaviour. Firstly, the linear bias, b_1, is scale dependent with a contribution $\nabla\delta$, which is ignored in our simplified treatment and making the linear bias degenerate with γ_3^-. Secondly, γ_3^- is formulated in the Eulerian coordinate, while the local biasing schemes are compatible with the Lagrangian bias only when matter evolution and structure formation is well within the linear and local regime (Matsubara, 2011). Therefore varying γ_3^- should result in a more accurate value and this conclusion is

consistent with the previous findings (Grieb et al., 2017). In the results below we shall always vary γ_3^-.

The Alcock-Paczynski effect

The baryon acoustic oscillation can be well approximated by a spherical shape with fixed radius at given redshift. As one measures the clustering signal parallel and perpendicular to the line of sight, a set of parameters known as the Alcock-Paczynski (AP; Alcock & Paczynski 1979) parameters can be introduced to account for the rescaling of the BAO feature in both the radial and angular directions:

$$q_\perp = \frac{D_A(z_\mathrm{m})}{D'_A(z_\mathrm{m})}\,, \qquad q_\parallel = \frac{H'(z_\mathrm{m})}{H(z_\mathrm{m})}\,, \tag{3.4.37}$$

where the $'$ denotes quantities in the fiducial cosmology. In terms of s and μ, these equations can be written as

$$s = s' q(\mu')\,, \qquad \mu = \mu' \frac{q_\perp}{q(\mu')}\,, \tag{3.4.38}$$

where

$$q(\mu') = \sqrt{q_\parallel^2(\mu')^2 + q_\perp^2\,(1-(\mu')^2)}. \tag{3.4.39}$$

With Eq. (3.4.39), the correlation function predicted by the model for a fiducial cosmology can be transformed into the prediction for different cosmologies $\xi(s',\mu') \to \xi(s,\mu)$. When measuring the two point correlation function, we have used the true position of the objects. Since the expansion history is tuned to be the same for each cosmological model, we effectively always know the "true cosmology", and would therefore expect to find $q_\perp = q_\parallel = 1$ for all the cases.

As we will see in Appendix A.3, the constraints on AP parameters for different cosmological models are very close to one, this is a good news when applying to a real survey. Despite the shape of the distortion at all range of scales due to the RSD, the AP test can faithfully pick up the correct information given by the BAO position.

Parameter inference with the nonlinear model

To obtain cosmological constraints, we use Bayesian statistics and maximise the likelihood,

$$\mathcal{L}(\boldsymbol{\xi}|\boldsymbol{\lambda}) \propto \exp\left[-\frac{1}{2}\left(\boldsymbol{\xi}-\boldsymbol{\xi}_{\rm model}(\boldsymbol{\lambda})\right)^{\rm T}\Psi\left(\boldsymbol{\xi}-\boldsymbol{\xi}_{\rm model}(\boldsymbol{\lambda})\right)\right], \tag{3.4.40}$$

where the $\Psi = {\rm C}^{-1}$ is the inverse of the covariance matrix. We applied the Gaussian recipe to estimate the covariance matrix (Grieb et al., 2016), which is then rescaled by the number of simulations. The input power spectrum is calculated by the nonlinear model based on the best fitting values obtained from the MCMC chain. Such Gaussian recipe has been tested recently in both Fourier and configuration space by comparing to covariance matrices generated by hundreds of N-body simulations as well as thousands of different fast mock simulations and found them to be in good agreement (Blot et al., 2019; Lippich et al., 2019). At the same time, there are also studies on including the corrections from higher-order statistics and super-sampling mode (Barreira et al., 2018). However, for the scales of interest in this study, there is no sensitivity to these corrections and the Gaussian covariance matrix should be a good approximation. We explore the parameter space using Monte Carlo Markovian Chains (MCMC) with the Metropolis-Hastings algorithm (Metropolis et al., 1953; Hastings, 1970). The parameters that enter the default fitting are $\{f\sigma_8, b_1, b_2, \gamma_3^-, a_{\rm vir}\}$, where $f\sigma_8$ is the product of the growth rate and the matter clustering amplitude. In the gRPT model, σ_8 is fixed and therefore does not enter in the MCMC fitting. When applying the AP test, two additional parameters enter the fitting $\{\alpha_\parallel, \alpha_\perp\}$. Finally, we marginalise over the nuisance parameters to find the probability distribution of the distortion parameter $\beta = f/b_1$.

Fig. 3.6 shows the constraints on β using the nonlinear gPRT+RSD model by running MCMC. The upper panels present the results for the three multipoles ($\xi_l(s)$, $l = 0, 2, 4$) of the correlation function for two ranges of scales: $s = 20 - 150\,h^{-1}$Mpc (left) and $s = 40 - 150\,h^{-1}$Mpc (right). For comparison, we display the results of using three wedges ($\xi_w(s)$) in the bottom panels of Fig. 3.6. We observe an overestimation of β for all models at all redshifts when the fit is done using $s_{\rm min} = 20\,h^{-1}$Mpc, for both multipoles and wedges. We have checked the linear bias fitted

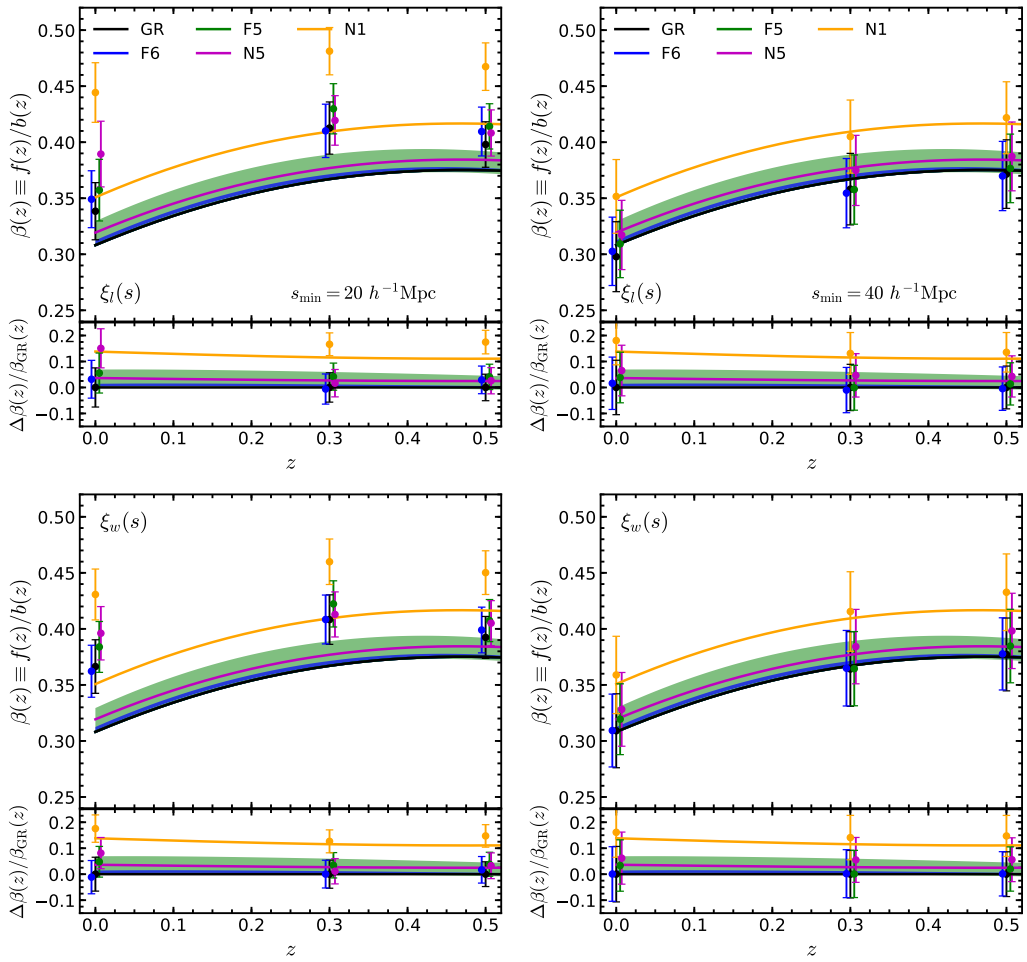

Figure 3.6: Similar to figure 3.5 but for the fits using the nonlinear model. The upper panel shows the multipole moments of the correlation functions, $\xi_l(s)$. The lower panel shows the clustering wedges $\xi_{w_i}(s)$. In both of the plots the AP parameters are treated as free.

from the nonlinear model and found it to be in good agreement with the values measured from the mock galaxy catalogues using Eq. (6.5.6); for a detailed discussion on the bias see Appendix A.1. This suggests that the higher estimation of β comes from the $f\sigma_8$; the same conclusion is in agreement with the one found by Barreira et al. (2016). In our case we have rescaled the covariance matrix by the number of simulations and the error bar is therefore smaller than the error bar presented in Barreira et al. (2016). When we used the range scale with $s_{\rm min} = 40\,h^{-1}$Mpc, the constraints are in good agreement with the fiducial values.

We note a slight difference between the results obtained from the multipoles-

based estimator and the wedges-based estimator. This is an indication for the non-negligible higher order statistics in the two-dimensional correlation function $\xi(s, \mu)$. To further explore this point, we have compared the difference between the multipoles directly measured from the mock catalogues and the multipoles obtained by transforming the measured wedges using Eq. (3.3.12), and found a difference in the hexadecapole at scale $\approx 20\,h^{-1}$Mpc (we do not show the plot here). The difference can lead to different constraints on the nuisance parameters and have consequential impact on the parameter of interest, which is a source for the biased constraints by setting $s_{\rm min} = 20\,h^{-1}$Mpc. For the case of $s_{\rm min} = 40\,h^{-1}$Mpc, the minimum length scale used in the fitting is larger enough, and the impact of higher-order statistics is smaller, which explains why the agreement is improved at all three redshifts.

In the lower subpanels of Fig. 3.6 we plot the relative differences between the modified gravity models and GR. Similar to the findings using linear theory, we find that the two variants of $f(R)$ gravity studied here are indistinguishable from GR given the size of the statistical error. While N5 shows stronger deviation from GR, it is also not clearly distinguishable from the latter. N1 is the only one of our four MG models that could be distinct from GR at 1-σ given the statistical uncertainties, and not including systematic errors. These results are similar to what we found by using the linear Kaiser model above.

3.4.3 Discussion

The results can have a few implications:

First, RSD on linear and mildly-nonlinear scales does not seem to be a great probe of modified gravity, in particular for $f(R)$ gravity. This conclusion is expected to hold true for other MG models depending on chameleon screening to recover GR in high-density regions, for which the effect of the fifth force is generally restricted to at most $\mathcal{O}(10)$ Mpc (Brax et al., 2012a,b). This conclusion, however, may not apply to RSD on small and highly nonlinear scales, where the velocity field could be significantly enhanced by the fifth force in chameleon models (see, e.g., He et al., 2018). We suspect similar conclusions should hold for the symmetron (Hinterbichler

& Khoury, 2010) and dilaton (Brax et al., 2010) models, for which the fifth force is also of the Yukawa type, with an inverse Compton mass of $\lesssim \mathcal{O}(10)$ Mpc. Vainshtein screening models, such as nDGP, on the other hand, has a fifth force that is non-negligible on large scales, which is why the constraint is stronger.

Second, given the weak constraining power from large-scale RSD and the relatively large scale ($s_{\rm min} = 40\,h^{-1}$Mpc) needed to get unbiased constraints even for GR, a theoretical model based on linear theory prediction or higher-order perturbation calculation developed for GR does not seem to lead to noticeably biased constraints on the β parameter. This suggests a faster way to explore the MG model and parameter space, at least at the initial stage of delineating models and parameters.

Third, we have explicitly checked that the real-space galaxy correlation functions of the MG models deviate more significantly from GR prediction if the mock galaxy catalogues were constructed using the same HOD parameters as GR, or if haloes were used instead of HOD galaxies. As argued above, in this study the HOD parameters for MG models are tuned so that the real-space $\xi_{\rm gg}$ match between the different models, which is motivated by the fact that there is only one Universe from which the observed $\xi_{\rm gg}$ are to be derived, and whatever the cosmological model, it should be required to reproduce such an observation to start with. A more detailed theoretical model of RSD on linear and mildly-nonlinear scales should take this into account. In practice, there is no real-space $\xi_{\rm gg}$ from observations to match with, and the HOD parameters are often tuned to match the observed projected two-point correlation function $w(\theta)$ to get rid of RSD effects: doing this will leave more freedom for the choices of HOD parameters, and we expect it to also lead to larger uncertainties in the constraints on β.

3.5 Summary

The objective of this Chapter is threefold: first, we want to explore whether for realistic mock galaxy catalogues the distortion parameter, β, is sufficiently different between the different gravity models so that future galaxy surveys can be used to

distinguish or constrain them; second, we study the extent to which simple theoretical models such as linear theory or GR-based perturbation theory recipes can faithfully recover the correct β values for different MG models, given the current statistical uncertainties; finally, we also compare different estimators of the RSD effect and test various systematic effects in modelling RSD.

To do so, we use cosmological dark-matter-only N-body simulations and populated dark matter haloes with galaxies following a halo occupation distribution prescription. We did this analysis for three low redshifts, respectively at $z = 0$, 0.3 and 0.5, because the modified gravity models studied here are expected to deviate from GR more significantly at late times. Since the nature of gravity is different in every model, we tuned the HOD parameters such that essentially every catalogue matches the number density and the real space correlation function measured for the BOSS CMASS DR9 (Anderson et al., 2012; Manera et al., 2012). We used the distant-observer approximation to map galaxies from real- to redshift-space coordinates along three line-of-sight directions (chosen to be parallel to the three axes of the simulation box) for each realisation of mock galaxy catalogue. For the theoretical predictions of the RSD effects, we applied a linear (Kaiser, 1987; Hamilton, 1992) and a nonlinear (Scoccimarro 2004; Crocce & Scoccimarro 2006; Chan et al. 2012; Crocce et al., in prep.) RSD model to our mocks to estimate the value of β. We used different estimators to extract information about the distortion parameter in each model. In linear theory we have the ratios $R(s)$ and $Q(s)$ besides the clustering wedges $\xi_w(s)$. For the nonlinear model we have used the multipole moments $\xi_l(s)$ and the clustering wedges of the correlation function. For both RSD models we performed fits over two ranges of scales, $s = 20-150\,h^{-1}$Mpc and $s = 40-150\,h^{-1}$Mpc.

In general, we found that the linear model fails to recover the true value of the distortion parameter even in the linear regime of scales ($s_{\rm min} = 40\,h^{-1}$Mpc). This is because, due to the lack of the FoG term in this model, it (over-)underestimates the value of β on the quasi-linear regime ($s_{\rm min} = 20\,h^{-1}$Mpc). This is not surprising since previous work has demonstrated that the Kaiser model suffers from limitations (see e.g., Kwan et al., 2012, and references therein). On the other hand, the nonlinear model used here overpredicts the value of β when considering $s_{\rm min} = 20\,h^{-1}$Mpc;

this trend was also found by Barreira et al. (2016) using the same range scale. In the large-scale regime ($s_{\rm min} = 40\,h^{-1}$Mpc), the nonlinear model is able to recover the true value of β, especially for clustering wedges. Another study reported by White et al. (2015) found unbiased estimations of the growth rate for scales $s > 30\,h^{-1}$Mpc. However, there are some differences between the work presented by White et al. (2015) and ours. First, they fitted only the monopole and quadrupole of the correlation function. Second, opposite to our findings they underpredicted the linear growth rate when considered scales with $s_{\rm min} = 20\,h^{-1}$Mpc.

Our results suggest that, with the upcoming galaxy surveys such as DESI, 4MOST and Euclid, there is a realistic possibility to put constraints on the growth rate of matter and make distinctions between certain MG models and GR. Such studies will potentially benefit from combining with cosmological data that probe different regimes (e.g., environments), scales and special theoretical properties of the models. For instance, the expected error bar of these future galaxy surveys would help to put tighter constraints on the linear growth rate and help to make a clearer distinction between different gravity models. Also, to be more realistic, it will be useful to test the constraining power of RSD using different tracers and number densities, and include systematic effects such as survey geometric and masks, galaxy redshift distribution and evolution, incompleteness due to fibre collisions and observing conditions, and so on. It is also interesting to study if including higher-order statistics, such as the 3-point correlation function or bispectrum in redshift space, can improve the constraining power of the surveys. These possibilities are beyond the scope of this Chapter and will be left for future work.

Chapter 4

Galaxy formation in the brane world

4.1 Introduction

The standard cosmological model (Λ cold dark matter; ΛCDM) based on Einstein's general relativity (GR) has been widely studied using numerical simulations over the past three decades (see Kuhlen et al., 2012; Vogelsberger et al., 2020, for reviews). In the last five years in particular, hydrodynamical simulations of galaxy formation have been able to model the galaxy population in cosmological volumes, achieving encouraging matches to observations and providing a detailed description of the properties and evolution of galaxies over cosmic time (see, e.g., Vogelsberger et al., 2014; Schaye et al., 2015; Feng et al., 2016; McCarthy et al., 2017; Pillepich et al., 2018a, 2019; Lee et al., 2020). For instance, the IllustrisTNG (TNG) project is one of the most complete suites of cosmological simulations of galaxy formation to date (see e.g., Pillepich et al., 2018b; Nelson et al., 2018; Springel et al., 2018; Naiman et al., 2018; Marinacci et al., 2018; Pillepich et al., 2019; Nelson et al., 2019). The TNG simulations cover cosmological volumes of $\sim 50^3\mathrm{Mpc}^3$ (TNG50), $\sim 100^3\mathrm{Mpc}^3$ (TNG100) and $\sim 300^3\mathrm{Mpc}^3$ (TNG300). The TNG300 is one of the largest full-physics simulations currently available which allows us to study baryonic effects on the clustering of matter on relatively large-scales.

The past decade has seen an increasing interest in alternative theories of gravity

that modify GR on large scales (Koyama, 2016; Ishak, 2019), leading to a large body of literature on their cosmological behaviours and possible observational tests. However, there has been little work on hydrodynamical simulations of non-standard gravity models (e.g., Arnold et al., 2014, 2015; Hammami et al., 2015; He & Li, 2016; Arnold et al., 2016; Ellewsen et al., 2018; Arnold et al., 2019). Exploring the effect of modified gravity on galactic scales in a cosmological context hence remains an important open topic that requires more quantitative work. Hydrodynamical cosmological simulations provide the missing link that connect the properties of dark matter haloes with luminous galaxies.

The Dvali-Gabadadze-Porrati (DGP) braneworld model (Dvali et al., 2000) is one of the most widely-studied modified gravity models that employs the Vainshtein screening mechanism (Vainshtein, 1972). In this model, normal matter is confined to a 4-dimensional brane embedded in a 5-dimensional spacetime, the bulk. The model leads to two branches of cosmological solutions, dubbed as the *self-accelerating* branch (sDGP) and the *normal* branch (nDGP). In the sDGP branch, gravity leaks from the brane to the bulk leading to an accelerating expansion without the need to invoke a cosmological constant or dark energy component. However, this model is ruled out by cosmological observations (see e.g., Song et al., 2007; Fang et al., 2008) and by the problem of *ghost* instabilities (negative kinetic energy) in the gravitational sector. On the other hand, the nDGP model does not suffer from ghost instabilities, but it is necessary to include a component of dark energy to match the observed late-time accelerated expansion of the Universe (Schmidt, 2009b). The nDGP model nevertheless offers the possibility to test the Vainshtein screening mechanism using astrophysical and cosmological probes.

The first numerical simulations of the DGP model were performed by Schmidt (2009a,b), followed by simulations for both the self-accelerated and the normal branches of the DGP model carried out with the adaptive-mesh-refinement (AMR) code ECOSMOG-V (Li et al., 2013a). The performance of both codes was tested by Winther et al. (2015), who found excellent agreement for the prediction of the dark-matter distribution and halo statistics over cosmic time.

To date, the nDGP model has been widely tested using a range of astrophys-

ical and cosmological probes. For example, Falck et al. (2014, 2015) studied the morphology and the local environmental density of dark matter haloes in the nDGP model. Moreover, Falck et al. (2018) investigated the effect of the Vainshtein screening mechanism on cosmic voids. Using a halo occupation distribution (HOD) model, Barreira et al. (2016) and Hernández-Aguayo et al. (2019) studied galaxy clustering through redshift-space distortions for two different nDGP models. An additional study of cosmic voids in nDGP models was carried out by Paillas et al. (2019). More recently, Devi et al. (2019) investigated the galaxy-halo connection and the environmental dependence of the galaxy luminosity function using a subhalo abundance matching approach in modified gravity (including the nDGP model). All the studies mentioned above are dark matter only N-body simulations carried out using the ECOSMOG-V code. Hence, the realisation of full-physics hydrodynamical simulations for galaxy formation is a natural step to continue testing the nDGP model.

Here, we present an extension of the SHYBONE (Simulating HYdrodynamics BeyONd Einstein) simulations (Arnold et al., 2019) by exploring galaxy formation in the nDGP model with an identical expansion history to ΛCDM (Schmidt, 2009b). To carry out these simulations, we extended the AREPO code (Springel, 2010) to include the nDGP model and employed its AMR modified gravity solver together with the IllustrisTNG galaxy formation model (Pillepich et al., 2018a). Our simulations represent a further step in the understanding of modified gravity theories on galactic scales.

The first series of the SHYBONE simulations were devoted to studying the interplay between baryonic physics and modifications of gravity in the $f(R)$ gravity model of Hu & Sawicki (2007). Arnold et al. (2019) presented the first results on galaxy properties in these models. Arnold & Li (2019) analysed the statistics of matter, haloes and galaxies, making predictions for the matter and halo correlation functions, the halo and galaxy host halo mass functions, the subhalo and satellite galaxy counts, and the correlation function of stars. Using these simulations Leo et al. (2019) studied the effects of modified gravity on the abundance of HI-selected galaxies and their power spectra.

This Chapter is structured as follows. Section 4.2 presents our simulation methodology and discusses technical aspects of the numerical implementation. In Section 4.3, we show some tests to ensure that our implementation works accurately. We describe our SHYBONE-nDGP simulations in Section 4.4. The first analysis of the new full-physics simulations is presented in Section 4.5. Finally, we summarise the results in Section 4.6.

4.2 Numerical methodology

N-body cosmological simulations have played an important role in the study of alternative gravity models, allowing to study the impact of modified gravity on the clustering of galaxies. Such simulations are necessary for the construction of synthetic galaxy catalogues. In this section we present the numerical methods used to implement the nDGP model into Arepo. Combined with the IllustrisTNG galaxy formation model, this allows us to run full hydrodynamical simulations in the nDGP model.

4.2.1 N-body algorithm

The equation of motion of the scalar field, Eq. (1.2.34), can be written using the code units (see Weinberger et al., 2020, for details) of Arepo as

$$\nabla^2\varphi + \frac{R_{\rm c}^2}{3\beta_{\rm nDGP}\, a^3}\left[(\nabla^2\varphi)^2 - (\nabla_i\nabla_j\varphi)^2\right] = \frac{8\pi\, G\, a^2}{3\beta_{\rm nDGP}}\delta\rho\,, \tag{4.2.1}$$

where G the gravity constant in internal code units. In this equation we have introduced a new dimensionless quantity,

$$R_{\rm c} \equiv \frac{r_{\rm c}}{c} = \frac{1}{2H_0\sqrt{\Omega_{\rm rc}}}\,, \tag{4.2.2}$$

with r_c the crossover scale and c the speed of light in code units. Eq. (4.2.1) can be expressed, after applying the operator-splitting trick (Chan & Scoccimarro, 2009), as follows

$$(1-w)\left(\nabla^2\varphi\right)^2 + \alpha\nabla^2\varphi - \Sigma = 0, \tag{4.2.3}$$

where

$$\alpha = \frac{3\beta_{\rm nDGP}a^3}{R_{\rm c}^2}, \tag{4.2.4}$$

$$\Sigma = (\nabla_i\nabla_j\varphi)^2 - w\left(\nabla^2\varphi\right)^2 + \frac{\alpha}{3\beta_{\rm nDGP}}8\pi G a^2\delta\rho\,, \tag{4.2.5}$$

and w is a constant numerical factor which has to be chosen as $1/3$ for the numerical algorithm to converge. Eq. (4.2.3) can be solved once to yield

$$\begin{aligned}\nabla^2\varphi &= \frac{1}{2(1-w)}\left[-\alpha \pm \sqrt{\alpha^2 + 4(1-w)\Sigma}\right] \\ &= \frac{1}{2(1-w)}\left[-\alpha + \frac{\alpha}{|\alpha|}\sqrt{\alpha^2 + 4(1-w)\Sigma}\right],\end{aligned} \tag{4.2.6}$$

where in the second line we have specialised to the relevant branch of the solution (Li et al., 2013a).

The discrete version of the field derivatives are

$$\nabla\varphi = \frac{1}{2h}\left(\varphi_{i+1,j,k} - \varphi_{i-1,j,k}\right), \tag{4.2.7}$$

$$\nabla^2\varphi = \frac{1}{h^2}\left(\varphi_{i+1,j,k} + \varphi_{i-1,j,k} - 2\varphi_{i,j,k}\right), \tag{4.2.8}$$

$$\begin{aligned}\nabla_x\nabla_y\varphi = \frac{1}{4h^2}\Big(&\varphi_{i+1,j+1,k} + \varphi_{i-1,j-1,k} - \varphi_{i+1,j-1,k} \\ &- \varphi_{i-1,j+1,k}\Big),\end{aligned} \tag{4.2.9}$$

where h is the cell length and we have assumed one dimension for simplicity for $\nabla\varphi$ and $\nabla^2\varphi$.

Instead of solving the full modified Poisson equation, (1.2.33), to obtain the total gravitational potential Φ, we split the force calculation into two parts: (i) solving the standard Poisson equation to get the Newtonian potential $\Phi_{\rm N}$ and hence calculate the Newtonian force, and (ii) solving the scalar field φ to obtain the fifth force. The Newtonian force is obtained from the standard gravity solver implemented in Arepo (see Springel, 2010; Weinberger et al., 2020, for details).

The EOM for the scalar field, Eq. (4.2.6), can be written as an operator equation

$$\mathcal{L}^h(\varphi_{i,j,k}) = 0, \tag{4.2.10}$$

with

$$\mathcal{L}^h(\varphi_{i,j,k}) \equiv \frac{1}{h^2}\Big(\varphi_{i+1,j,k}+\varphi_{i-1,j,k}+\varphi_{i,j+1,k}+\varphi_{i,j-1,k}+\varphi_{i,j,k+1}+\varphi_{i,j,k-1}-6\varphi_{i,j,k}\Big) - \frac{1}{2(1-w)}\left[-\alpha+\frac{\alpha}{|\alpha|}\sqrt{\alpha^2+4(1-w)\Sigma_{i,j,k}}\right], \tag{4.2.11}$$

n which the superscript ^{h} is used to label the level of the mesh (or equivalently the size of the cell of that level), and we have defined

$$\begin{aligned}\Sigma_{i,j,k} \equiv\ & \frac{1-w}{h^4}\Bigg[\Big(\varphi_{i+1,j,k}+\varphi_{i-1,j,k}-2\varphi_{i,j,k}\Big)^2+\Big(\varphi_{i,j+1,k}+\varphi_{i,j-1,k}-2\varphi_{i,j,k}\Big)^2 \\ & +\Big(\varphi_{i,j,k+1}+\varphi_{i,j,k-1}-2\varphi_{i,j,k}\Big)^2\Bigg] \\ & -\frac{2}{h^4}w\left(\varphi_{i+1,j,k}+\varphi_{i-1,j,k}-2\varphi_{i,j,k}\right)\left(\varphi_{i,j+1,k}+\varphi_{i,j-1,k}-2\varphi_{i,j,k}\right) \\ & -\frac{2}{h^4}w\left(\varphi_{i+1,j,k}+\varphi_{i-1,j,k}-2\varphi_{i,j,k}\right)\left(\varphi_{i,j,k+1}+\varphi_{i,j,k-1}-2\varphi_{i,j,k}\right) \\ & -\frac{2}{h^4}w\left(\varphi_{i,j+1,k}+\varphi_{i,j-1,k}-2\varphi_{i,j,k}\right)\left(\varphi_{i,j,k+1}+\varphi_{i,j,k-1}-2\varphi_{i,j,k}\right) \\ & +\frac{1}{8h^4}\Big(\varphi_{i+1,j+1,k}+\varphi_{i-1,j-1,k}-\varphi_{i+1,j-1,k}-\varphi_{i-1,j+1,k}\Big)^2 \\ & +\frac{1}{8h^4}\Big(\varphi_{i+1,j,k+1}+\varphi_{i-1,j,k-1}-\varphi_{i+1,j,k-1}-\varphi_{i-1,j,k+1}\Big)^2 \\ & +\frac{1}{8h^4}\Big(\varphi_{i,j+1,k+1}+\varphi_{i,j-1,k-1}-\varphi_{i,j+1,k-1}-\varphi_{i,j-1,k+1}\Big)^2+\frac{\alpha}{3\beta_{\rm nDGP}}8\pi G a^2\delta\rho_{i,j,k}.\end{aligned} \tag{4.2.12}$$

and

$$\delta\rho_{i,j,k}=\frac{m_{i,j,k}}{h^3}-\bar{\rho}(a)\,, \tag{4.2.13}$$

where $m_{i,j,k}$ is the mass assigned to cell (i,j,k) using a cloud-in-cell scheme, and $\bar{\rho}(a)=\bar{\rho}_0/a^3$ is the mean physical matter density as a function of the scale factor.

This equation can be solved by using the multigrid relaxation method, for which the code iterates to update the value of $\varphi_{i,j,k}$ in all cells, and at each iteration the field values changes as

$$\varphi^{h,\rm new}_{i,j,k}=\varphi^{h,\rm old}_{i,j,k}-\frac{\mathcal{L}^h\left(\varphi^{h,\rm old}_{i,j,k}\right)}{\frac{\partial\mathcal{L}^h\left(\varphi^{h,\rm old}_{i,j,k}\right)}{\partial\varphi^{h,\rm old}_{i,j,k}}}, \tag{4.2.14}$$

where

$$\begin{aligned}\frac{\partial\mathcal{L}^h\left(\varphi^{h,\rm old}_{i,j,k}\right)}{\partial\varphi^{h,\rm old}_{i,j,k}} \equiv\ & -\frac{6}{h^2}+\frac{\alpha}{|\alpha|}\frac{4(1-3w)}{h^4\sqrt{\alpha^2+4(1-w)\Sigma_{i,j,k}}}\Big(\varphi_{i+1,j,k}+\varphi_{i-1,j,k}+\varphi_{i,j+1,k} \\ & +\varphi_{i,j-1,k}+\varphi_{i,j,k+1}+\varphi_{i,j,k-1}-6\varphi_{i,j,k}\Big).\end{aligned} \tag{4.2.15}$$

Note that the choice $w = 1/3$ also greatly simplifies this expression by making the second term on the right-hand side vanish.

Each time the modified gravity forces are to be updated (refer to Arnold et al., 2019, for details of the MG solver and our local time-stepping scheme) we initialise the field value in the Arepo AMR grid solver with the solution from the previous timestep. We then perform a number of red-black sweeps to update the field values in the cells according to Eq. (4.2.14). At the end of each iteration, an error is calculated for $\varphi_{i,j,k}$ as,

$$e_{i,j,k} = \frac{r_{i,j,k}}{\alpha} \tag{4.2.16}$$

where $r_{i,j,k} = \mathcal{L}^h(\hat{\varphi}_{i,j,k})$ (Eq. (4.2.11)) is the residual for the approximate solution $\hat{\varphi}_{i,j,k}$. We stop the iterations when our convergence criterion

$$\max(e_{i,j,k}) < 10^{-2}\,, \tag{4.2.17}$$

is fulfilled. This criterion is equivalent to requesting that the approximate solution for the field in any cell is at least 1% accurate.

4.2.2 Multigrid acceleration

To solve the scalar field equation of motion, Eq. (4.2.1), we employ the multigrid acceleration technique using V-cycles, following the same prescription as presented by Arnold et al. (2019). To numerically solve Eq. (4.2.10), we start the relaxation with some initial guess of the scalar field, $\varphi_{i,j,k} = 0$ in all cells. After a few iterations we have

$$\mathcal{L}^h(\hat{\varphi}^h) = r^h\,, \tag{4.2.18}$$

for an approximate solution $\hat{\varphi}^h$ with residual r^h. After coarsifying, we obtain the equation on the coarse level,

$$\mathcal{L}^H(\hat{\varphi}^H) = \mathcal{L}(\mathcal{R}\hat{\varphi}^h) - \mathcal{R}r^h\,, \tag{4.2.19}$$

where $\mathcal{R}$ is the restriction operator which is given by the summation over the 8 daughter cells of the coarse cell. Eq. (4.2.19) is used to obtain an approximate coarse-level solution of $\hat{\varphi}^H$. Finally, the fine-level solution can be corrected as,

$$\hat{\varphi}^{h,\mathrm{new}} = \hat{\varphi}^h + \mathcal{P}(\hat{\varphi}^H - \mathcal{R}\varphi^h)\,, \tag{4.2.20}$$

where $\mathcal{P}$ is the prolongation operator. All the finer levels are solved by V-cycles using corrections from the two respectively coarser grid levels.

4.2.3 Force calculation

From Eq. (1.2.33), it is straightforward to identify the modified gravity contribution to the gravitational acceleration,

$$\boldsymbol{a}_{\rm MG} = -\frac{1}{2}\boldsymbol{\nabla}\varphi. \tag{4.2.21}$$

We apply a 5-point finite difference scheme to calculate $\boldsymbol{\nabla}\varphi$ at the centres of cells, and use the cloud-in-cell interpolation (which is the same as the mass assignment scheme to calculate the density field $m(\boldsymbol{x})$) to interpolate the force field from the grid to the particle positions. This method allows us to calculate the fifth force directly from the particle distribution using Eq. (4.2.21). Recall that the GR force is obtained from Arepo's gravity solver, we only employ the AMR solver to calculate the fifth force.

4.3 Code tests

Following Li et al. (2013a), we perform a series of tests to check that our new Arepo MG field solver is working correctly. To do so, we run low-resolution simulations with 256^3 particles in a box with size $L = 256\,h^{-1}$Mpc. All tests were performed using the Arepo AMR mesh with 2^9 cells per side at the present time $a = 1$ ($z = 0$).

4.3.1 Uniform density field

For this test, we have set $\delta\rho_{i,j,k} = 0$ and chosen a set of random values that follow a uniform distribution in the range $[-0.05, 0.05]$ as initial guesses of $\varphi_{i,j,k}$. Because the density field is uniform and equal to the cosmological background value, we expect to obtain a smooth and homogeneous φ. In this test, the residual value, Eq. (4.2.17), is reached before the solution converges, for this reason the code stopped when the residual gets a value of $\max(e_{i,j,k}) < 10^{-6}$, when the solution is well converged. Note that our error criteria is different from that used in ecosmog-V (Li et al.,

2013a) (cf. Eq. (4.2.16)). The result of this test is shown in the upper left panel of Fig. 4.1, where the green dots represent the initial guess and the green solid line is the numerical solution.

4.3.2 One dimensional density field

For the first one-dimensional density field test we use a sine-type density field given by,

$$\delta\rho(x) = \frac{3\beta_{\rm nDGP}}{8\pi\, G\, a^2} \sin\left(\frac{2\pi x}{L}\right) , \tag{4.3.22}$$

where L is the box-size. The analytical solution of Eq. (4.2.1) for this density field is

$$\varphi(x) = -\frac{L^2}{4\pi^2} \sin\left(\frac{2\pi x}{L}\right) . \tag{4.3.23}$$

The solution of this test is presented as blue dots (numerical) and blue solid lines (analytical) in the upper right panel of Fig. 4.1, where we see very good agreement between the two estimates.

The second test uses a Gaussian-type density field, given by

$$\begin{aligned}\delta\rho(x) = \frac{3\beta_{\rm nDGP}}{8\pi\, G\, a^2} \frac{2J\alpha}{w^2} \left[1 - 2\frac{(x/L - 0.5)^2}{w^2}\right] \\ \times \exp\left[-\frac{(x/L - 0.5)^2}{w^2}\right] ,\end{aligned} \tag{4.3.24}$$

which corresponds to an exact analytic solution

$$\varphi(x) = L^2 J \left[1 - \alpha \exp\left(-\frac{(x/L - 0.5)^2}{w^2}\right)\right] . \tag{4.3.25}$$

Here J, α, w are constants which we take to be

$$J \;=\; 0.02, \quad \alpha \;=\; 0.9999, \quad w \;=\; 0.15\,. \tag{4.3.26}$$

The solution is shown by the red dots (numerical) and red solid line (analytical) in the upper right panel of Fig. 4.1. Again, the numerical solution agrees very well with the analytic prediction.

4.3.3 Spherical overdensity

The previous tests were done using a 1D density field. Now, we test the three dimensional density field. The simplest case is considering the spherically symmetric configuration with constant density.

For the spherical test, it is most convenient to express Eqs. (1.2.44), (1.2.45) in code units. First of all, since we are assuming that $\delta\rho$ is constant inside the sphere then we can find the expressions for $g_{\rm N}(r)$ and $r_{\rm S}$,

$$g_{\rm N}(r) = \frac{GM(r)}{r^2} = \frac{4\pi G}{3}\delta\rho\, r \tag{4.3.27}$$

$$r_{\rm S} = \frac{2GM(R)}{c^2} = \frac{8\pi G}{3c^2}\delta\rho\, R^3. \tag{4.3.28}$$

Hence, using code units and $a = 1$, Eqs. (1.2.44) and (1.2.45) can be written as

$$\frac{{\rm d}\varphi}{{\rm d}r} = \frac{3\beta_{\rm nDGP}}{4R_{\rm c}}\left[\sqrt{1 + \frac{16R_{\rm c}}{9\beta^2_{\rm nDGP}}\frac{4\pi G}{3}\delta\rho} - 1\right] r, \tag{4.3.29}$$

for $r \leq R$ and

$$\frac{{\rm d}\varphi}{{\rm d}r} = \frac{3\beta_{\rm nDGP}}{4R_{\rm c}}\left[\sqrt{1 + \frac{16R_{\rm c}}{9\beta^2_{\rm nDGP}}\frac{4\pi G}{3}\frac{R^3}{r^3}\delta\rho} - 1\right] r, \tag{4.3.30}$$

for $r \geq R$, where r is the comoving coordinate, while R is the radius of the spherical overdensity and $\delta\rho$ is the overdensity.

We place the overdensity in the centre of the simulation box, hence r is given by

$$r = \sqrt{(x - L/2)^2 + (y - L/2)^2 + (z - L/2)^2}\,, \tag{4.3.31}$$

where x, y and z are the Cartesian coordinates. We adopt the values $\delta\rho = 0.001$, $R = 0.075L$, and the Arepo solution is shown as black dots in the lower-left panel of Fig. 4.1. Meanwhile, given the value of $\varphi(r = 0)$, Eqs. (4.3.29) and (4.3.30) can be integrated to obtain $\varphi(r > 0)$ numerically, and the result is shown as the black solid curve in the lower-left panel of Fig. 4.1.

We can see that the two solutions agree very well, especially at small r, i.e., close to the centre of the simulation box, where the overdensity is placed. Far from the centre, the agreement becomes less perfect because the analytical solution does

not assume periodicity of the spherical overdensity, while the numerical code uses periodic boundary conditions so that the field sees the overdensities in the replicated boxes as well.

4.3.4 3D matter power spectrum of a cosmological run

Finally, we compare the dark matter power spectrum at the present time measured from our test simulations with those from a similar resolution run using the ECOSMOG-V code (Li et al., 2013a), the ELEPHANT simulations (Paillas et al., 2019). The lower right panel of Fig. 4.1 shows this comparison. We can see that our results display good agreement with previous measurements, and in particular our modified version of AREPO reproduces well the amplitude of the power spectrum enhancement in the nDGP model relative to GR on all scales.

Note that the amplitudes of the matter power spectrum from both codes are slightly different. This is due to the differences in the background cosmology and simulation set-up. The ELEPHANT simulations were run in a box of size $L = 1024\,h^{-1}$Mpc and $N_p = 1024^3$ particles using the WMAP-9 simulation parameters (Hinshaw et al., 2013), while the AREPO test was run in a box of $256\,h^{-1}$Mpc with 256^3 dark matter particles using the Planck 15 best-fit parameters (Planck Collaboration XIII, 2016).

4.4 The SHYBONE-nDGP simulations

The SHYBONE-nDGP runs consist of a suite of nine simulations covering three gravity models (GR, N5 and N1) at two resolutions. The larger box has a size of $L = 62\,h^{-1}$Mpc (L62) and contains 512^3 dark-matter particles and 512^3 gas elements, giving a mass resolution of $m_{\rm DM} = 1.28 \times 10^8\,h^{-1}{\rm M}_\odot$ and $m_{\rm gas} = 2.40 \times 10^7\,h^{-1}{\rm M}_\odot$. We have also run a smaller box with size $L = 25\,h^{-1}$Mpc (L25) and 2×512^3 resolution elements giving a baryon mass resolution of $1.57 \times 10^6\,h^{-1}{\rm M}_\odot$ and dark matter particle mass of $8.41 \times 10^6\,h^{-1}{\rm M}_\odot$. In addition, we ran DM-only versions of the L62 runs (L62-DMO); in this case the mass of the dark matter particle is $1.52 \times 10^8\,h^{-1}{\rm M}_\odot$. The softening lengths for DM particles and stars are 1.25 and

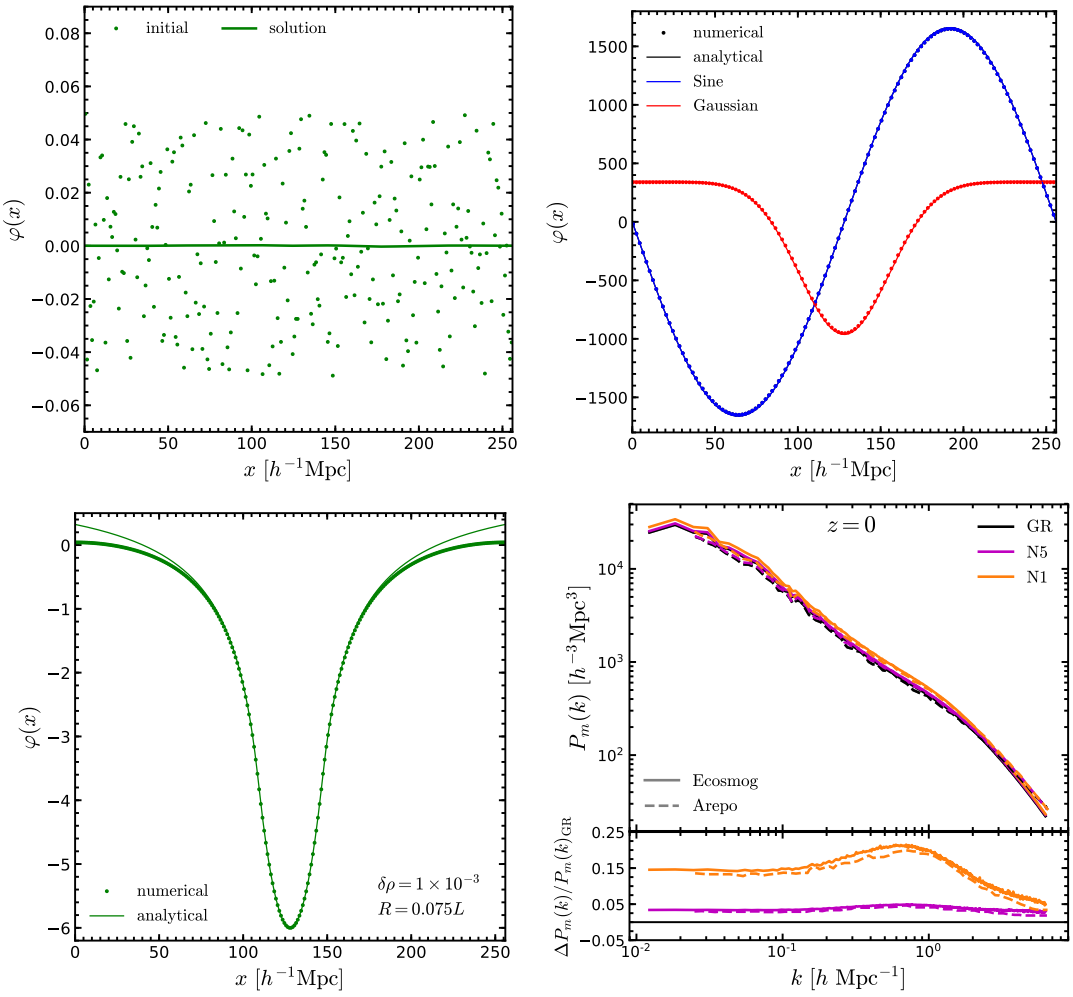

Figure 4.1: Results of code tests. *Upper left panel:* Uniform density test, where the green dots represent the random initial values of the scalar field in the range $[-0.05, 0.05]$ and the solid green line shows the final solution. *Upper right panel:* The 1D sine (blue dots) and Gaussian (red dots) density field tests. The solid lines show the analytical solutions. *Lower left panel:* Spherical overdensity test using $\delta\rho = 0.001$ and $R = 0.075L$. The line represents the analytical solution while the dots correspond to our simulation test result. *Lower right panel:* Measured dark matter power spectrum from our test simulations (dashed lines) and from the ELEPHANT simulations run with the ECOSMOG-V code (solid line). In this panel we show the predictions of GR (black lines), N5 (magenta lines) and N1 (orange lines). The lower subpanel displays the relative difference between the nDGP models and GR for the two different codes.

$0.5\,h^{-1}$kpc for the L62 and L25 runs, respectively. Table 4.1 summarises the set-up of our simulations.

For all simulations, we use the same linear perturbation theory power spectrum to generate the initial conditions at $z_{\rm ini} = 127$ with the N-GenIC code (Springel et al., 2005), which allies the Zeldovich approximation. The cosmological parameters are chosen from those reported by Planck Collaboration XIII (2016):

$$\{\Omega_{\rm b}, \Omega_{\rm m}, h, n_s, \sigma_8\} = \{0.0486, 0.3089, 0.6774, 0.9667, 0.8159\}.$$

For each set of GR, N5 and N1 simulations we use the same initial condition, since at $z = 127$ the effect of modified gravity is expected to be negligible, and the initial power spectrum depends only on the other cosmological parameters.

The modified gravity solver is combined with the IllustrisTNG galaxy formation model (Pillepich et al., 2018a) to follow the formation and evolution of realistic synthetic galaxies through cosmic time. The TNG model is an updated version of the original Illustirs model (Vogelsberger et al., 2014) which allows the formation and evolution of galaxies in cosmological gravo-magnetohydrodynamical simulations. The model incorporates prescriptions for star formation, stellar evolution, chemical enrichment, primordial and metal-line cooling of the gas, stellar feedback with galactic outflows, black hole formation and AGN feedback (Weinberger et al., 2017; Pillepich et al., 2018a). The TNG model has been 'tuned' to reproduce the observed galaxy stellar mass function and the stellar-to-halo mass relation, the total gas mass content of massive groups (within r_{500c}), the black hole to stellar mass and the stellar mass to galaxy size relations at the present time, and the star formation rate density at $z \lesssim 10$ (see Pillepich et al., 2018a, for details). The TNG simulations were run with the moving-mesh Arepo code which solves the equations of ideal, continuum magnetohydrodynamics coupled with self-gravity (Pakmor et al., 2011; Pakmor & Springel, 2013). The self-gravity is solved with the Tree-PM approach, while the fluid dynamics employs a Godunov (finite-volume) type method, with a spatial discretisation based on an unstructured, moving, Voronoi tessellation of the domain. We do not tune the TNG model for the nDGP simulations, and instead use the same galaxy formation prescription for all gravity models. In theory, such a tuning is needed for any new model. However, as we shall see later, the Illus-

Table 4.1: Numerical parameters of the SHYBONE-nDGP simulations.

Simulation	Gravity model	$L_{\rm box}$ $[h^{-1}{\rm Mpc}]$	$N_{\rm DM}$	$N_{\rm gas}$	$m_{\rm DM}$ $[h^{-1}{\rm M}_\odot]$	$m_{\rm gas}$ $[h^{-1}{\rm M}_\odot]$
L62	GR, N5, N1	62	512^3	512^3	1.28×10^8	2.40×10^7
L25	GR, N5, N1	25	512^3	512^3	8.41×10^6	1.57×10^6
L62-DMO	GR, N5, N1	62	512^3	512^3	1.52×10^8	—

trisTNG model, which has been tuned for ΛCDM, also gives good predictions of the galaxy and gas properties for the nDGP models studied in this Chapter, therefore not necessitating a re-tuning.

The dark matter haloes (groups) and their substructures – subhaloes and galaxies – are identified with SUBFIND (Springel et al., 2001). The group catalogues (including subhalo and galaxy information) and the particle data are stored in 100 snapshots from $z \sim 20$ to $z = 0$. The large number of snapshots is ideal for generating halo merger trees which allows to run with semi-analytic models of galaxy formation.

A visual representation of the nDGP-L25 simulations at the present time is displayed in Fig. 4.2. The top (bottom) six panels show the densities of dark matter, gas and stars, gas temperature, the ratio between the amplitudes of the fifth and standard Newtonian forces, and the scalar field φ in the N1 (N5) model. The colour maps were generated with the SPHVIEWER package (Benitez-Llambay, 2015). The distribution of matter in our nDGP simulations seems indistinguishable between N1 and N5 (we have not shown the GR results as they are also indistinguishable visually), but we will quantify the impact of modified gravity on the clustering of matter components and on the galaxy properties in the following section. From the force ratio panels of Fig. 4.2 we can observe that high-density (green) regions experience a negligible force enhancement while low-density (yellow) regions experience an enhancement of $F_{5\text{th}} = (1/3\beta_{\text{nDGP}})F_{\text{GR}}$, where $\beta_{\text{nDGP}} = 2.69$ and $\beta_{\text{nDGP}} = 9.45$ [cf. Eq. (1.2.35)] for N1 and N5 at $z = 0$, respectively. In the scalar field panels of Fig. 4.2 we have subtracted the mean scalar field value measured in the whole simulation box, $\bar{\varphi}$. $\varphi - \bar{\varphi}$ then has a zero mean and can be regarded as the potential of the fifth force: as expected, this map is smoother and dominated by long-wavelength modes. Notice that the colour bars for the force ratio and scalar field panels are different between N5 and N1.

Fig. 4.3 shows the face-on images of a random selection of four disc galaxies from the nDGP full-physics simulations at $z = 0$. The first two rows show, respectively, one galaxy from each of the L25 and L62 runs for N1, while the last two rows show two disc galaxies for N5 (again one per box). We follow the prescription of

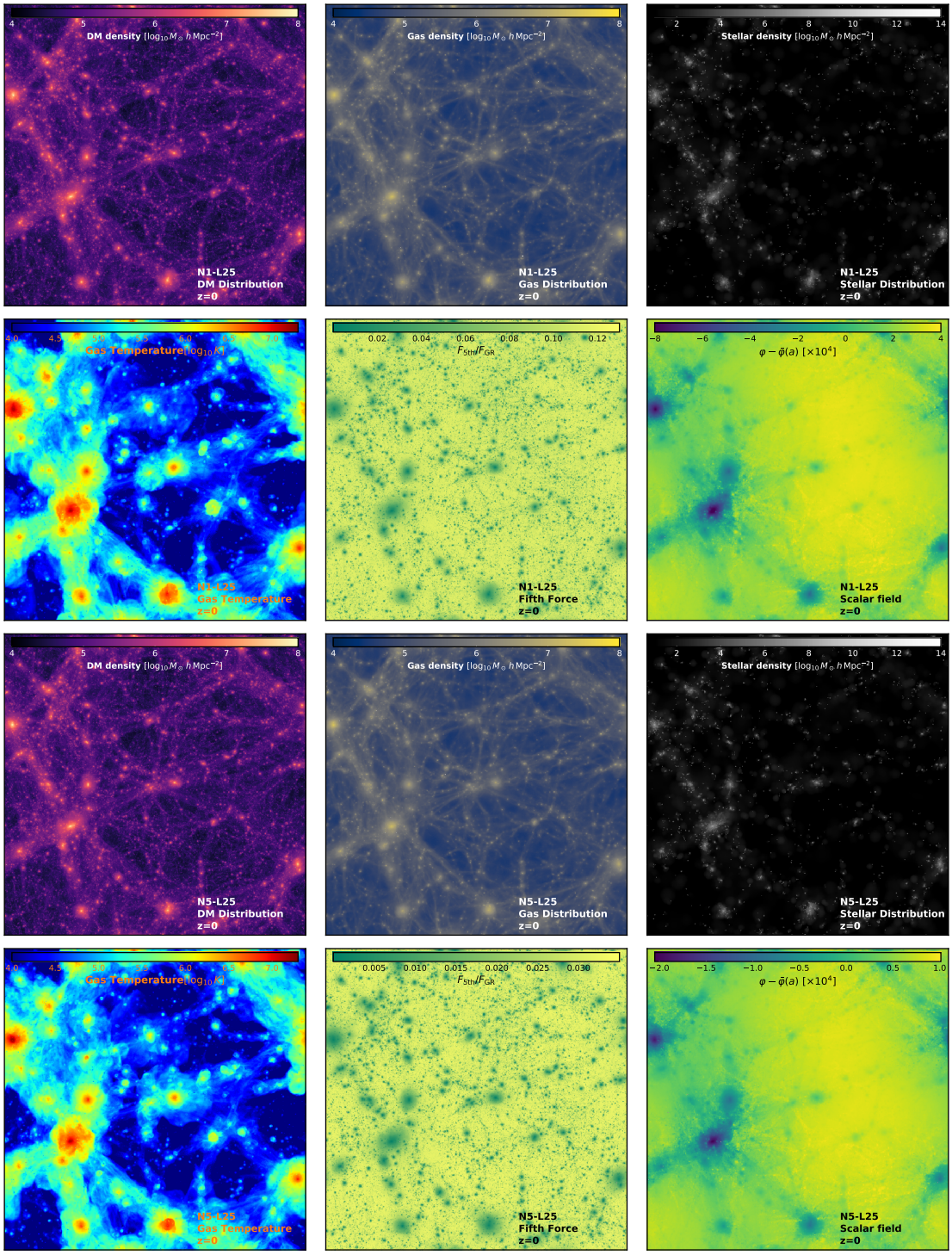

Figure 4.2: Visual inspection of the nDGP-L25 simulations showing the large-scale structure at $z = 0$. The *top six panels* show the column density of DM, the gas density, the stellar mass distribution, the temperature of the gas, the fifth to Newtonian force ratio, and the difference between the local and background mean values of the scalar field, $\varphi - \bar{\varphi}$ (in code unit), of the N1 model. The *bottom six panels* display the same matter and modified gravity quantities but for the N5 model.

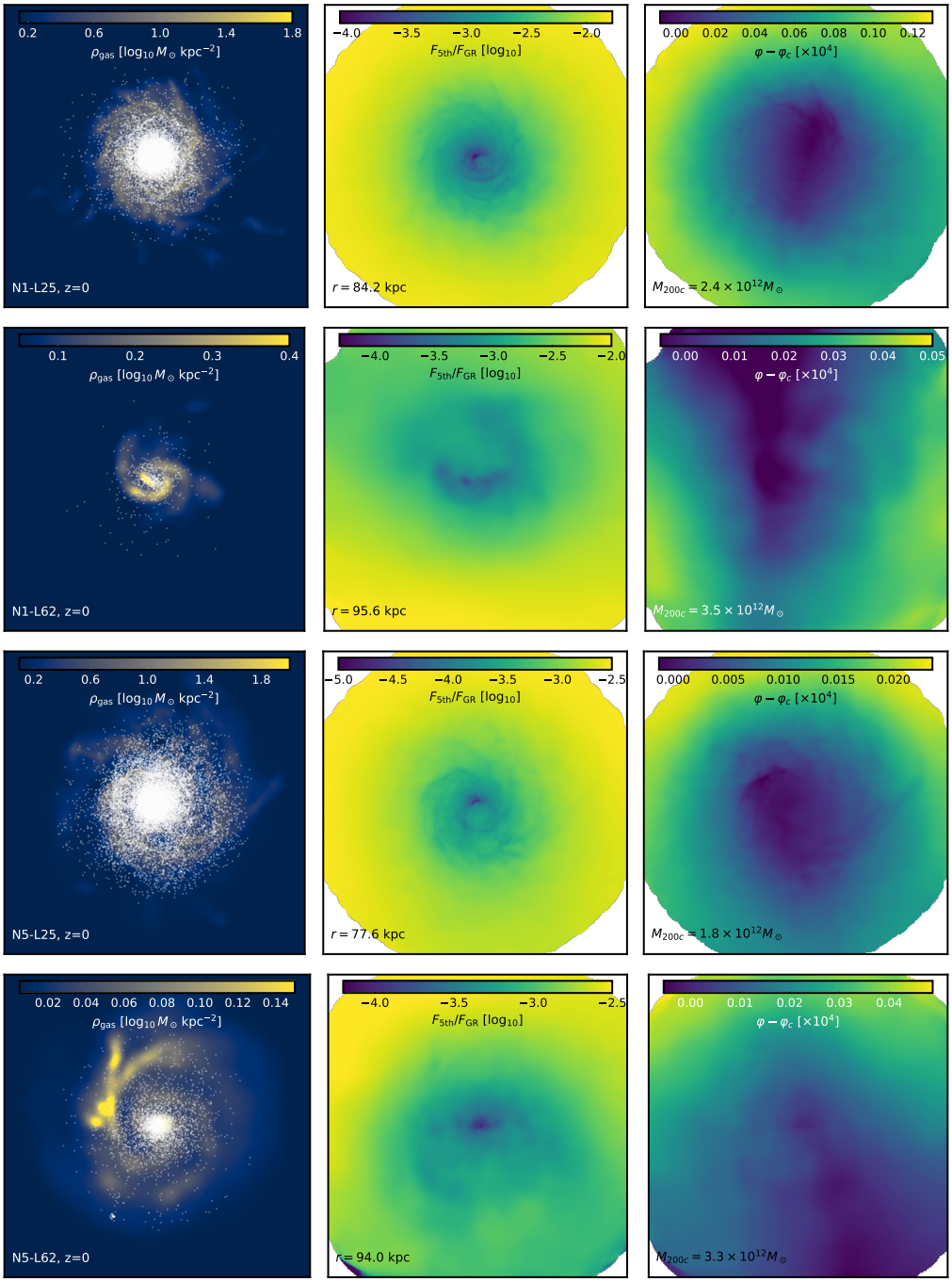

Figure 4.3: Visualisation of a selection of disc galaxies from the two boxes (L25 and L62), for both N1 (top two rows) and N5 (bottom two rows). *Left column*: the gas column density with stars (white dots) overplotted. *Central column*: the ratio between the magnitudes of the fifth force and standard gravity. *Right column*: the difference between the local value of the scalar field, φ, and its value at the galactic centre, φ_c. All galaxies are selected at $z = 0$ and all images are face-on. Numerical values are colour-coded as indicated by the colour bars in each panel, and various information, such as the disc radius and host halo mass, is also shown.

Arnold et al. (2019) to identify disc galaxies in our simulations. Essentially, we select galaxies that have $\kappa > 0.57$, with κ the rotational-to-total kinetic energy parameter (Ferrero et al., 2017). The first column displays the gas column density (the colour map) and star particles (white dots) of the galaxies. The second column presents the map of modified gravity force enhancement. The amplitude of the scalar field is shown in the third column. We see that the L25 box, owing to its higher resolution, gives rounder and more detailed galaxy images. The fifth force is indeed much weaker than Newtonian gravity inside and around the galactic disc: the ratio between their magnitudes is smaller than 10^{-2} and $10^{-2.5}$, for N1 and N5 respectively, in this region, showing that the Vainshtein mechanism effectively suppresses the fifth force. In the scalar field maps, we subtract φ_c, the scalar field value at the centre of the galaxy (note that this is different from Fig. 4.2), to eliminate the contribution from long-wavelength modes. This is because we want to see the spatial variations of the scalar field that are caused by the matter distribution in the galaxy itself. We observe that the scalar field increases in value from inside out, as expected given its role as the fifth force potential.

We have counted the number of disc galaxies from the simulations. The L25 runs produce 124, 126 and 118 such objects at $z = 0$, for GR, N5 and N1 respectively. The corresponding numbers from the L62 runs are much smaller (even with a larger box size), and so we do not quote them here – this reflects the fact that the formation of disc galaxies is sensitive to the simulation resolution. From these numbers we do not observe any statistically significant trend of the impact of modified gravity. This is different from the case of $f(R)$ gravity (Arnold et al., 2019), which in the case of $|f_{R0}| = 10^{-5}$ (F5) was found to produce significantly fewer disc galaxies than in GR. A possible explanation is the effect of modified gravity to enhance galaxy mergers, which makes it harder for disc galaxies to survive. In $f(R)$ gravity, we note a strong difference in halo abundance from GR (see, e.g., Shi et al., 2015), which indicates that halo formation is strongly affected by the fifth force. This is, however, not the case in the nDGP models studied here (Hernández-Aguayo et al., 2020a), implying a weaker effect of the fifth force on the halo formation (by mergers and accretions). We shall leave a more careful analysis of the halo merger history to a future work.

4.5 Results

4.5.1 Clustering of matter components

The measured power spectra and correlation functions for all types of matter components in our simulations are displayed in the upper panels of Figs. 4.4 and 4.5 at redshifts $z = 0, 1$ and 2. We show results for the clustering of all gas (including both hot and cold components; red lines), stars (yellow), dark matter (blue), and the combination of all components (grey). The middle and lower rows of Fig. 4.4 and Fig. 4.5 show the relative differences of the clustering measurements from the nDGP simulations with respect to GR for the L62 and L25 boxes, respectively. For the power spectrum (upper panels of Fig. 4.4) we additionally show the linear theory dark matter power spectrum for comparison as the light grey solid line.

From the upper panels of Fig. 4.4 we note that the power spectra of different matter components have different behaviour and amplitudes, with stars being more clustered than the other types of matter irrespective of the gravity model. The clustering of dark matter and the total matter distribution show almost the same amplitude and follow the linear theory prediction on large scales through cosmic time. The power spectrum of gas displays a decrease in amplitude at the present time on small and intermediate scales; this behaviour is due to strong feedback effects that suppress galaxy formation at late times (Springel et al., 2018).

We can also see the impact of the simulation particle resolution on the matter power spectrum by comparing the thick and thin lines in Fig. 4.4. The main differences are the lack of large-scale modes in the L25 box, while the results of the L62 boxes are affected by the relatively low resolution on small scales. The most affected component due to resolution effects is the stars, which display a consistently higher amplitude at $z = 2$ for the L62 box compare to the L25 box; However, this difference decreases at low redshifts. This is because stars in our low-resolution box (L62) tend to occupy higher-mass haloes than in the higher-resolution case and these haloes are more strongly biased. Also, as we will see later, the star formation rate is different between the L62 and L25 runs, which can also have an impact on the spatial distribution and clustering of stars. However, the GR results from both

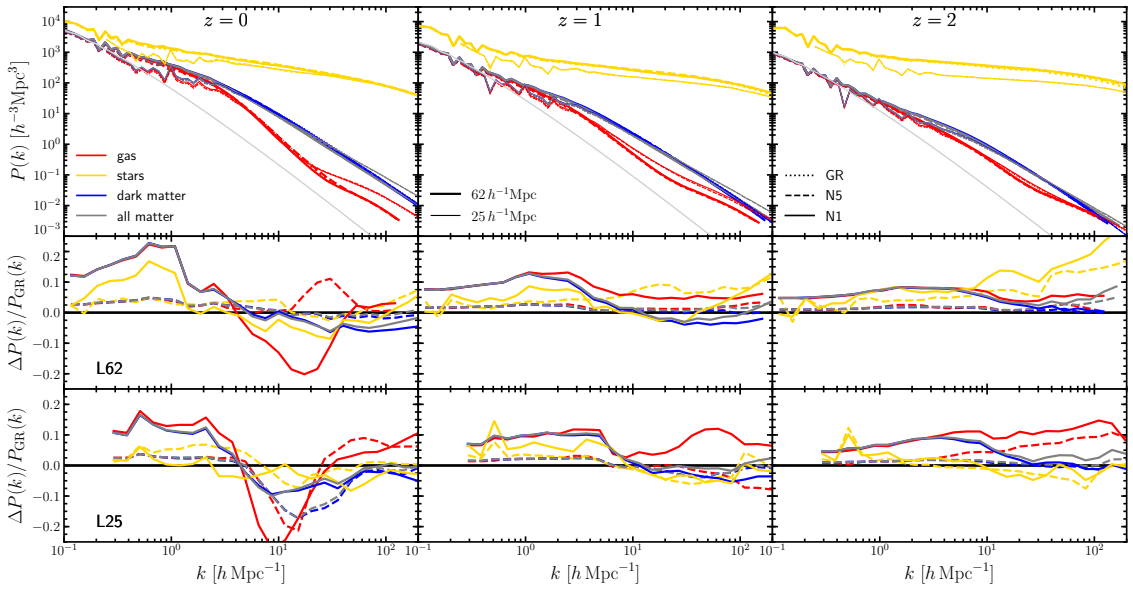

Figure 4.4: The measured power spectra of different matter components of our full-physics simulations at $z = 0$ (*left panel*), $z = 1$ (*middle panel*) and $z = 2$ (*right panel*). The *upper panels* show the absolute values of the power spectra of the gas (red lines), stars (yellow lines), dark matter (blue lines) and total matter (grey lines) components. Thick lines indicate the results from the $L = 62\,h^{-1}$Mpc box, while thin lines show the results from the $L = 25\,h^{-1}$Mpc case. *Dotted lines* show results for GR, *dashed lines* for N5 and *solid lines* for N1. The *middle* and *lower rows* display the relative differences with respect to GR predictions for the $L = 62\,h^{-1}$Mpc and $L = 25\,h^{-1}$Mpc boxes, respectively.

simulation boxes (thick and thin dashed lines, respectively) are consistent with the IllustrisTNG findings at different resolutions reported by Springel et al. (2018). The same discussion on resolution effects on power spectrum applies to nDGP models as well.

The interplay between baryons and modified gravity can be seen in the middle and bottom panels of Fig. 4.4 for the L62 and L25 boxes, respectively. For dark matter, we can observe an enhancement on large scales ($k \lesssim 1\,h\,\mathrm{Mpc}^{-1}$) due to the fifth force, leading to a maximum difference of $\sim 5\%$ and $\sim 20\% - 25\%$ for the N5 (dashed lines) and N1 (solid lines) models, respectively. This enhancement is consistent with results found with DM-only simulations (see, e.g., Winther et al., 2015). On small scales, we note a suppression due to the Vainshtein screening mechanism. At $z \leq 1$, there is a decrease of matter clustering in nDGP compared to GR at $k/(h\mathrm{Mpc}^{-1}) \gtrsim 10$. This may be partly due to the gravitational effect of gas and stars, but as we will see below, even in the DMO L62 simulations we see a similar suppression of dark matter power spectrum on these scales, which is a new feature only seen at high resolution.

The gas power spectrum (red lines) follows the same behaviour as dark matter on large scales at all redshifts. At early times ($z \geq 1$), we observe that the gas power spectrum is less suppressed than dark matter on small scales; this is due to haloes that were able to accrete more gas from their surroundings, leading to a higher concentration of gas inside haloes, particularly for the N1 model. At the present time, the gas power spectrum is suppressed by $\sim 20 - 25\%$ for N1 in both boxes, while for N5 this effect is only observed for the L25 box on intermediate scales $5 < k/[\,h\,\mathrm{Mpc}^{-1}] < 40$. A possible reason for this is the combination of stellar and AGN feedback processes that expel gas from inside massive haloes and modified gravity effects that enhance the growth of structure. Also, the interaction between MG and baryons could lead to a stronger baryonic feedback in the nDGP models (especially for N1) changing the clustering signal on intermadiate scales at the present time.

The clustering of stars (yellow lines) is less affected by modified gravity than gas and dark matter, for which we find differences of $\lesssim 5\%$ for both N5 and N1 models

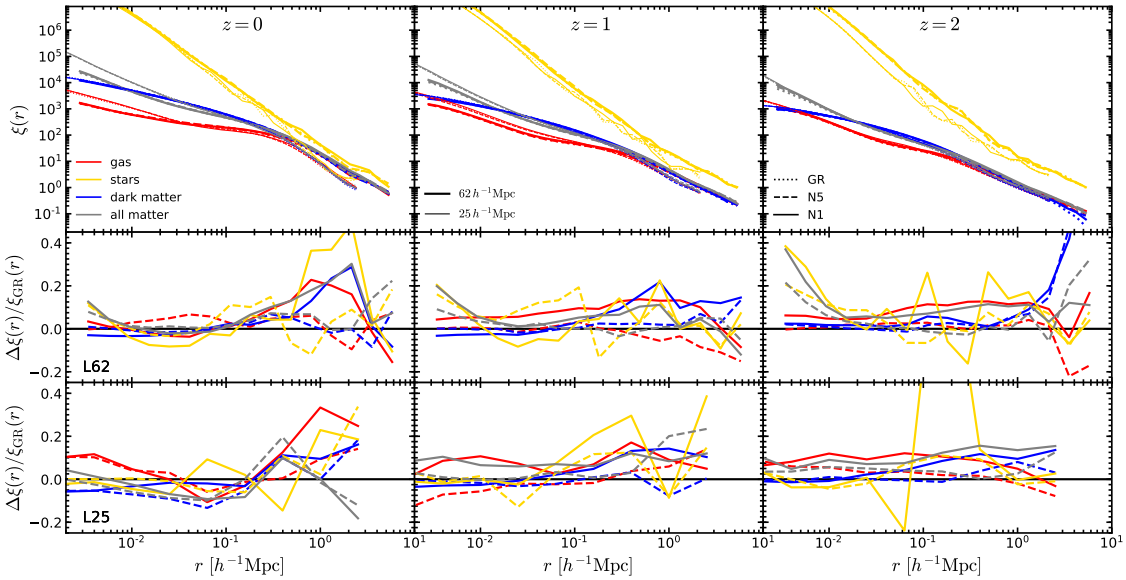

Figure 4.5: The same as Fig. 4.4 but for the correlation functions of the different matter components.

and all redshifts, except at $z = 2$ for the L62 box where the clustering of stars shows an increased clustering of $> 10\%$ for both nDGP models (we caution about the L62 results regarding stars, given that the star clustering is strongly resolution dependent). The small difference between star clustering in the different models is the result of the Vainshtein screening mechanism inside haloes. Note that this is conceptually different to the behaviour of the stellar power spectrum in $f(R)$ gravity, where the clustering of stars is strongly influenced by the MG model even at $z = 2$ (Arnold et al., 2019).

In Fig. 4.5 we show the correlation functions results for the same matter components and redshifts shown in Fig. 4.4. We find consistent trends with the power spectrum results discussed above. We note that the gas correlation function starts to deviate from the dark matter and total matter correlation functions on scales $r \sim 0.2\,h^{-1}$Mpc at $z = 2$. This evolves with time, when at $z = 0$ the gas is much less clustered than dark matter on small scales. Again, the overall behaviour of the correlation functions and the resolution effects due to different box size is the same as the found for power spectrum. The relative differences between the nDGP models and GR are consistent with the power spectrum findings (see middle and bottom panels of Fig. 4.5). In this case, we find that the correlation function of stars is

noise dominated, making it difficult to observe a consistent difference between both nDGP models and GR as seen from the power spectrum.

4.5.2 Impact of baryonic physics on the clustering of matter

In the first series of the SHYBONE simulations, Arnold et al. (2019) presented results on the degeneracy between the baryonic processes and modified gravity using the Hu-Sawicki $f(R)$ model (Hu & Sawicki, 2007). Here, we are able to extend these findings to the nDGP braneworld model. Recall that we only produced DM-only runs for the L62 box (see Table 4.1 for details), hence the results shown in Figs. 4.6 and 4.7 correspond to the large box of the SHYBONE-nDGP simulations.

Fig. 4.6 shows the relative differences between the full-physics power spectra of all matter in the three gravity models with respect to the dark (or equivalently all) matter power spectrum of the DM-only GR simulation at $z = 0$, 1 and 2. We also show the predictions from the DM-only nDGP simulations (dashed lines) at the same redshifts. On large scales ($k < 2\,h\,\mathrm{Mpc}^{-1}$) we find a consistent enhancement of the DM-only power spectrum of the N5 and N1 models (dashed lines) with the dark matter component of the full-physics runs (see blue lines in the middle panels of Fig. 4.4)

At $z = 0$, we can see a suppression in the matter power spectrum of $\sim 20\%$ for GR and N5 models at scales $k \sim 20\,h\,\mathrm{Mpc}^{-1}$, while for N1 the power is suppressed by $\sim 25\%$. This suppression becomes smaller with increasing redshift; as shown in Springel et al. (2018) and Arnold et al. (2019), one should expect a negligible baryonic effect on intermediate and large scales at $z > 3$. For comparison, we also show the results from the IllustrisTNG (Springel et al., 2018) and Eagle (Hellwing et al., 2016) simulations at $z = 0$, noting the good agreement with our GR results. The significant enhancement of the matter power spectrum for $k > 40\,h\,\mathrm{Mpc}^{-1}$ is consistent with the IllustrisTNG result, but in our case in the highly resolution-affected regime.

The dotted lines display the estimated effect of baryonic feedback from the GR full-physics simulation added to the predictions from the DM-only nDGP simula-

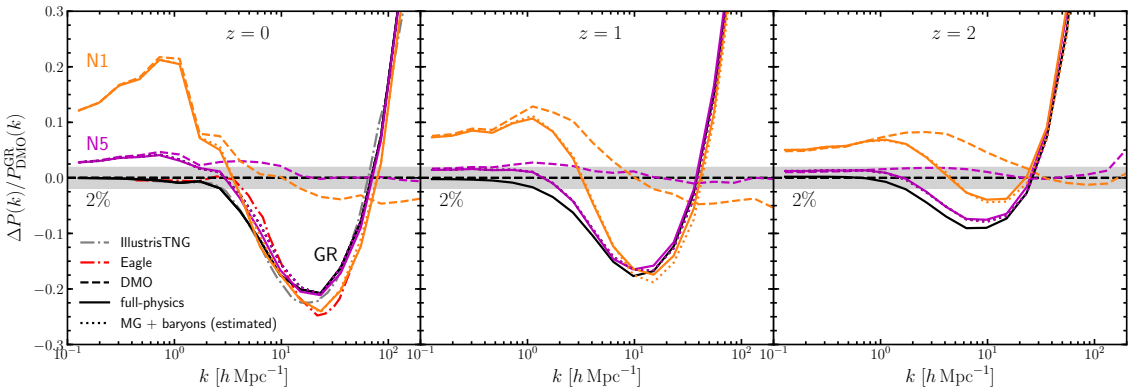

Figure 4.6: The relative differences of the total matter power spectra from the full-physics (solid lines) and DM-only (dashed lines) L62 runs with respect to the matter power spectrum of the DM-only GR runs at $z = 0$ (*left panel*), $z = 1$ (*middle panel*) and $z = 2$ (*right panel*). The grey and red dash-dotted lines show the impacts of baryons on the total matter power spectrum in the IllustrisTNG (Springel et al., 2018) and Eagle (Hellwing et al., 2016) simulations at $z = 0$. Solid lines illustrate results from full-physics runs, dashed lines their DM-only counterparts. Dotted lines show an estimate for the combination of baryonic feedback and modified gravity effects, obtained by adding the relative differences of the nDGP DMO results to the GR full-physics run, cf. Eq. (4.5.32). The different colours represent different gravity models as indicated in the *left panel* (black for GR, magenta for N5 and orange for N1). The light grey shaded region indicates a relative difference of 2 per cent.

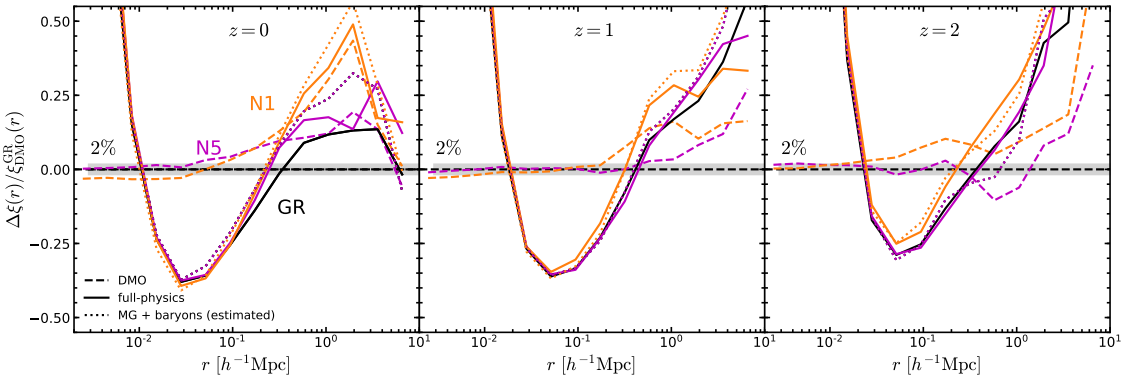

Figure 4.7: The same as Fig. 4.6 but for the correlation function.

tions:

$$\frac{\Delta P(k)}{P^{\rm GR}_{\rm DMO}(k)} = \left[\frac{P^{\rm nDGP}_{\rm DMO}(k)}{P^{\rm GR}_{\rm DMO}(k)} - 1\right] + \left[\frac{P^{\rm GR}_{\rm full-physics}(k)}{P^{\rm GR}_{\rm DMO}(k)} - 1\right]. \tag{4.5.32}$$

The idea is that the impacts of baryonic physics and modified gravity can be relatively clearly separated and their back-reaction effects on each other are negligible (Arnold et al., 2019). This figure shows this simple model is accurate enough to reproduce the full-physics results in nDGP simulations: comparing the magenta and orange dotted lines with their solid line counterparts, we can see the agreement is generally at percent level at all scales up to $k \simeq 100\,h\,{\rm Mpc}^{-1}$. On scales $k \lesssim 1\,h\,{\rm Mpc}^{-1}$, the effect of baryons is negligible in both DGP models and at all redshifts, showing that the relative differences are dominated by the modified gravity effect reaching a maximum value with the same amplitude as the DM-only simulations.

In Fig. 4.7 we explore the impact of the baryonic feedback effects on the correlation functions at the same redshifts ($z = 0$, 1 and 2). We find several differences from the power spectrum results. First, the clustering in configuration space also shows a suppression on small scales, but the difference is larger than that found for the power spectrum. In this case, the relative change is ~ 40 per cent at $z = 0$, decreasing with redshift to 25 per cent at $z = 2$ (recall that we find a maximum difference of 25 per cent at $z = 0$ and about 10 per cent at $z = 2$ in the power spectrum). We observe the same enhancement on very small scales ($r < 10\,h^{-1}{\rm kpc}$) as the power spectrum. But the clustering of matter shows an increase of 10 per cent at $r = 1\,h^{-1}{\rm Mpc}$ for the GR simulations at $z = 0$, which becomes even larger

at earlier times.

In the nDGP models, the full-physics matter correlation functions follow the same trend as in GR, but the enhancement on large scales is bigger for the N1 model which reaches a maximum difference of 50 per cent at the present epoch, followed by the N5 model which presents a similar value to the GR case. Nevertheless, due to the relatively small box size of our simulations and the comparatively more noisy measurement of the correlation function at large radii, we do not observe the constant enhancement at large-scales as shown in the power spectrum.

From Fig. 4.7 we also note that estimating the feedback impact by adding the GR full-physics effect to the DM-only difference in modified gravity models (dotted lines), does lead to good agreement with the nDGP full-physics results as seen in the power spectrum, especially on scales $< 0.5\,h^{-1}$Mpc. This approximation works less well on scales beyond $0.5\,h^{-1}$Mpc, where we find larger differences in the relative values by comparing the solid and dotted lines in all panels of Fig. 4.7. We caution again that the differences on large-scales between the full-physics and the estimated impact of baryons in the nDGP models (solid and dotted lines in Fig. 4.7) could be due to the limited size of our simulation box.

The dark matter clustering measured from the DM-only simulations (dashed lines) of the nDGP models shows a similar trend to the dark matter component of the full-physics run (see Fig. 4.5). We find that on very small scales, the clustering of the dark matter is very close to GR, but the N1 model displays a slight suppression at $z \leq 1$, which is consistent to the small scale suppression of the matter power spectra in Fig. 4.6 (see also the discussion of Fig. 4.4 above). On scales $> 100\,h^{-1}$kpc the effect of modified gravity increases the amplitude of the clustering at all redshifts. This is also consistent with the power spectrum results presented in Fig. 4.6.

4.5.3 Fifth force profiles

We can also explore the interplay between modified gravity and baryonic effects by looking at the fifth force profiles of dark matter haloes. The median of the fifth-to-Newtonian force ratio profiles in our nDGP-L62 (full-physics and DM-only) runs using four mass bins: $M_{200c} = (5 \times 10^{11} - 10^{12})\,h^{-1}\mathrm{M}_{\odot}$, $(10^{12} - 5 \times 10^{12})\,h^{-1}\mathrm{M}_{\odot}$,

$(5 \times 10^{12} - 10^{13})\, h^{-1}\mathrm{M}_\odot$ and $(10^{13} - 10^{14})\, h^{-1}\mathrm{M}_\odot$ at $z = 0$, 1 and 2 as a function of r/r_{200c} (with r the distance from the halo centre) is shown in Fig. 4.8.

We observe the suppression of the fifth force inside the haloes due to the Vainshtein screening mechanism. Far from the centre, the fifth force approaches the value

$$F_{5\mathrm{th}} = \frac{1}{3\beta_{\mathrm{nDGP}}} F_{\mathrm{GR}}, \tag{4.5.33}$$

as expected [cf. Eq. (1.2.47)]. This value is showed as the dotted lines in Fig. 4.8. There is a strong suppression of the fifth force in the inner regions of the haloes ($r < 0.1\, r_{200c}$) at all three redshifts, due to higher densities close to the centres of the haloes. This can be seen from the following solution to $\mathrm{d}\varphi/\mathrm{d}r$ for a general spherical density profile $\rho(r)$, which can be obtained from Eq. (1.2.41) or (1.2.43):

$$\frac{\mathrm{d}\varphi}{\mathrm{d}r} = \frac{\sqrt{1 + \frac{64\pi G r_{\mathrm{c}}^2}{27\beta_{\mathrm{nDGP}}^2 c^2}\bar{\rho}(< r)} - 1}{\frac{16\pi G r_{\mathrm{c}}^2}{9\beta_{\mathrm{nDGP}} c^2}\bar{\rho}(< r)} g_{\mathrm{N}}(r), \tag{4.5.34}$$

where $\bar{\rho}(< r)$ denotes the mean matter density within radius r from the halo centre, and we have again set $a = 1$ for simplicity. In high-density regions, the second term in the square root of the numerator dominates over the first term, so that the fifth-to-Newtonian force ratio decays as $\bar{\rho}(< r)^{-1/2}$. For the same reason, in the inner regions we see that the fifth force is more suppressed in the full-physics than in the DM-only runs, since gas and stars condensate at halo/galactic centres, increasing $\bar{\rho}(< r)$ there.

We also find that the force ratio profiles in Fig. 4.8 do not show a noticeable dependence on the halo mass, consistent with previous findings of DMO simulations (Winther et al., 2015). This behaviour can also be explained using Eq. (4.5.34), which indicates that the force ratio only depends on $\bar{\rho}(< r)$. At $r = r_{200c}$, we have that $\bar{\rho}(< r)$ is equal to 200 times the critical density, independent of halo mass; a weak dependence on halo mass is introduced due to the different density profiles (concentrations), but the effect is small.

4.5.4 Galaxy properties in braneworld models

In Fig. 4.9 we show the results on galaxy demographics of the SHYBONE-nDGP simulations. Recall that we did not re-tune the IllustrisTNG galaxy formation model

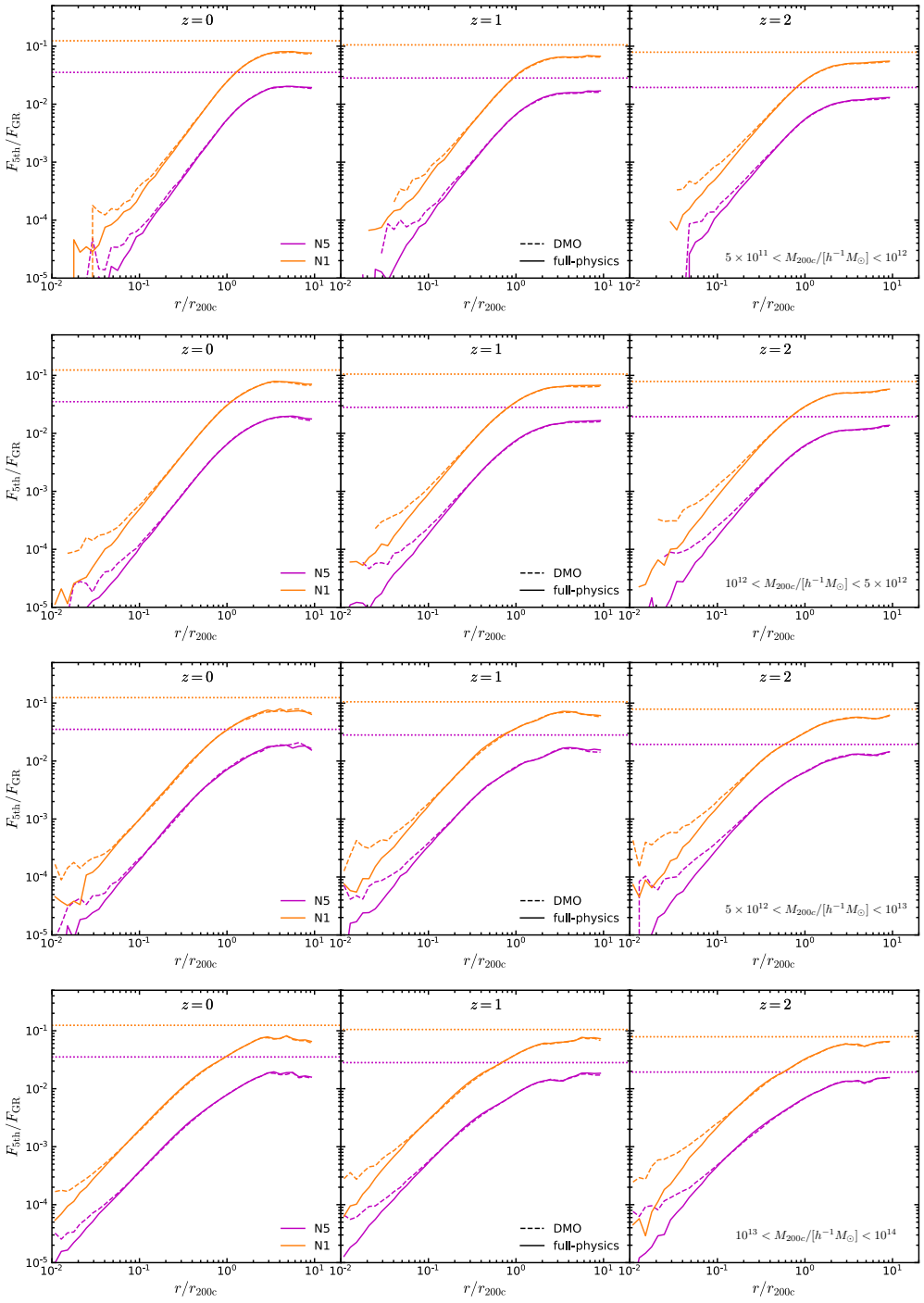

Figure 4.8: Radial profiles of the fifth-to-Newtonian force ratio of dark matter haloes in the full-physics (solid lines) and DM-only (dashed lines) nDGP-L62 simulations (magenta for N5 and orange for N1) at $z = 0$ (*left panels*), $z = 1$ (*middle panels*) and $z = 2$ (*right panels*). We show the results for four mass bins: $M_{200c} = (5 \times 10^{11} - 10^{12})\, h^{-1}\mathrm{M}_\odot$, $(10^{12} - 5 \times 10^{12})\, h^{-1}\mathrm{M}_\odot$, $(5 \times 10^{12} - 10^{13})\, h^{-1}\mathrm{M}_\odot$ and $(10^{13} - 10^{14})\, h^{-1}\mathrm{M}_\odot$ (from *top* to *bottom*). The horizontal dotted lines show the value, $F_{5\mathrm{th}}/F_{\mathrm{GR}} = 1/3\beta_{\mathrm{nDGP}}(a)$, for each nDGP model and redshift.

to match observations in modified gravity, hence we use the same hydrodynamical model for all gravity models. In all panels of Fig. 4.9 we compare our results with the TNG-L25 boxes reported by Pillepich et al. (2018a). These TNG-L25 test simulations were run using a box with size of $L = 25\,h^{-1}$Mpc and three mass resolutions: 2×512^3 (high-resolution, TNG-L25N512), 2×256^3 (medium-resolution, TNG-L25N256) and 2×128^3 (low-resolution, TNG-L25N128) dark matter and gas elements. Depending on the panel and galaxy property, we show observational data of the stellar-to-halo mass ratio and star formation rate density from Behroozi et al. (2013b), galaxy stellar mass from Baldry et al. (2012), Bernardi et al. (2013) and D'Souza et al. (2015); and gas fractions from Giodini et al. (2009) and Lovisari et al. (2015). We do not expect our L62 results to match the obervational data, since the TNG model was tuned for the TNG-L25N512 test simulations using the galaxy properties mentioned above (as well as the black hole mass - stellar mass relation and the galaxy size at redshift $z = 0$; Pillepich et al., 2018a) and it has been demonstrated that the stellar properties of galaxies depend on the simulation resolution in the TNG model (see Appendix A of Pillepich et al., 2018a,b, for details).

The upper left panel of Fig. 4.9 shows the stellar-to-halo mass ratio multiplied by the inverse of the baryon fraction ($\Omega_\mathrm{b}/\Omega_\mathrm{m}$), as a function of the total host halo mass (M_{200c}) for our six full-physics simulations at $z = 0$. The stellar mass was measured within 30 kpc from the halo centre. First, we note that the L62 simulations (dashed coloured lines) are in good agreement with the TNG-L25N128 (grey dotted line) run at the high-mass end, but is lower than the TNG-L25N256 (grey dashed line) and TNG-L25N512 (grey solid line) results, which is as expected given the resolutions of these runs. Our L25 runs (solid coloured lines) predict higher stellar mass fractions than the TNG-L25N512 (grey solid line), despite the fact that these simulations have the same resolution. The differences are due to the combination of the different initial condition realisations we used to run our simulations (i.e., cosmic variance) and the small number of high mass objects in the small boxes. Note that the final TNG100 run (blue solid line; Pillepich et al., 2018b) also has disagreements with the TNG-L25N512 test run, for the same reason. Nevertheless, our L25 predictions are in good agreement with observational estimates (light grey area) and with TNG100

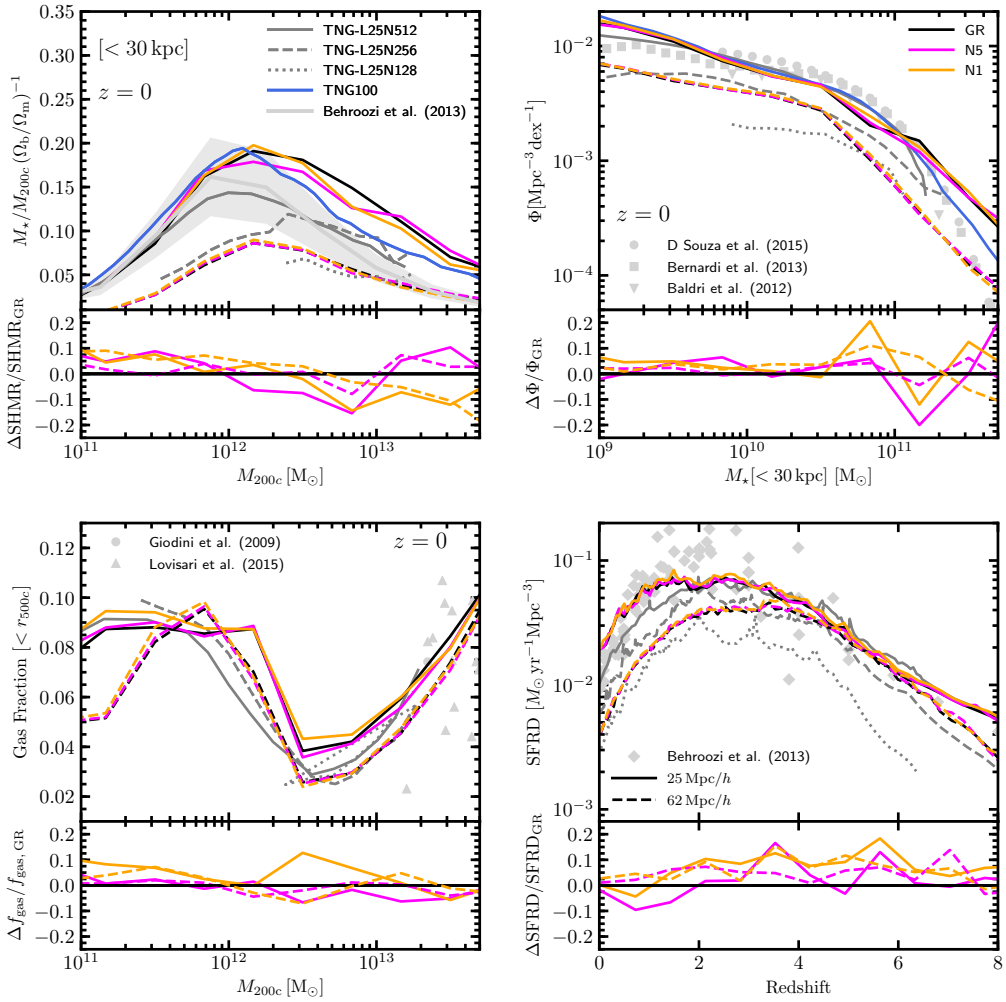

Figure 4.9: Stellar and gaseous galaxy properties at $z = 0$ (unless otherwise stated). *Upper left:* Stellar-to-halo mass ratio as a function of halo mass. The stellar mass is measured within 30 kpc from the halo centre. *Upper right:* Galaxy stellar mass function measured within 30 kpc from the centre of the halo. *Bottom left:* The halo gas fraction within r_{500c} as a function of the total halo mass. *Bottom right:* Star-formation rate density as a function of redshift. Different colours represent different gravity models as specified in the legend. Solid colour lines show results from our L25 simulations while dashed coloured lines are from our L62 boxes. All lower subpanels show the relative differences between the galaxy properties of nDGP and GR models. In all panels we compare our results with the IllustrisTNG results at three different resolutions (Pillepich et al., 2018a): TNG-L25N512 (solid grey curves), TNG-L25N256 (dashed grey curves) and TNG-L25N128 (dotted grey curves). The blue solid line in the upper panels shows the results from the TNG100 simulation (Pillepich et al., 2018b). Light-grey symbols represent observational measurements from: Behroozi et al. (2013b) Baldry et al. (2012), Bernardi et al. (2013), D'Souza et al. (2015), Giodini et al. (2009) and Lovisari et al. (2015).

at $M_{200c} \lesssim 2 \times 10^{12} M_{\odot}$. We find that the modified gravity effects induce a $\sim 10\%$ change with respect to GR for small haloes in both nDGP models, and the relative differences in the L62 and L25 boxes are consistent with each other over most of the mass range. However, the nDGP-L25 runs produce a higher model difference in the stellar mass fraction for haloes with mass $M_{200c} \sim 10^{13} M_{\odot}$, than their L62 counterparts. However, we again caution here that at this mass the simulations, especially L25, may suffer from cosmic variance.

The galaxy stellar mass functions (GSMF) measured within 30 kpc from halo centres are shown in the upper right panel of Fig. 4.9. Our L62 results are consistent with the TNG-L25N256 simulations, while the L25 GSMFs are in excellent agreement with the TNG-L25N512 and TNG100 simulations at $M_{\star} \lesssim 2 \times 10^{11} M_{\odot}$. For both nDGP models, both L25 and L62 display small differences, $\sim 5\%$, with respect to the GR counterparts, at $M_{\star} \lesssim 4 \times 10^{10} M_{\odot}$. At even higher stellar masses, the relative difference curves are noisier and the agreement between L25 and TNG100 is poorer, due to the small box size and due to the low number of galaxies in the high-mass end. Overall, we conclude that the GSMF is not significantly altered by either of the nDGP models studied here.

The lower left panel of Fig. 4.9 displays the galaxy gas fractions within r_{500c} as a function of halo mass. We can see that, considering the scatters of observational data (grey circles and triangles), both sets of SHYBONE-nDGP simulations are in good overall agreement with the three TNG-L25 tests, except for the L62 run for masses $M_{200c} \lesssim 4 \times 10^{11} M_{\odot}$ due to the limited mass resolution. In addition, for both L62 and L25, the relative differences between the nDGP models and GR are consistent with each other in almost the entire halo mass range. The small difference in the relative difference lines between L62 and L25 is again likely to be noise, and this plot does not point to a strong effect of modified gravity.

We present the star-formation rate densities (SFRD) as a function of time in the lower right panel of Fig. 4.9. We confirm the findings of Pillepich et al. (2018a) and Arnold et al. (2019) that the SFRDs are resolution dependent, particularly at low redshift. Our L62 simulations show a higher star formation rate than the TNG-L25N256 and TNG-L25N128 at high redshift ($z > 4$), while at lower redshifts

($z < 3$) the curves fall between the low- and medium-resolution TNG-L25 boxes, as expected from their resolution. The L25 boxes are in excellent agreement with the TNG-L25N512 run, but display a higher SFRD at lower redshifts ($z < 2$), which is nevertheless still in agreement with the observational data (light grey symbols). Note that the nDGP-L62 relative differences are in good agreement with our high-resolution runs (L25) displaying a maximum relative change of $\sim 15\%$ with respect to GR. However, at the present time, the SFRD in both nDGP models match the GR predictions within a 3% margin.

Due to the small (compared to scatters in observational data) differences that the nDGP models induce in the properties of galaxies, we arrive at the same conclusion as for $f(R)$ gravity in Arnold et al. (2019): a re-tuning of the TNG model for nDGP gravity is not necessary and this allows us to study different gravity models using the same prescription for galaxy formation. This also indicates that the global galaxy properties shown in Fig. 4.9 cannot be used to distinguish between the different gravity models, at least not with the current level of observational and simulation uncertainties.

The small impact of modified gravity on the global galactic and gas properties can be partly explained by the Vainshtein screening mechanism which, as we have seen, effectively suppresses the fifth force inside haloes, cf. Fig. 4.8. However, we do see nDGP effects at the level of about $5 - 15\%$ in Fig. 4.9: this is because galaxy formation is a complicated process that is not confined to the inner regions of haloes, but the recycle of gas actually involves regions in the outer parts of, or even outside, haloes, where Vainshtein screening is less effective.

4.6 Summary

In this Chapter, we introduced a new set of galaxy formation simulations in the DGP braneworld model. In order to run these simulations, we extended the modified version of the Arepo code for $f(R)$ gravity presented by Arnold et al. (2019), so that it can be used to simulate structure formation in the DGP model. We performed a series of tests to verify that the new code gives reliable results. We also

compared the matter power spectrum predicted by the new code with predictions by the ECOSMOG-V code (Li et al., 2013a), finding excellent agreement on all scales.

This implementation, together with the IllustrisTNG galaxy formation model desribed by Pillepich et al. (2018a), makes the new set of full-physics hydrodynamical simulations in DGP gravity possible. The simulations we used in our analysis employ 2×512^3 dark matter particles and gas cells. We studied two cosmological volumes: a large-volume simulation with box size $L = 62\,h^{-1}$Mpc (L62 runs), and a small-volume with box size $L = 25\,h^{-1}$Mpc (L25 runs). For each set, the simulations cover three gravity models – GR, N5 and N1. These are supplemented by DM-only simulations for the same models and using the same specifications as the L62 full-physics runs. We have saved 100 snapshots per run, which contain all the particle data and group catalogues generated using SUBFIND.

We studied the real-space clustering in Fourier and configuration space of stars, gas, dark matter and the total matter distribution. The clustering of dark matter in the full-physics nDGP simulations displays an enhancement compared to its GR counterpart on large scales ($k < 4\,h\,\mathrm{Mpc}^{-1}$ for the power spectrum), consistent with previous findings from DM-only simulations (Winther et al., 2015). The clustering of gas and the total matter distribution follows a similar trend to the dark matter on almost all scales, and the clustering of the stellar content seems to be less affected by changes in the gravity model in Fourier space.

We find that the interplay between baryonic feedback processes and modified gravity is complex. However, the impact of baryons on the clustering of matter has a similar impact in all gravity models, with a suppression of $\sim$ 25 per cent in the power spectrum and up to $\sim$ 40 per cent in the correlation function at the present time. In particular, the impacts of baryons and modified gravity on the matter power spectrum – and to a similar extent on the correlation function – can be modelled additively by summing up their changes to the GR dark matter power spectrum, with a percent-level accuracy, cf. Figs. 4.6 and 4.7.

The fifth force to normal gravity ratio in dark matter haloes, $F_{\rm 5th}/F_{\rm GR}$, is also affected by baryons. We found a suppression of the ratio due to higher densities in the inner regions (close to the centre) of the haloes in full-physics runs relative to

DMO. Additionally, we showed that the force profiles have only a weak dependence on halo mass, confirming the findings of DM-only simulations presented by Winther et al. (2015), and note that this is a feature that is expected for Vainshtein screening.

The stellar and gaseous properties of galaxies are only mildly affected by the modifications to gravity in the nDGP models, mirroring the results found by Arnold et al. (2019) for the case of $f(R)$ gravity. The differences induced by the nDGP model are nevertheless even smaller than those caused by $f(R)$ gravity. Therefore, we conclude that given the current size of uncertainties in the relevant galactic observables, there is no need to ru-tune the baryonic physics model for these modified gravity models.

Chapter 5

Measuring the BAO peak position with different galaxy selections

5.1 Introduction

The baryon acoustic oscillations (BAO) scale is a standard ruler that can be used to measure the cosmological redshift - distance relation (Eisenstein & Hu, 1998; Blake & Glazebrook, 2003; Linder, 2003; Xu et al., 2013; Ross et al., 2015). This characteristic scale is approximately the horizon scale at recombination and corresponds to the largest distance that a sound wave can travel in the photon – baryon fluid up to this epoch. The sound horizon at recombination has been measured at the sub-percent level using the cosmic microwave background (CMB) radiation (Planck Collaboration XIII, 2016). It is possible to measure the BAO scale from the clustering of galaxies using two-point statistics such as the correlation function or its Fourier transform, the power spectrum (see e.g., Cole et al., 2005; Eisenstein et al., 2005; Beutler et al., 2017; Ross et al., 2017). This allows us to probe the redshift – distance relation, which depends on the cosmological model and hence, given the existing constraints from the CMB, constrains the late-time behaviour of the dark energy.

In this Chapter, we explore if there is an optimal way to target galaxies to extract the BAO scale. We do this by ranking galaxies by either their luminosity, colour, or environment within the same volume, and then assess how well we can extract the

BAO scale for different subsamples of galaxies in each case. The initial idea behind using subsamples of galaxies was to sparsely sample a flux limited catalogue to efficiently map a large survey volume, without measuring a redshift for every galaxy (Kaiser, 1986). This technique was successfully applied to early redshift surveys to yield impressive constraints on cosmological parameters from modest numbers of galaxy redshifts (Efstathiou et al., 1990; Loveday et al., 1992). A development of this approach was to target a particular class of object rather than to randomly sample a flux limited catalogue. LRGs were isolated from the photometric catalogue of the Sloan Digital Sky Survey to probe a larger volume of the Universe than that reached by the original flux limited survey (Eisenstein et al., 2001). The argument here is that the LRGs should be strongly biased tracers of the underlying dark matter, because they are bright galaxies, thereby boosting the signal-to-noise of the clustering measurement for a fixed number density of targets (Feldman et al., 1994). Similar strategies were devised to map the large-scale structure of the Universe out to $z \sim 1$ using galaxies with strong emission lines (ELGs) (Drinkwater et al., 2010). Recently, Ruggeri & Blake (2019) re-analysed the data from the 6dFGS, WiggleZ, BOSS and eBOSS galaxy surveys to study how assumptions about the errors and sample variance affect the recovery of the BAO scale.

Characterising how the BAO signal varies between different galaxy populations is also important for understanding systematic biases in the position of the BAO peak. For example, overdense regions contract, pulling the BAO peak inwards, while underdense regions expand, pushing the BAO peak to larger scales (Sherwin & Zaldarriaga, 2012; Neyrinck et al., 2018). Different galaxy populations sample the underlying density field differently and thus the size of this effect can vary between galaxy populations (e.g. Angulo et al., 2008; McCullagh et al., 2013; Achitouv & Blake, 2015). Such systematic effects are small, but nonetheless are important for current and future precision measurements. To a first approximation, this effect, as well as the smearing of the BAO peak, is captured by "BAO reconstruction" techniques, such at those based on Lagrangian linear theory (e.g. Eisenstein et al., 2007b; Padmanabhan et al., 2012) and the more recent non-linear reconstruction techniques (e.g. Ata et al., 2015; Zhu et al., 2017; Hada & Eisenstein, 2018; Shi

et al., 2018; Birkin et al., 2019; Jasche & Lavaux, 2019). However, these methods are rather involved and it remains to be understood if they fully account for the BAO systematics present in different galaxy samples. This is why here we study the BAO signal in the galaxy distribution without applying a BAO reconstruction step.

To address the question of what is the best way to measure BAO, we use a mock catalogue built by implementing a technique based on halo occupation distribution modelling into one of the largest N-body simulations ever run, the Millennium-XXL (Angulo et al., 2012; Smith et al., 2017). We test how well the BAO scale can be constrained for galaxy samples selected in different ways using a power spectrum analysis. Our goal is to establish how the strength of the BAO feature, and thus the accuracy with which the BAO scale can be measured, depends on galaxy properties such as brightness, colour and local density. In particular, we investigate what are the best ways to select galaxies such that we optimise the BAO measurement for future spectroscopic surveys. The results of our study can inform the survey strategy of upcoming projects.

The Chapter is organised as follows: In Section 5.2, we describe the construction of the galaxy catalogue and the theoretical BAO model. In Sec. 5.3, we show the results of the power spectrum fitting and a description of the galaxy-halo connection of the galaxy samples. Finally, the summary the Chapter is given in Sec. 5.4.

5.2 Galaxy samples and methodology

5.2.1 Galaxy catalogue

We build the galaxy mock catalogue using the Millennium-XXL (MXXL) dark matter only N-body simulation output at $z = 0.11$ (Angulo et al., 2012). The redshift of the MXXL snapshot is consistent with the median redshift of the SDSS Main Galaxy Sample (SDSS MGS; Strauss et al., 2002; Ross et al., 2015). The MXXL simulation covers a comoving volume of $(3000\ h^{-1}\mathrm{Mpc})^3$ and contains 6720^3 particles of mass $6.17 \times 10^9\, h^{-1}\mathrm{M}_\odot$. The cosmological parameter values adopted in the MXXL simulation are the same as those used in the original Millennium simulation (Springel et al., 2005) and are consistent with the WMAP-1 mission results (Spergel

et al., 2003): $\Omega_{\rm m} = 0.25$, $\Omega_\Lambda = 0.75$, $\sigma_8 = 0.9$, $h = 0.73$, and $n_s = 1$. The large volume of the simulation makes it ideal to study BAO.

The construction of the mock galaxy catalogue uses the halo occupation distribution (HOD) method presented by Smith et al. (2017, which is based on Skibba et al. 2006 and Skibba & Sheth 2009). This method uses a set of HODs constrained using clustering measurements from the Sloan Digital Sky Survey (SDSS), for different volume limited samples, defined using r-band absolute magnitude cuts (Zehavi et al., 2011). These HODs are used to populate dark matter haloes in the simulation, which are identified using the SUBFIND algorithm (Springel et al., 2001). We use $M_{\rm 200m}$ as the halo mass definition, which corresponds to the mass enclosed by a sphere in which the average density is 200 times the mean density of the universe. Interpolating between the HODs for different magnitude limits allows each object to be assigned a magnitude, but a modification is made to the functional form of the 5-parameter HOD model to prevent the unphysical crossing of HODs for different luminosity cuts. We denote absolute magnitudes as ${}^{0.1}M_r - 5\log_{10} h$, where the superscript 0.1 indicates that this filter has been k-corrected to redshift 0.1, which is close to the median redshift of the main SDSS sample. The HODs are also evolved with redshift to reproduce the luminosity function measured from the SDSS at low redshifts, and the luminosity function of the GAMA survey at higher redshifts (see Smith et al. for references). Each object is also assigned a ${}^{0.1}(g-r)$ colour, using a parametrisation of the colour-magnitude diagram. Following Smith et al. (2017), the red and blue sequences of the colour-magnitude diagram are parametrised as two Gaussians with a mean and rms that are linear functions of magnitude. A galaxy is randomly chosen to be red or blue, then a colour is drawn from the appropriate Gaussian.

In Smith et al. (2017), the HOD methodology outlined above was used to populate a halo lightcone. Here, instead of using a lightcone, we use the simulation output at $z = 0.11$. The parent galaxy catalogue has a number density of $n_g = 7.5 \times 10^{-3}\ h^3\,{\rm Mpc}^{-3}$, giving 201 million galaxies in the MXXL volume, which corresponds to retaining galaxies brighter than a magnitude cut of ${}^{0.1}M_r - 5\log_{10}h = -20$.

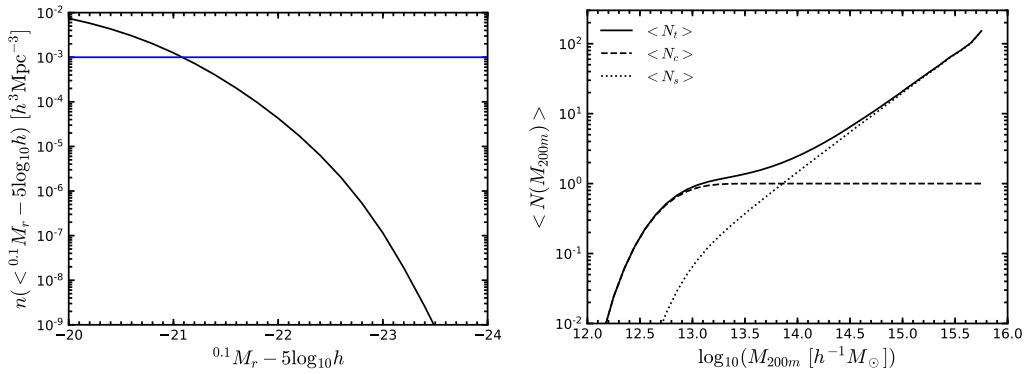

Figure 5.1: *Left panel:* r-band cumulative luminosity function of the parent galaxy catalogue at $z = 0.11$. The horizontal blue line indicates the number density of the full sample, $n = 10^{-3}h^3\,\mathrm{Mpc}^{-3}$, which corresponds to retaining galaxies brighter than a magnitude cut of ${}^{0.1}M_r - 5\log_{10}h = -21.08$. *Right panel:* Halo occupation distribution of the full sample. The occupation functions of all, central and satellite galaxies are shown as solid, dashed and dotted lines, as specified in the legend.

The left panel of Fig. 5.1 shows the cumulative r-band luminosity function of the parent galaxy catalogue. The horizontal blue line shows a cut in number density of $n = 1 \times 10^{-3}\,h^3\,\mathrm{Mpc}^{-3}$. We will refer to this as the "full sample". The HOD of the full sample is shown in the right panel of Fig. 5.1. We can see that the shape of the HOD, by construction, follows the standard functional form proposed by Zheng et al. (2005), where the mean number of central galaxies per halo reaches unity above a threshold halo mass (i.e. every halo above this mass contains a central galaxy) and the occupation of satellite galaxies follows a power-law in massive haloes.

Here we study the clustering of galaxies ranked by environment (density), luminosity and colour. We divide the full sample into four equal parts, i.e., each subsample has the same number density $n_\mathrm{Q} = 2.5 \times 10^{-4}\,h^3\,\mathrm{Mpc}^{-3}$.

Selection of samples

We first select galaxies by luminosity, retaining those which satisfy cuts in magnitude. The vertical lines in the left panel of Fig. 5.2 show the magnitude bins used to define the luminosity quartiles: the Q_1 subsample corresponds to the brightest 25 per cent of galaxies while Q_4 is the subsample with the 25 per cent faintest galaxies.

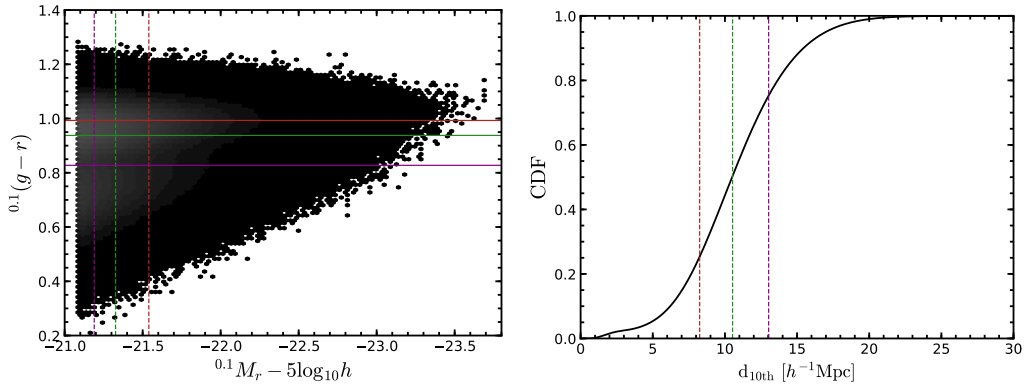

Figure 5.2: Selection cuts applied to the full sample to get subsamples defined by magnitude, colour or density. *Left panel:* Colour-magnitude diagram for the full sample. Lines of different colour show the cuts in magnitude (vertical dashed lines) and colour (horizontal solid lines) applied to divide the sample into either luminosity or colour subsamples. *Right panel:* Cumulative distribution of the distance to the $10^{\rm th}$ nearest neighbour ($d_{\rm 10th}$); vertical dashed lines show the cuts applied to the full sample to define density quartiles.

We next apply the colour cuts listed in Table 5.1 to define the colour subsamples, shown by the horizontal lines in the left panel of Fig. 5.2, where $\rm Q_1$ is the subsample with the 25 per cent reddest galaxies and $\rm Q_4$ contains the 25 per cent bluest galaxies. Finally, to define samples by environment we apply a cut in local density. The local density is estimated using the distance to the $10^{\rm th}$ nearest neighbour, $d_{\rm 10th}$, and the galaxies are ranked by this property. The right panel of Fig. 5.2 shows the cumulative distribution function of $d_{\rm 10th}$ where the vertical dotted lines show the quartiles. The first quartile of the sample ($\rm Q_1$) contains the 25 per cent of galaxies in the densest environments (i.e. those with the smallest values of $d_{\rm 10th}$) and $\rm Q_4$ is the subsample with the 25 per cent of the galaxies in the least-dense environments. $\rm Q_2$ and $\rm Q_3$ are the subsamples in intermediate density regions. The values of $d_{\rm 10th}$ used to define the density samples are listed in Table 5.1.

The left panels of Fig. 5.3 display the real-space power spectrum measured from galaxy samples ranked by magnitude (top), colour (middle) and density (bottom) as listed in Table 5.1. The black points in each panel correspond to the power spectrum of the full galaxy sample, in which we can clearly see the BAO wiggles in Fourier

Table 5.1: The selection cuts applied to define galaxy subsamples in terms of luminosity ($^{0.1}M_r - 5\log_{10}h$), colour ($^{0.1}(g-r)$) or density ($d_{10\mathrm{th}}/\,h^{-1}\mathrm{Mpc}$).

$^{0.1}M_r - 5\log_{10}h$					
	full	Q_1	Q_2	Q_3	Q_4
bright limit	-23.70	-23.70	-21.52	-21.32	-21.18
faint limit	-21.08	-21.53	-21.33	-21.19	-21.08
$^{0.1}(g-r)$					
	full	Q_1	Q_2	Q_3	Q_4
blue limit	0.21	1.00	0.94	0.83	0.21
red limit	1.28	1.28	0.99	0.93	0.82
$d_{10\mathrm{th}}/\,h^{-1}\mathrm{Mpc}$					
	full	Q_1	Q_2	Q_3	Q_4
most dense	0.26	0.26	8.26	10.54	13.04
least dense	33.95	8.25	10.53	13.03	33.95

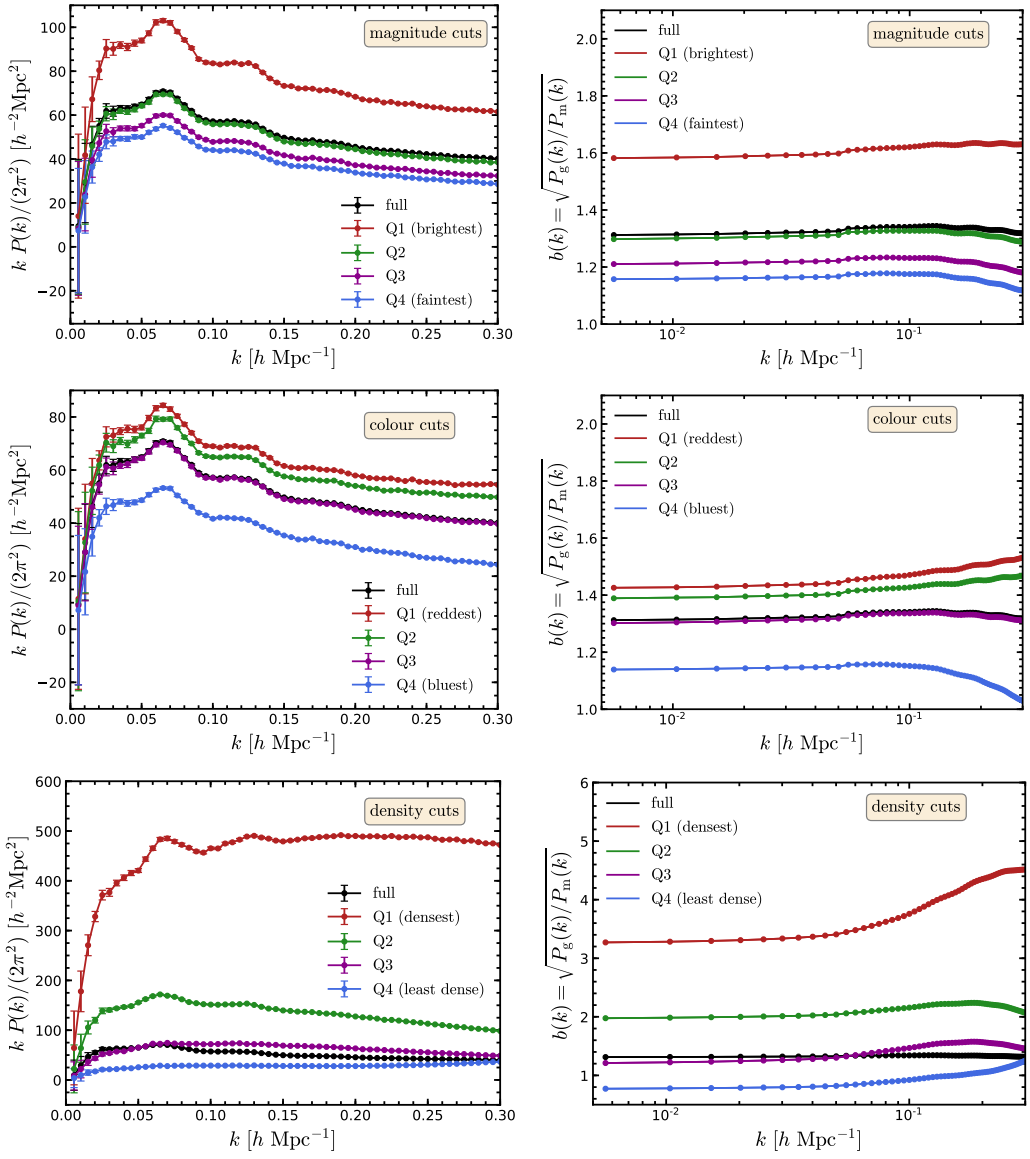

Figure 5.3: The measured power spectrum, $P(k)$ (*left column*), and the galaxy bias, $b(k) = \sqrt{P_\mathrm{g}(k)/P_\mathrm{m}(k)}$ (*right column*), of the four subsamples for each galaxy selection: magnitude (*upper panels*), colour (*middle panels*) and density (*lower panels*). Different colours represent different subsamples as labelled: red (Q1), green (Q2), magenta (Q3) and blue (Q4). In each panel we show the measured power spectrum (*left*) and galaxy bias (*right*) from the full sample (black solid points) for comparison. Note that the y-axis range plotted is different in each panel.

space.

It is evident when comparing measurements across different selections that the Q_1 subsamples (i.e. the brightest, reddest and densest galaxies) shown in Fig. 5.3 are more clustered and therefore show a higher galaxy bias than the overall sample. It is interesting to see that the magnitude subsample Q_2 (green solid line in the top-left panel) and the colour subsample Q_3 (magenta solid line in the middle-left panel) have almost the same clustering amplitude as the full sample. The BAO peaks measured from the densest subsample are *significantly* stronger than those seen in the measurements made from the other samples (note the y-axis range plotted is different in each panel). The BAO peaks are barely visible for the least dense sample (Q_4, bottom-left panel).

The right column of Fig. 5.3 shows the galaxy bias for every subsample. The bias is obtained as

$$b(k) = \sqrt{\frac{P_{\rm g}(k)}{P_{\rm m}(k)}}\,, \tag{5.2.1}$$

where $P_{\rm g}(k)$ is the measured galaxy power spectrum for each subsample (the same as shown in the left panels of Fig. 5.3) and $P_{\rm m}(k)$ is the non-linear dark matter power spectrum at $z = 0.11$. We can see that the galaxy bias inferred for each subsample is constant on large scales ($k \lesssim 0.1\,h\,{\rm Mpc}^{-1}$). The scale dependence becomes evident at higher wavenumbers, with the bias increasing (e.g. for the reddest, densest and brightest subsamples) and decreasing for the bluest and faintest subsamples. The scale dependence of the bias is particularly strong for the subsamples defined by local density.

In Fig. 5.4 we show the two-point correlation function on scales around $r \sim 100\,h^{-1}$Mpc that correspond to the location of the BAO peak. The figure shows the two-point correlation for the full sample of galaxies (black line) as well as for the density-selected quartiles. Similar trends are observed for the magnitude- and colour-selected subsamples, which, for brevity, we do not show. As expected from our power spectrum results, the Q_1 density-subsample displays the strongest clustering, i.e. galaxies in the densest regions are more likely to reside in more massive haloes, which are more biased, and hence we measure a higher clustering amplitude for this subsample. The BAO wiggles are clearer for this sample in the power spectrum

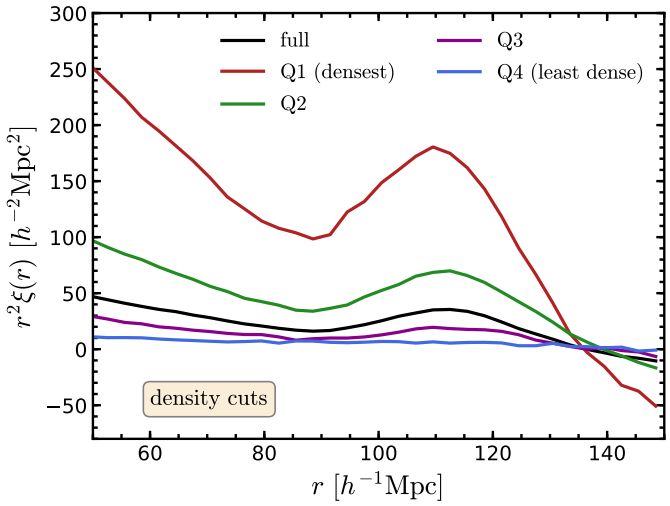

Figure 5.4: The correlation function of the galaxy samples defined by density, plotted as $r^2\xi(r)$, on a linear-linear scale. The black line shows the correlation function measured for the full galaxy sample and the coloured lines show the clustering for the subsample quartiles ranked by density, as labelled.

and the BAO peak is stronger in the correlation function (see bottom-left panel of Fig. 5.3 and Fig. 5.4). We also note that non-linear effects are more evident in the densest sample on small-scales. There is an increase in the power for scales $k > 0.15\,h\,\mathrm{Mpc}^{-1}$, and a steeper slope in the correlation function at $r < 70\,h^{-1}\mathrm{Mpc}$ (Fig. 5.4). We note that the BAO feature is slightly shifted to smaller scales in the highest density subsample, i.e. the position of the peak is moved to higher k values in the power spectrum and to lower r values in the correlation function (as predicted by Neyrinck et al., 2018).

5.2.2 BAO model

Here, we measure the BAO scale in the power spectrum of galaxies. To do this, we follow a similar approach to that presented by Ross et al. (2015, see also Eisenstein et al. 2007a). We start by modelling the power spectrum as the product of a smooth component and the BAO signal. That is, we write the model power spectrum, $P_{\rm fit}(k)$, as

$$P_{\rm fit}(k) = P_{\rm sm}(k)\mathrm{O}_{\rm damp}(k/\alpha)\,, \tag{5.2.2}$$

where $P_{\rm sm}(k)$ is a smooth power spectrum, i.e., without any BAO feature, and $\mathrm{O}_{\rm damp}(k/\alpha)$ represents the damped BAO signal. The damping factor is parametrised in terms of the α dilation parameter that characterises any shift in the position of the BAO peak in the measured power spectrum compared to the model; if $\alpha > 1$ the peak is moved to smaller scales, while $\alpha < 1$ moves the peak to larger scales (Angulo et al., 2008; Anderson et al., 2014; Ross et al., 2015). This template can be used to analyse the galaxy power spectrum in both real and redshift space.

We model the smooth power spectrum component as

$$P_{\rm sm}(k) = B_p^2 P_{\rm nw}(k) + A_1 k + A_2 + \frac{A_3}{k}\,, \tag{5.2.3}$$

where $P_{\rm nw}(k)$ is a smooth "no-wiggle" template obtained using the fitting formula of Eisenstein & Hu (1998), B_p is a large-scale bias parameter, and A_1, A_2 and A_3 are further free parameters. This functional form is similar to that used by Ross et al. (2015), however with fewer (4 instead of 6) free parameters. We find that this function provides a very good description of the non-linear galaxy power spectrum down to $k = 0.3\,h\,\mathrm{Mpc}^{-1}$.

The oscillatory component of the power spectrum is given by,

$$\mathrm{O}_{\rm damp}(k) = 1 + (\mathrm{O}_{\rm lin}(k) - 1)\, e^{-\frac{1}{2}k^2\Sigma_{\rm nl}^2}\,, \tag{5.2.4}$$

where $\Sigma_{\rm nl}$ is a damping parameter and $\mathrm{O}_{\rm lin}(k)$ is the ratio between the linear power spectrum and the smooth no-wiggle power spectrum, i.e. $P_{\rm lin}(k)/P_{\rm nw}(k)$.

We estimate the analytical power spectrum with the NBODYKIT toolkit (Hand et al., 2018), using the CLASS transfer function for the linear power spectrum (Blas et al., 2011; Lesgourgues, 2011) and the analytical approximation of Eisenstein & Hu (1998) for the no-wiggle power spectrum in Eqs. (5.2.3) and (5.2.4). We also use NBODYKIT to measure the power spectrum from the simulation outputs for wavenumbers between $0.0025 < k/[\,h\,\mathrm{Mpc}^{-1}] < 0.3$ using bins with width $\Delta k = 0.005\,h\,\mathrm{Mpc}^{-1}$.

To measure the position of the BAO peak, we fit the measured real-space power spectrum of our subsamples to the model given by Eq. (5.2.2) and extract information about the dilation parameter α. To obtain the best-fitting α value, we use

Bayesian statistics and maximise the likelihood, $\mathcal{L} \propto \exp(-\chi^2/2)$ by fitting the measurements from the galaxy samples on scales with $k < 0.3\,h\,\mathrm{Mpc}^{-1}$. We estimate errors on the measurements using 8 jackknife partitions along each coordinate of the simulation box (Norberg et al., 2009). To find the best-fitting α value and its confidence levels we use the Monte Carlo Markov Chain technique implemented in the EMCEE python package (Foreman-Mackey et al., 2013).

For the density-selected samples, the measured power spectrum cannot be adequately described by Eq. (5.2.3). We reduce the scale dependence of the measured power spectrum by defining a k-space window flattening function, $B_{k-\mathrm{window}}(k)$, which is the ratio between the power spectrum measured for one of the density quartile samples, divided by the power spectrum of the full sample. A similar approach was employed in Angulo et al. (2008). In this exercise, the two power spectra in question are first rebinned into broader k-bins ($\Delta k = 0.1\,h\,\mathrm{Mpc}^{-1}$) before taking the ratio. The measured power spectrum is then divided by the flattening function, $B_{k-\mathrm{window}}(k)$, before being fitted. The window width is chosen to be larger than the scale of the BAO oscillations, and thus should be largely insensitive to the presence of the BAO signal. We have tested that this procedure does not introduce biases in α or in its uncertainties by testing that the luminosity- and colour-selected quartiles return the same α best fit values when fitting directly the sub-sample power spectrum or the one normalised using the flattening function we just discussed. Since, $B_{k-\mathrm{window}}(k)$ is only used for the measured power spectrum of the density-selected samples, the fitting template Eq. (5.2.3) remains unchanged.

5.3 Galaxy clustering

5.3.1 Measuring BAO positions

In the left panel of Fig. 5.5 we show the power spectrum measured from the full galaxy sample compared to the best-fitting model. One can see that the model described by Eqs. (5.2.2)-(5.2.4) provides a good match to the measurements from the mock catalogue. The right panel of Fig. 5.5 displays the measured and best-fitting power spectra divided by the smooth component, $P_{\mathrm{nw}}(k)$, of the best-fitting

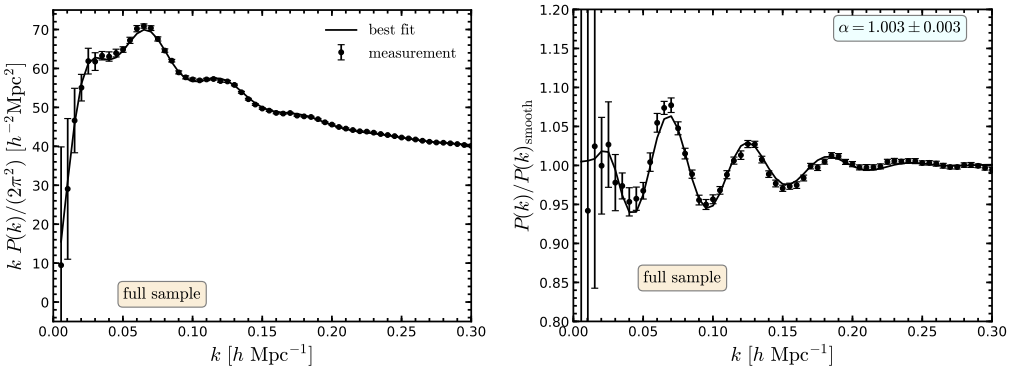

Figure 5.5: *Left panel:* The measured power spectrum, $P(k)$, (points with error-bars) and the best-fitting model (solid curve) for the full galaxy sample. *Right panel:* The same as the left panel but now the power spectrum is plotted divided by the smooth (no-wiggle) component of the best-fitting model. This panel highlights the BAO signature, which corresponds to the oscillations of the curve. The upper label in the right panel indicates how accurately we can measure the BAO scale, as parametrised in terms of the α dilation parameters (see main text for details).

model. We recover an unbiased estimate of the BAO position, with $\alpha = 1.003 \pm 0.003$ (these figures correspond to the maximum likelihood value and 68 per cent confidence interval), that is consistent at the 1σ-level with the expected value of $\alpha = 1$. Small differences in the value of α from unity are not necessarily worrying since they could indicate a small mismatch between the formulation of the power spectrum used to imprint the BAO feature onto the initial conditions of the simulation and the BAO templates used to extract this signature. Recall that all cosmological parameters are fixed for $P_{\rm lin}(k)$ and $P_{\rm nw}(k)$ in Eqs. (5.2.2)-(5.2.4). The best-fitting model is characterised by a reduced chi-square value, $\chi^2/\mathrm{dof} = 1.15$, which indicates that our model gives a good description of the galaxy power spectrum. The quality of the fit is most clearly illustrated in the right panel of Fig. 5.5, which also clearly highlights the BAO wiggles. In particular, we can see up to four maxima located at $k/(\,h\,\mathrm{Mpc}^{-1}) \approx 0.065$, 0.13, 0.185 and 0.24. For the rest of the Chapter, we will compare the BAO position measured in the various galaxy subsamples against this reference value.

In Fig. 5.6 we show the results of fitting the BAO template, Eq. (5.2.2), to

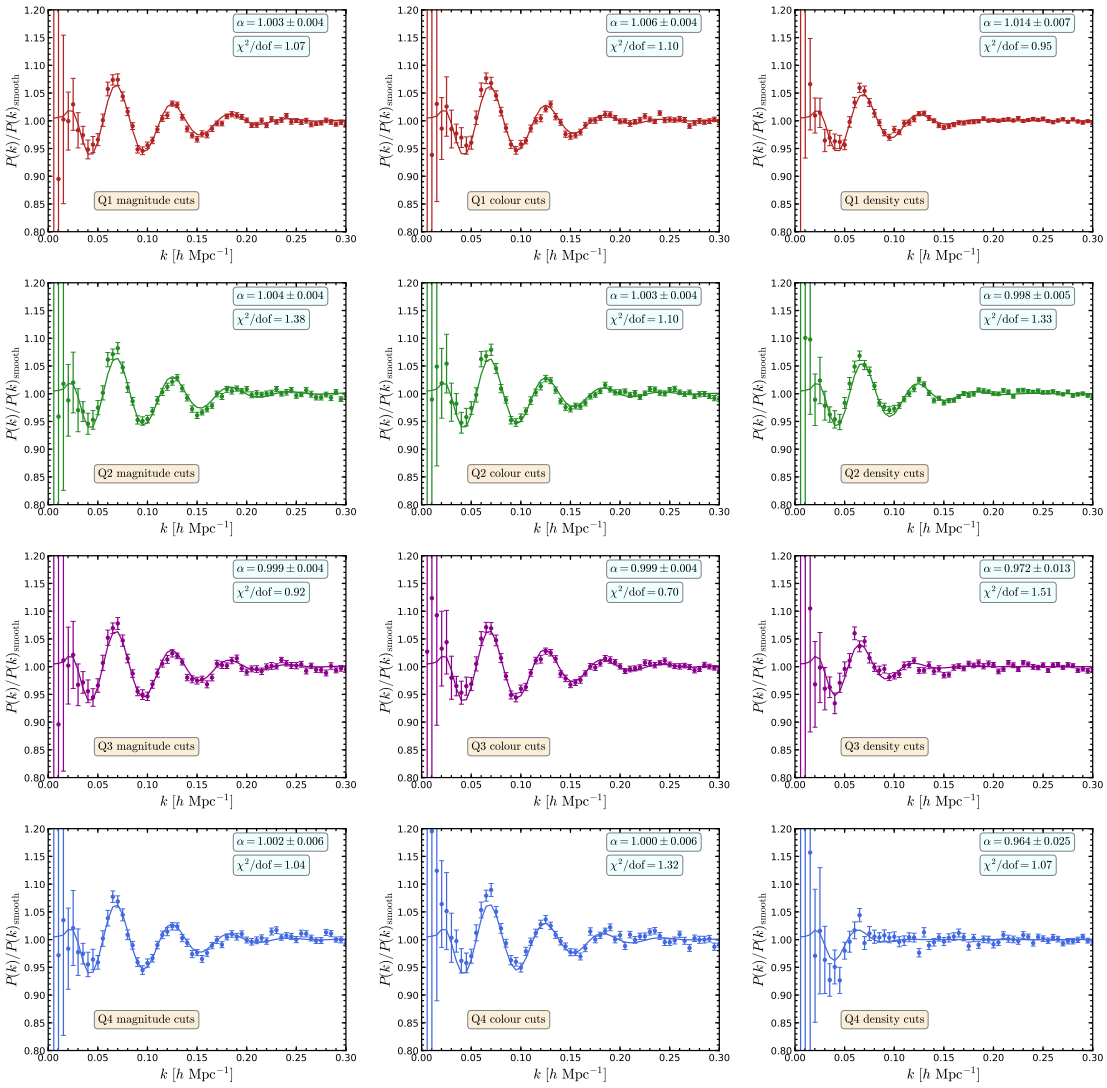

Figure 5.6: The measured power spectrum, $P(k)$, (points with error bars) and the best-fitting model (solid curves) divided by the smooth (no-wiggle) power spectrum for magnitude (*left column*), colour (*middle column*) and density (*right column*) cuts. Each row shows a different subsample as specified in the bottom-left corner of each panel. The strength of the BAO feature for each panel can be inferred from the uncertainties associated with the determination of the α dilation parameter (the maximum likelihood value and 68% confidence interval of α are given in the top-right corner of each panel).

the various luminosity-, colour- and density-selected galaxy subsamples described in Section 5.2.1. To better highlight the quality of the fits and the changes in the BAO signature between the various subsamples, we show the power spectrum divided by the smooth component of the best-fitting model (see Eq. 5.2.3).

We find that all the magnitude- and colour-selected subsamples show the same BAO features, with little variation between the different subsamples. Considering the best-fitting α parameters, we find that most values are in good agreement, given the quoted interval, with the value measured for the full sample of $\alpha = 1.003 \pm 0.003$. There is potentially a very weak trend, such that fainter or bluer galaxies have slightly lower α values than their brighter or redder counterparts, but this trend is very small and we would need much larger galaxy samples to be able to confirm it. The only significant difference between the various quartiles is that the BAO signature is weaker for the Q4 samples, i.e. the faintest or bluest galaxies. This can be seen in the actual power spectrum (the fourth BAO wiggle is weaker for Q4 than in the other subsamples) and is best quantified by the uncertainty associated with the α measurement: the Q4 sample has an error on α of 0.6% versus the errors of 0.4% associated with the other quartiles. We also find that despite having four times fewer objects than the full sample, the α uncertainty ranges estimated for the Q1 to Q3 quartiles are only slightly larger than for the full sample (0.4% versus 0.3%). This means that the various quartiles are highly correlated and that increasing the sample size by a factor of four does not reduce the errors by half, as expected in the case of independently and Gaussianly distributed measurements.

The right column of Fig. 5.6 shows how the BAO signal varies for the four density-selected galaxy subsamples. Compared to the other two selection methods just discussed, we find that the density selection leads to much larger differences in the BAO signature compared to the full galaxy sample as well as between the different density quartiles. Firstly, we see that fewer BAO wiggles can be distinguished, for example the lowest density sample (Q_4) has one weak maximum, the Q_1 and Q_3 samples have two maxima, and Q_2 has three maxima. This is quite a striking difference, since in the full sample we clearly find four maxima (see right-hand panel in Fig. 5.5). The smaller number of BAO wiggles for the highest density

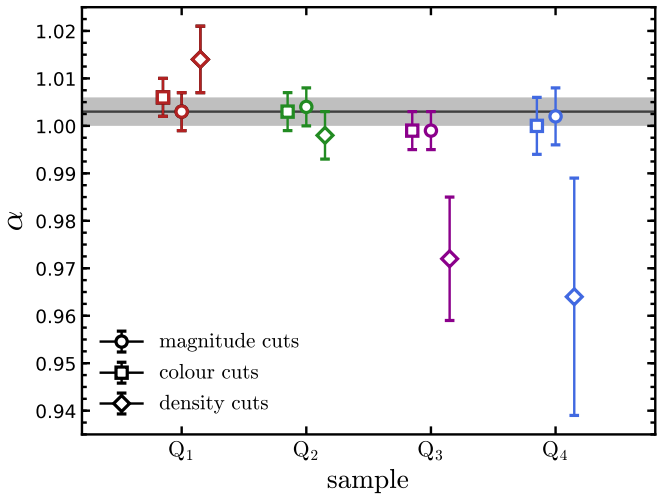

Figure 5.7: The maximum likelihood value and 68% confidence interval associated with the determination of the BAO dilation parameter, α. The horizontal solid line and the associated shaded region show the result for the full galaxy sample. The points with error bars show the results for the quartiles of the galaxy populations ranked according to: luminosity (circles), colour (squares) and density (diamonds). The Q1 subsamples corresponds to the brightest / reddest / densest galaxies, while the Q4 subsamples correspond to the faintest / bluest / least dense galaxies.

quartile, Q_1, could be due to these galaxies residing in higher density regions where structure formation proceeds more rapidly and thus where non-linear effects, which dampen the BAO feature, are more pronounced. The result that the lowest density quartile, Q_4, has only one BAO wiggle is more surprising, since, structure formation is somewhat delayed in lower density regions and thus more of the initial BAO signature should be preserved. However, we find that this is not the case. This could be due to a combination of how galaxies are placed in haloes through the HOD scheme and the density definition we are using. We will explore in more detail the HOD of each subsample in the following subsection.

The degradation in the BAO signal for the density-selected galaxy subsamples is best highlighted by comparing the uncertainties in determining α using the various quartiles. We find that the error is lowest for Q_2 (0.5%) and only slightly higher for Q_1 (0.7%), and increases dramatically for the lower density quartiles: 1.3% and 2.5% respectively for Q_3 and Q_4. Thus galaxies in intermediate-density environments (i.e.

the Q_2 quartile) are a better target to measure the BAO feature than those in the densest regions or least dense regions. Furthermore, the uncertainty in determining α in the Q_2 quartile is slightly larger than those associated with the luminosity- and colour-selected samples, indicating that selecting a galaxy subsample based on local density does *not* lead to a more precise BAO measurement than using colour or luminosity. In particular, the Q_1 and Q_2 density-quartiles have larger bias than the other luminosity- and colour-selected subsamples (see right column of Fig. 5.3), implying that a sample with larger bias does not necessarily lead to a more precise determination of the BAO scale.

Another important result for the density-selected quartiles is that the α parameter systematically decreases with density. This is best illustrated in Fig. 5.7, which shows the maximum likelihood values and the 68% confidence intervals on the determination of α for the various galaxy subsamples studied here. For the luminosity- and colour-selected quartiles the α value is approximately the same and in good agreement with the measurement obtained using the full galaxy sample. In contrast, the density-selected quartiles show a statistically significant trend that is in agreement with our expectations (see e.g. Sherwin & Zaldarriaga, 2012; Neyrinck et al., 2018): the BAO peak is shifted to smaller scales (i.e. larger α) for the densest quartile and to larger scales for the two least dense quartiles.

5.3.2 Halo occupation distribution

To further investigate and understand the differences between the clustering results for different galaxy selections, we explore the halo occupation distribution in each subsample in the left column of Fig. 5.8. In each case, we plot the contribution of central galaxies (dashed lines), satellite galaxies (dotted lines) and the total mean number of galaxies per halo (solid lines), which is the sum of centrals and satellites. The HOD of the full sample is displayed by the black curves, while the contribution of different subsamples is shown by the red (Q_1), green (Q_2), magenta (Q_3) and blue (Q_4) curves in each panel.

The HOD of magnitude-selected galaxies is shown in the top left panel of Fig. 5.8. We note that the HOD of the brightest galaxy quartile, Q_1, is composed of galaxies

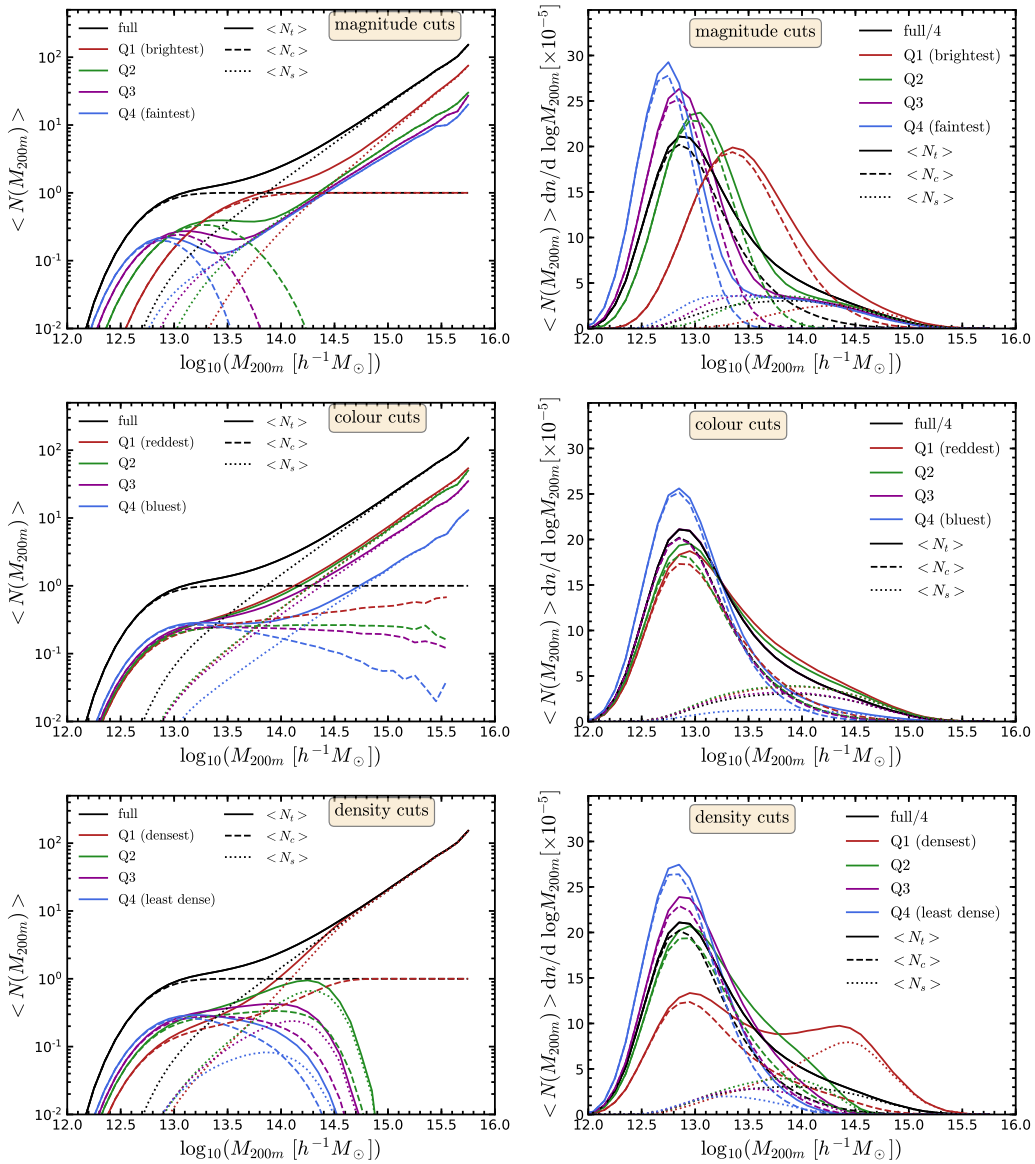

Figure 5.8: *Left column:* Halo occupation distribution for the galaxy quartiles, Q_i, selected according to: magnitude (*top panel*), colour (*middle panel*) and density (*bottom panel*). In each panel we show the HOD of the full sample (black lines) for comparison. The occupation of total, central and satellite galaxies are shown as solid, dashed and dotted lines, respectively, as specified in the legend. *Right column:* The number density of central (dashed lines), satellite (dotted lines) and total (solid lines) galaxies for each selection and subsample obtained by multiplying the HOD by the differential halo mass function of the MXXL snapshot at $z = 0.11$, in the case of the full sample we have divided the distribution by four for better visualisation. Different colours represent different subsamples: red lines (Q1), green lines (Q2), magenta lines (Q3) and blue lines (Q4).

that predominantly populate the most massive haloes, i.e., Q_1 contains all the central galaxies of haloes with $M_{200m} > 10^{14}\,h^{-1}M_\odot$ and also the majority of the satellites found in these haloes. The fainter samples are composed of central galaxies in lower mass haloes and of satellite galaxies in high mass haloes. In particular, the mean number of satellites as a function of halo mass is roughly the same in the Q_2, Q_3 and Q_4 quartiles, showing only a weak dependence on galaxy luminosity.

In the case of the HOD of galaxies ranked by colour (middle-left panel of Fig. 5.8), we find a non-standard form for the mean number of central galaxies. For low halo masses, $M_{200m} < 10^{13.4}\,h^{-1}M_\odot$, there is a plateau at $\langle N_c \rangle \sim 0.25$ for all quartiles. Interestingly, $\langle N_c \rangle$ stays constant with increasing halo mass for the Q_2 sample; for the Q_3 and Q_4 samples, the mean fraction of haloes with centrals declines for $M_{200m} > 10^{13.5}\,h^{-1}M_\odot$, and increases with halo mass for Q_1. For satellites, we find similar $\langle N_s \rangle$ values for the Q_1, Q_2 and Q_3 quartiles, with only a weak trend with galaxy colour. In contrast, the bluest quartile contains a significantly lower mean satellite number for a given host halo mass. We note that the HOD of the Q_2 quartile has the same shape as the full sample but with mean values that are four times smaller; this might explain why this the BAO features measured for this sample best resemble those of the full galaxy population. In contrast, the Q_4 quartile preferentially contains galaxies in low mass haloes (see middle-right panel of Fig. 5.8), and has the weakest BAO signature.

The bottom-left panel of Fig. 5.8 shows the HOD of density-selected galaxy quartiles. We see that the densest subsample (Q_1) contains almost *all* the satellite galaxies, as well as all the central galaxies that live in haloes more massive than $\log_{10}(M_{200m}/\,h^{-1}M_\odot) = 14.6$. Thus, a large fraction of Q_1 galaxies are in clusters and other highly overdense regions, whose gravity pulls in the surrounding matter, which explains why the BAO peak is shifted towards smaller scales for this sample. We see that the Q_2 sample contains no galaxies (centrals and satellites) which reside in haloes of mass $\log_{10}(M_{200m}/\,h^{-1}M_\odot) > 14.9$, and the distribution peaks at a total mean occupation number of almost one at $\log_{10}(M_{200m}/\,h^{-1}M_\odot) = 14.4$. In this subsample, galaxies are selected from intermediate-density regions, explaining the lack of galaxies in clusters. The Q_3 and Q_4 subsamples contain galaxies that populate

low-mass haloes ($\log_{10}(M_{200\mathrm{m}}/\,h^{-1}\mathrm{M}_{\odot}) \approx 12.5-13.5$) and are dominated by central galaxies. In these cases we can see that the fraction of satellite galaxies is small. These low-mass haloes represent small density peaks in the dark matter distribution, and typically live in regions like filaments and voids; these samples display a weak BAO signal, and the position of the peak is shifted to larger scales (we can see from the lower-left panel of Fig. 5.3 and Fig. 5.4 that the BAO signal in the Q_4 subsample is hard to discern).

The right panels of Fig. 5.8 show the number density of galaxies (in units of $10^{-5}h^3\mathrm{Mpc}^{-3}$) as a function of their host halo mass for the three selections: magnitude (top panel), colour (middle panel) and density (bottom panel), in all panels we show the distribution of galaxies for the full sample divided by four for comparison. The results presented in these panels confirm our findings from the HOD of the different selections. As an example, in magnitude-selected galaxies we can observe a trend in their distribution (top panel of right column in Fig. 5.8), i.e., we can find more of the faintest (brightest) galaxies in low-(high-)mass haloes. In the case of colour-selected galaxies, the distribution of galaxies remains almost unchanged for the Q_1, Q_2 and Q_3 samples; the bluest sample (Q_4) predominantly populate haloes with mass $\log_{10}(M_{200\mathrm{m}}/\,h^{-1}\mathrm{M}_{\odot}) \approx 12.7$. The bottom-right panel of Fig. 5.8 shows the distribution of galaxies ranked by environment, we can see that galaxies from low-density to intermediate-density regions reside in low-mass haloes, while galaxies in the densest environments are found in high-mass haloes.

5.4 Summary

In this Chapter, we have studied the clustering and the position of the BAO feature for subsamples of mock galaxies ranked by density (defined by the distance to 10^{th} nearest neighbour), luminosity (r-band magnitude) and ${}^{0.1}(g-r)$ colour.

We have used a magnitude-limited, ${}^{0.1}M_r - 5\log_{10}h < -21.08$, mock catalogue at redshift $z = 0.11$, obtained from the Millennium-XXL N-body simulation (Smith et al., 2017). This corresponds to a galaxy number density of $n = 1\times10^{-3}\,h^3\,\mathrm{Mpc}^{-3}$ that, given the large volume of the simulation, includes a total of 27 million galaxies.

We split the full sample into four subsamples (Q_1, Q_2, Q_3 and Q_4), defined in different ways (see below) with a corresponding number density of one quarter of the full sample ($n_Q = 2.5 \times 10^{-4}\, h^3\,\mathrm{Mpc}^{-3}$) by applying cuts according to the galaxy property of interest (see Sec. 5.2.1). The subsamples are defined as follows, 1) magnitude: from brightest to faintest galaxies, 2) colour: from reddest to bluest galaxies and 3) density: from high- to low-density regions. We confirmed that the galaxy bias of each subsample is constant on linear scales, $k \lesssim 0.1\, h\,\mathrm{Mpc}^{-1}$. We have measured the power spectrum of each subsample and fit it to an analytical BAO template to extract the position of the BAO peak through the dilation parameter, α (see Eq. 5.2.2).

We have found that the best-fitting value of α for the full sample is $\alpha = 1.003 \pm 0.003$ and in each subsample the best sample to extract the BAO peak position is, 1) magnitude: Q_1 with $\alpha = 1.003 \pm 0.004$, 2) colour: Q_2 with $\alpha = 1.003 \pm 0.004$ and 3) density: Q_2 with $\alpha = 0.998 \pm 0.005$. In general, all measurements for the luminosity- and colour-selected galaxy subsamples are in good agreement with the reference value of the full sample. However, for density-selected galaxies, the Q_1, Q_3 and Q_4 quartiles recover poorly the position of the peak and are characterised by large uncertainties in the recovered BAO scale.

We have studied the HOD of each subsample to understand what are the host haloes corresponding to various galaxy selections and how this affects the BAO signal measurement. The luminosity- and colour-selected samples have broadly similar HODs, with the most important differences being: i) the brightest quartile consists of mostly galaxies in the most massive haloes, and ii) the bluest quartile contains few galaxies in high mass haloes, with most objects residing in lower mass hosts. The density-selected quartiles show the largest difference in HOD distributions: the densest quartile contains all the central and satellite galaxies of high-mass haloes, while the lowest density quartile consists of galaxies which are predominantly in low-mass haloes.

Our main results can be summarised as follows,

- The magnitude- and colour-selected samples have unbiased BAO signatures, i.e. the α dilation parameter is consistent with that of the full galaxy popu-

lation, and the uncertainties with which the BAO peak can be measured are roughly the same for all the subsamples. The only exceptions are the faintest or the bluest quartiles, which have a $\sim$ 50 per cent times larger error on α than the other subsamples. Note that for an equal number density of tracers there is a small increase in the precision of the BAO measurement if we were to select only the reddest galaxies, but the effect is minor.

- The density selected samples show several interesting effects. Firstly, the recovery of α is biased between the different quartiles: densest galaxies have $\alpha > 1$, while the lowest density ones have $\alpha < 1$. Secondly, the α uncertainties are lowest for the Q_1 and Q_2 quartiles, while the Q_3 and Q_4 samples provide much poorer BAO constraints.

- Selecting galaxies by density does not improve the BAO measurements compared to a similar number density sample selected by either magnitude or colour.

- However, selecting galaxies by density shows the systematic shift in the BAO position expected for galaxies in overdense and underdense regions, as discussed in Neyrinck et al. (2018). High density peaks lead to a contraction of the peak to smaller radii (i.e. larger α), while low density region show an expansion of the BAO feature to larger radii (i.e. smaller α).

We have found that selecting galaxies by either luminosity or colour does not introduce any systematic biases in the BAO signal. Such effects may have been expected since galaxies show both a luminosity and colour segregation depending on their host halo mass, with brighter or redder galaxies preferentially populating the more massive haloes. The most massive haloes are mainly found in higher density regions, and thus potentially could be characterised by a contraction of the BAO peak at their position. If such a contraction exist, its size would be below the current uncertainties of this study, in which we have determined the BAO dilation parameter, α, with a precision $\lesssim 0.4\%$.

Chapter 6

Building a digital twin of a luminous red galaxy spectroscopic survey: galaxy properties and clustering covariance

6.1 Introduction

Luminous red galaxies (LRGs) have played an important role in the study of the large-scale structure of the Universe. As expected from their bright intrinsic luminosity and large stellar masses, LRGs display a strong clustering signal that make them an ideal tracer of the large-scale structure of the Universe (Zehavi et al., 2005). LRGs were used to extract the scale of the baryon acoustic oscillations (BAO) in the local large-scale structure from the Sloan Digital Sky Survey (SDSS) redshift-space correlation function (Eisenstein et al., 2005). LRGs have also been used to study the impact of redshift-space distortions (RSDs) on their small and large scale clustering (see e.g. Zehavi et al., 2005; Cabre & Gaztanaga, 2009a,b; Wake et al., 2008; Crocce et al., 2011; Samushia et al., 2012). Additionally, the large-scale clustering of LRGs has also been used to constrain the cosmological parameters (Eisenstein et al., 2005; Tegmark et al., 2006; Sánchez et al., 2009; Tröster et al., 2020), and to test modified gravity models (see e.g., Barreira et al., 2016; Hernández-Aguayo et al., 2019).

Our aim here is to provide a qualitative study of the properties and clustering of LRGs which meet the selection requirements of a real survey such as DESI (see Sec. 1.4 for a brief description of DESI). We select DESI-like LRGs from the output of the semi-analytic model (SAM) of galaxy formation GALFORM (Cole et al., 2000) run on the Planck-Millennium N-body simulation (Baugh et al., 2019), and provide estimates of the large-scale galaxy clustering using the GLAM code, which allows us to generate a substantial number of large galaxy mock catalogues (Klypin & Prada, 2018). This hybrid approach takes the SAM calculations made using a high-resolution, moderate volume N-body simulation and uses the results to populate a large number ($\mathcal{O}(10^3)$) of larger volume low-resolution simulations run with GLAM. This allows us to make predictions for the large-scale clustering of LRGs on scales, such as the BAO scale, that were inaccessible in the simulation used to run the SAM. Furthermore, by being able to generate a large number of independent realisations of the density field at relatively low computational cost, we can estimate the covariance on two-point statistics of the large-scale structure.

The use of SAMs to study the properties and clustering of LRGs is not new. Almeida et al. (2007, 2008) presented predictions for the abundance, structural and photometric properties of LRGs using two earlier versions of GALFORM (Baugh et al., 2005; Bower et al., 2006). The authors found that their predictions were in good agreement with different observations from the SDSS (Bernardi et al., 2003, 2005; Wake et al., 2006). More recently, Stoppacher et al. (2019) used the GALACTICUS SAM (Benson, 2012) run on the MultiDark Planck 2 simulation (Klypin et al., 2016) to study the galaxy-halo connection and clustering of the BOSS-CMASS DR12 sample (Alam et al., 2015), finding good agreement between predictions and observations.

Recently, Zhou et al. (2020) presented small-scale ($r \lesssim 20\,h^{-1}$Mpc) clustering measurements of DESI-like LRGs selected from the DESI Legacy Imaging Surveys[1] (Dey et al., 2019) and fitted their results using the halo occupation distribution (HOD) framework. Since spectroscopic redshifts are not yet available for these tar-

[1] http://www.legacysurvey.org

gets, these authors estimated photometric redshifts (photo-z) using the Dark Energy Camera Legacy Survey (DECaLS) imaging. There are a number of differences between the work carried out by Zhou et al. (2020) and ours: first, we are interested in providing a study of the impact of the DESI-LRG target selection on galaxy properties and the galaxy-halo connection using a physical model of galaxy formation, GALFORM; and second, we focus on the large-scale galaxy clustering and in the generation of a large number of mock catalogues to provide an accurate estimate of the covariance of the clustering measurements. Both of these objectives are beyond the reach of the original simulation used to run the SAM and mark a key advantage of our hybrid approach.

In order to extract the cosmological information from our GLAM mock catalogues for the DESI LRG tracers, it is necessary to meet the requirements of the expected error budget for DESI. Hence, it is imperative to construct covariance matrices for our clustering measurements (see e.g. Baumgarten & Chuang, 2018; Blot et al., 2019; Colavincenzo et al., 2019; Lippich et al., 2019, and references therein). Here, we make predictions of the linear-growth rate through a linear theory description of RSDs (Kaiser, 1987; Hamilton, 1992), and an isotropic analysis of the BAO scale (see e.g., Anderson et al., 2014) in configuration and Fourier space using the covariance matrices constructed from our GLAM catalogues.

The outline of the Chapter is as follows. In Section 6.2 we present the simulations used in our analysis. Section 6.3 describes the selection of DESI-like LRGs from GALFORM. In Section 6.4 we provide a detailed study of the galaxy-halo connection of DESI-like LRGs. Our results for the galaxy clustering and covariance errors are presented in Section 6.5. Finally, in Section 6.6 we give the summary of our results.

6.2 Simulations and Galaxy formation in semi-analytical models

Here we introduce the Planck Millennium N-body simulation and the galaxy formation model (Sec. 6.2.1). The GLAM simulations are described in Section 6.2.2. In Section 6.2.3 we show the halo mass function and halo clustering of our simulations.

6.2.1 Galaxy formation in the Planck Millennium simulation

The Planck Millennium N-body simulation (hereafter the PMILL simulation; Baugh et al., 2019) follows the evolution of 5040^3 dark matter particles in a cosmological volume of $542.16^3\,h^{-3}\mathrm{Mpc}^3$ ($800^3\mathrm{Mpc}^3$). The simulation was run using a reduced memory version of the GADGET-2 N-body code (Springel, 2005), employing the cosmological parameters corresponding to the 2014 results from the Planck collaboration (Ade et al., 2014):

$$\{\Omega_\mathrm{b}, \Omega_\mathrm{m}, h, n_s, \sigma_8\} = \{0.04825, 0.307, 0.6777, 0.9611, 0.8288\}.$$

The large number of dark matter particles used in the PMILL simulation gives a mass resolution of $1.06 \times 10^8\,h^{-1}\mathrm{M}_\odot$ and a halo mass limit, corresponding to 20 particles, of $2.12 \times 10^9\,h^{-1}\mathrm{M}_\odot$. The simulation starts at $z = 127$, with initial conditions generated using second-order Lagrangian perturbation theory (Jenkins, 2010) and the PANPHASIA code (Jenkins, 2013). The halo properties and selected particle information are saved in 271 snapshots. Haloes and sub-haloes were identified with SUBFIND (Springel et al., 2001). SUBFIND first identifies haloes using a friend-of-friends (FOF) algorithm with a linking length of $b = 0.2$ times the mean interparticle separation. Then, these FOF groups (main or distinct haloes) are split into subhaloes of bound particles. SUBFIND uses several definitions of halo mass; we use M_{200m} which is the mass enclosed within a radius where the average overdensity is 200 times the mean density of the Universe. The subhalo mass is just the sum of the mass of the particles that are gravitationally bound to that subhalo. The haloes and subhaloes are used to build halo merger trees using the DHALO code (Jiang et al., 2014).

Here, we use the GALFORM semi-analytical model of galaxy formation (Cole et al., 2000; Baugh, 2006; Gonzalez-Perez et al., 2014; Lacey et al., 2016) to populate the dark matter haloes in the PMILL simulation with galaxies. We use the recalibration of the Gonzalez-Perez et al. (2014) model presented by Baugh et al. (2019) to identify LRGs and study their clustering. In order to match local observations of galaxies, just two of the parameters describing the physical processes mod-

elled in GALFORM were changed slightly by Baugh et al., from the values adopted by Gonzalez-Perez et al., to take into account the change in cosmology and mass resolution in the PMILL compared with the original N-body simulation used by Gonzalez-Perez et al., and an improvement to the treatment of galaxy mergers (see Baugh et al. 2019 for further details of these changes; we note that Gonzalez-Perez et al. 2018 used an updated version of their model, which also included the new galaxy merger scheme first implemented by Campbell et al. 2015 and explained in full by Simha & Cole 2017).

6.2.2 GLAM simulations

GLAM is a new N-body Parallel Particle-Mesh (PM) code developed for the massive production of large volume mock galaxy catalogues (Klypin & Prada, 2018). GLAM first generates the density field at an early epoch, including peculiar velocities, for a particular cosmological model and initial conditions. The code uses a regularly spaced three-dimensional mesh of size $N_{\rm g}^3$ that covers the cubic domain L^3 of a simulation box using $N_{\rm p}^3$ particles. The size of a cell, $\Delta x = L/N_{\rm g}$, and the mass of each particle, $m_{\rm p}$, define the force and mass resolutions, respectively (see Appendix A of Klypin & Prada, 2018, for details).

We generate 1000 GLAM simulations using the same cosmology and linear perturbation theory power spectrum as used in the PMILL simulation. Because our goal is to study the clustering of LRGs, the GLAM simulations follow the evolution of 2000^3 particles of mass $1.06 \times 10^{10}\, h^{-1}{\rm M}_{\odot}$ in a cubic box of size $1\, h^{-1}$Gpc with $N_{\rm s} = 136$ time-steps, and mesh of $N_{\rm g} = 4000$. This numerical set-up yields a spatial resolution of $\Delta x = 0.25\, h^{-1}$Mpc. The initial conditions were generated using the Zeldovich approximation starting at $z_{\rm ini} = 100$.

Haloes in GLAM are identified with the bound density maximum (BDM) halo finder (Klypin & Holtzman, 1997). Only distinct haloes are saved in our catalogues. In BDM the virial mass, $M_{\rm vir}$, is adopted as the definition of halo mass. The virial mass of a halo corresponds to the mass enclosed within a spherical overdensity of radius $R_{\rm vir}$, such that the mean overdensity within this radius is $\Delta_{\rm vir} \approx 330$ times the mean matter density of the Universe at the present time. The virial overdensity,

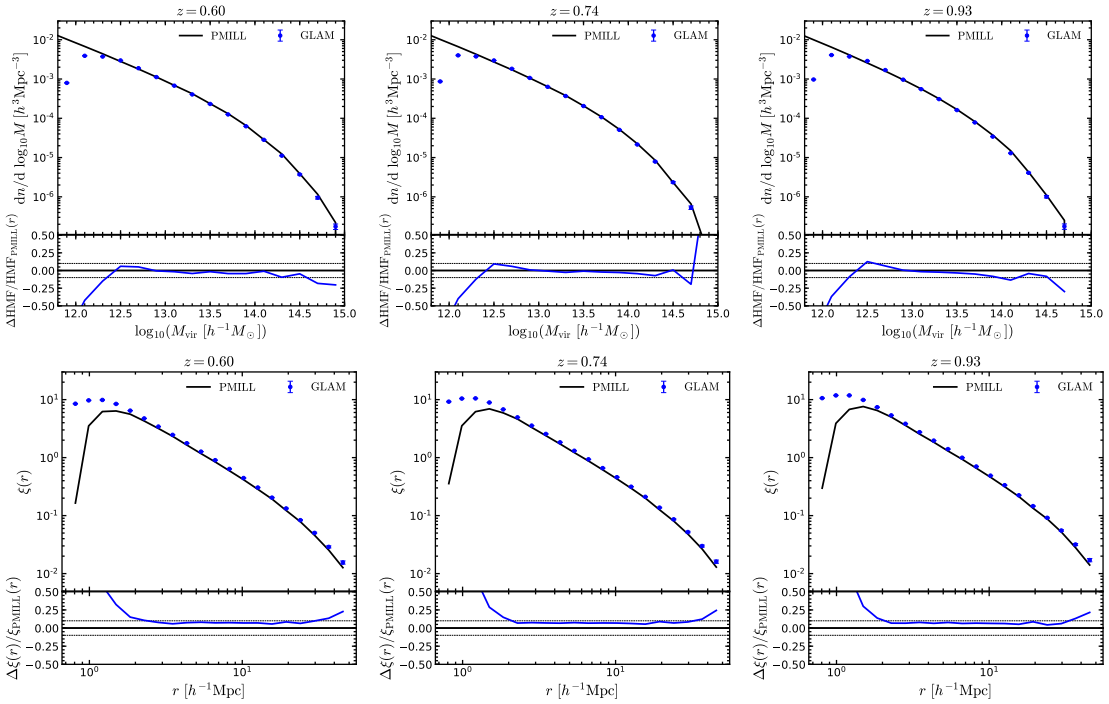

Figure 6.1: *Top row*: differential halo mass function in the PMILL (black solid lines) and the mean of 1000 GLAM simulations (blue dots) as a function of $M_{\rm vir}$. *Bottom row*: Real-space halo two-point correlation function measured from the PMILL (black solid lines) and the mean of 1000 GLAM simulations (blue dots) for haloes with mass $M_{\rm vir} > 10^{12.5}\,h^{-1}{\rm M}_{\odot}$. We show measurements at $z = 0.60$ (*left column*), $z = 0.74$ (*middle column*) and $z = 0.93$ (*right column*). Errobars correspond to the 1σ standard deviation over 1000 GLAM realisations. The lower subpanels show the relative difference between the GLAM measurements and that from the PMILL. The horizontal dashed indicates a 10 per cent difference.

$\Delta_{\rm vir}(z)$, is computed using the approximation of Bryan & Norman (1998). Only halo catalogues are saved in 21 snapshots between $0 < z < 1.2$ for each realisation.

6.2.3 Halo mass function and halo clustering

To check the performance of our GLAM simulations we compare the halo mass function and the halo two-point correlation function measured from them with those obtained from the PMILL simulation. Since we are interested in LRGs at $z \geq 0.6$ we use halo catalogues corresponding to snapshots at $z = 0.6$, 0.74 and 0.93, where

$z = 0.74$ corresponds to the median redshift of the expected $n(z)$ distribution of LRGs in DESI (DESI Collaboration et al., 2016; Zhou et al., 2020). In a future work we plan to build proper light-cones using all the GLAM halo catalogues available in the relevant redshift range.

The upper panels in Fig. 6.1 show the differential halo mass function measured at $z = 0.6$, 0.74 and 0.93 from the PMILL run (black solid lines) and the GLAM simulations (blue dots with errobars) using $M_{\rm vir}$ as the halo mass definition. We use the mass conversion algorithm of Hu & Kravtsov (2003) to convert M_{200m} into $M_{\rm vir}$ for the PMILL measurements. We find good agreement between the GLAM and PMILL results, with a difference of less than 10% (see lower subpanels in the top row of Fig. 6.1) for haloes with mass $\log_{10}(M_{\rm vir}/\,h^{-1}{\rm M}_\odot) > 12.5$ at all redshifts. This mass value is well below the typical LRG host halo mass (see below). The differences seen between the results from GLAM and PMILL for lower mass haloes are due to the lower resolution in the GLAM simulations. The differences seen at the high-mass end are due to the much smaller volume of the PMILL simulation compared with that used in the GLAM simulations.

The real-space clustering of haloes of mass $\log_{10}(M_{\rm vir}/\,h^{-1}{\rm M}_\odot) > 12.5$ is shown in the lower panels of Fig. 6.1 at different redshifts. We find good agreement in the clustering measured on scales $r > 2\,h^{-1}$Mpc between the two types of simulations. There is a 10 per cent difference over the separation range $2 < r/\,h^{-1}{\rm Mpc} < 40$, as shown in the lower subpanels of the bottom row in Fig. 6.1. Nevertheless, GLAM predicts a higher clustering amplitude for $r \sim 1\,h^{-1}$Mpc with respect to that measured in the PMILL simulation. This effect is due to the different algorithms used to find dark matter haloes, i.e. BDM predicts more halo pairs at small separations, hence resulting in a higher clustering amplitude on small scales. As we will see in Section 6.5, the difference in the halo clustering does not affect the clustering of LRGs when an appropriate HOD is applied to the GLAM catalogues.

6.3 Selection of luminous red galaxies

The DESI team plan to use the 3.4 μm band ($W1$) from the space-based Wide-Field Infrared Survey Explorer (WISE), in combination with the r and z bands from the DESI Legacy Imaging Surveys (Dey et al., 2019), to select LRGs efficiently in the redshift range $0.6 < z < 1.0$ (DESI Collaboration et al., 2016). Zhou et al. (2020) described an updated version of the DESI LRG target selection, which we adopt here:

$$z < 20.41 \tag{6.3.1}$$

$$-0.6 < (z - W_1) - 0.8(r - z)\,, \tag{6.3.2}$$

$$r - z > 0.9\,, \tag{6.3.3}$$

$$r - z > (z - 17.18)/2\,. \tag{6.3.4}$$

Galform outputs observer frame absolute magnitudes with dust attenuation, $M_{\rm AB}$, so we need to convert these into apparent magnitudes, $m_{\rm AB}$, in order to apply the above cuts:

$$m_{\rm AB} = M_{\rm AB} + 5\log_{10}(d_L(z)/\,h^{-1}{\rm Mpc}) + 25 - 2.5\log_{10}(1+z)\,, \tag{6.3.5}$$

where the magnitudes are on the AB-magnitude system, $d_L(z)$ is the cosmological luminosity distance in units of h^{-1}Mpc, and the factor $-2.5\log_{10}(1+z)$ is from the band shifting of the filter width.

The left panel of Fig. 6.2 shows Galform galaxies in the redshift range $0.6 < z < 1$ in the $(r-z)-(z-W_1)$ colour-colour plane. The black contours show the locus of galaxies with stellar mass in excess of $10^9\,h^{-1}{\rm M}_\odot$ and the red contours show the galaxies that meet the DESI LRG selection criteria set out in Eqs. (6.3.2) and (6.3.3). The right panel of Fig. 6.2 shows the distribution of galaxies in the $z-(r-z)$ colour-magnitude plane, again showing all galaxies with stellar mass above $10^9\,h^{-1}{\rm M}_\odot$ (black contours) along with those which satisfy the LRG selection (red contours). The stellar mass cut of $10^9\,h^{-1}{\rm M}_\odot$ is much lower than we expect for the stellar mass of LRGs (see below), but is applied for illustrative purposes, to allow us to see the locus of the Galform galaxies in the colour-magnitude planes, before the photometric LRG selection is applied. Note that in these panels we simply show

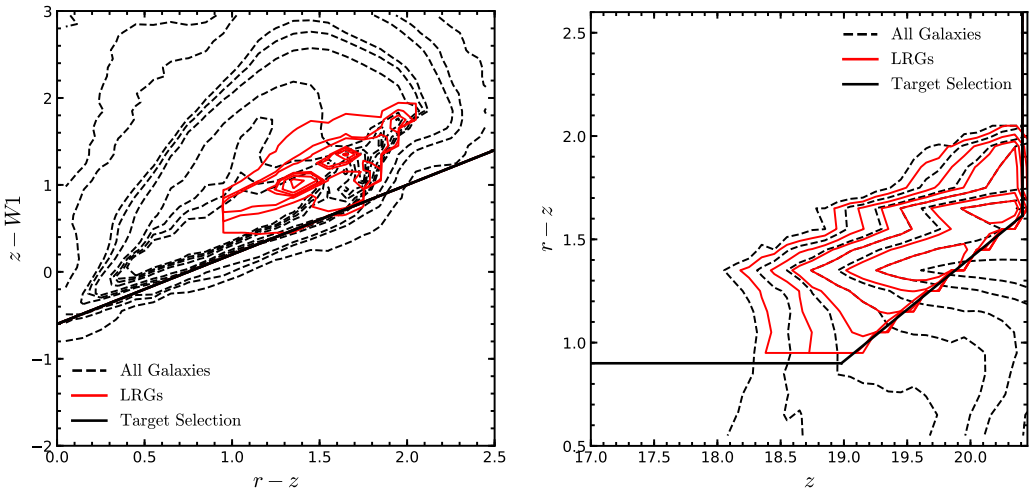

Figure 6.2: Colour-colour (*left*) and colour-magnitude (*right*) diagrams predicted using the GALFORM snapshots at $z = 0.6$ to $z = 1$ and using the r, z and $W1$ bands. Dashed black lines represent the distribution of all galaxies with stellar mass $M_* > 10^9\,h^{-1}\mathrm{M}_\odot$ from the GALFORM output. Red solid lines show the locus of GALFORM galaxies which remain after applying the DESI LRG selection cuts. The solid black polygons indicate the DESI LRG photometric selection given by Eqs. (6.3.1)-(6.3.4), the same used by Zhou et al. (2020).

all of the galaxies that pass the stellar mass cut or LRG selection from *each* of the nine PMILL snapshots that fall within the redshift interval. As such, we are mainly interested in the locus of the GALFORM galaxies in these colour-magnitude planes, rather than the detailed changes in the density of points.

Reassuringly, the red contours in the $(r - z) - (z - W_1)$ colour-colour plane are well within the black polygons denoting the selection boundaries; the blue colour boundary of the $r-z$ vs. z selection box is a key component in setting the space density of LRGs, as the red contours touch this cut. At $z = 0.6$ GALFORM predicts that around 6.2 million galaxies in the PMILL volume have stellar mass $M_* > 10^9\,h^{-1}\mathrm{M}_\odot$ but only a small fraction (0.84 per cent) of these galaxies are selected as LRGs.

Fig. 6.3 shows the space density, $n(z)$, of DESI LRGs predicted using GALFORM. We have applied the colour-magnitude cuts (Eq. (6.3.1) to Eq. (6.3.4)) to nine PMILL snapshots in the redshift range $0.6 < z < 1$ to obtain the abundance of LRGs – the redshift of the snapshots is indicated by the points in Fig. 6.3. In

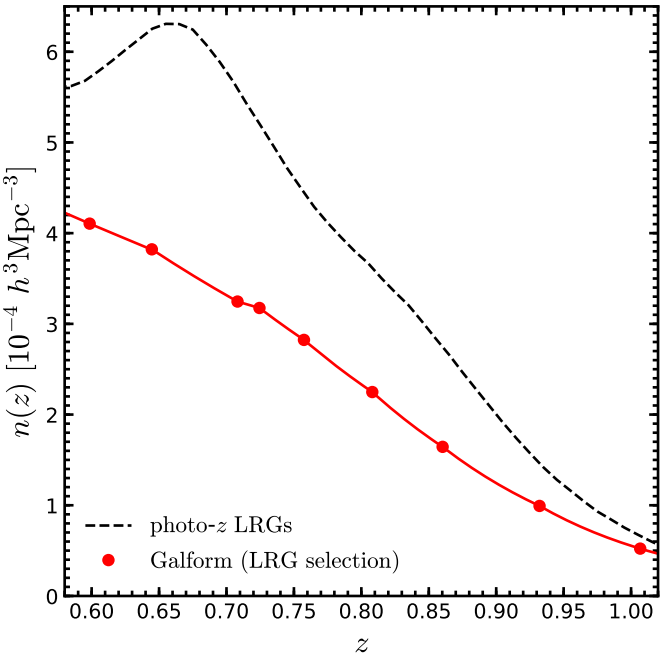

Figure 6.3: The space density of LRGs meeting the DESI selection criteria, as predicted using Galform, as a function of redshift. We show the nine Pmill snapshots between $0.6 < z < 1$ (red dots). The red solid line simply connects the points. The dashed black line shows the space density of DESI-LRGs estimated observationally using photometric redshifts by Zhou et al. (2020).

the same figure, we show the number density of DESI-like LRGs inferred from observations using photometric redshifts from Zhou et al. (2020) (black dashed line). We note that Galform underpredicts the abundance of LRGs at all redshifts, with the discrepancy reaching a factor of ≈ 1.7 at $z \sim 0.66$. The predicted space densities could be reconciled with those inferred observationally using photometric redshifts by perturbing, for example, the $r-z$ selection to a bluer colour in Fig. 6.2. Nevertheless, here we are interested in showing the theoretical predictions from the Galform model and the applications on the large-scale clustering of our glam catalogues.

To further investigate the impact of the LRG colour-magnitude selection on the galaxy population predicted by Galform we present, in Fig. 6.4, the stellar mass and luminosity functions for all galaxies and for those selected as DESI LRGs. The top panels of Fig. 6.4 show the evolution with redshift of the stellar mass function

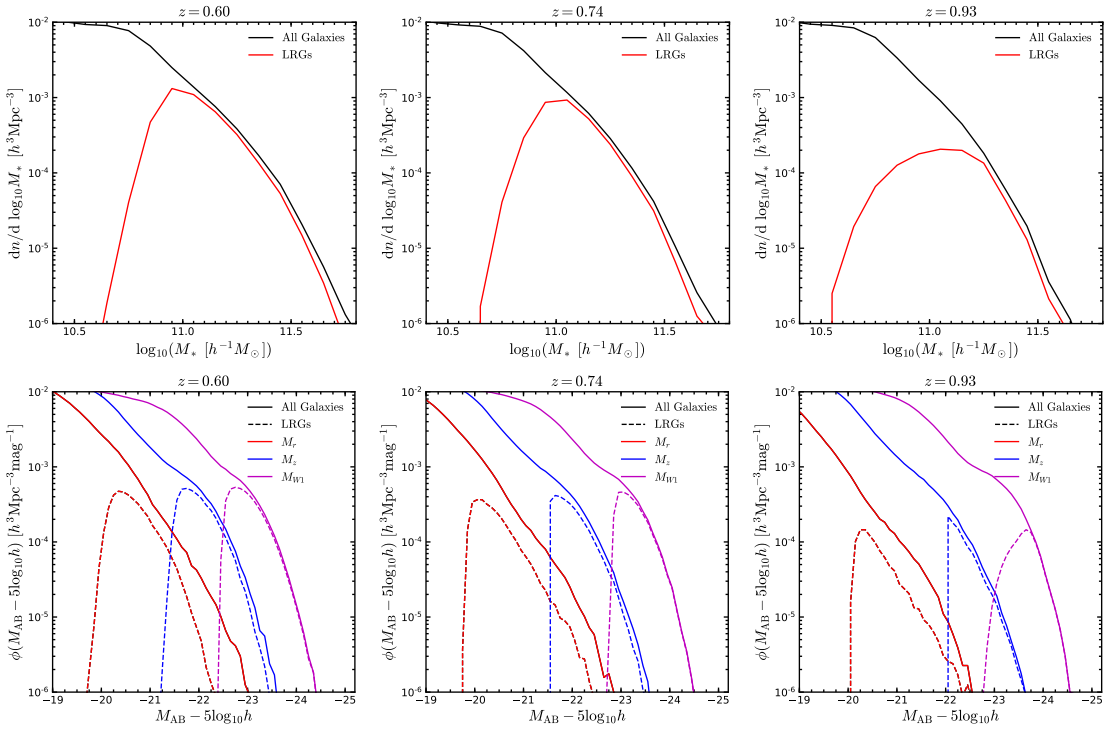

Figure 6.4: Stellar mass (*upper panels*) and luminosity (*lower panels*) functions predicted by GALFORM at $z = 0.6$ (*left*), $z = 0.74$ (*middle*) and $z = 0.93$ (*right*) for all galaxies from the GALFORM output and LRGs. Different colours and line styles indicate different properties and selections as indicated in the legend.

(sMF) for all galaxies and for LRGs, for $z = 0.6$, $z = 0.74$ and $z = 0.93$. Given the halo mass resolution of the Pmill, robust predictions can be made using Galform for galaxies with stellar masses $M_* > 10^7\,h^{-1}\mathrm{M}_\odot$ (Baugh et al., 2019). As expected, the LRG sample is dominated by massive galaxies, although not *all* massive galaxies are LRGs. These massive galaxies are predicted to be in massive dark matter haloes above the mass at which heating by active galactic nuclei suppresses gas cooling (Contreras et al., 2015; Mitchell et al., 2016). Some massive galaxies, however, have recent star formation driven by the cold gas accreted in galaxy mergers, making their $r - z$ colour too blue to be selected as LRGs. The predicted stellar mass function of LRGs drops sharply below $\log_{10}(M_*/\,h^{-1}\mathrm{M}_\odot) = 11.1$, but is similar to the overall SMF for larger stellar masses. The amplitude of the LRG SMF is similar at $z = 0.6$ and $z = 0.74$, which reflects the lack of evolution seen in the overall SMF. As we can see from Fig. 6.3, the number density of LRGs drops from $4.11 \times 10^{-4}\,h^3\,\mathrm{Mpc}^{-3}$ at $z = 0.6$ to $3.02 \times 10^{-4}\,h^3\,\mathrm{Mpc}^{-3}$ at $z = 0.74$, while at $z = 0.93$ the abundance of LRGs is $0.99 \times 10^{-4}\,h^3\,\mathrm{Mpc}^{-3}$.

Similar to the plots showing the galaxy stellar mass function, in the lower panels of Fig. 6.4, we show, at the same redshifts as used in the top row, the luminosity functions for the r, z and $W1$ bands for all galaxies and for LRGs. We find a similar trend as that discussed for the stellar mass functions. The fraction of bright galaxies that are selected as LRGs increases with the wavelength of the band: above a threshold luminosity, all galaxies in the W_1-band are LRGS, whereas only a fraction, around a half, of galaxies that are bright in the r-band are LRGs. Below the threshold luminosity, the fraction of galaxies that are LRGs plunges dramatically.

6.4 The galaxy−(sub)halo connection of DESI luminous red galaxies

To explore the galaxy-(sub)halo connection of the DESI-like LRGs predicted by Galform we first examine their halo occupation distribution (HOD). The HOD is an useful tool to understand the galaxy-halo connection, clustering and evolution of galaxies in general (see the review by Wechsler & Tinker 2018). The HOD specifies

the average number of galaxies (centrals and satellites) hosted by a dark matter halo. Previous observational studies have described the HOD of LRGs using a functional form that distinguishes between central and satellite galaxies (see e.g., Blake et al., 2008; Brown et al., 2008; Padmanabhan et al., 2009; Zheng et al., 2009). In a traditional HOD there is a transition in the mean number of central galaxies from $\langle N_c \rangle = 0$ to $\langle N_c \rangle = 1$ with increasing halo mass and the occupation by satellites ($\langle N_s \rangle$) follows a power-law in halo mass (Zheng et al., 2005).

Fig. 6.5 shows the evolution of the HOD of DESI LRGs as predicted by Galform in the redshift range $z = 0.6 - 1$. We show the predicted HOD for the nine redshifts we used to measure the evolution of the LRG number density distribution in Fig. 6.3. At first glance we see that the occupancy of central galaxies ($\langle N_c \rangle$) does not reach the canonical value of unity at high halo masses, and even begins to decline after a peak at intermediate halo masses. This behaviour is typically seen in the models when galaxies are selected by their star-formation rate instead of a property that correlates more closely with stellar mass (Contreras et al., 2013; Cowley et al., 2016; Jiménez et al., 2019). More recently Gonzalez-Perez et al. (2018) found similar behaviour for the HOD of emission-line galaxies selected by the colour-magnitude cuts that will be used by the DESI emission-line galaxy survey (see also Merson et al. 2019 and Gonzalez-Perez et al. 2020). The LRG population is dominated by central galaxies and contains a satellite fraction of $f_{\rm sat} \sim 0.10$ to $f_{\rm sat} \sim 0.04$ in the redshift range $z = 0.6 - 1$, where the mean number of satellites $\langle N_s \rangle$ is close to a power-law. Since the HOD is predicted directly by Galform and does not have a canonical shape (as discussed above), we do not attempt to extract HOD parameters by fitting one of the functional forms typically adopted in the literature to model observational samples. Instead we use a tabulated version of the Galform HOD which captures the full shape more accurately than a simple parametric form could ever do.

Fig. 6.5 shows that there is a clear turnover in the HOD predicted by Galform for central galaxies at intermediate redshifts ($z = 0.74, 0.80$). At higher redshifts than this the trend is less clear due to the evolution in the halo mass function and the resulting lack of high mass haloes. One might have expected that the mean number

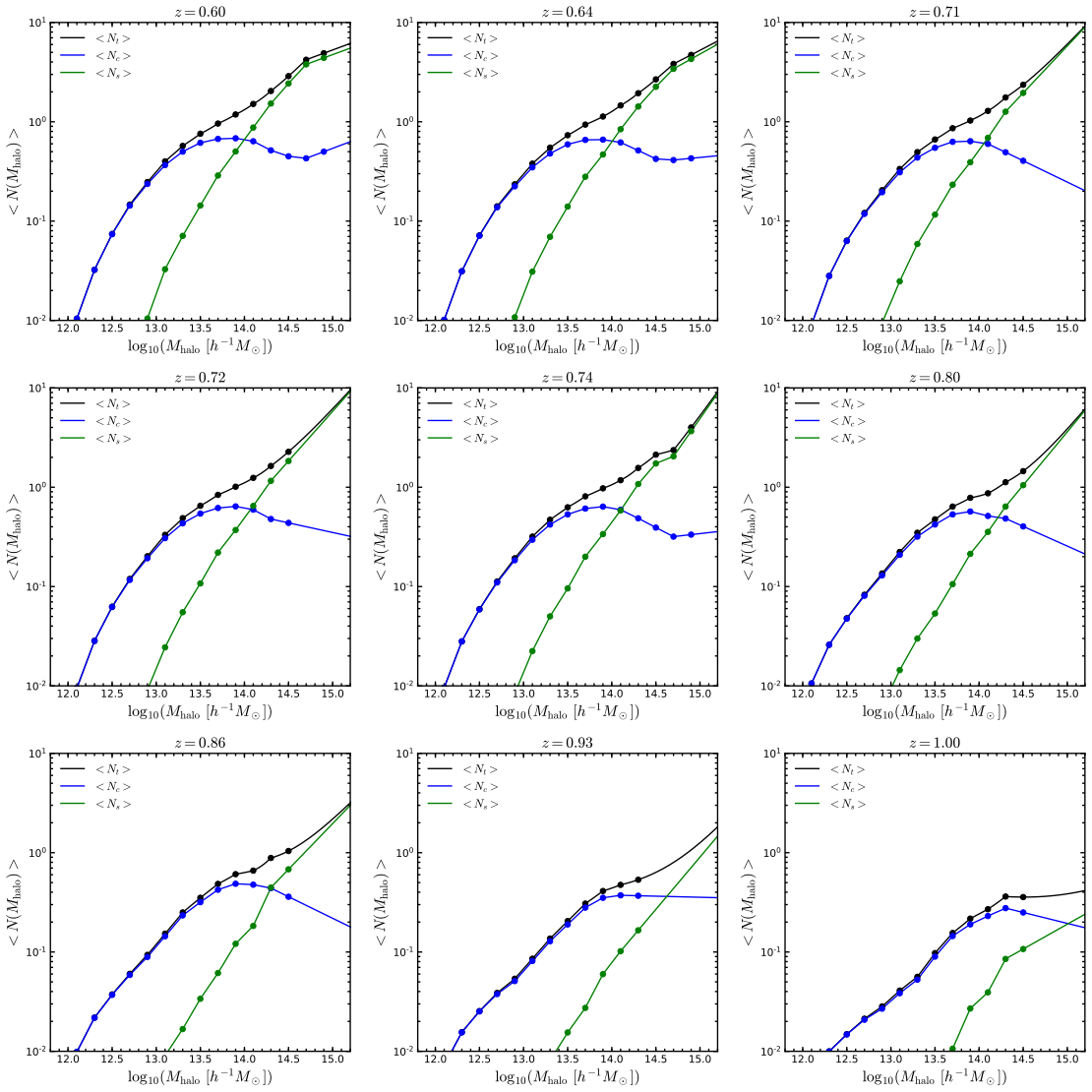

Figure 6.5: Halo occupation distribution of DESI-like LRGs predicted by GALFORM (symbols) as a function of their host halo masses. Each panel shows a different redshift between $z = 0.6$ and $z = 1$ as labelled. The solid lines connect the symbols. Outside the mass range for which model predictions are available, the solid lines show a power-law extrapolation of the HOD for centrals and satellites, based on the last measured points. The total, central and satellite galaxy occupancy is shown in black, blue and green, as labelled.

of centrals would reach unity in massive haloes, due to the suppression of gas cooling through the heating of the hot gas halo by active galactic nuclei. However, some central galaxies in massive haloes can become too blue to be selected as LRGs due to star formation triggered by mergers, which use the cold gas brought in by the merging galaxy.

To develop a deeper understanding of the galaxy-(sub)halo connection we now explore which *subhaloes* are able to host an LRG. To do so, we consider the number of subhaloes in haloes of different mass and the subhalo mass function, including a version that shows only those subhaloes that host an LRG. We also define a new galaxy sample for comparison purposes by ranking galaxies in order of decreasing stellar mass, and choosing a stellar mass cut to match the number density of the LRG sample. This comparison sample allows us to understand the impact of the selection cuts on the haloes and subhaloes that host LRGs; we call this the stellar mass selected sample.

The upper panels of Fig. 6.6 show the HOD for the LRG and stellar mass selected galaxy samples, which we compare to the total number of subhaloes available to host an LRG (see below for how this is defined). Focusing on the galaxy HODs first, the black, blue and green lines in Fig. 6.6 show the number, respectively, of all galaxies, central galaxies and satellites galaxies as a function of halo mass; solid lines show the model predictions for the LRG sample and the dashed lines for the stellar mass selected sample. The light blue dashed lines show the number of subhaloes more massive than $M_{\rm subhalo} > 10^{12.5}\,h^{-1}{\rm M}_{\odot}$ as a function of the mass of their main host halo. This mass cut is arbitrary but was chosen because the HODs for the galaxy samples are significant for halo masses above this value. In an illustrative sense, a subhalo mass of $M_{\rm subhalo} \approx 10^{12.5}\,h^{-1}{\rm M}_{\odot}$, based on the mass coverage of the galaxy sample HODs, could be loosely thought of as the minimum subhalo mass needed to host an LRG or a galaxy in the comparator stellar mass selected sample.

Fig. 6.6 shows us that only a small fraction of subhaloes with masses above $M_{\rm subhalo} > 10^{12.5}\,h^{-1}{\rm M}_{\odot}$ host an LRG: this fraction reduces from 22% to 8% as the redshift increases from $z = 0.6$ to $z = 0.93$. The shape of the total (centrals+satellites) and satellite-only HOD is similar for LRGs and the stellar mass

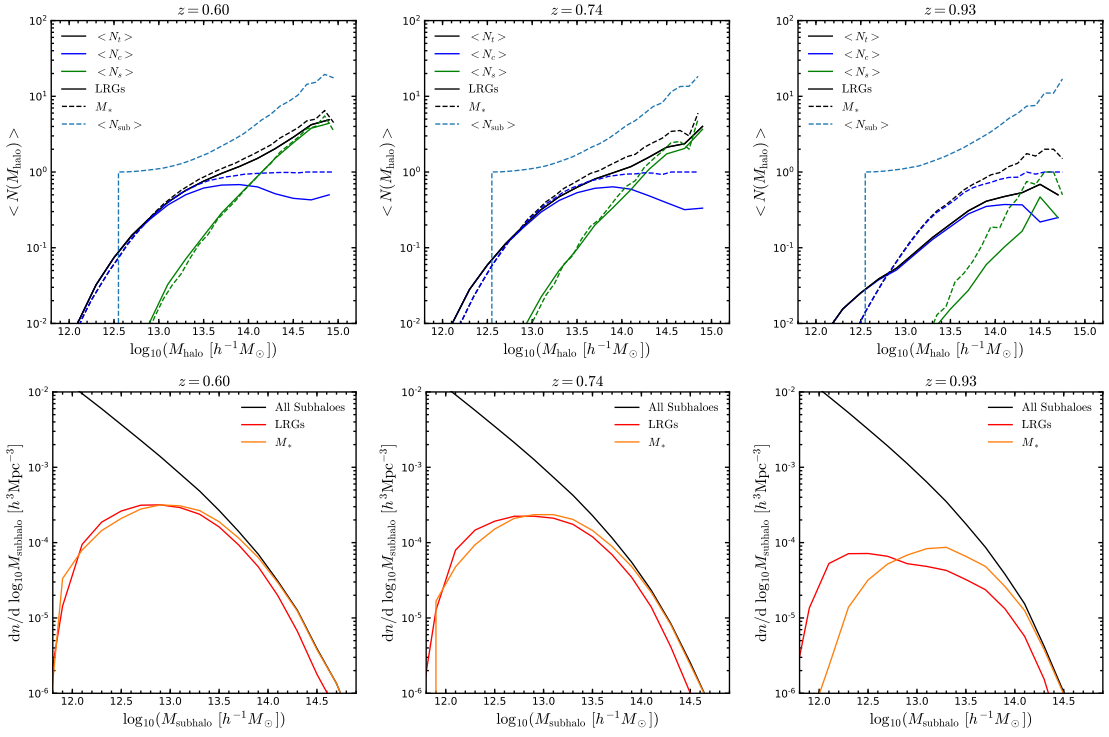

Figure 6.6: *Upper panels:* Halo occupation distribution of subhaloes (dashed cyan line), LRGs (solid lines) and galaxies ranked by stellar mass (dashed lines) at $z = 0.6$ (*left panel*), $z = 0.74$ (*middle panel*) and $z = 0.93$ (*right panel*). For galaxies, the occupation of total, centrals and satellites are specified as black, blue and green lines respectively. *Lower panels:* Subhalo mass functions measured using all galaxies (black solid lines), LRGs (red solid lines) and galaxies ranked by stellar mass (orange solid lines) at at $z = 0.6$ (*left panel*), $z = 0.74$ (*middle panel*) and $z = 0.93$ (*right panel*).

selected sample at $z = 0.6$ and 0.74. However, at $z = 0.93$ the DESI LRG selection cuts modify the form of the LRG HOD away from that of the stellar mass selected sample. The HODs of central galaxies in the two samples are markedly different at all redshifts shown in Fig. 6.6. The HOD of stellar mass selected central rises to unity with increasing halo mass, but for the LRGs it turns over after reaching a maximum below unity. This behaviour is swamped by the satellite HOD so that the overall HODs for the LRG and stellar mass samples differ less than the central HODs. At the highest redshift shown in Fig. 6.6, the transition from zero to peak occupancy fraction for centrals is slower for the LRGs than for the stellar mass sample. As centrals dominate the overall sample at lower halo masses, this produces a significant difference in the HOD for LRGs and the stellar mass selected sample.

To gain further insight into the LRG subhalo population, we show the subhalo mass function in the lower panels of Fig. 6.6. Two versions of the subhalo mass function are shown: one is the 'dark matter view' in which we include all subhaloes and the other is the 'galaxy view', in which case a subhalo is only included if it contains a galaxy in the sample. If the 'galaxy view' version of the subhalo mass function coincides with the 'dark matter view', then all subhaloes at that mass that could host a galaxy do so. In the case of the stellar mass selected samples shown in the bottom row of Fig. 6.6, we see that the most massive subhaloes all host a galaxy. As we move to lower masses, the galaxy-view subhalo mass function falls below the dark-matter view version; for these masses only a fraction of the available subhaloes host a galaxy. Eventually, as we continue to mover towards even lower subhalo masses, there is a dramatic downturn in the galaxy-view subhalo mass function, with only a tiny fraction, less than one in a thousand subhaloes hosting a galaxy. Qualitatively, the galaxy-view subhalo mass functions for the LRGs are similar to those for the stellar mass selected sample, with one exception: at the massive end, not all subhaloes host an LRG. This difference becomes more pronounced with increasing redshift. The conclusion of this comparison is that it is essential to perform the full colour-magnitude selection to define the LRG sample. Applying a stellar mass cut to attain a target number density of objects is a fair approximation to performing the full photometric selection at low redshifts, but

results in a fundamentally different set of subhaloes being chosen with increasing redshift.

6.5 Galaxy Clustering

In previous sections we explored the impact of the DESI LRG colour-magnitude selection on galaxy statistics such as the stellar mass function and the luminosity functions at different wavelengths. We also presented predictions for which haloes and subhaloes contain LRGs. Here we take this a step further by investigating the evolution of the clustering in configuration and Fourier space, in both real- and redshift-space. We measure the clustering from the simulations with the NBODYKIT toolkit (Hand et al., 2018).

6.5.1 Galaxy clustering in the PMILL and GLAM simulations

First, we present in Fig. 6.7 a comparison of the predicted real-space galaxy two-point correlation function for pair separations in the range $0.7 < r/[\,h^{-1}\mathrm{Mpc}] < 50$ at redshifts 0.6, 0.74 and 0.93 for LRGs and the stellar mass selected sample. Since LRGs do not populate all of the most massive (sub)haloes, as seen in the lower panels of Fig. 6.6, the LRG sample is less biased than the stellar mass selected one, leading to a smaller clustering amplitude on all scales. We find a constant offset in the clustering amplitude of around 10% between the samples at $z = 0.6$ and $z = 0.74$ on all scales. At higher redshifts, where the DESI-LRG colour-magnitude cuts have a bigger impact on which subhaloes host LRGs, we find that the difference in clustering amplitude increases to 50% on large scales, rising to $\sim 150\%$ on small scales. The larger difference on small-scales at $z = 0.93$ is due to the abundance of satellite galaxies in the different galaxy samples; as seen in the upper right panel of Fig. 6.6, the stellar mass selected sample has a larger satellite fraction than the DESI-LRG sample. This comparison shows that selecting LRGs using stellar mass as a proxy for the full colour-magnitude selection leads to a significant change in the predicted clustering signal.

As we mentioned before, one of our aims is to produce a large number of mock

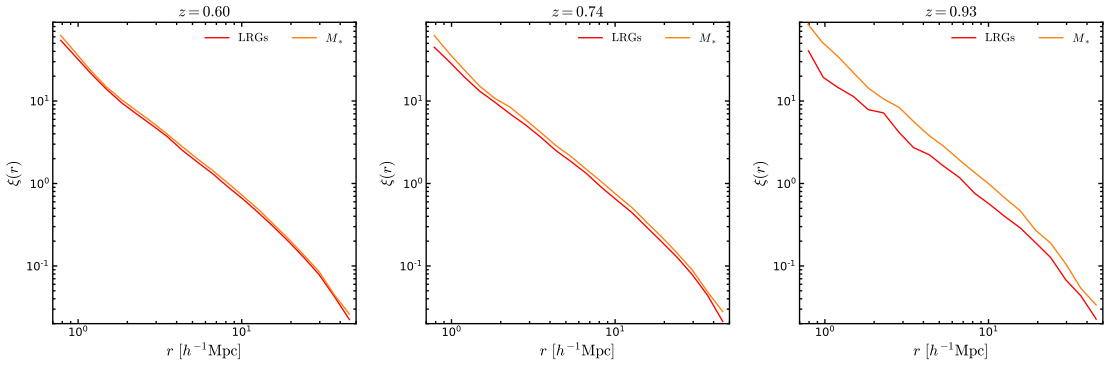

Figure 6.7: The real-space galaxy correlation functions predicted by GALFORM for LRGs (red lines) and the stellar mass selected sample (orange line) at $z = 0.6$ (*left panel*), $z = 0.74$ (*middle panel*) and $z = 0.93$ (*right panel*).

DESI LRG catalogues using the GLAM code to give an accurate estimate of the galaxy clustering signal and its full covariance matrix of errors. For this reason, we populate our 1000 GLAM simulations with LRGs using the tabulated HOD predicted by GALFORM (see Fig. 6.5), as explained below.

Since GALFORM predicts an HOD for DESI-LRGs that does not appear to follow any of the popular parametric forms in the literature (see Appendix A of Contreras et al. 2013), we bypass carrying out a fit altogether and instead use the tabulated model predictions for the HOD directly to populate GLAM haloes with LRGs. Hence, in order to populate a given GLAM halo we interpolate between the HOD values predicted by GALFORM to the GLAM halo mass (see below for further details). In the case of the most massive haloes we extrapolate beyond the halo mass range of the HOD values; we do not have robust predictions for these haloes from the PMILL simulation due to its smaller volume compared to the GLAM boxes. This method was used recently by Merson et al. (2019), where the authors extracted the HOD of Hα galaxies from the GALACTICUS SAM catalogue (Benson, 2012; Merson et al., 2018), and used this to populate the Millennium-MXXL halo light-cone from Smith et al. (2017).

In detail our HOD method is as follows. We assign a central galaxy to a GLAM halo if $\langle N_c \rangle > \mathcal{U}(0,1)$, where $\langle N_c \rangle$ is the mean number of central galaxies that could be found in a GLAM halo obtained by interpolating the HOD tabulated from

the GALFORM output shown in Fig. 6.5 and $\mathcal{U}(0,1)$ is a uniform random number between 0 and 1. Recall that the GALFORM predictions for the HOD of central galaxy LRGs never reach unity. We place the central galaxy at the centre of mass of the host halo, and give it the velocity of the centre of mass. The number of satellite galaxies is drawn from a Poisson distribution with mean equal to $\langle N_s \rangle$, as derived from the tabulated HOD predicted using GALFORM. Satellite galaxies are radially distributed within the virial radius, $(0 < r < R_{\rm vir})$, following a Navarro-Frenk-White (NFW) density profile (Navarro et al., 1996, 1997), with a uniform angular distribution. The satellite is assigned a velocity that is made up of the halo velocity plus a perturbation along the x, y and z coordinates drawn from a Gaussian distribution with variance equal to the 1D velocity dispersion of the host halo.

We measure the real- and redshift-space clustering in configuration and Fourier space from the GLAM-HOD catalogues and compare these with their PMILL counterparts to corroborate the precision of our method. In addition, the real-space clustering measurements provide us a relation between the distribution of galaxies and the underlying dark-matter density field via the galaxy bias (Peebles, 1980). The galaxy bias is directly measured from our GLAM LRG mocks as

$$b(k,z) = \sqrt{\frac{P_{\rm g}(k,z)}{P_{\rm m}(k,z)}} \quad \text{or} \quad b(r,z) = \sqrt{\frac{\xi_{\rm g}(r,z)}{\xi_{\rm m}(r,z)}}\,, \tag{6.5.6}$$

where $P_{\rm g}(k,z)$ ($\xi_{\rm g}(r,z)$) and $P_{\rm m}(k,z)$ ($\xi_{\rm g}(r,z)$) are the real-space galaxy and dark matter power spectra (correlation functions) at a given redshift, respectively. We tried both approaches to estimating the bias and found consistent answers, $b(z) = 1.84, 1.96, 2.06$ at $z = 0.6, 0.74$ and 0.93, respectively. The DESI-like LRG bias has been estimated from the measured angular power spectrum and from the halo model of the photo-z LRGs giving the following relations, $b(z) = 1.6/D(z)$ (Kitanidis et al., 2020) and $b(z) = 1.5/D(z)$ (Zhou et al., 2020). Note these relations are slightly different to the value of $b(z) = 1.7/D(z)$ reported in DESI Collaboration et al. (2016), where $D(z)$ is the linear growth factor at redshift z, with $D(z=0) = 1$. For the cosmological parameters used in the PMILL simulation, the linear growth factor is $D(z = 0.6) = 0.73$, $D(z = 0.74) = 0.69$ and $D(z = 0.93) = 0.63$, which means that the values we recover for the bias are slightly lower than those inferred from

the observations, more similar to $b(z) = (1.3 - 1.4)/D(z)$.

We use the distant-observer approximation to shift the positions of galaxies from real- to redshift-space, treating the z-axis as the line of sight,

$$\mathbf{s} = \mathbf{r} + \frac{(1+z)v_z}{H(z)}\hat{e}_z\,, \tag{6.5.7}$$

where $\mathbf{r}$ is the coordinate vector in real space, $\mathbf{s}$ is the equivalent of this in redshift-space, and z is the redshift of the simulation snapshot used to generate the galaxy catalogue. $H(z)$ is the Hubble parameter, v_z and $\hat{e}_z$ are the components of the velocity and the unit vector along the z-direction.

We measure the monopole and quadrupole moments of the redshift-space correlation function, $\xi_l(s)$, and power spectrum, $P_l(k)$, using

$$\xi_l(s) = (2l+1)\int_0^1 \xi(s,\mu)\mathcal{L}_l(\mu)\,\mathrm{d}\mu\,, \tag{6.5.8}$$

$$P_l(k) = (2l+1)\int_0^1 P(k,\mu)\mathcal{L}_l(\mu)\,\mathrm{d}\mu\,, \tag{6.5.9}$$

where $\xi(s,\mu)$ and $P(k,\mu)$ are the full two-dimensional correlation function and power spectrum, μ is the cosine of the angle between the separation vector, $\mathbf{s}$ or $\mathbf{k}$, and the line-of-sight in configuration or Fourier space, respectively. The $\mathcal{L}_l(\mu)$ are the Legendre polynomials where $l = 0$ is the monopole and $l = 2$ is the quadrupole. We use 20 bins logarithmically spaced over the separation range $0.7 < s/[\,h^{-1}\mathrm{Mpc}] < 50$ in which to measure the correlation function. The power spectrum is measured in the range $0 < k/[\,h\,\mathrm{Mpc}^{-1}] < k_{\rm Nyq}$ using linear bins in k with separation $\Delta k = 0.006\,h\,\mathrm{Mpc}^{-1}$, where $k_{\rm Nyq} = \pi N_{\rm mesh}/L_{\rm box}$ is the 1D Nyquist frequency, $N_{\rm mesh} = 512$ and $L_{\rm box}$ is the box size of the PMILL or GLAM simulations. In all cases we adopt 30 linearly spaced bins between 0 and 1 for μ.

In the upper panels of Fig. 6.8 we display the real-space clustering measured from the GALFORM output (black line) and the GLAM LRG mock catalogues (blue symbols with errorbars). Additionally, we show the best-fitting power law fit to the correlation function reported by Kitanidis et al. (2020) ($r_0 = 7.78\,h^{-1}\mathrm{Mpc}$, $\gamma = 1.98$) which agrees well with our measurements, especially on scales $r \geq r_0$. Note that Kitanidis et al. fitted the angular correlation function in the range $0.001^\circ < \theta < 1^\circ$ which translates to comoving separation $\theta_{\rm min}D_{\rm A}(z) < r/[\,h^{-1}\mathrm{Mpc}] < \theta_{\rm max}D_{\rm A}(z)$,

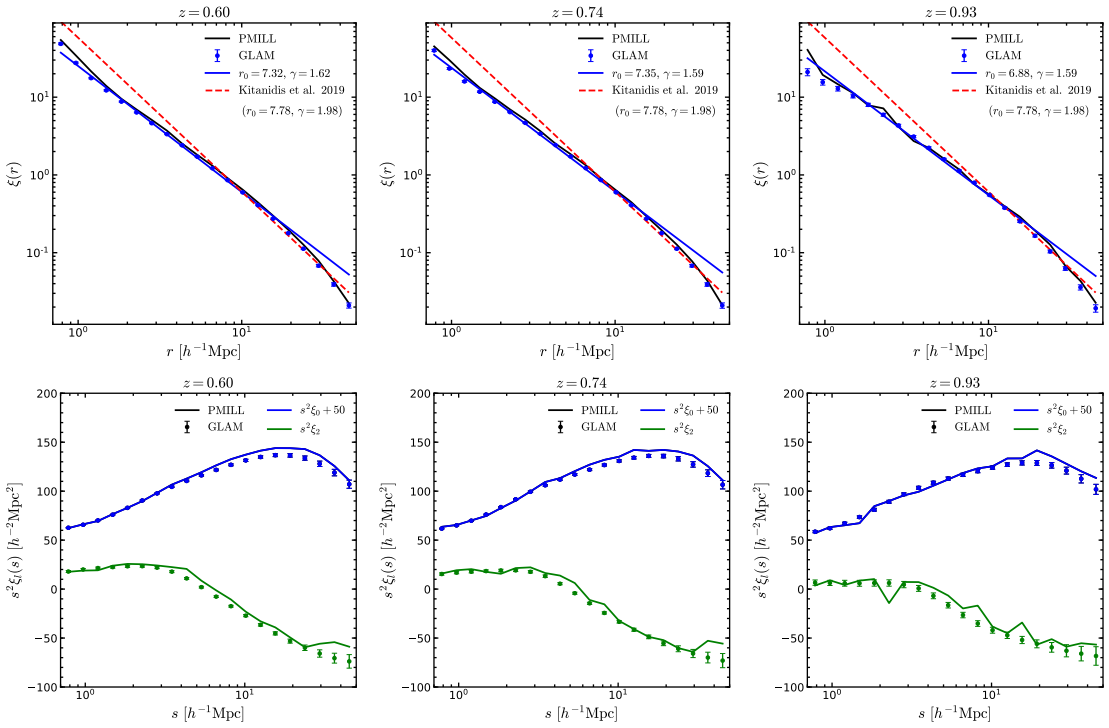

Figure 6.8: *Upper panels:* Real-space galaxy correlation function of the Galform-Pmill LRGs (black lines) and the HOD-glam LRGs (blue symbols with error bar). We also show the best fitting power-law form, $\xi(r) = (r/r_0)^{-\gamma}$, to the DESI-LRG measurements reported by Kitanidis et al. (2020, red dashed lines) and to our measurements (blue solid lines). *Lower panels:* Redshift-space monopole and quadropole moments of the correlation function for Galform-Pmill LRGs (solid lines) and glam-HOD LRGs (symbols with error bar). Note that the monopole has been shifted upwards for clarity. In the case of the glam-HOD LRGs measurements, we show the mean and standard deviation over 1000 realisations. The measurements are made at $z = 0.6$, 0.74 and 0.93, as labelled at the top of each panel.

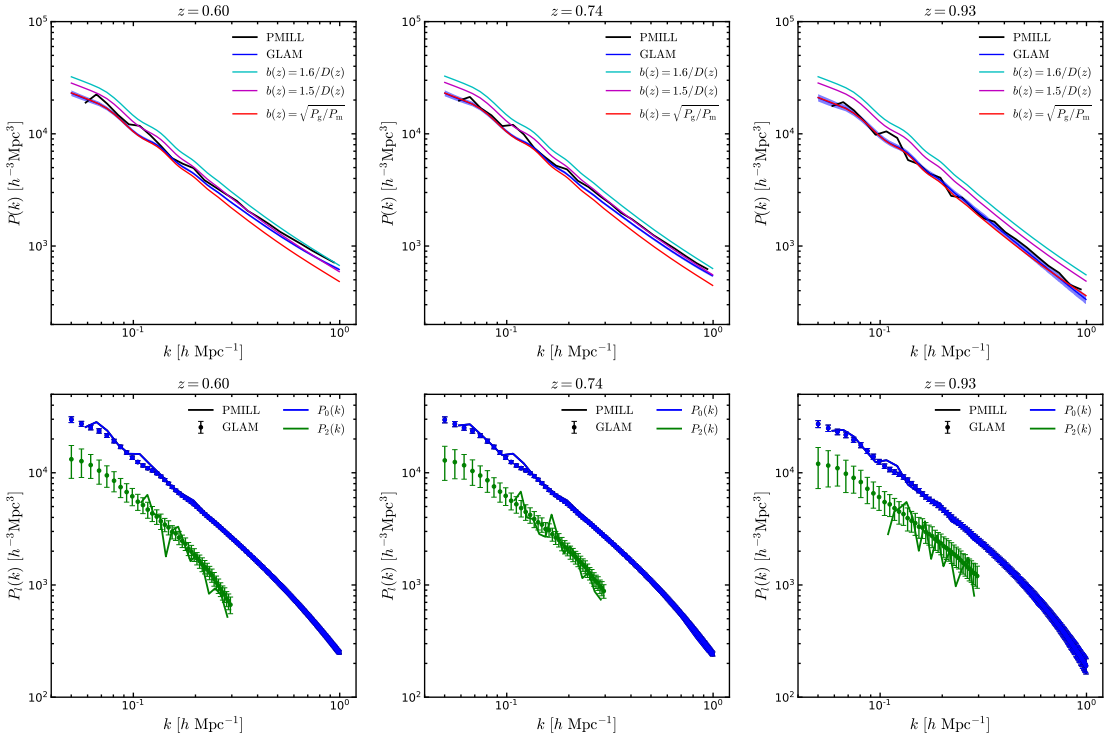

Figure 6.9: *Upper panels:* Real-space galaxy power spectrum of the GALFORM-PMILL LRGs (black lines) and the GLAM-HOD LRGs (blue lines, the shaded region represents the 1σ error over 1000 realisations), we also show the dark-matter power spectrum multiplied by the galaxy bias squared estimations of Kitanidis et al. (2020, cyan solid lines), Zhou et al. (2020, magenta solid lines) and from Eq. (6.5.6) (red solid line). *Lower panels:* Redshift-space monopole and quadropole moments of the power spectrum for GALFORM LRGs (solid lines) and GLAM LRGs (symbols with error bar). For the GLAM-HOD LRGs measurements, we show the mean and standard deviation over 1000 realisations. The measurements are made at $z = 0.6$, 0.74 and 0.93, as labelled at the top of each panel.

where $D_{\rm A}$ is the angular-diametre distance. We also show results when fitting our GLAM measurements with a power-law using the range mentioned above, $\xi(r) = (r/r_0)^{-\gamma}$, finding $r_0/[\,h^{-1}{\rm Mpc}] = (7.316 \pm 0.022, 7.346 \pm 0.024, 6.883 \pm 0.04)$ and $\gamma = (1.623 \pm 0.006, 1.592 \pm 0.007, 1.589 \pm 0.012)$ at $z = 0.6$, 0.74 and 0.93.

The lower panels of Fig. 6.8 shows the predicted multipoles of the redshift-space correlation function of the GLAM-HOD LRGs (symbols with errorbars), plotted in comparison with their GALFORM counterparts (black line). We find excellent agreement between the clustering measured in both real- and redshift-space for the GLAM and GALFORM LRGs at all scales and all redshifts.

In Fig. 6.9 we display the clustering measurements in Fourier space. First, we note the good agreement between the GALFORM (black lines) and GLAM (blue lines) measurements on all scales to better than 5 per cent. In the upper panels of Fig. 6.9 we also show the measured dark-matter power spectrum scaled by the galaxy bias squared relations of Kitanidis et al. (2020, cyan lines), Zhou et al. (2020, magenta lines) and from our simulations, Eq. (6.5.6). We find that our measurements slightly underpredict the bias value compare to the measured relations estimated by Kitanidis et al. (2020) and Zhou et al. (2020). In the lower panels of Fig. 6.9 we show the multipole moments of the redshift space power spectrum, finding almost perfect agreement between the GALFORM and GLAM measurements on scales $k > 0.1\,h\,{\rm Mpc}^{-1}$. Nevertheless, there is a noisy signal for the GALFORM quadrupole of the redshift-space power spectrum, due to the smaller box size of the PMILL. Nevertheless, this signal is in good agreement with the predictions from GLAM over the range $0.1 < k/[\,h\,{\rm Mpc}^{-1}] < 0.3$.

We conclude that populating GLAM haloes using our interpolated-HOD method reproduces accurately the clustering of LRGs predicted directly by GALFORM on all scales of interest.

6.5.2 Large-scale galaxy clustering and covariance matrices

In general it is not possible to measure the three dimensional clustering of galaxies in real-space from observations. Some compromise involving projection is usually required to obtained a real-space statistic, such as the angular correlation function

or the projected correlation function. The most direct three dimensional clustering measurements from surveys provide statistics in redshift-space, which are affected by peculiar velocities. Moreover, future surveys like DESI aim to measure galaxy clustering on scales up to $\sim 200\,h^{-1}$Mpc. Hence, taking advantage of our GLAM-HOD machinery, here we present predictions for the large-scale galaxy clustering and covariance matrices of DESI-like LRGs for the correlation function and power spectrum. These quantities are fundamental for error estimates on the measurements of BAO and RSD (see e.g., Alam et al., 2017).

In the following, we focus our attention on the large-scale clustering of DESI-like LRGs for pair separations in the range $0 < s/[\,h^{-1}\text{Mpc}] < 150$ for the correlation function. For the power spectrum we show results in the wavenumber range $0.01 < k/[\,h\,\text{Mpc}^{-1}] < 0.3$.

The upper panels of Figs. 6.10 and 6.12 display the mean and standard deviation of the multipoles of the correlation function and the power spectrum calculated over 1000 GLAM DESI-like LRGs realisations at $z = 0.6$, 0.74 and 0.93. We also measure the covariance matrix, $\mathbf{C}$, of each estimator $\mathbf{E}$, as follows,

$$C_{ij} = \frac{1}{N_s - 1} \sum_{k=1}^{N_s} \left(E_i^k - \bar{E}_i\right) \left(E_j^k - \bar{E}_j\right) \,, \tag{6.5.10}$$

where $N_s = 1000$ is the number of mocks, $\bar{E}_i = 1/N_s \sum_k E_i^k$ is the mean value of the estimator in the i-th separation bin, and E_i^k is the corresponding measurement from the k-th mock. The standard deviation is estimated from the diagonal elements of the covariance matrix,

$$\sigma_i = \sqrt{C_{ii}}\,. \tag{6.5.11}$$

We show the diagonal error contribution, σ_{E_i}/E_i, of the moments of the correlation function and power spectrum in the lower subpanels of the upper row of Figs. 6.10 and 6.12. We observe an increase in the size of the error contribution at large-scales, especially for the monopole and quadrupole in configuration space.

We display the correlation matrix,

$$r_{ij} = \frac{C_{ij}}{\sqrt{C_{ii} C_{jj}}}\,, \tag{6.5.12}$$

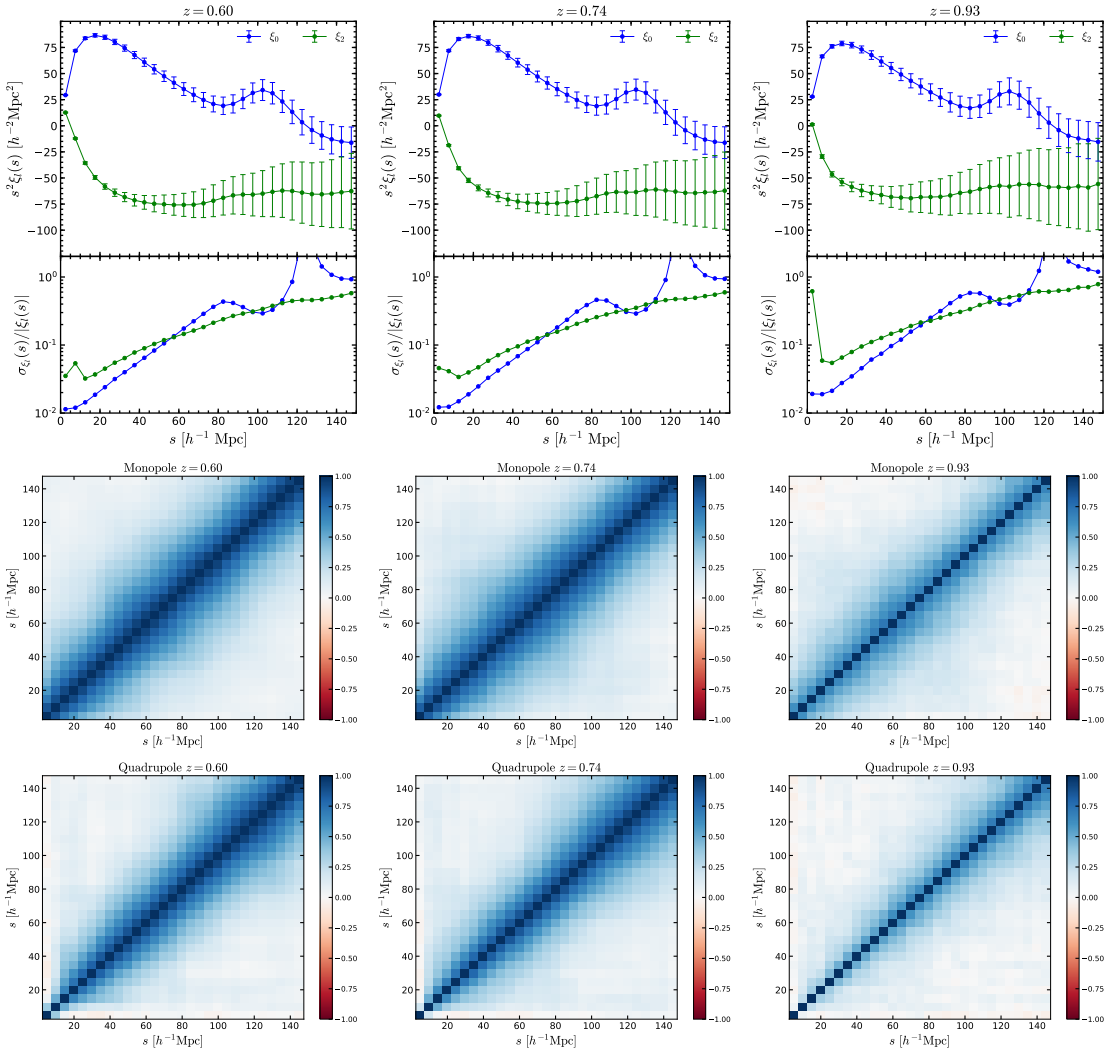

Figure 6.10: *Upper panels:* Measured monopole (blue lines) and quadrupole (green lines) of the redshift-space two-point correlation function of DESI-like LRGs from our GLAM-HOD catalogues, the lower subpanels show the diagonal error contribution to the monopole and the quadrupole. The error is calculated using Eq. (6.5.11). *Middle panels:* Correlation matrix, Eq. (6.5.12), of the monopole. *Bottom panels:* Correlation matrix, Eq. (6.5.12), of the quadrupole. The colour bar in the correlation matrices display values from $-1 \leq R(s_i, s_j) \leq 1$. The measurements are made at $z = 0.6$, 0.74 and 0.93, as labelled at the top of each panel.

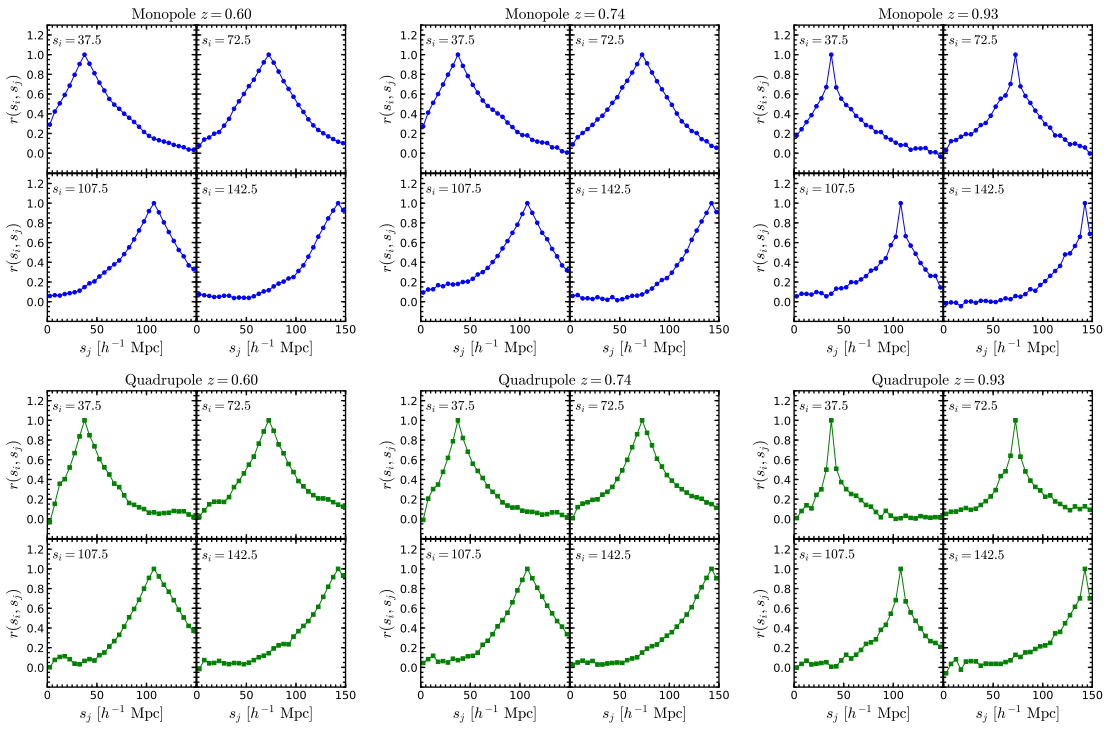

Figure 6.11: Cuts through the correlation matrix of the monopole (*upper panels*) and the quadrupole (*bottom panels*) of the redshift-space correlation function at four different values of s_i in units of $[h^{-1}\text{Mpc}]$ as indicated in the panels. The measurements are made at $z = 0.6$, 0.74 and 0.93, as labelled at the top of each panel.

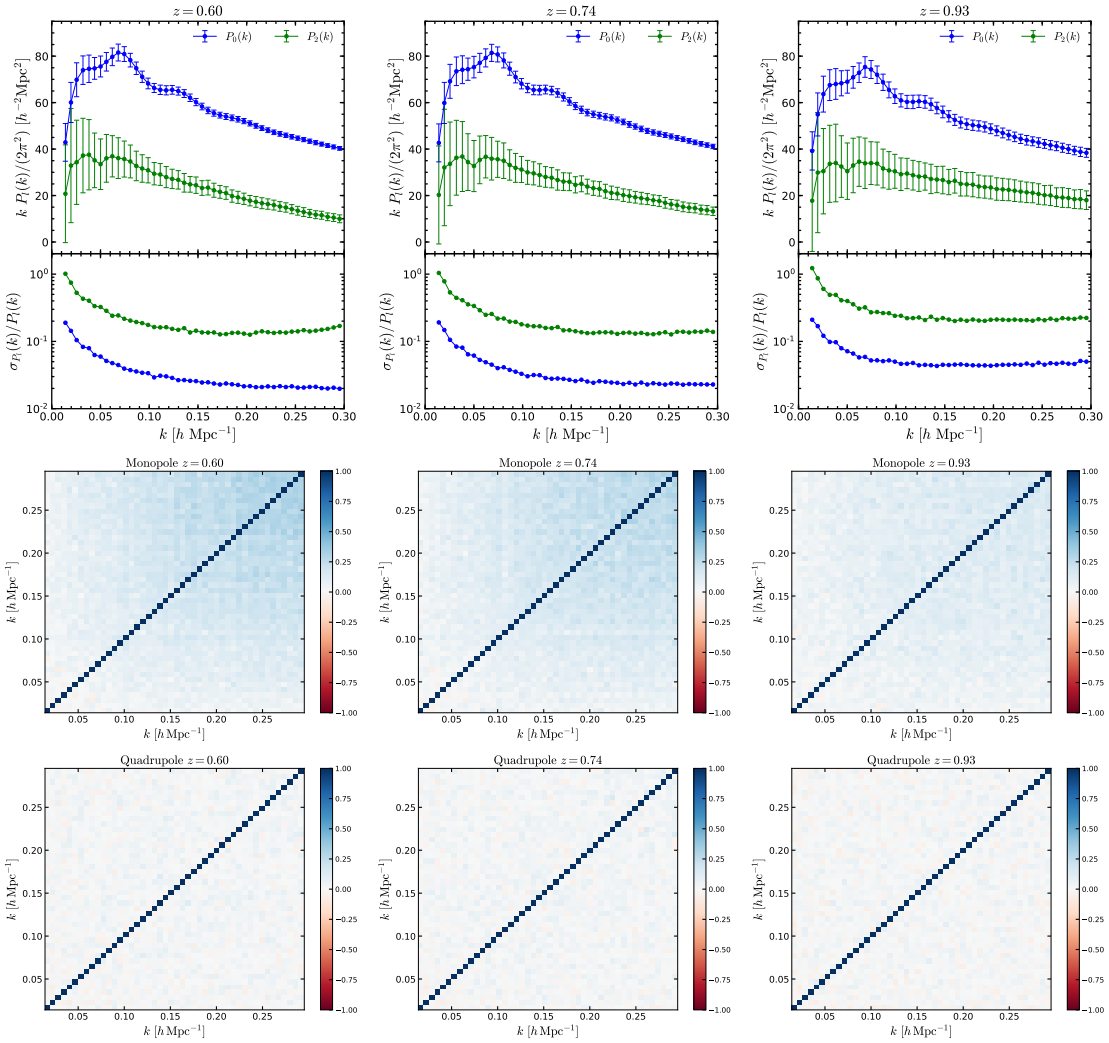

Figure 6.12: Same as Figure 6.10 but for the multipoles of the power spectrum.

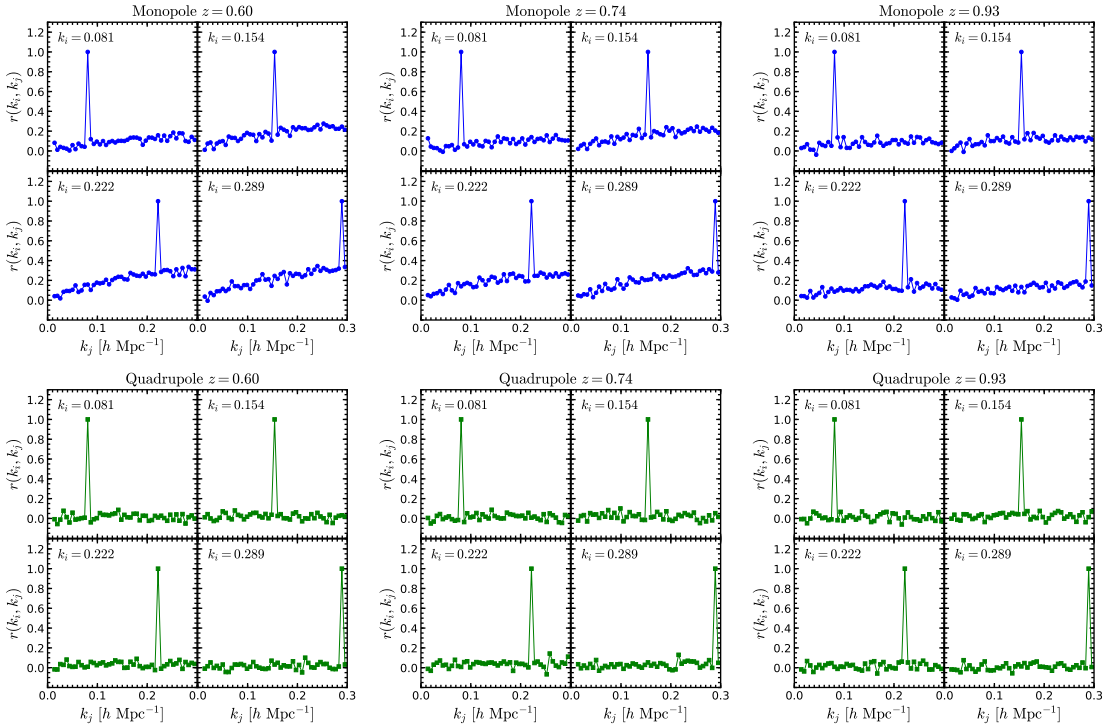

Figure 6.13: Same as Figure 6.11 but for the multipoles of the power spectrum. In this case, we show the cuts through the correlation matrices at four different values of k_i in units of [$h\,\mathrm{Mpc}^{-1}$].

in the middle (monopole) and bottom (quadrupole) panels of Figs. 6.10 and 6.12 for the correlation function and power spectrum, respectively. The diagonal and non-diagonal components have different magnitudes and evolve differently with redshift. Figs. 6.11 and 6.13 show cuts through the correlation matrices corresponding to our measurements in configuration and Fourier space, respectively. These diagrams help us to better display the level of correlation and the structure of the matrices. In the case of the moments of the correlation function (Fig. 6.11), we show the cuts at four different separation bins, $s_i = (37.5, 72.5, 107.5, 142.5)\, h^{-1}\mathrm{Mpc}$, while in Fourier space (Fig. 6.13) we use $k_i = (0.081, 0.154, 0.222, 0.289)\, h\,\mathrm{Mpc}^{-1}$. We see a strong correlation between the bins close to the diagonal elements in the monopole and quadrupole of the correlation function at $z = 0.60$ and $z = 0.74$; this correlation becomes weaker at $z = 0.93$ (Fig. 6.11). In the case of the multipoles of the power spectrum, the off-diagonal elements are much less correlated than the diagonal components, with values close to zero (Fig. 6.13). This trend is strongest for the quadrupole of the power spectrum.

Klypin & Prada (2018) carried out an extensive study of the covariance and correlation matrix associated with the dark-matter power spectrum of GLAM simulations. Our results for the estimation of errors from the GLAM-HOD catalogues extends the work of Klypin & Prada to galaxies and to the correlation function. In detail, Fig. 6.14 shows the covariance analysis of the real-space DM and LRG power spectra. We summarise our findings as follows. First, in the upper panels we display the measurements from our simulations, we observe that the size of the error is similar for both DM and LRGs at large-scales ($k < 0.05\, h\,\mathrm{Mpc}^{-1}$) but on smaller scales the amplitude of the error of the galaxy power spectrum becomes larger with increasing redshift. We also show the DM power spectrum and its errors scaled by the LRG bias squared (see Sec. 6.5.1 for details) as a blue solid line (with a shaded region showing the 1σ error) in the upper panel of the first row of Fig. 6.14. Second, the correlation matrices are shown in the middle panels (upper middle panels for DM and lower middle panels for LRGs), we find that the amplitude of the DM correlation matrices are consistent with those reported by Klypin & Prada (2018). On the other hand, the correlation amplitude of the LRG power spectrum is sim-

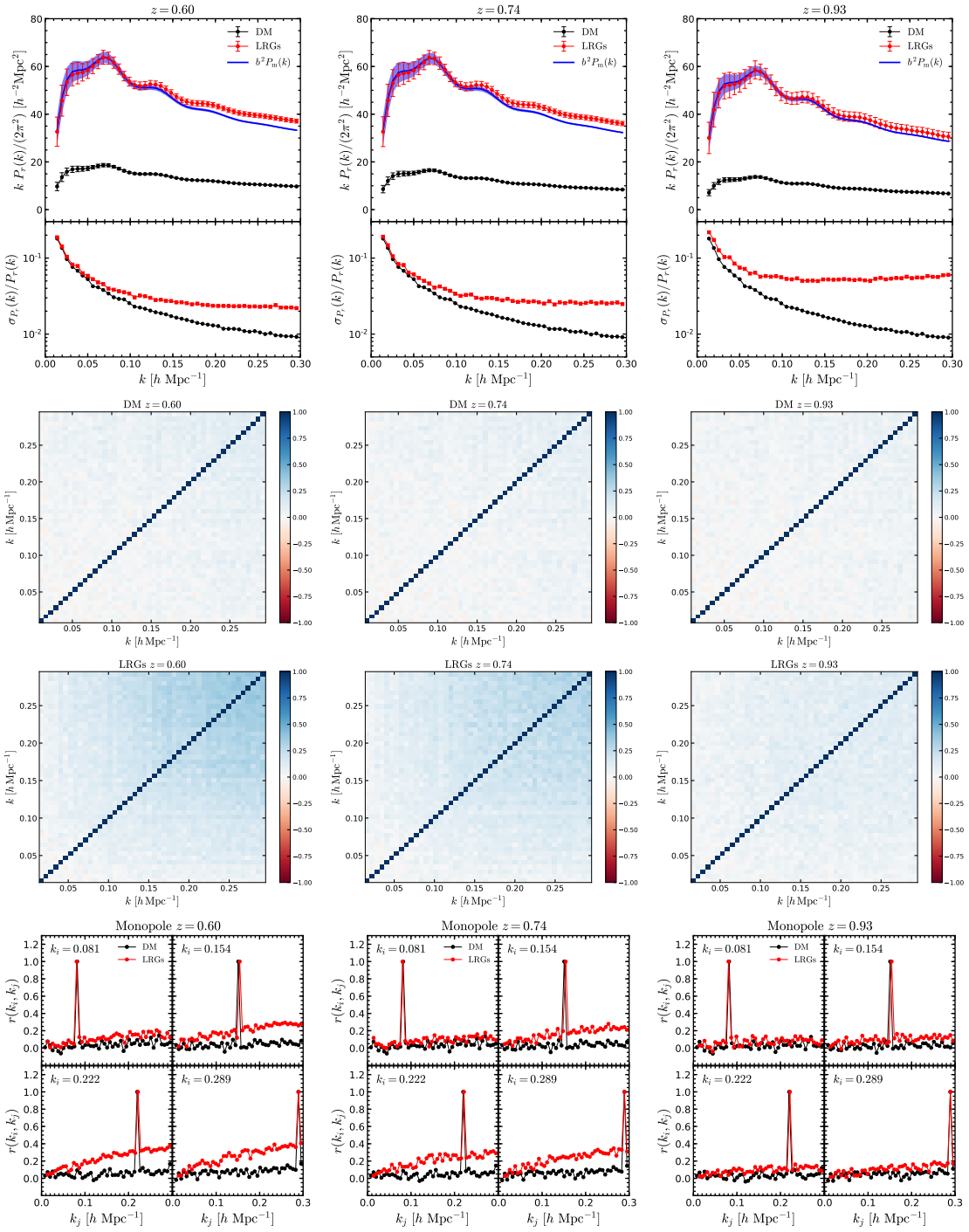

Figure 6.14: Covariance analysis of the real-space dark matter and LRG power spectra at $z = 0.6$, 0.74 and 0.93. *Upper panels:* Measured DM (black lines) and LRG (red lines) power spectrum from our GLAM simulations together with the DM power spectrum multiplied by the bias squared (blue lines; Eq. (6.5.6)), the *lower subpanels* show the error contribution. *Middle top* and *middle lower:* Correlation matrices of the real-space power spectrum for the DM density field and LRGs, respectively. *Bottom panels:* Slices through the correlation matrices at different values of k_i in units of $[\,h\,\mathrm{Mpc}^{-1}]$.

ilar to its analogue in redshift space (see middle panels of Fig. 6.12). Lastly, the evolution of the non-diagonal terms of the correlation matrices are displayed in the bottom panels of Fig. 6.14. We compare the level of correlation at four values of the separation bin, $k_i = (0.081, 0.154, 0.222, 0.289)\, h\,\mathrm{Mpc}^{-1}$, finding a more complex behaviour from the LRGs correlation matrices with an increase amplitude at small scales, this behaviour is also consistent with our findings in redshift space (see Fig. 6.12). Moreover, the amplitude of the non-diagonal elements are similar for both DM and LRGs at $z = 0.93$ (bottom right panel of Fig. 6.14).

Finally, we can use the covariance matrix of each estimator to define a chi-squared to find the best-fitting cosmological parameters as follows,

$$\chi^2 = \sum_{i,j=1}^{N_s} \left(E_i^{\mathrm{th}} - E_i^{\mathrm{obs}}\right) C_{ij}^{-1} \left(E_j^{\mathrm{th}} - E_j^{\mathrm{obs}}\right) , \tag{6.5.13}$$

where C_{ij}^{-1} is the inverse of the covariance matrix, Eq. (6.5.10), E^{th} is the theoretical expectation of the estimator that depends on the cosmological parameters and E^{obs} is the measured estimator from our GLAM-HOD catalogues. Note that the inverse of the covariance matrix should be corrected using the Hartlap factor (Hartlap et al., 2007),

$$\tilde{C}_{ij}^{-1} = \frac{N_{\mathrm{mock}} - N_b - 2}{N_{\mathrm{mock}} - 1} C_{ij}^{-1} , \tag{6.5.14}$$

where N_{mock} is the number of mock catalogues and N_b is the number of separation bins used in the fitting. This definition is used in Sec. 6.5.3 and Sec. 6.5.4.

It is instructive to compare the errors we obtain in the GLAM simulation boxes with the errors expected in the DESI measurements. DESI will measure the clustering of LRGs in a series of redshift shells over a solid angle of 14 000 square degrees. We anticipate that DESI will sample a comoving volume of $V/[h^{-3}\mathrm{Gpc}^3] = 2.63$, 3.15 and 4.10 respectively on bins centred at redshifts of $z = 0.65$, 0.75 and 0.95 (DESI Collaboration et al., 2016). Hence, to get a rough impression of how our error estimates (on the cosmological parameters) will scale to those expected for DESI, we can scale the GLAM errors by the square root of the inverse volume ratio (e.g. Feldman et al. 1994): $\sigma'(z) = \sigma(z)\sqrt{V_{\mathrm{GLAM}}/V_{\mathrm{DESI}}(z)}$, where $V_{\mathrm{GLAM}} = 1\, h^{-3}\mathrm{Gpc}^3$. Note that we refrain from carrying out a more detailed comparison with the errors

reported in DESI Collaboration et al. (2016), as these were obtained using a Fisher matrix method, which assumes Gaussian errors and no off-diagonal terms.

6.5.3 Linear redshift-space distortions

In large volume galaxy surveys we can extract information about the growth of structure through the linear growth rate, f, which is defined as the logarithmic derivative of the linear growth function of density perturbations, D, with respect to the scale factor, a,

$$f \equiv \frac{\mathrm{d}\ln D}{\mathrm{d}\ln a}\,. \tag{6.5.15}$$

In linear perturbation theory, the relation between the redshift-space galaxy power spectrum, P_s, and its real-space counterpart, P_r, is given by (Kaiser, 1987):

$$P_\mathrm{s}(k,\mu) = (1+\beta\mu^2)^2 P_\mathrm{r}(k)\,. \tag{6.5.16}$$

From Eq. (6.5.16) we can see that the amplitude of the RSD is related to the distortion parameter β, defined as

$$\beta(z) \equiv \frac{f(z)}{b(z)}\,, \tag{6.5.17}$$

where f is the linear growth rate (Eq.(6.5.15)), and b is the linear galaxy bias both of which vary with redshift, Eq. (6.5.6).

The monopole and quadrupole moments of the power spectrum can be estimated from Eqs. (6.5.9) and (6.5.16),

$$P_0(k) = \left(1+\frac{2\beta}{3}+\frac{\beta^2}{5}\right)P_\mathrm{r}(k)\,, \tag{6.5.18}$$

$$P_2(k) = \left(\frac{4\beta}{3}+\frac{4\beta^2}{7}\right)P_\mathrm{r}(k)\,, \tag{6.5.19}$$

where $P_\mathrm{r}(k)$ is galaxy power spectrum in real-space.

On the other hand, the redshift-space correlation function can be expressed as follows (Hamilton, 1992, 1998):

$$\xi(s,\mu) = [1+\beta(\partial/\partial z)^2(\nabla^2)^{-1}]^2\xi(r)\,, \tag{6.5.20}$$

In linear theory, the monopole and quadrupole of the correlation function can be estimated using (Hamilton, 1992), i. e.,

$$\xi_0(s) = \left(1 + \frac{2\beta}{3} + \frac{\beta^2}{5}\right)\xi(r)\,, \tag{6.5.21}$$

$$\xi_2(s) = \left(\frac{4\beta}{3} + \frac{4\beta^2}{7}\right)[\xi(r) - \bar{\xi}(r)]\,, \tag{6.5.22}$$

where $\xi(r)$ is the galaxy correlation function in real-space and $\bar{\xi}$ is its volume integral out to pair separation r:

$$\bar{\xi}(r) = \frac{3}{r^3}\int_0^r \xi(r')r'^2\,\mathrm{d}r'\,. \tag{6.5.23}$$

From Eqs. (6.5.18)−(6.5.19) and Eqs. (6.5.21)−(6.5.22) we can define two estimators to obtain the distortion parameter, β, or the linear growth rate, f, (Cole et al., 1994; Hawkins et al., 2003),

$$R(k/s) = \frac{P_0(k)}{P_{\rm r}(k)} = \frac{\xi_0(s)}{\xi(r)} = 1 + \frac{2\beta}{3} + \frac{\beta^2}{5}\,, \tag{6.5.24}$$

and

$$Q(k/s) = \frac{P_2(k)}{P_0(k)} = \frac{\xi_2(s)}{\xi_0(s) - \bar{\xi}_0(s)} = \frac{(4/3)\beta + (4/7)\beta^2}{1 + (2/3)\beta + (1/5)\beta^2}\,, \tag{6.5.25}$$

where $\mathcal{F}(k/s)$ indicates that the quantity $\mathcal{F}$ can be a function of k or s and

$$\bar{\xi}_0(s) = \frac{3}{s^3}\int_0^s \xi_0(s')s'^2\,\mathrm{d}s'\,, \tag{6.5.26}$$

is the volume average of the monopole in redshift space, the analogue of Eq. 6.5.23.

Fig. 6.15 shows our measurements of the $R(k/s)$, and the $Q(k/s)$ estimators from our DESI-GLAM LRG mock catalogues at the median redshift $z = 0.74$. The black dashed line in each panel corresponds to the linear theory predictions. From the measurements in Fourier space (left panels of Fig. 6.15), we can see that both estimators become closer to the linear theory predictions at scales $k \lesssim 0.1\,h\,\mathrm{Mpc}^{-1}$, this means that linear theory is only valid on sufficiently large-scales. On small scales, where the non-linear motions of galaxies dominate, we observe a downturn in the signal of each estimator. The trend is similar in configuration space (right panel of Fig. 6.15), where we observe that the linear theory limit is reached on scales $s > 20\,h^{-1}\mathrm{Mpc}$. All panels in Fig. 6.15 show the same range of values on the vertical

Table 6.1: Results for the best-fitting values of the linear-growth rate, f, at redshifts 0.60, 0.74 and 0.93 for our estimators $R(k/s)$, Eq. (6.5.24), and $Q(k/s)$, Eq. (6.5.25).

Measurement	Redshift	Fiducial	$R(k)$	$Q(k)$	$R(s)$	$Q(s)$
f	$z = 0.60$	0.786	0.778 ± 0.024	0.776 ± 0.067	0.803 ± 0.041	0.758 ± 0.036
f	$z = 0.74$	0.823	0.822 ± 0.025	0.817 ± 0.066	0.839 ± 0.053	0.815 ± 0.039
f	$z = 0.93$	0.861	0.847 ± 0.033	0.842 ± 0.071	0.838 ± 0.070	0.861 ± 0.061

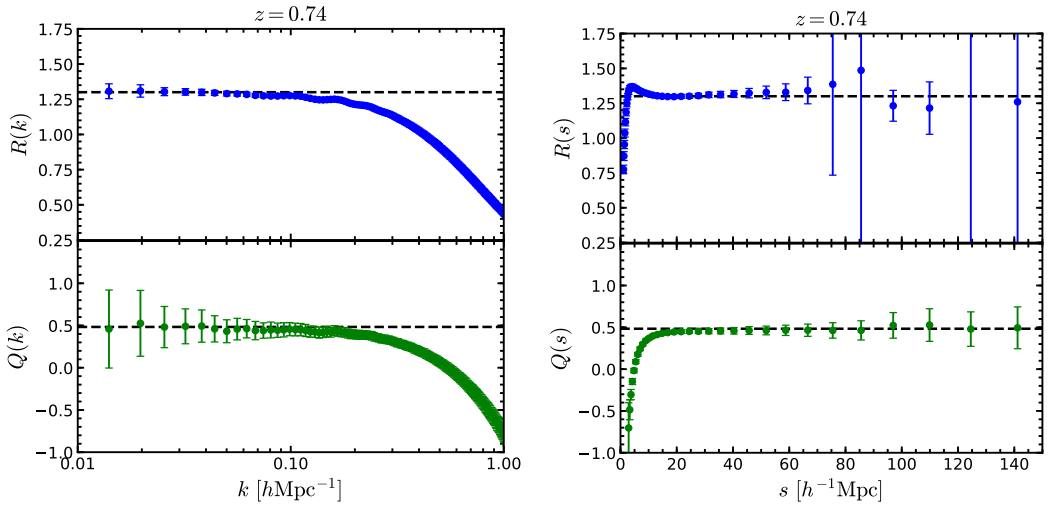

Figure 6.15: Estimators R (*upper subpanels*) (Eq. (6.5.24)) and Q (*lower subpanels*), (Eq. (6.5.25)) as function of separation in Fourier (*left panels*) and configuration (*right panels*) space at $z = 0.74$. Symbols with errorbars show the mean and standard deviation of the estimator measured from our 1000 GLAM catalogues. The black dashed line in each panel represents the fiducial linear theory value.

axis, allow us to see that the errors are slightly different in Fourier and configuration space, especially in R.

To extract the linear growth rate, f, from our measurements, we perform a likelihood analysis by minimising χ^2 defined by Eq. (6.5.13) by fitting the measurements of $R(k/s)$, Eq. (6.5.24), and $Q(k/s)$, Eq. (6.5.25) over the range of scales $k < 0.1\,h\,\mathrm{Mpc}^{-1}$ in Fourier space and $s > 20\,h^{-1}\mathrm{Mpc}$ in configuration space. We fix the galaxy bias and just allow the linear growth rate to vary. To do so, we employ the Monte Carlo Markov Chain (MCMC) technique implemented in the EMCEE python package (Foreman-Mackey et al., 2013).

In Fig. 6.16, we compare the predictions for the linear growth rate $f(z)$ obtained from our DESI-GLAM LRG mocks at $z = 0.6$, 0.74 and 0.93 with the current observational measurements from large galaxy surveys, including 6dFGRS at $z = 0.067$ (Beutler et al., 2012), SDSS MGS at $z = 0.15$ (Howlett et al., 2015), 2dFGRS at $z = 0.17$ (Percival et al., 2004), GAMA at $z = 0.18$ and 0.38 (Blake et al., 2013), WiggleZ at $z = 0.22$, 0.41, 0.6 and 0.78 (Blake et al., 2011a), BOSS DR12 at $z = 0.32$, 0.51 and $z = 0.61$ (Alam et al., 2017), FastSound at $z = 1.4$ (Okumura

et al., 2016) and the eBOSS DR14 QSO sample at $z = 1.52$ (Zarrouk et al., 2018). The black errorbars over the ΛCDM predictions indicate the estimated error from the DESI forecast (see table 2.3 of DESI Collaboration et al., 2016). Note that in this work we do not include the light-cone and survey geometry effects on our mocks. These will be considered in a forthcoming project.

Table 6.1 summarises the best-fitting values of the linear growth rate, f, at $z = 0.60$, 0.74 and 0.93 obtained from the estimators R (Eq. (6.5.24)) and Q (Eq. (6.5.25)) in configuration and Fourier space. We also show the values from the fidiciual cosmology. We find very good agreement between our estimations and the theoretical predictions. The largest errors come from the R estimator in configuration space and Q in Fourier space, this might be due to the size of the error contribution of our measurements (see Sec. 6.5.2 for details). The best case is R in Fourier case, which estimates the linear growth rate with a precision better than 4 per cent. As we mentioned above, we should expect that our errors differ up to a factor of two when comparing to the DESI forecast.

It is expected that DESI will provide a means to distinguish between gravity models. For this reason, in Fig. 6.16, we also show the theoretical expectations from two representative modified gravity models: the $f(R)$ Hu-Sawicki model (Hu & Sawicki, 2007) and the normal branch of the DGP model (nDGP; Dvali et al., 2000). Previously, Hernández-Aguayo et al. (2019) presented predictions for the linear and non-linear RSDs in configuration space for these models but for the BOSS-CMASS sample at $z \leq 0.5$ (Manera et al., 2012).

In Fig. 6.16 we show the theoretical values of the linear growth rate, Eq. 1.2.39, of these models for the cases: $f_{R0} = -10^{-5}$ and the range of scales $0.01 \leq k/[\,h\,\mathrm{Mpc}^{-1}] \leq 0.1$ for $f(R)$ gravity and $\Omega_{\rm rc} = 0.25$ for the nDGP model.

We see that the size of the errors from the DESI forecast is small enough to distinguish between the ΛCDM and the nDGP model. However, it is still unclear if we will be able to rule out $f(R)$ gravity models using RSDs.

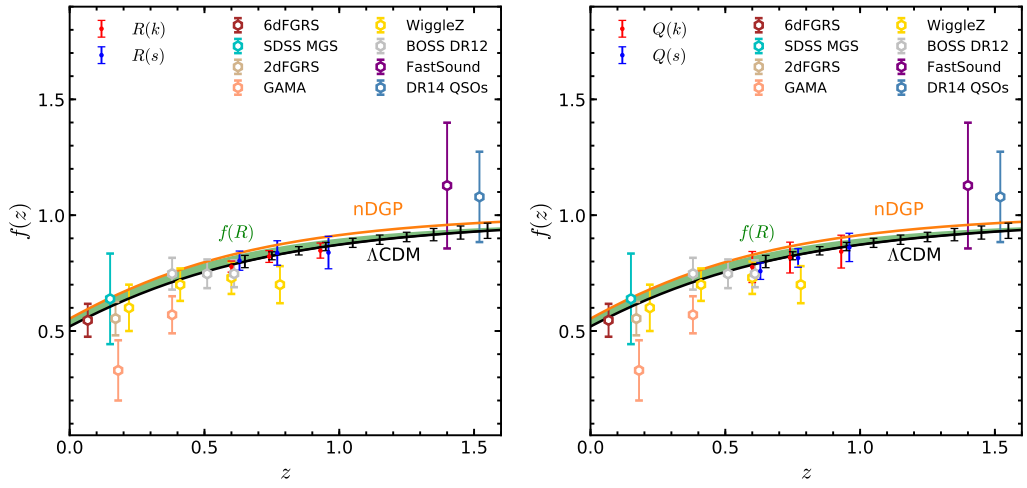

Figure 6.16: Evolution of the linear growth rate, f, as a function of redshift. Our estimations from R and Q are shown in the left and right panel in configuration (red dots with errobars) and Fourier (blue dots with errorbars) space, respectively. The coloured symbols display measurements from different surveys at different redshifts as specified in the legend. Solid curves show the prediction for ΛCDM (black), nDGP (orange) and $f(R)$-gravity (green shaded region that represent wavenumbers $0.01 \leq k/[\,h\,\mathrm{Mpc}^{-1}] \leq 0.1$) models. The black errorbars over the ΛCDM prediction represent the DESI 14K forecast for $k_{\mathrm{max}} = 0.1\,h\,\mathrm{Mpc}^{-1}$ (see table 2.3 of DESI Collaboration et al., 2016).

6.5.4 Isotropic measurements of the baryon acoustic oscillations scale

Another direct application of our GLAM-HOD catalogues is the prediction of the BAO feature for DESI-like LRGs at different redshifts. This scale was not accessible in the PMILL run due to its volume. We extract the BAO scale through the dilation parameter, α, which is related to physical distances via (Eisenstein et al., 2005)

$$\alpha \equiv \frac{D_{\rm V}(z) r_{\rm d}^{\rm fid}}{D_{\rm V}^{\rm fid}(z) r_{\rm d}} \,, \tag{6.5.27}$$

where

$$D_{\rm V}(z) = \left[cz(1+z)^2 D_{\rm A}^2(z) H^{-1}(z) \right] \,, \tag{6.5.28}$$

$D_{\rm A}(z)$ is the angular-diametre distance, $r_{\rm d}$ is the sound horizon at the baryon drag epoch ($z_{\rm d} \sim 1020$) and the superscript 'fid' indicates the value of the distances in our fiducial cosmology, i.e., the PMILL cosmology (see Sec. 6.2.1). In our fiducial cosmology, the values of $D_{\rm V}(z)$ and $r_{\rm d}$ are,

$$D_{\rm V}^{\rm fid}(z = 0.60) = 2141.07\,{\rm Mpc} \tag{6.5.29}$$

$$D_{\rm V}^{\rm fid}(z = 0.74) = 2502.62\,{\rm Mpc} \tag{6.5.30}$$

$$D_{\rm V}^{\rm fid}(z = 0.93) = 2926.11\,{\rm Mpc} \tag{6.5.31}$$

$$r_{\rm d}^{\rm fid} = 148.13\,{\rm Mpc}\,. \tag{6.5.32}$$

The BAO scale can be extracted by fitting the monopole of the power spectrum (or correlation function) to a template that includes the dilation parameter. Therefore, the monopole of the power spectrum is modelled as the product of a smooth component and the BAO signal as (e.g. Anderson et al. 2014; Ross et al. 2015),

$$P_{0,\rm fit}(k) = P_{\rm sm}(k) {\rm O}_{\rm damp}(k/\alpha) \,, \tag{6.5.33}$$

where $P_{\rm sm}(k)$ is a smooth power spectrum, i.e., without any BAO feature, and ${\rm O}_{\rm damp}(k)$ represents the damped BAO signal (see below for the definitions of these quantities).

The smooth power spectrum component is modelled as (Anderson et al., 2014; Ross et al., 2015; Hernández-Aguayo et al., 2020b)

$$P_{\rm sm}(k) = B_p^2 P_{\rm nw}(k) + A_1 k + A_2 + \frac{A_3}{k} \,, \tag{6.5.34}$$

where $P_{\rm nw}(k)$ is a smooth "de-wiggled" template obtained using the fitting formula of Eisenstein & Hu (1998), B_p is a large-scale bias parameter, and A_1, A_2 and A_3 are further free parameters.

The oscillatory component of the power spectrum is given by,

$$\mathrm{O}_{\rm damp}(k) = 1 + \left(\frac{P_{\rm lin}(k)}{P_{\rm nw}(k)} - 1\right) e^{-\frac{1}{2}k^2\Sigma_{\rm nl}^2}\,, \tag{6.5.35}$$

where $\Sigma_{\rm nl}$ is a damping parameter.

The monopole of the redshift-space correlation function is given by the model (Anderson et al., 2014; Ross et al., 2015),

$$\xi_{0,\rm fit}(s) = B_s^2\xi_{\rm lin,\,damp}(\alpha s) + \frac{a_1}{s^2} + \frac{a_2}{s} + a_3\,, \tag{6.5.36}$$

where $\xi_{\rm lin,\,damp}(s)$ is the Fourier transform of $P_{\rm nw}(k)\mathrm{O}_{\rm damp}(k)$, B_s is the equivalent of B_p mentioned above, and a_1, a_2 and a_3 are polynomial free parameters.

To obtain the best-fitting α value, we use Bayesian statistics and maximise the likelihood, $\mathcal{L} \propto \exp(-\chi^2/2)$ (where χ^2 is defined by Eq. (6.5.13)) by fitting the measurements of the monopole of the power spectrum on scales with $k < 0.3\,h\,\mathrm{Mpc}^{-1}$ and on scales with $s > 40\,h^{-1}\mathrm{Mpc}$ for the monopole of the correlation function. To find the best-fitting α value and its confidence levels we again use the MCMC technique via the package EMCEE.

Fig. 6.17 displays the BAO feature in Fourier (left panel) and configuration space (right panel) at $z = 0.74$ (similar trends were found at $z = 0.60$ and $z = 0.93$). The BAO feature was isolated by dividing the best-fitting model and measurements of the monopole of the power spectrum by the smooth component of the best-fitting model. In the case of the monopole of the correlation function, we subtract the smooth component of the best-fitting model to the best-fitting model and measurements. We can see a clear BAO signal in both cases.

Our estimates of the dilation parameter are shown in Fig. 6.18 together with isotropic BAO measurements from the 6dFGRS at $z = 0.11$ (Beutler et al., 2011), the SDSS MGC at $z = 0.15$ (Ross et al., 2015), BOSS DR12 at $z = [0.38, 0.61]$ (Alam et al., 2017), WiggleZ at $z = [0.44, 0.6, 0.73]$ (Blake et al., 2011b), eBOSS DR14 LRGs at $z = 0.72$ (Bautista et al., 2018) and eBOSS DR14 QSO sample at $z = 1.52$ (Ata et al., 2018). The black errorbars are from the DESI forecast

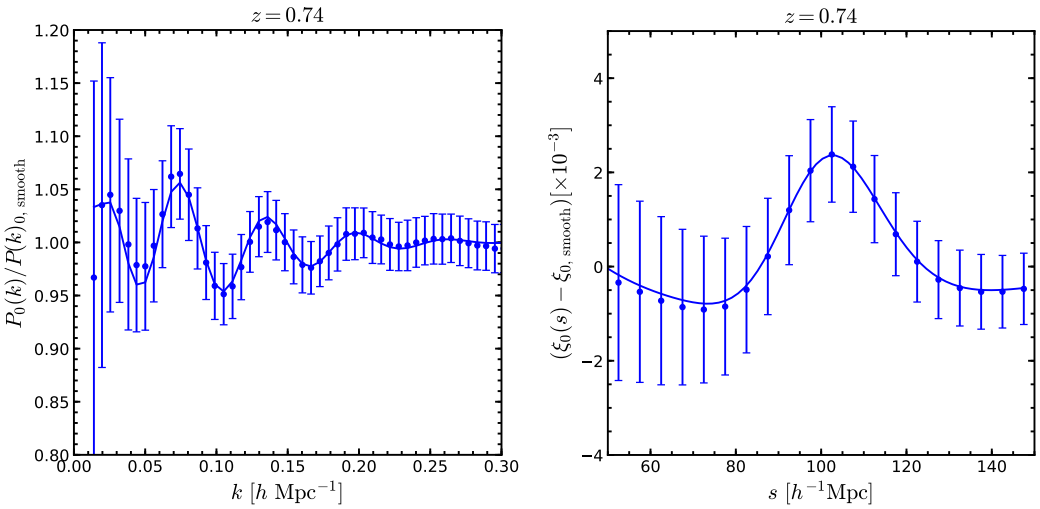

Figure 6.17: BAO signals in the monopole of the power spectrum (*left panel*) and correlation function (*right panel*) at $z = 0.74$. Blue dots with error bars come from the measurements from our GLAM-LRG catalogues. The solid lines show the predictions from the best-fitting BAO models. In order to highlight the BAO features, we have divided the $P(k)$ measurements and the best-fitting model by the no-wiggle power spectrum of the best-fitting model. In configuration space we have also subtracted the smooth component of the best-fitting model.

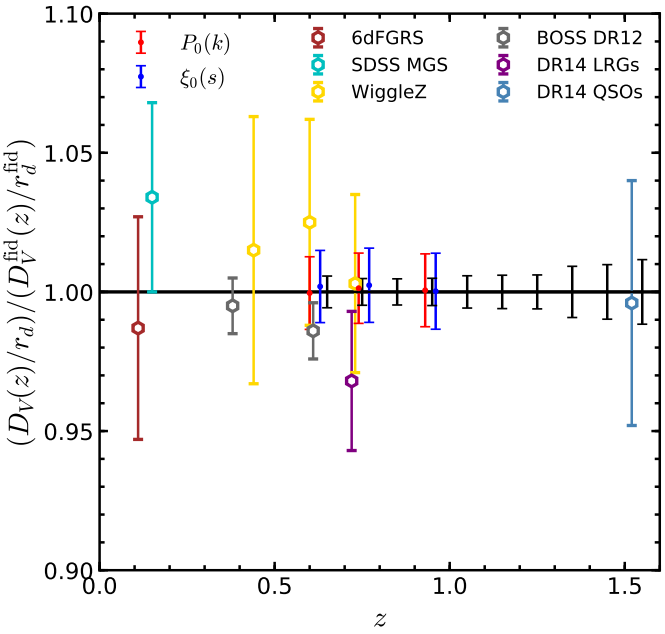

Figure 6.18: Isotropic BAO measurements as a function of redshift. Our estimates from the monopole of the power spectrum are shown by the red dots with errorbars while the blue dots with errobars represent the best-fitting values from the monopole of the correlation function. We show the measurements from different galaxy surveys as labelled. The black errorbars show the DESI 14K forecast presented in DESI Collaboration et al. (2016).

(see table 2.3 of DESI Collaboration et al., 2016). At a first glance, our estimates of the errorbar bars (red and blue symbols) have almost the same amplitude as those predicted for DESI; the simple discussion above in terms of the comparison of the GLAM simulation volume and the volume of the redshift shells to be probed by DESI suggest that the errors could differ by a factor of around two, although different assumptions are made in arriving at the two estimates.

Using the fiducial values of $D_{\rm V}^{\rm fid}$, Eqs. (6.5.29)−(6.5.31), we convert our best-fitting α values into distance measurements via Eq. (6.5.27),

$$D_{\rm V}(z=0.60) = \begin{cases} 2140 \pm 28\,(r_{\rm d}/r_{\rm d}^{\rm fid})\,{\rm Mpc} & P_0(k)\,, \\ 2145 \pm 27\,(r_{\rm d}/r_{\rm d}^{\rm fid})\,{\rm Mpc} & \xi_0(s)\,, \end{cases} \tag{6.5.37}$$

$$D_{\rm V}(z=0.74) = \begin{cases} 2505 \pm 31\,(r_{\rm d}/r_{\rm d}^{\rm fid})\,{\rm Mpc} & P_0(k)\,, \\ 2508 \pm 33\,(r_{\rm d}/r_{\rm d}^{\rm fid})\,{\rm Mpc} & \xi_0(s)\,, \end{cases} \tag{6.5.38}$$

$$D_{\rm V}(z=0.93) = \begin{cases} 2927 \pm 38\,(r_{\rm d}/r_{\rm d}^{\rm fid})\,{\rm Mpc} & P_0(k)\,, \\ 2926 \pm 40\,(r_{\rm d}/r_{\rm d}^{\rm fid})\,{\rm Mpc} & \xi_0(s)\,. \end{cases} \tag{6.5.39}$$

We find good agreement between our estimates and the fiducial values of $D_{\rm V}(z)$. The agreement is well within the 1σ level. In our case, the monopole of the correlation function gives slightly better constraints than the power spectrum. In general, we can estimate the isotropic BAO distance to better than 1.3 per cent in both spaces.

6.6 Summary

In this Chapter, we have presented predictions for the properties and clustering of LRGs selected using the colour-magnitude cuts in the $r, z, W1$ bands that will be applied in the DESI LRG survey (DESI Collaboration et al., 2016). The predictions were made using the GALFORM semi-analytic model of galaxy formation run on the PMILL N-body simulation (Baugh et al., 2019) and a suite of low-resolution, larger volume simulations run with the Parallel-PM N-body code GLAM (Klypin & Prada, 2018).

We made predictions for the abundance of DESI-like LRGs and explore how the target selection cuts affect which galaxies are selected and how these populate haloes and subhaloes. We find that a small but important fraction of the most massive galaxies (those with stellar mass $\log_{10}(M_*/\,h^{-1}\mathrm{M}_\odot) > 11.15$) are *not* selected as LRGs (see Fig. 6.4). A similar trend is seen in the galaxy luminosity function, and is most pronounced at shorter wavelengths: essentially all bright galaxies in the $W1$-band luminosity function are LRGs, but only roughly half of the galaxies in the bright end of the r-band luminosity function are LRGs. This shows that applying the full photometric selection is essential to reproduce LRGs in a galaxy formation model and that using a proxy, such as stellar mass, to select LRGs is at best an approximation. We explored the galaxy-(sub)halo connection of LRGs through the halo occupation distribution and the subhalo mass function. We find that the shape of the HOD does not follow the canonical shape proposed by Zheng et al. (2005); in particular, the occupation of central galaxies does not reach unity for the most massive haloes (see Fig. 6.5), and drops with increasing mass.

We compared the HOD and the subhalo mass functions of galaxies selected by their stellar mass with those measured for the LRGs (see Fig. 6.6). By doing this exercise, we reaffirm that the DESI-LRG cuts affect the selection of subhaloes that are populated by LRGs. Mass alone is not enough to determine if a subhalo hosts an LRG. By comparing the clustering of these galaxy samples (Fig. 6.7) we found a difference that ranges from 10% at $z = 0.6 - 0.74$ to up to 150% at $z = 0.93$. Hence, we conclude that using galaxy stellar mass as a proxy for selecting LRGs could change the expected clustering signal.

To prepare for the clustering measurements of DESI we ran 1000 GLAM simulations. When comparing the halo statistics between the GLAM simulation ensemble and the PMILL high-resolution run, we found good agreement between the halo mass functions, but differences of $\sim 10\%$ in the halo clustering (see Fig. 6.1). This difference can be attributed to the different halo finder used in the PMILL and GLAM simulations. Despite the difference in halo clustering, the galaxy clustering statistics measured from the GLAM-LRG catalogues are in good agreement with that in the PMILL-GALFORM LRG sample in both configuration and Fourier space. To popu-

late the GLAM halo catalogues with DESI-like LRGs we used the tabulated HODs obtained from GALFORM. We also found a good agreement between our clustering measurements in real-space with those reported by Kitanidis et al. (2020) and Zhou et al. (2020) (see upper panels of Figs. 6.8 and 6.9).

We extended the analysis of covariance and correlation matrices of GLAM simulations started by Klypin & Prada (2018) to galaxies and correlation functions (see Figs. 6.10-6.14). We found that the galaxy correlation matrix shows a different and more complex pattern than its dark-matter counterpart.

We presented predictions for the large-scale clustering of DESI-like LRGs in configuration and Fourier space, by extracting the linear growth rate from the linear Kaiser RSD model and the BAO scale from the isotropic dilation parameter. In a follow-up project, we plan to extend this study to non-linear models of RSDs and an anisotropic analysis of the BAO scale, including the impact of the light-cone survey geometry and observational systematic.

Using our GLAM-LRG catalogues we estimated the growth of structure from the ratio of the monopole in redshift space to the real-space power spectrum with a precision of $\sim 3-4\%$, and we can measure the BAO scale with a 1.3% precision in both configuration and Fourier space. Nevertheless, if we want to compare the precision of our measurements with those expected from DESI (table 2.3 of DESI Collaboration et al., 2016), our error estimations should take into account the contribution from the expected volume covered by DESI (see Sec. 6.5.2 for details). However, the amplitude of the statistical errors estimated from our best-fitting search on the linear growth rate and BAO scale are consistent with the forecast presented by DESI Collaboration et al. (2016).

Chapter 7

Conclusions

7.1 Summary of the thesis

7.1.1 Marked correlation functions in $f(R)$ gravity

In Chapter 2, we investigated if the differences of the unmarked correlation functions between three Hu & Sawicki $f(R)$ chameleon models with fixed $n = 1$ and $|f_{R0}| = 10^{-6}, 10^{-5}, 10^{-4}$ (denoted F6, F5 and F4) and GR could be boosted by using an alternative approach to measure galaxy clustering with the marked correlation function (Sheth et al., 2005; White, 2016). For this purpose we use two definitions for the environment of galaxies/haloes: a) the number density field and b) the Newtonian gravitational potential of the host halo. For the former we analyse three marks: i) an inverse power-law which enhances low-density regions (see Eq. (2.3.11)), ii) a log-transform mark which up-weighs intermediate- and high-density regions (see Eq. (2.3.12)) and iii) a Gaussian mark given by Eq. (2.3.17) which allows us to up-weight only intermediate-density regions, $\rho_R = 1.25 - 1.88$. For the latter we use a Gaussian mark which allows us to up-weight haloes (and galaxies within those haloes) with mass $10^{13} < M_{200c}/[h^{-1}M_{\odot}] < 10^{14}$.

If we consider the statistical errors presented in this chapter, then the differences between the $f(R)$ signals with respect to GR are significant. It should be feasible to test the differentiating power of marked clustering statistics using real data from current galaxy surveys. In future work we need to improve the resolution

of the simulations and make more realistic mock galaxy catalogues to allow a fairer comparison with upcoming observations.

In Chapter 2 we have demonstrated the potential of the marked correlation function to differentiate between gravity models. The next step is to extend these calculations, which were presented for massive galaxies, to the emission line galaxies that will be selected by the DESI and Euclid redshift surveys.

7.1.2 Redshift spaced distortions in modified gravity theories

In Chapter 3, we have presented results on the estimation of the redshift space distortion parameter, β, which is directly related to the linear growth rate of matter in the Universe. In order to understand the potential of using this parameter to constrain cosmological models, we have tested the estimation of this parameter for five different gravity models: a flat ΛCDM model based on General Relativity (GR), two variants of the Hu & Sawicki (2007) $f(R)$ gravity model (F6 and F5) and two variants of the normal branch of the DGP (Dvali et al., 2000) model (N5 and N1).

Our main conclusions from Chapter 3 are as follows:

1. Measurements of redshift space distortions on large scales can help us to distinguish between some gravity models, such as N1, but in general the model differences from GR are small compared with statistical and theoretical uncertainties (which depends on survey specifications), in particular for $f(R)$ or chameleon models in general.

2. Chameleon and Vainshtein models have distinct model predictions, which are directly related to the different properties of the fifth forces in the models: in chameleon-type models the fifth force is of Yukawa type and gets suppressed on scales above the inverse Compton mass of the scalar field (typically ~ 10 Mpc or smaller), while for Vainshtein-type models the fifth force is long ranged and can alter the large-scale velocity field substantially.

3. The lack of a Fingers-of-God term in the linear Kaiser model produces an over

and underestimation of the β parameter when using the statistics $R(s)$ and $Q(s)/\xi_w(s)$, respectively.

4. The linear Kaiser prediction is independent of the model of gravity, while the nonlinear model in its current form is based on GR only and we have tested it in $f(R)$ gravity models for the first time (the same nonlinear model was used to validate the estimation of the growth rate for nDGP models in Barreira et al. (2016)). The fact that the use of this 'incorrect' non-linear model produces reasonable constraints for β for the modified gravity models studied here offers a practical way to measure possible signatures of modified gravity in the large-scale structure of the Universe.

5. We have tested the effect of using different ranges of scales in the fitting, and found that for $s_{\rm min} = 20\,h^{-1}$Mpc the nonlinear model cannot recover β correctly at all redshifts for all models including GR. In spite of the theory predicting a higher β at the scale range with $s_{\rm min} = 20\,h^{-1}$Mpc, the relative difference between the MG models and GR agrees well with the fiducial values from the simulation. The higher, biased value recovered for β can be mitigated by excluding data between 20 and $40\,h^{-1}$Mpc, at the expense of increased measurement error.

6. Using different estimators such as multipoles and wedges can produce different constraints because of the different information they encode, but the difference is not statistically significant.

We note that our conclusions are different from other recent works, such as He et al. (2018). This is due to the focus on different scales (He et al. concentrated on small and highly nonlinear scales), and reflects the strong scale-dependence of the behaviours in some MG models.

7.1.3 Galaxy formation in braneworld models

In Chapter 4, we introduced a new set of full-physics hydrodynamical simulations of the nDGP braneworld model. We extended the SHYBONE (Simulating HYdrody-

namics BeyONd Einstein) simulations (Arnold et al., 2019) by exploring galaxy formation in the N5 and N1 nDGP models in boxes of sizes $62\,h^{-1}$Mpc and $25\,h^{-1}$Mpc using 2×512^3 dark matter particles and initial gas cells. This allowed us to explore, for the first time, the impact of baryonic physics on galactic scales in braneworld models of modified gravity and made predictions on the stellar content of dark matter haloes and galaxy evolution through cosmic time in these models.

We found significant differences between the GR and nDGP models in the power spectra and correlation functions of gas, stars and dark matter of up to ~ 25 per cent on large scales. Similar to their impact in the standard cosmological model (ΛCDM), baryonic effects can have a significant influence over the clustering of the overall matter distribution, with a sign that depends on scale. Studying the degeneracy between modified gravity and galactic feedback in these models, we found that these two physical effects on matter clustering can be cleanly disentangled, allowing for a method to accurately predict the matter power spectrum with baryonic effects included, without having to run hydrodynamical simulations.

Depending on the braneworld model, we found differences compared with GR of up to ~ 15 per cent in galaxy properties such as the stellar-to-halo-mass ratio, galaxy stellar mass function, gas fraction and star formation rate density. The amplitude of the fifth force is reduced by the presence of baryons in the very inner part of haloes, but this reduction quickly becomes negligible above ~ 0.1 times the halo radius.

The SHYBONE-nDGP simulations aim to assist future galaxy surveys by making predictions for the small-scale galaxy clustering and stellar properties in galaxies.

7.1.4 BAO peak position from different galaxy selections

In Chapter 5, we investigated if, for a fixed number density of targets and redshift, there is an optimal way to select a galaxy sample in order to measure the baryon acoustic oscillation (BAO) scale, which is used as a standard ruler to constrain the cosmic expansion.

We used the mock galaxy catalogue built by Smith et al. (2017) in the Millennium-XXL N-body simulation with a technique to assign galaxies to dark matter haloes based on halo occupation distribution modelling, we considered the clustering of

galaxies selected by luminosity, colour and local density. We assessed how well the BAO scale can be extracted by fitting a template to the power spectrum measured for each sample.

We found that the BAO peak position is recovered equally well for samples defined by luminosity or colour, while there is a bias in the BAO scale recovered for samples defined by density. The BAO position is contracted to smaller scales for the densest galaxy quartile and expanded to large scales for the two least dense galaxy quartiles. For fixed galaxy number density, density-selected samples have higher uncertainties in the recovered BAO scale than luminosity- or colour-selected samples.

Our results are derived in the context of a HOD mock catalogue (Smith et al., 2017) in which galaxies are assigned magnitudes (r-band) and colours ($^{0.1}(g-r)$) such that they provide a reasonable match to the projected two-point correlation function as measured in the SDSS and GAMA surveys (Zehavi et al., 2011; Farrow et al., 2015). It remains to be seen if the same conclusions are valid when using more complex but more physically realistic methods to populate haloes with galaxies, such as hydrodynamic simulations or semi-analytic models of galaxy formation. These physical models do not assume a particular form for the halo occupation distribution, but instead predict the galactic content of haloes. This is directly relevant to the case of applying different selections to construct galaxy samples. Furthermore, hydrodynamical simulations can address the displacement of matter due to baryonic physics, which may have an impact on the BAO signal. Due to computational cost and the requirement for high resolution for robust implementation of the physics, hydrodynamical simulations are not yet able to reach the gigaparsec volumes needed for BAO studies can easily be simulated, however semi-analytic models (e.g. Henriques et al., 2015; Lacey et al., 2016; Lagos et al., 2018; Baugh et al., 2019) look more promising on short time scales. Such studies will be crucial to characterise any systematic shift in the BAO position resulting from selecting galaxy subsamples based on luminosity, colour, environment or emission lines.

7.1.5 Covariance and clustering of DESI-like LRGs

In Chapter 6, we described a novel technique which uses the semi-analytical model of galaxy formation GALFORM, embedded in the high-resolution N-body Planck-Millennium simulation, to populate with DESI-like LRGs a thousand halo catalogues generated using the Parallel-PM N-body GLAM code.

Our hybrid scheme allows us to make clustering predictions on scales that cannot be modelled in the original PMILL N-body simulation. LRGs are selected in the redshift range $z = 0.6-1$ from the GALFORM output using similar colour-magnitude cuts in the r, z and $W1$ bands to those that will be applied in the Dark Energy Spectroscopic Instrument (DESI) survey.

We found that the LRG-halo connection is non-trivial, leading to the prediction of a non-standard halo occupation distribution; in particular, the occupation of central galaxies does not reach unity for the most massive haloes, and drops with increasing mass. The GLAM catalogues reproduce the abundance and clustering of the LRGs predicted by GALFORM, and show good agreement with recent measurements of the clustering of DESI-like LRGs using photometric redshifts. We use the GLAM mocks to compute the covariance matrices for the two-point correlation function and power spectrum of the LRGs and their background dark matter density field, revealing important differences. We also make predictions for the linear-growth rate and the baryon acoustic oscillations distances at $z = 0.6$, 0.74 and 0.93.

We conclude that the colour-magnitude cuts have a big impact on the properties and clustering of LRGs, showing that LRGs are different than stellar mass selected galaxies. But more importantly, the analysis presented in this Chapter provided accurate estimates on the galaxy clustering expected by DESI-LRGs thanks to our GLAM-HOD pipeline. Moreover, our pipeline can be easily adapted to the specifications of other next generation surveys such as Euclid, the Vera Rubin Observatory (formerly the LSST), PFS and 4MOST.

7.2 Future work

7.2.1 Unveiling the nature of gravity with future cosmological simulations and galaxy surveys

As we discussed throughout this thesis, cosmological simulations play a central role in the preparation for future surveys, so we need to adapt existing N-body codes to study the clustering of galaxies at an unprecedented level of accuracy. Future surveys will only be able to meet their goal of understanding the cosmic acceleration if we have predictions for galaxy formation that match such accuracy in models beyond Einstein's General Relativity (GR). However, simulating an MG universe is not an easy task (as we showed in Chapters 2-4). Given the non-linear nature of the differential equations to be solved, an MG simulation can be more than 10 times slower than a GR simulation. For this reason, the investigation of fast N-body simulations techniques (e.g., GLAM Klypin & Prada (2018)) to generate synthetic sky catalogues in MG models is crucial.

We are planning to adapt the GLAM code, presented in Chapter 6, to run large N-body simulations of MG models. The performance of GLAM has been tested against other approximate methods such as COLA and FastPM showing a speed-up of 1.5× and 3.9×, respectively (Klypin & Prada, 2018), making it ideal to adapt for MG and insert into our pipeline to analyse galaxy clustering for future surveys. We are going to implement the chameleon $f(R)$ gravity model (Hu & Sawicki, 2007) and the nDGP braneworld model (Dvali et al., 2000) into GLAM. As an example of possible applications of this new code, we will generate mock catalogues of luminous red and emission-line galaxies (LRGs and ELGs) for the DESI following the method developed in Chapter 6. As we mentioned before, this method can easily be extended to other surveys, e.g., Euclid, the LSST, SKA and the Subaru-PFS.

The galaxy catalogues we will build will be used for a wide range of research topics. We are interested in constraining chameleon $f(R)$ gravity and Vainshtein type (e.g., nDGP) models by combining galaxy clustering measurements, from two-point statistics (correlation functions and power spectrum) to higher-order estimators (e.g., bispectrum) including redshift space distortions analysis and gravitational

lensing statistics. Also, we will be able to constrain chameleon $f(R)$ gravity using the clustering of emission-line galaxies. ELGs tend to populate low-mass haloes where the chameleon screening mechanism is inefficient, so their clustering pattern will be modified by the faster growth of small haloes in modified gravity. This study will complement the results of Chapters 2 and 3.

A rigorous analysis of the estimators and their ability to constrain MG models requires us to generate a substantial number of realisations of simulations to explore the statistical properties of the estimators and characterise the significance of the differences observed (as shown in Chapter 6). Furthermore, for comparing models one also needs the covariance matrices to accurate estimate the errors in the measurements and to reach the level of statistical precision needed for future surveys, this require the generation of thousands mock catalogues and will be possible with our MG version of GLAM.

7.2.2 Exploring the galaxy-halo connection in modified gravity models

Besides the study of the large-scale distribution of galaxies in the Universe, it is important to understand the evolution of individual galaxies in different gravity models by exploring the distribution of gas and stars on galactic scales and to confront theoretical expectations with observations of the Milky-Way obtained by e.g. the GAIA mission (Gaia Collaboration et al., 2016).

An important aspect which will be enabled our SHYBONE-nDGP simulations (presented in Chapter 4) is a deeper understanding of the galaxy-halo connection, especially in non-standard cosmological models. This connection is essential to constrain cosmological models using galaxy surveys and to explain the properties and distribution of dark matter with galaxies.

In addition, the high-resolution and the large number of snapshots of the DM-only version of the SHYBONE simulations offer the possibility to explore galaxy formation using semi-analytical models such as GALFORM. These results will complement our predictions of the galaxy content of dark matter haloes from the full-hydrodynamical simulations.

Also, we will study the small-scale galaxy clustering using different galaxy properties, such as galaxy stellar mass, luminosity in different bands, star formation rate and others. We will use these properties to study the redshift-space clustering at scales $s \leq 10\,h^{-1}$Mpc in different gravity models to find signatures of modified gravity on the smallest scales.

Finally, we plan to continue improving our MG numerical simulations, for example, to simulate Milky-Way and Local-Group like systems through zoom techniques. These simulations will help us to understand the impact of modified gravity on small cosmological scales and the more complex of the astrophysical processes.

7.3 Concluding remarks

Cosmology is entering into a golden era of high precision measurements and more detailed numerical simulations. The data that will be provided by DESI, Euclid, 4MOST, PFS, etc., will be used to reveal the nature of the accelerated expansion of the Universe. In this thesis, we have highlighted the importance of making accurate predictions of the galaxy formation and clustering in the standard and non-standard cosmological scenarios. We hope that the results presented in this thesis will help in the analysis and preparation of future galaxy surveys to put tight constraints in modified gravity models and to test the nature of gravity on cosmological scales.

Appendix A

Tests of systematic effects

In this Appendix we include some tests of the systematic effects in the constraints presented in Chapter 3, and materials that contain additional information to the results shown in the main text.

A.1 Systemtics validation: linear bias

Figure A.1 shows the linear bias parameter derived from the fitting using the non-linear model compared to the actual values measured from the mock galaxy catalogues. The left panel shows the bias values obtained by using a minimum fitting scale $s_{\rm min} = 20\,h^{-1}$Mpc and the right panel corresponds to using $s_{\rm min} = 40\,h^{-1}$Mpc. In the MCMC fitting, the matter power spectrum was calculated by calling the CAMB code with an input of fiducial σ_8. The amplitude of the matter power spectrum is therefore degenerate with the linear bias the b_1. In Figure A.1, the linear bias is obtained by a rescaling, $b_1 = b_{1_{\rm MCMC}}\sigma_8^{\rm input}/\sigma_8^{\rm true}$. The initial conditions of our simulations were generate using Zel'dovich approximation at $z_{\rm ini}$, which has a worse-than-percent-level accuracy (Crocce et al., 2006); therefore the $\sigma_8^{\rm true}$ value we used in this rescaling is 0.844, which was obtained by requiring that the resulting CAMB power spectrum to best agree with the one measured directly from the N-body initial condition.

The filled and open symbols in Figure A.1 are respectively the linear bias b_1 for the different models and redshifts rescaled using the corresponding the constraints

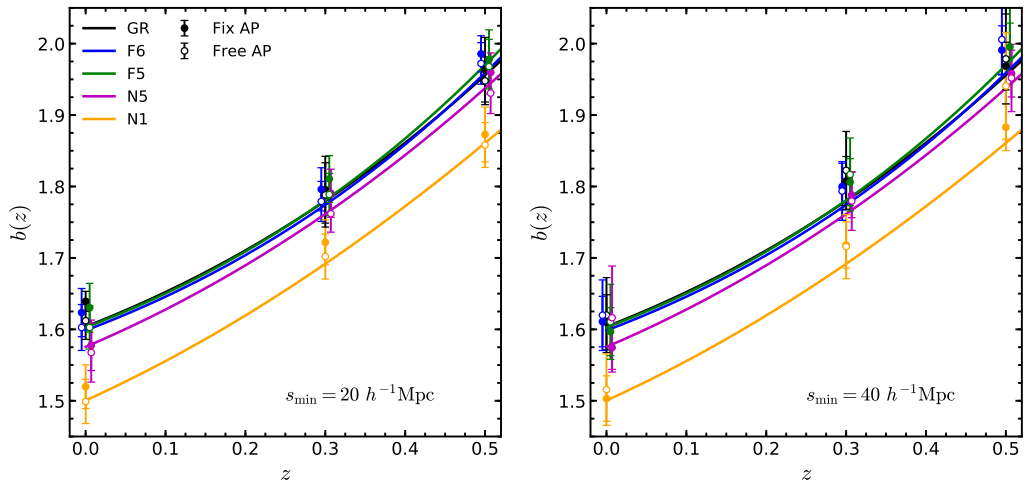

Figure A.1: A comparison of the linear bias parameter b_1 obtained by appropriately rescaling the best-fit value $b_{1_{\rm MCMC}}$ using the nonlinear model (symbols) and from direct measurements using the mock galaxy catalogues (lines), for the three redshifts (as shown by the horizontal axis) and all models (see legend). The filled and open symbols are respectively from MCMC fittings where the AP parameters $q_\perp, q_\parallel$ are fixed and are left free to vary; the left and right panels are respectively from MCMC fittings with $s_{\rm min} = 20$ and $40h^{-1}$Mpc.

on $b_{1_{\rm MCMC}}$ values where the AP parameters are fixed and left free to vary during the MCMC fitting. We can see that in both cases they agree well with the true results measured from the mock galaxy catalogues (the coloured curves) for GR, F6, F5 and N5. For N1 the constraint on the bias values are significantly higher compared with the true values, which is because the $\sigma_8^{\rm true}$ used in the rescaling is the GR value, and the corresponding N1 value is larger (for the other MG models the difference of $\sigma_8^{\rm true}$ from GR is smaller). We also find that the b_1 values are well recovered for both $s_{\rm min} = 20$ and $40\,h^{-1}$Mpc.

A.2 The impact of covariance matrix

In the constraints based on linear perturbation theory in Section 3.4.1, the error bars in the χ^2 minimisation were obtained as the standard deviations from the 5 realisations with 3 different LOS of redshift-space galaxy catalogues for each model,

which neglects the correlation between the different s bins. Here we would like to check the impact of including such correlations on the parameter inference for β.

To this end we have redone the fitting of β by using the covariance matrix from the Gaussian approximation instead of the standard deviations from the 15 realisations in Eq. (6.5.13). We consider two estimators predicted using the linear Kaiser model, clustering wedges and $Q(s)$ (see Sec. 3.4.1 for details), for this test. Since we are taken the covariance matrix, we minimise a χ^2 given by

$$\chi^2(\beta) = [E(s_i) - E^{\rm th}(s_i;\beta)]^T C_{ij}^{-1(E)} [E(s_j) - E^{\rm th}(s_j;\beta)]\,, \tag{A.2.1}$$

where $E(s)$ is the measured estimator, $E^{\rm th}(s;\beta)$ is the theoretical prediction from the linear model and $C_{ij}^{(E)}$ is the covariance matrix for each estimator.

For linear clustering wedges, we use the covariance matrix from their non-linear analogue. In the left panel of Fig. A.2 we can find the results of this exercise for scales $s_{\rm min} = 40\,h^{-1}$Mpc. The result shows substantial difference from that displayed in the lower right panel of Fig. 3.5. This suggests that the exact way to estimate the error budget can have a non-negligible impact on the calculation of χ^2, and consequently on the estimation of β. As we found in Sec. 3.4.1, the best-fitting β values when $s_{\rm min} = 40\,h^{-1}$Mpc are closer to the true values than the results at $s_{\rm min} = 20\,h^{-1}$Mpc. However, these estimations are once again well below to the true values of β as measured from the mock galaxy catalogues. One of the explanation for this behaviour could be due to the correlation between the error and the data itself. As pointed out by (Dodelson & Schneider, 2013) when the error is estimated from data and especially when it is positively correlated with the data, the inferred parameters are likely to be biased high. Also we have to consider the fact that the 15 realizations have certain overlap among each other. Further tests should be done in the future. Again, the relative differences between MG and GR are consistent with the previous findings in linear and nonlinear models.

We tried the same test for $Q(s)$, by using the Kaiser formula to predict its theoretical value and the same covariance matrix used for the nonlinear model to estimate the corresponding $Q(s)-$covariance matrix. Starting from the Gaussian covariance matrix for the correlation multipoles, we applied a basis transformation

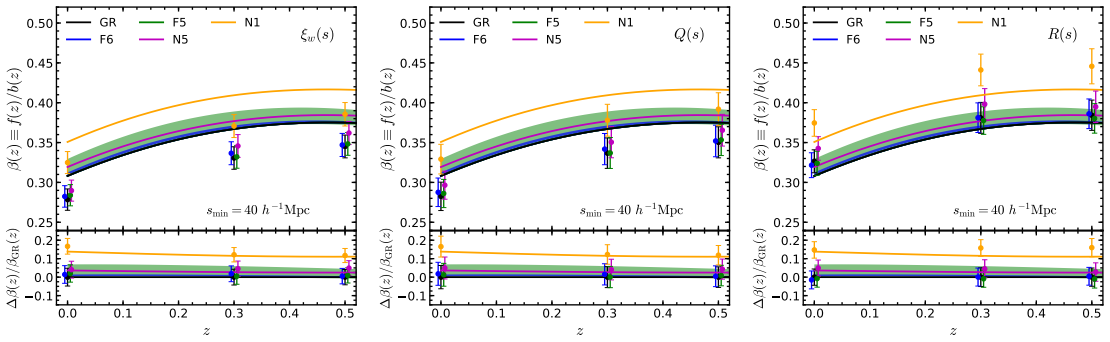

Figure A.2: *Left panel*: Similar to the third row of Figure 3.5 but now we have used the full covariance matrix from the nonlinear Markov chains to estimate the best-fit values and error bars for β by minimising the χ^2 described in the text. *Middle panel*: the same as the left panel, but the estimator used in the constraint is $Q(s)$. *Right panel*: the same as the previous panels, but using the $R(s)$ estimator.

and obtained a covariance for the $Q(s)$ estimator,

$$C^Q_{ij} \equiv \sum_{l,m} \frac{\partial Q_i}{\partial V_l} \frac{\partial Q_j}{\partial V_m} C_{lm}, \tag{A.2.2}$$

where C_{lm} is the covariance matrix for $[\xi_0, \xi_2]$ and $\mathbf{V} = [\xi_0, \xi_2]$ is the data vector. These tests showed similar qualitative behaviour to the case of using correlation function wedges discussed above, with more biased constraints on β, and the results are shown in the middle panel of Figure A.2.

Following a similar procedure to the $Q(s)$ estimator, we generated a covariance matrix for $R(s)$. The covariance matrix for the $R(s)$ estimator requires the knowledge of the covariance between the real space correlation function and the redshift space monopole. To achieve that, first, we modified the Eq. (15) in Grieb et al. (2016) by inserting the product of power spectrum both in real and redshift space. Second, a basis transformation similar to Eq. (A.2.2) is applied,

$$C^R_{ij} \equiv \sum_{p,q} \frac{\partial R_i}{\partial U_p} \frac{\partial R_j}{\partial U_q} C_{pq}\,, \tag{A.2.3}$$

where C_{pq} is the covariance matrix for $[\xi_0, \xi_r]$ with data vector $\mathbf{U} = [\xi_0, \xi_r]$. The biggest impact of the covariance matrix is the reduction of the error bar for all models at all redshifts (see right panel of Fig. A.2). The best-fitting β values are

higher than the fiducial values because there is an offset between the simulation measurements and the theoretical expectations (see left panel of Fig. 3.4).

On the other hand, we have checked explicitly (not shown here) including correlations between different s bins, i.e., the non-diagonal elements of the covariance matrix, leads to small changes in the best-fitting β values.

A.3 Posterior distributions of parameters

In the discussions in the main text, we have mainly focused on the constraints and posterior distribution of the parameter β. However, constraints on the other, nuisance, parameters could also be of interest, not only because they can help us to understand/interpret the results, but also because some of these parameters are physically meaningful quantities which may be affected by modified gravity.

Figure A.3 shows the posterior distribution of the parameters in the MCMC fit. The different colours correspond to different cosmological models (following the same colour scheme as used in all the other plots). In these MCMC runs, all parameters including the AP parameters $q_\perp, q_\parallel$ were allowed to vary freely. The estimators used are the three multipole moments ξ_l, with $s_{\rm min} = 40\,h^{-1}$Mpc. All results are at $z = 0.5$. We can see that $f\sigma_8$ shows by far the largest difference between the different gravity models, while most other parameters are fairly similar in all models. We have also checked the same figure from using the three wedges (ξ_w) as the estimators, and found the resulting posterior distributions of all parameters to be nearly identical (not shown here).

For the case of $s_{\rm min} = 20h^{-1}$Mpc, we found that using correlation function wedges ($\xi_w(s)$) and multipole moments ($\xi_l(s)$) can lead to quite distinct posterior distributions for some parameters, in particular b_2 and $a_{\rm vir}$ (see Fig. A.4). This is not surprising given that the two estimators differ by the small-scale information they contain, which are most relevant to these two parameters. The constraints on the other parameters are more or less consistent between the two estimators. Comparing Figs. A.3 and A.4, we can see that (i) the constraint $f\sigma_8$ is stronger in the case of $s_{\rm min} = 20\,h^{-1}$Mpc, similar to what was found in Figure 3.6 and by

Barreira et al. (2016), and (ii) the uncertainties in the parameter constraints are smaller in the case of $s_{\rm min} = 40\,h^{-1}$Mpc, reflecting the fact that more information (on smaller scales) is used. These indicate the importance of using a more accurate model for the theoretical predictions for parameter constraints and inferences.

We have also tested the effects of fixing the AP parameters in the MCMC fitting, and found its effect on the nuisance parameters is much smaller than that of using different estimators (multipoles vs. wedges). Regarding the β parameters the difference of free/fixing AP parameter is within one σ for different models over the redshifts. The results are not shown here for simplicity.

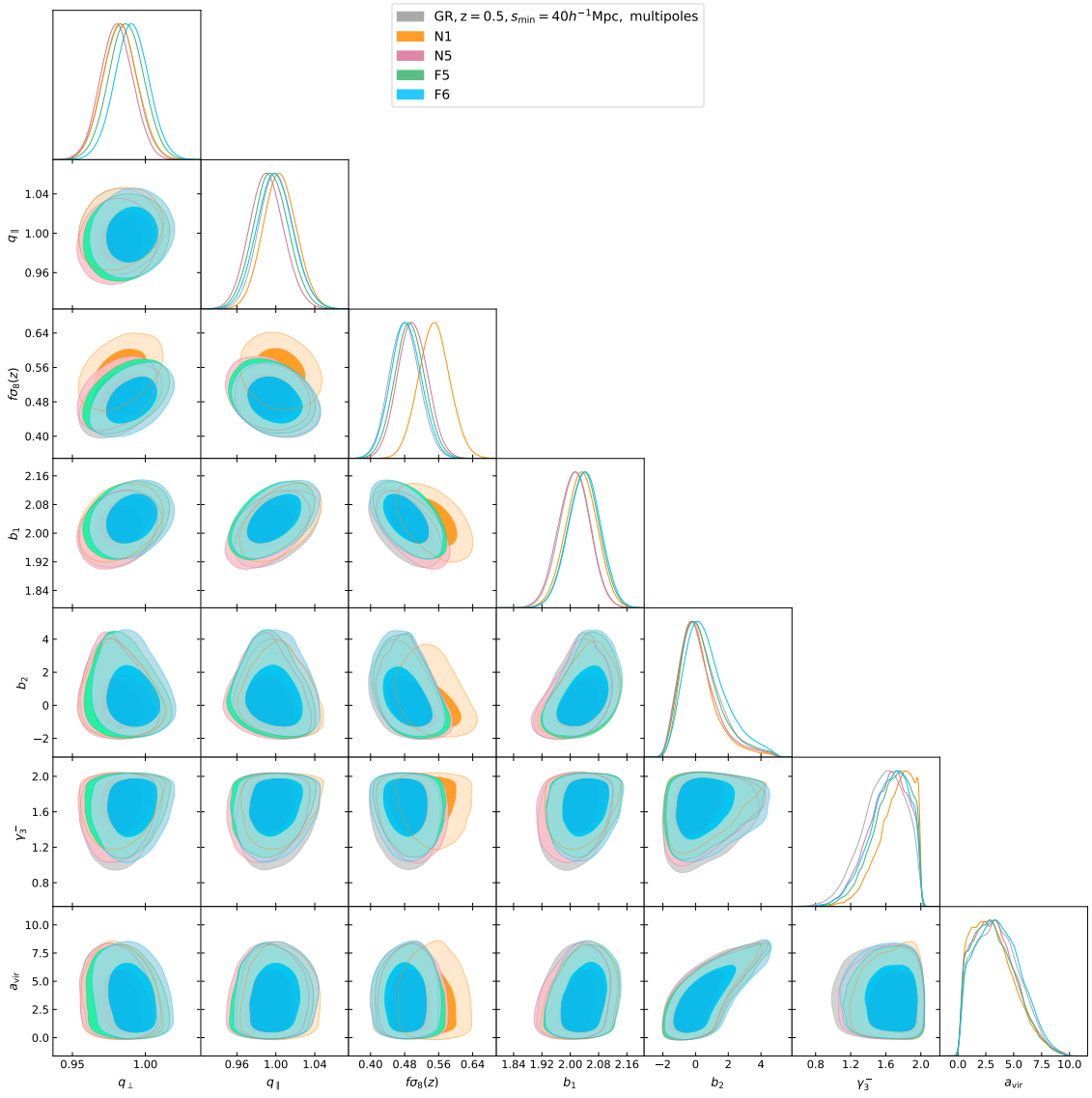

Figure A.3: Posterior distribution of the parameters using three multipoles $\xi_{\ell=0,2,4}$ with a minimum fitting range $s_{\rm min} = 40\,h^{-1}$Mpc for different cosmological models. The distribution is evaluated at redshift $z = 0.5$. The contours represent the 68% (darker region) and 95% (lighter region) confidence level.

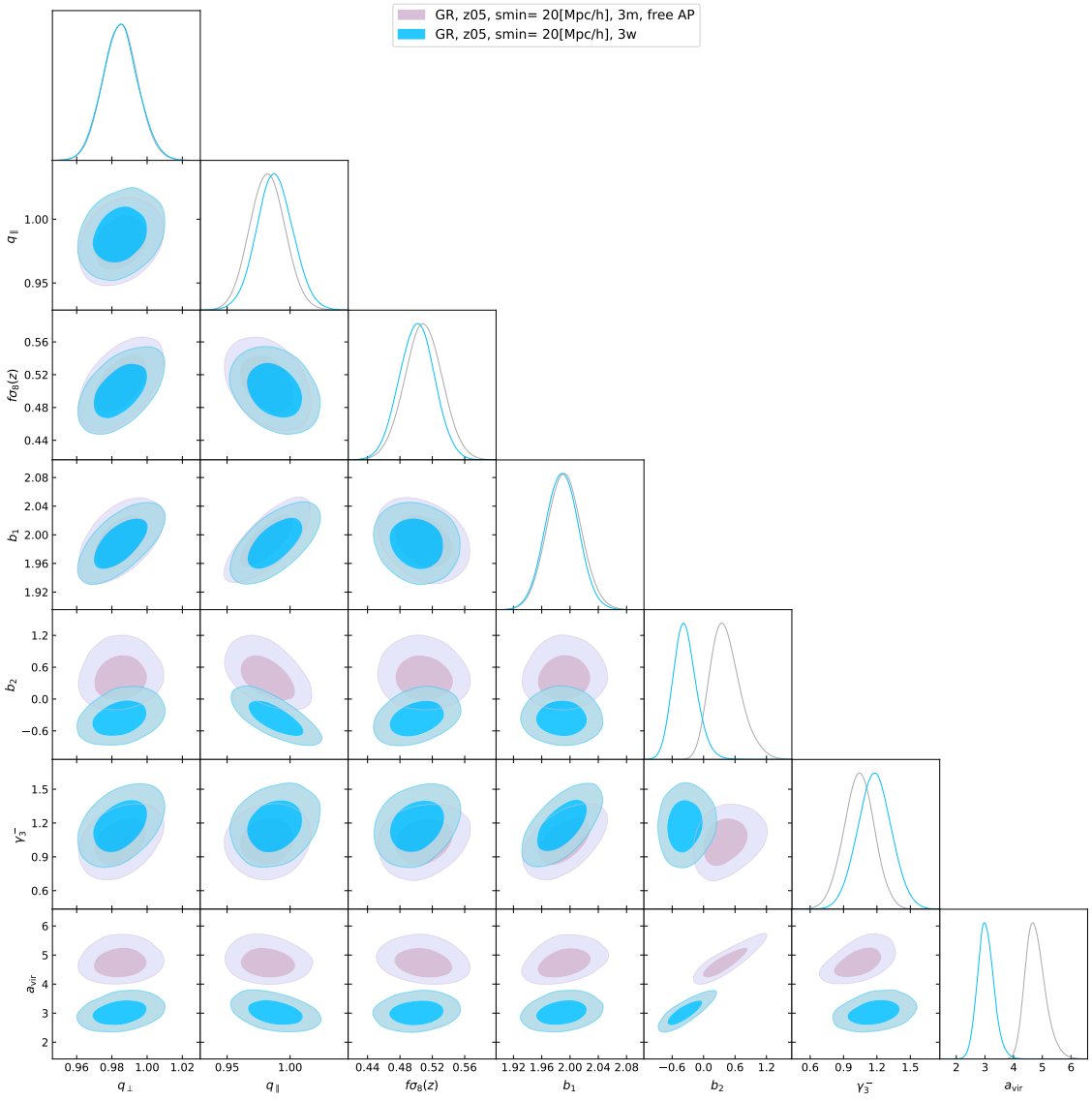

Figure A.4: Posterior distribution of parameters using three multipole moments ($\xi_l(s)$, purple colour) and three correlation function wedges ($\xi_w(s)$, blue colour). The dark and light shaded regions are respectively the 1σ and 2σ contours, and the 1D marginalised distributions for the different parameters are shown as curves. The results are from the MCMC chains for GR at $z = 0.5$, where the AP parameters were left free to vary, and the minimum scale used for the fitting was $s_{\rm min} = 20h^{-1}$Mpc.

Bibliography

Achitouv I., Blake C., 2015, Phys. Rev. D, 92, 083523

Ade P. A. R., et al., 2014, Astron. Astrophys., 571, A16

Alam S., et al., 2015, Astrophys. J. Suppl., 219, 12

Alam S., et al., 2017, Mon. Not. Roy. Astron. Soc., 470, 2617

Alcock C., Paczynski B., 1979, Nature, 281, 358

Allen S. W., Schmidt R. W., Ebeling H., Fabian A. C., van Speybroeck L., 2004, Mon. Not. Roy. Astron. Soc., 353, 457

Allen S. W., Rapetti D. A., Schmidt R. W., Ebeling H., Morris G., Fabian A. C., 2008, Mon. Not. Roy. Astron. Soc., 383, 879

Almeida C., Baugh C. M., Lacey C. G., 2007, Mon. Not. Roy. Astron. Soc., 376, 1711

Almeida C., Baugh C., Wake D., Lacey C., Benson A., Bower R., Pimbblet K. A., 2008, Mon. Not. Roy. Astron. Soc., 386, 2145

Anderson L., et al., 2012, Mon. Not. Roy. Astron. Soc., 427, 3435

Anderson L., et al., 2014, Mon. Not. Roy. Astron. Soc., 441, 24

Angulo R. E., Baugh C. M., Frenk C. S., Lacey C. G., 2008, Mon. Not. Roy. Astron. Soc., 383, 755

Angulo R. E., Springel V., White S. D. M., Jenkins A., Baugh C. M., Frenk C. S., 2012, Mon. Not. Roy. Astron. Soc., 426, 2046

Armijo J., Cai Y.-C., Padilla N., Li B., Peacock J. A., 2018, Mon. Not. Roy. Astron. Soc., 478, 3627

Arnalte-Mur P., Hellwing W. A., Norberg P., 2017, Mon. Not. Roy. Astron. Soc., 467, 1569

Arnold C., Li B., 2019, Mon. Not. Roy. Astron. Soc., 490, 2507

Arnold C., Puchwein E., Springel V., 2014, Mon. Not. Roy. Astron. Soc., 440, 833

Arnold C., Puchwein E., Springel V., 2015, Mon. Not. Roy. Astron. Soc., 448, 2275

Arnold C., Springel V., Puchwein E., 2016, Mon. Not. Roy. Astron. Soc., 462, 1530

Arnold C., Leo M., Li B., 2019, Nat. Astron., 3, 945

Ata M., Kitaura F.-S., Müller V., 2015, Mon. Not. Roy. Astron. Soc., 446, 4250

Ata M., et al., 2018, Mon. Not. Roy. Astron. Soc., 473, 4773

Baldry I., et al., 2012, Mon. Not. Roy. Astron. Soc., 421, 621

Barreira A., Bose S., Li B., 2015, JCAP, 1512, 059

Barreira A., Sánchez A. G., Schmidt F., 2016, Phys. Rev., D94, 084022

Barreira A., Krause E., Schmidt F., 2018, JCAP, 6, 015

Baugh C. M., 2006, Rept. Prog. Phys., 69, 3101

Baugh C. M., Gaztanaga E., Efstathiou G., 1995, Mon. Not. Roy. Astron. Soc., 274, 1049

Baugh C. M., Lacey C. G., Frenk C. S., Granato G. L., Silva L., Bressan A., Benson A. J., Cole S., 2005, Mon. Not. Roy. Astron. Soc., 356, 1191

Baugh C. M., et al., 2019, Mon. Not. Roy. Astron. Soc., 483, 4922

Baumgarten F., Chuang C.-H., 2018, Mon. Not. Roy. Astron. Soc., 480, 2535

Bautista J. E., et al., 2018, Astrophys. J., 863, 110

Behroozi P. S., Wechsler R. H., Wu H.-Y., 2013a, Astrophys. J., 762, 109

Behroozi P. S., Wechsler R. H., Conroy C., 2013b, Astrophys. J., 770, 57

Benitez-Llambay A., 2015, py-sphviewer: Py-SPHViewer v1.0.0, doi:10.5281/zenodo.21703, http://dx.doi.org/10.5281/zenodo.21703

Benson A. J., 2010, Phys. Rept., 495, 33

Benson A. J., 2012, New Astron., 17, 175

Berlind A. A., Weinberg D. H., 2002, Astrophys. J., 575, 587

Bernardi M., et al., 2003, Astron. J., 125, 1866

Bernardi M., Sheth R. K., Nichol R. C., Schneider D., Brinkmann J., 2005, Astron. J., 129, 61

Bernardi M., Meert A., Sheth R., Vikram V., Huertas-Company M., Mei S., Shankar F., 2013, Mon. Not. Roy. Astron. Soc., 436, 697

Beutler F., et al., 2011, Mon. Not. Roy. Astron. Soc., 416, 3017

Beutler F., et al., 2012, Mon. Not. Roy. Astron. Soc., 423, 3430

Beutler F., et al., 2017, Mon. Not. Roy. Astron. Soc., 464, 3409

Birkin J., Li B., Cautun M., Shi Y., 2019, Mon. Not. Roy. Astron. Soc., 483, 5267

Blake C., Glazebrook K., 2003, Astrophys. J., 594, 665

Blake C., Collister A., Lahav O., 2008, Mon. Not. Roy. Astron. Soc., 385, 1257

Blake C., et al., 2011a, Mon. Not. Roy. Astron. Soc., 415, 2876

Blake C., et al., 2011b, Mon. Not. Roy. Astron. Soc., 418, 1707

Blake C., et al., 2013, Mon. Not. Roy. Astron. Soc., 436, 3089

Blas D., Lesgourgues J., Tram T., 2011, JCAP, 1107, 034

Blot L., et al., 2019, Mon. Not. Roy. Astron. Soc., 485, 2806

Bose B., Koyama K., 2016, JCAP, 1608, 032

Bose B., Koyama K., 2017, JCAP, 1708, 029

Bose S., Hellwing W. A., Li B., 2015, JCAP, 1502, 034

Bose B., Koyama K., Hellwing W. A., Zhao G.-B., Winther H. A., 2017a, Phys. Rev. D, 96, 023519

Bose S., Li B., Barreira A., He J.-h., Hellwing W. A., Koyama K., Llinares C., Zhao G.-B., 2017b, JCAP, 1702, 050

Bower R. G., Benson A., Malbon R., Helly J., Frenk C., Baugh C., Cole S., Lacey C., 2006, Mon. Not. Roy. Astron. Soc., 370, 645

Brax P., van de Bruck C., Davis A.-C., Shaw D., 2010, Phys. Rev., D82, 063519

Brax P., Davis A.-C., Li B., Winther H. A., 2012a, Phys. Rev., D86, 044015

Brax P., Davis A.-C., Li B., 2012b, Phys. Lett., B715, 38

Brown M. J. I., et al., 2008, Astrophys. J., 682, 937

Bryan G. L., Norman M. L., 1998, Astrophys. J., 495, 80

Bullock J. S., Boylan-Kolchin M., 2017, Ann. Rev. Astron. Astrophys., 55, 343

Burrage C., Sakstein J., 2018, Living Rev. Rel., 21, 1

Cabre A., Gaztanaga E., 2009a, Mon. Not. Roy. Astron. Soc., 393, 1183

Cabre A., Gaztanaga E., 2009b, Mon. Not. Roy. Astron. Soc., 396, 1119

Cabre A., Vikram V., Zhao G.-B., Jain B., Koyama K., 2012, JCAP, 1207, 034

Cai Y.-C., Padilla N., Li B., 2015, Mon. Not. Roy. Astron. Soc., 451, 1036

Cai Y.-C., Taylor A., Peacock J. A., Padilla N., 2016, Mon. Not. Roy. Astron. Soc., 462, 2465

Campbell D. J. R., et al., 2015, Mon. Not. Roy. Astron. Soc., 452, 852

Carroll S. M., Duvvuri V., Trodden M., Turner M. S., 2004, Phys. Rev., D70, 043528

Cataneo M., et al., 2015, Phys. Rev., D92, 044009

Cataneo M., Rapetti D., Lombriser L., Li B., 2016, JCAP, 1612, 024

Catelan P., Lucchin F., Matarrese S., Porciani C., 1998, Mon. Not. Roy. Astron. Soc., 297, 692

Cautun M., Paillas E., Cai Y.-C., Bose S., Armijo J., Li B., Padilla N., 2018, Mon. Not. Roy. Astron. Soc., 476, 3195

Chan K. C., Scoccimarro R., 2009, Phys. Rev. D, 80, 104005

Chan K. C., Scoccimarro R., Sheth R. K., 2012, Phys. Rev. D, 85, 083509

Chaves-Montero J., Angulo R. E., Schaye J., Schaller M., Crain R. A., Furlong M., Theuns T., 2016, Mon. Not. Roy. Astron. Soc., 460, 3100

Clampitt J., Cai Y.-C., Li B., 2013, Mon. Not. Roy. Astron. Soc., 431, 749

Colavincenzo M., et al., 2019, Mon. Not. Roy. Astron. Soc., 482, 4883

Cole S., Lacey C., 1996, Mon. Not. Roy. Astron. Soc., 281, 716

Cole S., Fisher K. B., Weinberg D. H., 1994, Mon. Not. Roy. Astron. Soc., 267, 785

Cole S., Lacey C. G., Baugh C. M., Frenk C. S., 2000, Mon. Not. Roy. Astron. Soc., 319, 168

Cole S., et al., 2005, Mon. Not. Roy. Astron. Soc., 362, 505

Conroy C., Wechsler R. H., Kravtsov A. V., 2006, Astrophys. J., 647, 201

Contreras S., Baugh C. M., Norberg P., Padilla N., 2013, Mon. Not. Roy. Astron. Soc., 432, 2717

Contreras S., Baugh C. M., Norberg P., Padilla N., 2015, Mon. Not. Roy. Astron. Soc., 452, 1861

Cooray A., Milosavljevic M., 2005, Astrophys. J., 627, L89

Copeland E. J., Sami M., Tsujikawa S., 2006, Int. J. Mod. Phys., D15, 1753

Cowley W. I., Lacey C. G., Baugh C. M., Cole S., 2016, Mon. Not. Roy. Astron. Soc., 461, 1621

Crain R. A., et al., 2015, Mon. Not. Roy. Astron. Soc., 450, 1937

Crocce M., Scoccimarro R., 2006, Phys. Rev. D, 73, 063519

Crocce M., Pueblas S., Scoccimarro R., 2006, Mon. Not. Roy. Astron. Soc., 373, 369

Crocce M., Gaztañaga E., Cabré A., Carnero A., Sánchez E., 2011, Mon. Not. Roy. Astron. Soc., 417, 2577

DESI Collaboration et al., 2016, preprint, (arXiv:1611.00036)

D'Souza R., Vegetti S., Kauffmann G., 2015, Mon. Not. Roy. Astron. Soc., 454, 4027

Dark Energy Survey Collaboration 2016, Mon. Not. Roy. Astron. Soc., 460, 1270

Dawson K. S., et al., 2013, Astron. J., 145, 10

Dawson K. S., et al., 2016, Astron. J., 151, 44

De Felice A., Tsujikawa S., 2010, Living Rev.Rel., 13, 3

Del Popolo A., Le Delliou M., 2017, Galaxies, 5, 17

Desmond H., Mao Y.-Y., Wechsler R. H., Crain R. A., Schaye J., 2017, Mon. Not. Roy. Astron. Soc., 471, L11

Devi N. C., Rodríguez-Puebla A., Valenzuela O., Avila-Reese V., Hernández-Aguayo C., Li B., 2019, Mon. Not. Roy. Astron. Soc., 488, 782

Dey A., et al., 2019, Astron. J., 157, 168

Dodelson S., Schneider M. D., 2013, Phys. Rev. D, 88, 063537

Drinkwater M. J., et al., 2010, Mon. Not. Roy. Astron. Soc., 401, 1429

Dvali G. R., Gabadadze G., Porrati M., 2000, Phys. Lett., B485, 208

Efstathiou G., Kaiser N., Saunders W., Lawrence A., Rowan-Robinson M., Ellis R. S., Frenk C. S., 1990, Mon. Not. Roy. Astron. Soc., 247, 10P

Einstein A., 1916, Annalen der Physik, 354, 769

Eisenstein D. J., Hu W., 1998, Astrophys. J., 496, 605

Eisenstein D. J., et al., 2001, Astron. J., 122, 2267

Eisenstein D. J., et al., 2005, Astrophys.J., 633, 560

Eisenstein D. J., Seo H.-J., White M., 2007a, Astrophys. J., 664, 660

Eisenstein D. J., Seo H.-J., Sirko E., Spergel D. N., 2007b, Astrophys. J., 664, 675

Ellewsen T. A., Falck B., Mota D. F., 2018, Astron. Astrophys., 615, A134

Falck B., Koyama K., Zhao G.-b., Li B., 2014, JCAP, 1407, 058

Falck B., Koyama K., Zhao G.-B., 2015, JCAP, 07, 049

Falck B., Koyama K., Zhao G.-B., Cautun M., 2018, Mon. Not. Roy. Astron. Soc., 475, 3262

Fang W., Wang S., Hu W., Haiman Z., Hui L., May M., 2008, Phys. Rev. D, 78, 103509

Farrow D. J., et al., 2015, Mon. Not. Roy. Astron. Soc., 454, 2120

Feldman H. A., Kaiser N., Peacock J. A., 1994, Astrophys. J., 426, 23

Feng Y., Di-Matteo T., Croft R. A., Bird S., Battaglia N., Wilkins S., 2016, Mon. Not. Roy. Astron. Soc., 455, 2778

Ferrero I., et al., 2017, Mon. Not. Roy. Astron. Soc., 464, 4736

Fitts A., et al., 2017, Mon. Not. Roy. Astron. Soc., 471, 3547

Flores R. A., Primack J. R., 1994, Astrophys. J. Lett., 427, L1

Fontanot F., Puchwein E., Springel V., Bianchi D., 2013, Mon. Not. Roy. Astron. Soc., 436, 2672

Foreman-Mackey D., Hogg D. W., Lang D., Goodman J., 2013, PASP, 125, 306

Friedmann A., 1924, Zeitschrift fur Physik, 21, 326

Fry J. N., 1996, Astrophys. J. Lett., 461, L65

Gaia Collaboration et al., 2016, A & A, 595, A1

Garrison L. H., Eisenstein D. J., Ferrer D., Tinker J. L., Pinto P. A., Weinberg D. H., 2018, Astrophys. J. Suppl., 236, 43

Gil-Marín H., et al., 2018, Mon. Not. Roy. Astron. Soc., 477, 1604

Giodini S., et al., 2009, Astrophys. J., 703, 982

Gonzalez-Perez V., Lacey C. G., Baugh C. M., Lagos C. D. P., Helly J., Campbell D. J. R., Mitchell P. D., 2014, Mon. Not. Roy. Astron. Soc., 439, 264

Gonzalez-Perez V., et al., 2018, Mon. Not. Roy. Astron. Soc., 474, 4024

Gonzalez-Perez V., et al., 2020, preprint (arXiv:2001.06560)

Grieb J. N., Sánchez A. G., Salazar-Albornoz S., Dalla Vecchia C., 2016, Mon. Not. Roy. Astron. Soc., 457, 1577

Grieb J. N., et al., 2017, Mon. Not. Roy. Astron. Soc., 467, 2085

Hada R., Eisenstein D. J., 2018, Mon. Not. Roy. Astron. Soc., 478, 1866

Hamaus N., Sutter P. M., Lavaux G., Wandelt B. D., 2015, JCAP, 1511, 036

Hamaus N., Cousinou M.-C., Pisani A., Aubert M., Escoffier S., Weller J., 2017, JCAP, 1707, 014

Hamilton A. J. S., 1992, Astrophys. J. Lett., 385, L5

Hamilton A. J. S., 1998, in Hamilton D., ed., Astrophysics and Space Science Library Vol. 231, The Evolving Universe. p. 185 (arXiv:astro-ph/9708102), doi:10.1007/978-94-011-4960-0˙17

Hammami A., Llinares C., Mota D. F., Winther H. A., 2015, Mon. Not. Roy. Astron. Soc., 449, 3635

Hand N., Feng Y., Beutler F., Li Y., Modi C., Seljak U., Slepian Z., 2018, Astron. J., 156, 160

Hartlap J., Simon P., Schneider P., 2007, Astron. Astrophys., 464, 399

Hastings W. K., 1970, Biometrika, 57, 97

Hawkins E., et al., 2003, Mon. Not. Roy. Astron. Soc., 346, 78

He J.-h., Li B., 2016, Phys. Rev. D, 93, 123512

He J.-h., Guzzo L., Li B., Baugh C. M., 2018, Nature Astron., 2, 967

Hellwing W. A., Schaller M., Frenk C. S., Theuns T., Schaye J., Bower R. G., Crain R. A., 2016, Mon. Not. Roy. Astron. Soc., 461, L11

Henriques B. M. B., White S. D. M., Thomas P. A., Angulo R., Guo Q., Lemson G., Springel V., Overzier R., 2015, Mon. Not. Roy. Astron. Soc., 451, 2663

Hernández-Aguayo C., Baugh C. M., Li B., 2018, Mon. Not. Roy. Astron. Soc., 479, 4824

Hernández-Aguayo C., Hou J., Li B., Baugh C. M., Sánchez A. G., 2019, Mon. Not. Roy. Astron. Soc., 485, 2194

Hernández-Aguayo C., Arnold C., Li B., Baugh C. M., 2020a, *in prep.*

Hernández-Aguayo C., Cautun M., Smith A., Baugh C. M., Li B., 2020b, Mon. Not. Roy. Astron. Soc., 494, 3120

Hernández-Aguayo C., Prada F., Baugh C. M., Klypin A., 2020a, preprint (arXiv:2006.00612)

Hernández-Aguayo C., Arnold C., Li B., Baugh C. M., 2020b, preprint (arXiv:2006.15467)

Hinshaw G., et al., 2013, Astrophys. J. Suppl., 208, 19

Hinterbichler K., Khoury J., 2010, Phys. Rev. Lett., 104, 231301

Hou J., et al., 2018, Mon. Not. Roy. Astron. Soc., 480, 2521

Howlett C., Ross A., Samushia L., Percival W., Manera M., 2015, Mon. Not. Roy. Astron. Soc., 449, 848

Hu W., Kravtsov A. V., 2003, Astrophys. J., 584, 702

Hu W., Sawicki I., 2007, Phys. Rev., D76, 064004

Icaza-Lizaola M., et al., 2020, Mon. Not. Roy. Astron. Soc., 492, 4189

Ishak M., 2019, Living Rev. Rel., 22, 1

Jackson J. C., 1972, Mon. Not. Roy. Astron. Soc., 156, 1P

Jasche J., Lavaux G., 2019, Astron. Astrophys., 625, A64

Jenkins A., 2010, Mon. Not. Roy. Astron. Soc., 403, 1859

Jenkins A., 2013, Mon. Not. Roy. Astron. Soc., 434, 2094

Jennings E., Baugh C. M., Li B., Zhao G.-B., Koyama K., 2012, Mon. Not. Roy. Astron. Soc., 425, 2128

Jiang L., Helly J. C., Cole S., Frenk C. S., 2014, Mon. Not. Roy. Astron. Soc., 440, 2115

Jiménez E., Contreras S., Padilla N., Zehavi I., Baugh C. M., Gonzalez-Perez V., 2019, Mon. Not. Roy. Astron. Soc., 490, 3532

Joyce A., Jain B., Khoury J., Trodden M., 2015, Physics Reports, 568, 1

Kaiser N., 1986, Mon. Not. Roy. Astron. Soc., 219, 785

Kaiser N., 1987, Mon. Not. Roy. Astron. Soc., 227, 1

Kazin E. A., Sánchez A. G., Blanton M. R., 2012, Mon. Not. Roy. Astron. Soc., 419, 3223

Khoury J., Weltman A., 2004, Phys. Rev., D69, 044026

Kitanidis E., et al., 2020, Mon. Not. Roy. Astron. Soc., 496, 2262

Klypin A., Holtzman J., 1997, preprint (arXiv:astro-ph/9712217)

Klypin A., Prada F., 2018, Mon. Not. Roy. Astron. Soc., 478, 4602

Klypin A. A., Kravtsov A. V., Valenzuela O., Prada F., 1999, Astrophys. J., 522, 82

Klypin A., Prada F., Yepes G., Hess S., Gottlober S., 2013, preprint (arXiv:1310.3740)

Klypin A., Yepes G., Gottlober S., Prada F., Hess S., 2016, Mon. Not. Roy. Astron. Soc., 457, 4340

Koyama K., 2016, Rept. Prog. Phys., 79, 046902

Koyama K., 2018, Int. J. Mod. Phys. D, 27, 1848001

Koyama K., Silva F. P., 2007, Phys. Rev. D, 75, 084040

Kravtsov A. V., Berlind A. A., Wechsler R. H., Klypin A. A., Gottloeber S., Allgood B., Primack J. R., 2004, Astrophys. J., 609, 35

Kuhlen M., Vogelsberger M., Angulo R., 2012, Phys. Dark Univ., 1, 50

Kwan J., Lewis G. F., Linder E. V., 2012, Astrophys. J., 748, 78

LSST Science Collaboration 2009, preprint, (arXiv:0912.0201)

Lacey C. G., et al., 2016, Mon. Not. Roy. Astron. Soc., 462, 3854

Lagos C. d. P., Tobar R. J., Robotham A. S. G., Obreschkow D., Mitchell P. D., Power C., Elahi P. J., 2018, Mon. Not. Roy. Astron. Soc., 481, 3573

Laureijs R., et al., 2011, preprint (arXiv:1110.3193)

Lee J., et al., 2020, preprint, (arXiv:2006.01039)

Leo M., Arnold C., Li B., 2019, Phys. Rev. D, 100, 064044

Lesgourgues J., 2011, preprint (arXiv:1104.2932)

Li B., Shirasaki M., 2018, Mon. Not. Roy. Astron. Soc., 474, 3599

Li B., Zhao G.-B., Teyssier R., Koyama K., 2012, JCAP, 1201, 051

Li B., Zhao G.-B., Koyama K., 2013a, JCAP, 5, 023

Li B., Hellwing W. A., Koyama K., Zhao G.-B., Jennings E., Baugh C. M., 2013b, Mon. Not. Roy. Astron. Soc., 428, 743

Li B., He J.-h., Gao L., 2016, Mon. Not. Roy. Astron. Soc., 456, 146

Linder E. V., 2003, Phys. Rev., D68, 083504

Linder E. V., Cahn R. N., 2007, Astroparticle Physics, 28, 481

Lippich M., et al., 2019, Mon. Not. Roy. Astron. Soc., 482, 1786

Liu X., et al., 2016, Physical Review Letters, 117, 051101

Llinares C., McCullagh N., 2017, Mon. Not. Roy. Astron. Soc., 472, L80

Lokas E. L., Mamon G. A., 2001, Mon. Not. Roy. Astron. Soc., 321, 155

Lombriser L., 2014, Annalen Phys., 526, 259

Lombriser L., Hu W., Fang W., Seljak U., 2009, Phys. Rev. D, 80, 063536

Lombriser L., Li B., Koyama K., Zhao G.-B., 2013, Phys. Rev., D87, 123511

Lombriser L., Simpson F., Mead A., 2015, Phys. Rev. Lett., 114, 251101

Loveday J., Peterson B. A., Efstathiou G., Maddox S. J., 1992, Astrophys. J., 390, 338

Lovisari L., Reiprich T., Schellenberger G., 2015, Astron. Astrophys., 573, A118

Manera M., et al., 2012, Mon. Not. Roy. Astron. Soc., 428, 1036

Marinacci F., et al., 2018, Mon. Not. Roy. Astron. Soc., 480, 5113

Marulli F., Veropalumbo A., Moscardini L., Cimatti A., Dolag K., 2017, Astron. Astrophys., 599, A106

Matsubara T., 2011, Phys. Rev. D, 83, 083518

McCarthy I. G., Schaye J., Bird S., Le Brun A. M., 2017, Mon. Not. Roy. Astron. Soc., 465, 2936

McCullagh N., Neyrinck M. C., Szapudi I., Szalay A. S., 2013, Astrophys. J. Lett., 763, L14

Merson A., Wang Y., Benson A., Faisst A., Masters D., Kiessling A., Rhodes J., 2018, Mon. Not. Roy. Astron. Soc., 474, 177

Merson A., Smith A., Benson A., Wang Y., Baugh C. M., 2019, Mon. Not. Roy. Astron. Soc., 486, 5737

Metropolis N., Rosenbluth A. W., Rosenbluth M. N., Teller A. H., Teller E., 1953, JCP, 21, 1087

Mitchell P. D., Lacey C. G., Baugh C. M., Cole S., 2016, Mon. Not. Roy. Astron. Soc., 456, 1459

Moore B., 1994, Nature, 370, 629

Moore B., Quinn T. R., Governato F., Stadel J., Lake G., 1999, Mon. Not. Roy. Astron. Soc., 310, 1147

Murray S. G., Power C., Robotham A. S. G., 2013, Astronomy and Computing, 3, 23

Naiman J. P., et al., 2018, Mon. Not. Roy. Astron. Soc., 477, 1206

Navarro J. F., Frenk C. S., White S. D. M., 1996, Astrophys. J., 462, 563

Navarro J. F., Frenk C. S., White S. D. M., 1997, Astrophys. J., 490, 493

Nelder J. A., Mead R., 1965, The Computer Journal, 7, 308

Nelson D., et al., 2018, Mon. Not. Roy. Astron. Soc., 475, 624

Nelson D., et al., 2019, Mon. Not. Roy. Astron. Soc., 490, 3234

Neyrinck M. C., Szapudi I., McCullagh N., Szalay A., Falck B., Wang J., 2018, Mon. Not. Roy. Astron. Soc., 478, 2495

Norberg P., Baugh C. M., Gaztañaga E., Croton D. J., 2009, Mon. Not. Roy. Astron. Soc., 396, 19

Okumura T., et al., 2016, Publ. Astron. Soc. Jap., 68, 38

Padmanabhan N., White M., Norberg P., Porciani C., 2009, Mon. Not. Roy. Astron. Soc., 397, 1862

Padmanabhan N., Xu X., Eisenstein D. J., Scalzo R., Cuesta A. J., Mehta K. T., Kazin E., 2012, Mon. Not. Roy. Astron. Soc., 427, 2132

Paillas E., Cautun M., Li B., Cai Y.-C., Padilla N., Armijo J., Bose S., 2019, Mon. Not. Roy. Astron. Soc., 484, 1149

Pakmor R., Springel V., 2013, Mon. Not. Roy. Astron. Soc., 432, 176

Pakmor R., Bauer A., Springel V., 2011, Mon. Not. Roy. Astron. Soc., 418, 1392

Peacock J. A., Smith R. E., 2000, Mon. Not. Roy. Astron. Soc., 318, 1144

Peebles P. J. E., 1980, The large-scale structure of the universe

Percival W. J., et al., 2004, Mon. Not. Roy. Astron. Soc., 353, 1201

Pillepich A., et al., 2018a, Mon. Not. Roy. Astron. Soc., 473, 4077

Pillepich A., et al., 2018b, Mon. Not. Roy. Astron. Soc., 475, 648

Pillepich A., et al., 2019, Mon. Not. Roy. Astron. Soc., 490, 3196

Planck Collaboration 2018, preprint (arXiv:1807.06209)

Planck Collaboration XIII 2016, Astron. Astrophys., 594, A13

Prakash A., et al., 2016, Astrophys. J. Suppl., 224, 34

Press W. H., Schechter P., 1974, Astrophys. J., 187, 425

Prunet S., Pichon C., Aubert D., Pogosyan D., Teyssier R., Gottloeber S., 2008, Astrophys. J. Suppl., 178, 179

Read J., Agertz O., Collins M., 2016, Mon. Not. Roy. Astron. Soc., 459, 2573

Reddick R. M., Wechsler R. H., Tinker J. L., Behroozi P. S., 2013, Astrophys. J., 771, 30

Reid B. A., et al., 2010, Mon. Not. Roy. Astron. Soc., 404, 60

Ross A. J., Samushia L., Howlett C., Percival W. J., Burden A., Manera M., 2015, Mon. Not. Roy. Astron. Soc., 449, 835

Ross A. J., et al., 2017, Mon. Not. Roy. Astron. Soc., 464, 1168

Ruggeri R., Blake C., 2019, preprint, (arXiv:1909.13011)

Sahni V., Shtanov Y., 2003, JCAP, 11, 014

Samushia L., Percival W. J., Raccanelli A., 2012, Mon. Not. Roy. Astron. Soc., 420, 2102

Sánchez A. G., Crocce M., Cabré A., Baugh C. M., Gaztañaga E., 2009, Mon. Not. Roy. Astron. Soc., 400, 1643

Sánchez A. G., et al., 2012, Mon. Not. Roy. Astron. Soc., 425, 415

Sánchez A. G., et al., 2017, Mon. Not. Roy. Astron. Soc., 464, 1640

Sawala T., et al., 2016, Mon. Not. Roy. Astron. Soc., 457, 1931

Schaller M., et al., 2018, SWIFT: SPH With Inter-dependent Fine-grained Tasking, Astrophysics Source Code Library (ascl:1805.020)

Schaye J., Crain R. A., Bower R. G., Furlong M., Schaller M., et al., 2015, Mon. Not. Roy. Astron. Soc., 446, 521

Schmidt F., 2009a, Phys. Rev., D80, 043001

Schmidt F., 2009b, Phys. Rev., D80, 123003

Schmidt F., Lima M. V., Oyaizu H., Hu W., 2009, Phys. Rev., D79, 083518

Scoccimarro R., 2004, Phys. Rev. D, 70, 083007

Scoccimarro R., Couchman H. M. P., Frieman J. A., 1999, Astrophys. J., 517, 531

Sherwin B. D., Zaldarriaga M., 2012, Phys. Rev. D, 85, 103523

Sheth R. K., Connolly A. J., Skibba R., 2005, preprint (arXiv:astro-ph/0511773)

Shi D., Li B., Han J., Gao L., Hellwing W. A., 2015, Mon. Not. Roy. Astron. Soc., 452, 3179

Shi D., Li B., Han J., 2017, Mon. Not. Roy. Astron. Soc., 469, 705

Shi Y., Cautun M., Li B., 2018, Phys. Rev. D, 97, 023505

Simha V., Cole S., 2017, Mon. Not. Roy. Astron. Soc., 472, 1392

Skibba R. A., Sheth R. K., 2009, Mon. Not. Roy. Astron. Soc., 392, 1080

Skibba R., Sheth R. K., Connolly A. J., Scranton R., 2006, Mon. Not. Roy. Astron. Soc., 369, 68

Skibba R. A., et al., 2009, Mon. Not. Roy. Astron. Soc., 399, 966

Skibba R. A., et al., 2012, Mon. Not. Roy. Astron. Soc., 423, 1485

Smith A., Cole S., Baugh C., Zheng Z., Angulo R., Norberg P., Zehavi I., 2017, Mon. Not. Roy. Astron. Soc., 470, 4646

Somerville R. S., Primack J. R., 1999, Mon. Not. Roy. Astron. Soc., 310, 1087

Song Y.-S., Sawicki I., Hu W., 2007, Phys. Rev. D, 75, 064003

Song Y.-S., et al., 2015, Phys. Rev. D, 92, 043522

Sotiriou T. P., Faraoni V., 2010, Rev.Mod.Phys., 82, 451

Spergel D. N., et al., 2003, Astrophys. J. Suppl., 148, 175

Springel V., 2005, Mon. Not. Roy. Astron. Soc., 364, 1105

Springel V., 2010, Mon. Not. Roy. Astron. Soc., 401, 791

Springel V., White S. D. M., Tormen G., Kauffmann G., 2001, Mon. Not. Roy. Astron. Soc., 328, 726

Springel V., et al., 2005, Nature, 435, 629

Springel V., et al., 2018, Mon. Not. Roy. Astron. Soc., 475, 676

Stark A., Miller C. J., Kern N., Gifford D., Zhao G.-B., Li B., Koyama K., Nichol R. C., 2016, Phys. Rev., D93, 084036

Stoppacher D., et al., 2019, Mon. Not. Roy. Astron. Soc., 486, 1316

Strauss M. A., et al., 2002, Astron. J., 124, 1810

Tamura N., et al., 2016, Proc. SPIE Int. Soc. Opt. Eng., 9908, 99081M

Taruya A., 2016, Phys. Rev. D, 94, 023504

Taruya A., Nishimichi T., Saito S., 2010, Phys. Rev. D, 82, 063522

Taruya A., Koyama K., Hiramatsu T., Oka A., 2014, Phys. Rev., D89, 043509

Tegmark M., et al., 2006, Phys. Rev., D74, 123507

Teyssier R., 2002, Astron. Astrophys., 385, 337

Tinker J. L., 2007, Mon. Not. Roy. Astron. Soc., 374, 477

Tinker J. L., Weinberg D. H., Zheng Z., 2006, Mon. Not. Roy. Astron. Soc., 368, 85

Tinker J. L., Robertson B. E., Kravtsov A. V., Klypin A., Warren M. S., Yepes G., Gottlober S., 2010, Astrophys. J., 724, 878

Tröster T., et al., 2020, Astron. Astrophys., 633, L10

Vainshtein A. I., 1972, Phys. Lett., B39, 393

Vale A., Ostriker J. P., 2004, Mon. Not. Roy. Astron. Soc., 353, 189

Valogiannis G., Bean R., 2018, Phys. Rev. D, 97, 023535

Vogelsberger M., Genel S., Springel V., Torrey P., Sijacki D., et al., 2014, Nature, 509, 177

Vogelsberger M., Marinacci F., Torrey P., Puchwein E., 2020, Nature Rev. Phys., 2, 42

Wake D., et al., 2006, Mon. Not. Roy. Astron. Soc., 372, 537

Wake D. A., et al., 2008, Mon. Not. Roy. Astron. Soc., 387, 1045

Wechsler R. H., Tinker J. L., 2018, Ann. Rev. Astron. Astrophys., 56, 435

Weinberg D. H., Bullock J. S., Governato F., Kuzio de Naray R., Peter A. H. G., 2014, Proc. Nat. Acad. Sci., 112, 12249

Weinberger R., et al., 2017, Mon. Not. Roy. Astron. Soc., 465, 3291

Weinberger R., Springel V., Pakmor R., 2020, Astrophys. J. Suppl., 248, 32

White M., 2016, JCAP, 1611, 057

White M., Padmanabhan N., 2009, Mon. Not. Roy. Astron. Soc., 395, 2381

White S. D. M., Rees M. J., 1978, Mon. Not. Roy. Astron. Soc., 183, 341

White M., et al., 2011, Astrophys. J., 728, 126

White M., Reid B., Chuang C.-H., Tinker J. L., McBride C. K., Prada F., Samushia L., 2015, Mon. Not. Roy. Astron. Soc., 447, 234

Winther H. A., Mota D. F., Li B., 2012, Astrophys. J., 756, 166

Winther H. A., et al., 2015, Mon. Not. Roy. Astron. Soc., 454, 4208

Xu L., 2015, Phys. Rev., D91, 063008

Xu X., Cuesta A. J., Padmanabhan N., Eisenstein D. J., McBride C. K., 2013, Mon. Not. Roy. Astron. Soc., 431, 2834

Yang X.-h., Mo H. J., van den Bosch F. C., 2003, Mon. Not. Roy. Astron. Soc., 339, 1057

Zarrouk P., et al., 2018, Mon. Not. Roy. Astron. Soc., 477, 1639

Zehavi I., et al., 2005, Astrophys. J., 621, 22

Zehavi I., et al., 2011, Astrophys. J., 736, 59

Zhai Z., et al., 2017, Astrophys. J., 848, 76

Zhao G.-B., Li B., Koyama K., 2011, Phys. Rev. Lett., 107, 071303

Zheng Z., et al., 2005, Astrophys. J., 633, 791

Zheng Z., Coil A. L., Zehavi I., 2007, Astrophys. J., 667, 760

Zheng Z., Zehavi I., Eisenstein D. J., Weinberg D. H., Jing Y., 2009, Astrophys. J., 707, 554

Zhou R., et al., 2020, preprint (arXiv:2001.06018)

Zhu H.-M., Yu Y., Pen U.-L., Chen X., Yu H.-R., 2017, Phys. Rev. D, 96, 123502

Zivick P., Sutter P. M., Wandelt B. D., Li B., Lam T. Y., 2015, Mon. Not. Roy. Astron. Soc., 451, 4215

de Jong R. S., et al., 2016, in Ground-based and Airborne Instrumentation for Astronomy VI. p. 99081O, doi:10.1117/12.2232832